SANDIA REPORT

SAND97–0071 • UC–700
Unlimited Release
Printed January 1997

Fuel Elements of Thermionic Converters

A.S. Gontar, M.V. Nelidov, Yu.V. Nikolaev, L.N. Schulepov

Regina L. Hunter, Editor

Prepared by
Sandia National Laboratories
Albuquerque, New Mexico 87185 and Livermore, California 94550
for the United States Department of Energy
under Contract DE-AC04-94AL85000

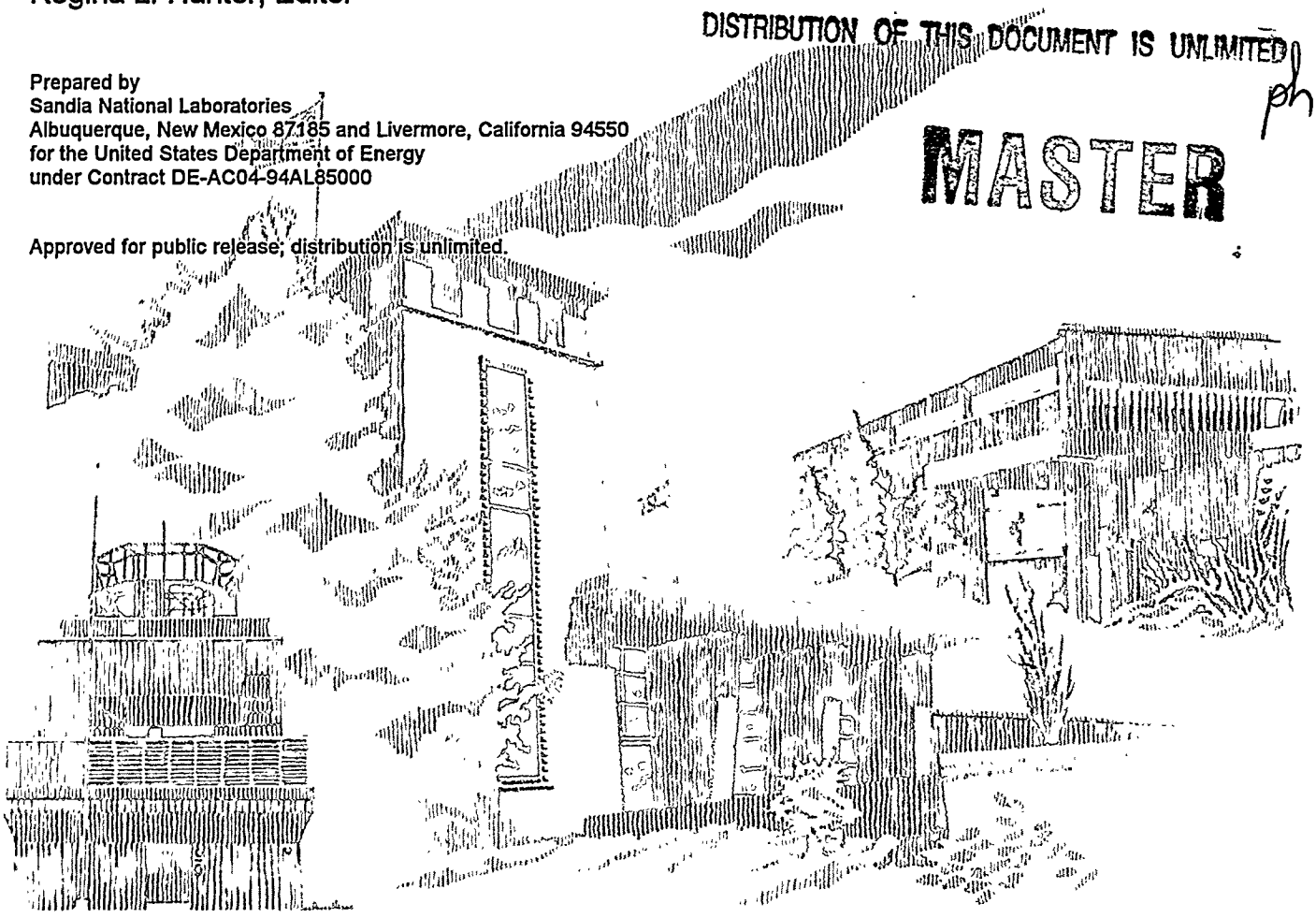

SF2900Q(8-81)

Issued by Sandia National Laboratories, operated for the United States Department of Energy by Sandia Corporation.

Available to DOE and DOE contractors from
Office of Scientific and Technical Information
P.O. Box 62
Oak Ridge, TN 37831

Prices available from (615) 576-8401, FTS 626-8401

Available to the public from
National Technical Information Service
U.S. Department of Commerce
5285 Port Royal Rd
Springfield, VA 22161

NTIS price codes
Printed copy: A13
Microfiche copy: A01

SAND97-0071
Unlimited Release
Printed January 1997

Distribution
Category UC-700

Fuel Elements of Thermionic Converters

A.S. Gontar
M.V. Nelidov
Yu.V. Nikolaev
L.N. Schulepov
RI SIA "Lutch," Podolsk, Moscow Region
Russian Federation

Regina L. Hunter, Ed.
Environmental Systems Assessment Dept.
Sandia National Laboratories
Albuquerque, NM 87185-0718

Abstract Follows

ABSTRACT

The thermionic reactor-convertor (TRC) incorporates a nuclear power source and a heat-to-electricity power convertor into a single assembly, allowing the production of electrical energy without an intermediate stage of heat-to-mechanical energy conversion. Nuclear power systems (NPSs) based on TRCs have many attractive properties that make them suitable candidates for power supplies in space applications, where compactness, light weight, and high efficiency of components is at a premium.

Work on thermionic nuclear power systems has been performed in Russia within the framework of the TOPAZ reactor program since the early 1960s. In the TOPAZ in-core thermionic convertor reactor design, the fuel element's cladding is also the thermionic convertor's emitter. Deformation of the emitter can lead to short-circuiting and is the primary cause of premature TRC failure. Such deformation can be the result of fuel swelling, thermocycling, or increased unilateral pressure on the emitter due to the release of gaseous fission products. Much of the work on TRCs has concentrated on preventing or mitigating emitter deformation by improving the following materials and structures:

- nuclear fuel (modified UO_2, UN, UC-UN, UC-US, UC-ZrC, UC-NbC, and UC-TaC);
- emitter materials (single crystal alloys of molybdenum and tungsten, including the W-184 isotope);
- electrical insulators (poly- and single-crystal alumina, scandia);
- moderator and reflector materials (zirconium and yttrium hydrides, beryllium, protective coatings, etc.);
- gas-exhaust device.

In addition, considerable effort has been directed toward the development of experimental techniques that accurately mimic operational conditions and toward the creation of analytical and numerical models that allow operational conditions and behavior to be predicted without the expense and time demands of in-pile tests.

New and modified materials and structures for the cores of thermionic NPSs and new fabrication processes for the materials have ensured the possibility of creating thermionic NPSs for a wide range of powers, from tens to several hundreds of kilowatts, with life spans of 5 to 10 years.

Acknowledgments

Mrs. N. Yu. Swistunova typed the text in Russian and English. Mr. W. A. Reshetnikov provided translation from Russian to English. Evan C. Dudley of Sandia National Laboratories prepared the final manuscript. We appreciate their support.

CONTENTS

TABLES

FIGURES

List of Abbreviations

TEC	thermionic energy converter
TFE	thermionic fuel element
TRC	thermionic reactor-converter
NPS	nuclear power system
NPPS	nuclear power propulsion system
PWR	pressurized water reactor
GFP	gaseous fission products
GED	gas exhaust device
IEG	inter-electrode gap
SC	short circuit
TD	theoretical density
LTEC	linear thermal expansion coefficient
IPPE	Institute of Physics and Power Engineering (Obninsk, Kaluga region)

FOREWORD

Beginning in the 1960s, in Russia, the United States, and a number of other countries, efforts focused on the direct conversion of heat to electric power using thermionic energy converters (TECs) increased greatly. The interest in this subject is based on the potential advantages of energy conversion without an intermediate stage of heat-to-mechanical-power conversion. Use of TECs in combination with a nuclear reactor allows the construction of a fundamentally new type of power system, in which the thermal power source and a heat-to-electricity power convertor are incorporated into a single assembly, the thermionic reactor-converter (TRC).

Nuclear power systems (NPSs) based on thermionics are, in view of their many attractive properties, suitable candidates for power supplies in space applications. Such properties include

- high temperature heat rejection, in comparison to other techniques for energy conversion, which provides a minimum radiator size;
- high specific power;
- localization of high temperature within the emitter and a moderate temperature in the rest of the plant;
- compactness and compatability with modern means of space transportation; and
- absence of vibration.

These features enable the creation of compact, light-weight, high-efficiency NPSs, competitive with NPSs based on thermoelectric and mechanical techniques for energy conversion.

Work on thermionic NPSs is being performed in Russia within the framework of the TOPAZ program, which began in the early 1960s [1]. TOPAZ reactors comprise thermionic reactor-convertors (TRCs) with either single-cell (TOPAZ-2) or multi-cell (TOPAZ-1) cylindrical thermionic fuel elements (TFEs) making up the reactor core. The TFE is the basic element of the reactor-convertor, in which the conversion of heat to electrical power takes place.

In 1987 and 1988, TOPAZ-1 was tested during the missions of the Kosmos-series spacecrafts [1]. For the first time, operability of the thermionic-type NPS was confirmed under space conditions. Successful long-term (~1.5 years) land-based tests of TOPAZ-2 NPSs were also conducted [2].

Russia has taken a leading role in creating thermionic power conversion plants. Much related research and development (R&D) has been completed, from the fundamental physical and technological basis to successful land-based and space tests of the nuclear power systems.. In the TOPAZ program, the Research Institute of SIA (RI SIA "Lutch") is the head organization in developing a single-cell TFE for TOPAZ-2 NPSs. In the course of these efforts, the infrastructure

required for subsequently advancing thermionic research has been built at RI SIA, including laboratory, experimental/testing stands, and processing and production facilities. Today, RI SIA's facilities and experience are being used to create a new generation of more efficient plants for space and terrestrial applications.

TECs having high efficiency and long life have become feasible only after development of a number of new materials. RI SIA "Lutch" has conducted a wide scope of R&D relating to materials for the cores of thermionic NPSs and fabrication processes for them [2]:

- nuclear fuel (modified UO_2, UN, UC-UN, UC-US, UC-ZrC, UC-NbC, UC-TaC);
- emitter materials (single-crystal alloys of molybdenum and tungsten, including the W-184 isotope);
- electroinsulation (poly- and single-crystal alumina, scandia); and
- moderator and reflector materials (zirconium and yttrium hydrides, beryllium, protective coatings, etc.).

The unique materials developed at the institute secure the possibility of creating thermionic NPSs for a wide range of powers, from tens to several hundreds of kilowatts, with life spans of 5 to 10 years [2]. Application of the materials and processes created at the organization to other engineering areas such as electronics, electrical technology, machine building, metallurgy, nuclear energetics, medicine, rocket manufacture, etc., is also promising.

Research, development, and attainment of practical results in these directions can be accelerated through cooperation between Russian scientists and experts in other countries.

REFERENCES

1. Ponomarev-Stepnoy, N.N. "The Nuclear Power in Space." *Atomic Energy*, 1989, v. 66, iss. 4, pp. 371-374.
2. Nikolaev, Yu.V. "RI SIA "Lutch"'s R&D in the Area of Materials for NPPs of Direct Conversion." Report at the 4th Branch Conference "Nuclear Power in the Space. Materials. Fuel." Podolsk, 1993.

CHAPTER 1

DATA ON OPERATING CONDITIONS OF THERMIONIC FUEL ELEMENTS, THEIR DESIGN, AND PROBLEMS OF DEVELOPING LONG LIFE CAPABILITIES

1.1. Fuel Element Operating Conditions

1.1.1. Temperature and Power Conditions of Fuel Element Operation

For the TOPAZ in-core thermionic reactor converter design, the fuel element's cladding is also the thermionic converter's emitter. This configuration allows the high temperature required to achieve high emission current density. Previous work [1] specified 1300 to 1400°C as minimum temperatures of the emitter at which parameters acceptable for a power plant may be feasible and provided characteristic temperature/power operating conditions for oxide fuel within different type fuel elements. Table 1.1 compares the characteristic operating conditions for pressurized-water-reactor (PWR) fuel elements and thermionic fuel elements.

Figure 1.1 shows the dependence of specific output electrical power on emitter temperature [2] for thermionic converter designs being developed at RI SIA "Lutch". As shown in the figure, output power grows almost linearly with elevation of the emitter temperature. However, raising the emitter temperature is limited by currently available structural and fuel materials. The aggregate of research results available suggest that to secure a long life, the emitter units'

Table 1.1. Characteristic operating conditions for PWR and thermionic fuel elements [1]

Fuel Element Type	Temperature, °C		Temperature Gradient, K/cm	Burnup, fiss./cm^3	Burnup Rate, fiss./(cm^3·s)
	Fuel Element Center	Fuel Element Surface			
PWR type fuel element	Up to melting point	300	Up to $3 \cdot 10^3$	Below $1.5 \cdot 10^{21}$	$1 \cdot 10^{13}$
Fuel element of thermionic converter	1500-2000	1400-1800	Up to 500	Below $3 \cdot 10^{20}$	$3 \cdot 10^{12}$

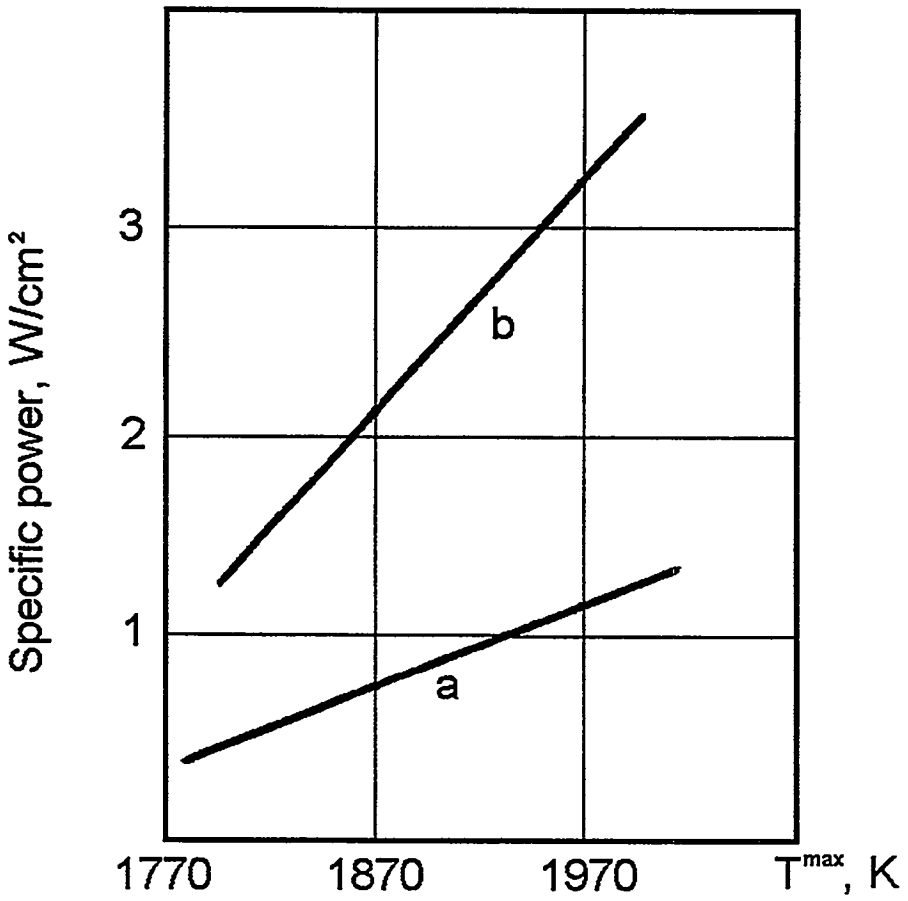

Figure 1.1. Specific power of TFE vs. temperature of emitter:
a) a single-cell TFE;
b) a multi-cell TFE.

temperature and mean specific output power of the converter must be restricted to values of 1800°C and 5 W/cm^2 [3].

Key operating parameters of TFEs, already developed and being designed at RI SIA "Lutch," are listed in Table 1.2. The temperature and power parameters of these TFEs lie in the middle of ranges given in Table 1.1 for operating temperatures and specific electrical power of thermionic fuel elements.

Table 1.2. Basic characteristics of single and multi-cell TFEs developed and being designed at RI SIA "Lutch" [2]

	TOPAZ-2 TFE	TOPAZ-3 TFE	Multi-Cell TFE
Output power, W	150	400	800
Current, A	170	500	200
Voltage, V	0.9	0.8	4.0
Mean Specific Electric Power, W/cm^2	0.65	1.4	2.5
Efficiency, %	5.3	7.7	10 to 12
Emitter Maximum Temperature, K	1830	1880	1880
Fuel Element Maximum Temperature, K	2000	2050	2200
Forecast Lifetime, years	3 to 5	7 to 10	7 to 10

1.1.2. Need for Ventilation of Fuel Elements of Thermionic Converters

A major requirement for reactors of nuclear power systems in space applications is the minimally feasible overall size and mass of such a reactor [4]. An adverse effect on the reactivity balance within the in-core type reactor-converter is exerted by the presence in the core of a greater number of structural materials (emitter, collector, spacers, insulation, commutation elements, etc.), as compared to reactors for terrestrial power plants. To compensate for this effect, a high-density, high-enrichment fuel appears to be necessary. Uranium dioxide with a density of over 95% of theoretical and enrichment of 90% U^{235} is routinely used [2].

In addition, a high temperature causes the structure of all or a significant portion of the fuel to convert to a column-type structure [1], characterized by much greater release of gaseous fission products (GFP) in comparison to as-fabricated fuel with equiaxial grain structure. These circumstances eliminate free

space sufficient to retain the GFPs within the thermionic fuel elements under tolerable pressures.

Estimates show that, for a fuel element with a cladding temperature of 1900 K, yearly burnup of $3 \cdot 10^{20}$ fissions/cm^3, and a central cavity space constituting 20% of the fuel element volume, the GFP pressure within the gas-tight cladding equals 10 MPa [1], which may cause an intolerable radial deformation of the cladding. Hence, thermionic fuel elements demand ventilation of the inner cavity of the fuel element, which complicates the TFE structure, specifically for exhaust systems in multi-cell TFEs. In the latter case, building a gas vent line throughout all the TFEs calls for fabrication of a large number of gas-tight high-temperature ceramic-metal units within the TFE core, which impairs tightness, extends the distance between fuel elements, and spoils the neutron physical parameters. There is a possibility of use of a TFE with communicating or partially separated fuel-element and inter-electrode gap (IEG) cavities, which substantially simplifies the design [2]. However, in this case the fuel element is an abundant source of IEG contamination. GFPs, residual gases from the fuel and structural materials, and products of fuel decomposition and of chemical reactions with the fission fragments pass through the IEG. In the fuel element version with partial separation of the fuel-element and IEG cavities, GFPs are also removed via the IEG, but the GFPs first pass through relatively cold channels within the collector body. Some components hazardous to the IEG, e.g., Cs_2CaO_3, are deposited on the channel walls. On the other hand, given communicating fuel-element and IEG cavities, the IEG gas atmosphere extends to the fuel element's inner cavity. Having a high chemical reactivity, cesium can attack some fission products, as well as some fuel compositions, and take part in the mass-transfer processes. This question is considered in Chapter 3.

1.1.3. Reactor Types for the Thermionic NPS and Reactors for TFE Tests

Reactor types for thermionic power plants developed in Russia have been described by Ponomarev-Stepnoy [5]. For plants of small power (up to 100 kW output electrical power), the developments are conducted on the basis of a small power reactor with zirconium hydride moderator. In such reactors, which have in their core a significant amount of the moderator and structural material, heat is emitted mainly through fission processes induced by thermal and intermediate neutrons.

Until now this research trend has taken priority, and here most results have been achieved. The recommended volume of such reactor cores is restricted to 80 l or less, since, given the converter's optimal design, these reactors will have a core volume comparable to or even exceeding the core volume of a fast neutron reactor-converter of minimum critical size [3]. That is why thermionic systems with power over 100 kW are developing on the basis of the fast reactor.

TFEs are experimentally tested in loop channels, usually in research reactors having a thermal neutron spectrum rather than the epithermal spectrum typical of the TOPAZ concepts. The difference in spectrum may strongly distort the power and temperature distribution within fuel elements; consequently the variation in U^{235} enrichment has been studied as a means to correct this problem. This problem is considered in Chapter 4.

Another essential distinction between fuel-element operating conditions in the reactor-converter and in the loop channels of research reactors is the different character of these reactors' operation mode. The thermionic reactor-converter is usually exploited either in the steady-state mode or at a small number of power alterations during its lifetime. In research-reactor operation, because of the large number of concurrently performed experiments during TFE tests, many power changes and reactor shut-downs take place. This power cycling is one possible cause of the emitter deformation [1], and its contribution must be taken into account in analyzing the results of TFE loop tests in research reactors.

A distinctive feature of operating conditions of reactors for space NPSs is a strong vibrational effect upon them during launch. Ceramic elements, specifically fuel pellets, undergo the most destruction. In land-based operation, vibration is absent; therefore in the course of the development of space reactors, the system and its individual elements are subjected to vibration tests. Results of fuel pellet vibration tests are considered in Chapter 5.

1.2. Design Schemes and Choice of Fuel Element Basic Dimensions

1.2.1. Fuel Element Designs for Single and Multi-Cell TFEs. Analysis of Their Merits and Disadvantages

The most consistent and detailed analysis of concepts for single-cell and multi-cell TFEs of the thermionic NPS [2] provided the TFE design schemes presented in Figure 1.2. The main difference between the two designs is that the single-cell TFE electrode length equals the core length, i.e., the TFE contains one fuel element and one converter, while in the multi-cell TFE several relatively short fuel elements and converters connected in series are stacked together along the core length. For the same current through the circuit of converters connected in series, the multi-cell TFE output voltage equals the sum of individual converter voltages and, as seen from Table 1.2, substantially exceeds the single-cell TFE output voltage. Thus, the same output power in the single-cell TFE requires much higher currents than in the multi-cell TFE. Because ohmic losses increase proportionally to the current squared, at high current levels the losses become comparable to the output power. In spite of these restrictions on single-cell TFE use, to date it is advisable to apply the TFE single-cell design to the thermionic NPSs of electrical power up to 50 kW [2]. This is because the single-cell design

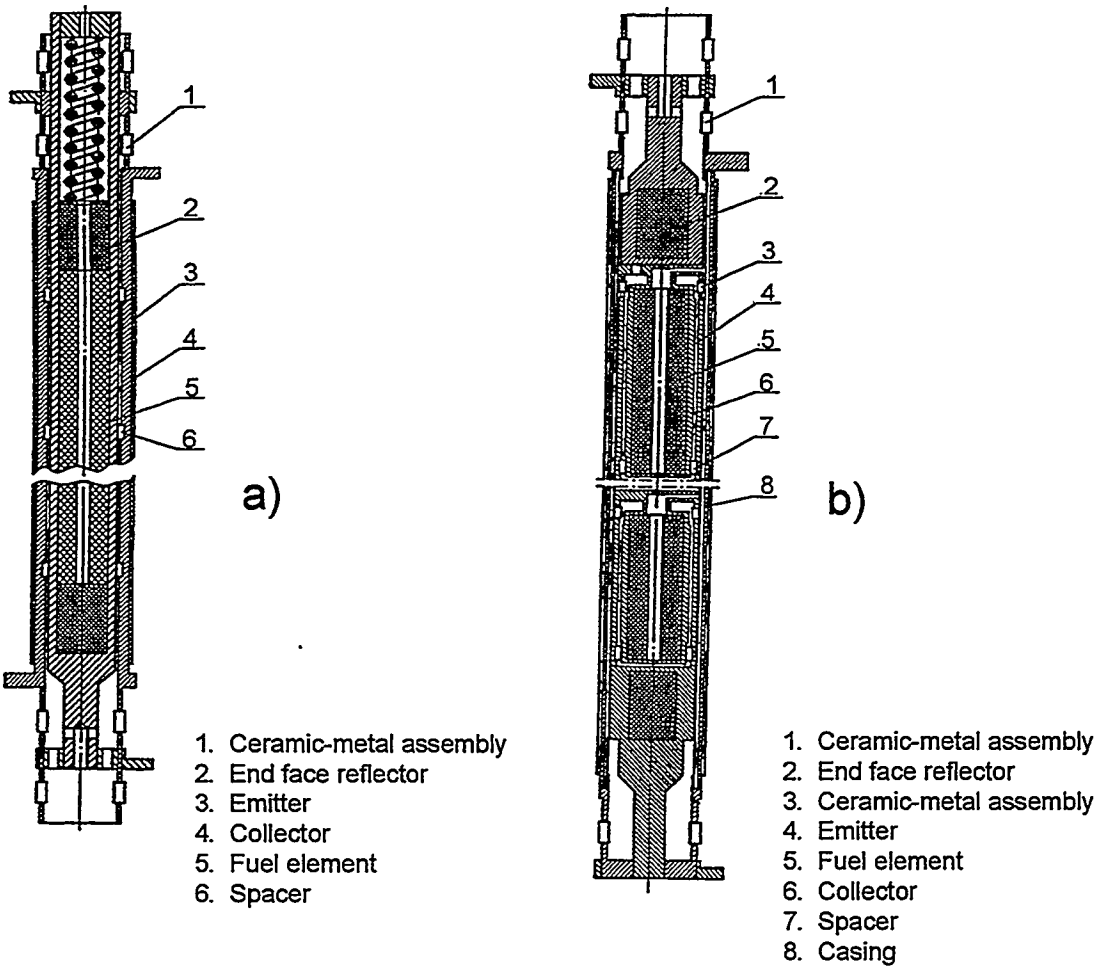

Figure 1.2. Construction diagrams of TFEs [2]:
a) a single-cell TFE;
b) a multi-cell TFE.

has a number of tangible advantages over the multi-cell design, chiefly the separation of the fuel-element and IEG cavities, which ensures stability of the TFE output parameters over the course of its life. One of the key problems in a long life—GFP removal from the fuel element inner space using the fuel stack's central channel with no dedicated gas-exhaust devices—is easily solved.

Another important advantage of single-cell design is the free access to the inner cavity of the single-cell TFE emitter, which significantly simplifies fabrication, testing, and operation. In tests, it is possible to test the TEC design in a testbed with electric heating of the emitter. It is possible to perform thermal treatment of the TEC in a vacuum at emitter operating temperatures and to check its gas-tightness and output heat/electric parameters during manufacturing to improve quality control. Fabrication, installation, and transportation of the reactor and NPS as a whole are simplified by the absence of fuel pellets in the TFE emitter cavity at these stages. The pellets may be assembled within the NPS immediately before preparing a spacecraft for launch. Finally, the reactor needs no additional fuel elements to adjust reactivity.

These advantages were used in creating the TFE of the TOPAZ-2 reactor, which was developed and tested using electrically heated testbeds, in-pile loop experiments, and tests in experimental reactor-converter cores. The overall merit of the single-cell design is shown by the longest operation with stable parameters having been achieved in a single-cell TFE reactor.

The TOPAZ-2 TFE lifetime forecasted from these results is not shorter than 3 years. Investigations have shown that improvement of the fuel constituent alone will allow lifetimes up to 5 or 6 years. The experience gained in the course of creating this TFE has revealed the margins of power potential for the single-cell electrogenerating channel. On this basis, a TFE design for a "TOPAZ-3" reactor of electrical power up to 40 kW has been developed. The main parameters of the TOPAZ-3 TFE are provided in Table 1.2.

1.2.2. Choice of Fuel Elements' Basic Dimensions

The most complete data on optimal geometric dimensions of the thermionic fuel elements were obtained using multi-parametric optimization [6]. Several factors were simultaneously optimized: emitter length and diameter; thicknesses of emitter, collector, and insulation; commutation jumper's cross-section; operating voltage as restricted by the need to provide the system criticality, and practical limitations on fabrication. Formulas for calculation of the fuel element parameters' optimal values have also been given by Sinyavsky et al. [7].

The reactor-converter's basic characteristics—core volume, fuel load, overall emission area, and emission area per unit core volume—are to a crucial extent governed by the TFE radial dimensions, since the fuel stack's and structural materials' fractions in the core are functions of fuel-stack diameter and the emitter

and collector thickness. Griaznov et al. [3] concluded that the emitter units' optimal diameter—to meet all the life-related demands on the channel design—must be chosen considering a number of conditions:

- reactor's critical size close to minimally feasible for emission areas up to 1 m^2 in the thermal neutron reactor-converter, taking into account required margins of reactivity;
- minimum critical size of fast neutron reactor-converter;
- specific area of emission as large as possible.

Andreev et al.'s work [8] in optimizing the TFE radial dimensions also takes into consideration the core structure: moderator fraction; fuel porosity; coolant fraction in the core; and contribution of commutation. As a result of their investigations they concluded [8] that, at output power up to 300 kW and value of the emission area up to 10 m^2, the optimal (i.e., meeting the considered conditions in the best way) radial dimensions of a TFE for both thermal neutron and fast reactors, have the following ranges:

$$15.5 \text{ mm} < d_p < 17.5 \text{ mm}$$
$$18 \text{ mm} < d_{em} < 20 \text{ mm}$$
$$22 \text{ mm} < d_{TFE} < 25 \text{ mm},$$

where: d_p - diameter of fuel pellets;
d_{em} - diameter of emitter;
d_{TFE} - diameter of TFE.

At higher output reactor power it is necessary to turn to smaller radial dimensions. According to Griaznov et al. [3], at high electrical power, seeking a maximum area of emission becomes crucial in the choice of the radial size, i.e., a minimum feasible diameter of the emitter unit is necessary, which appears to be 10 to 12 mm. For the TFE versions under development at RI SIA "Lutch", the radial size stays as a rule within the above-mentioned ranges for the optimal size. Maintaining the basic TOPAZ-2 TFE design scheme, with the objective of increasing power and lengthening life, only the emitter thickness has been modified considerably. Thus, in the transition from the TOPAZ-2 TFE to the SPACE-R reactor TFE, the emitter was thickened from 1.15 to 2.3 mm [9]. The inner diameter of the emitter prototype for the SPACE-R TFE, made in 1994, is 17.3 mm, as in the TOPAZ-2 TFE [9, 10].

The choice of number and lengths of fuel elements in the multi-cell TFE is made on the basis of optimizing the thermal and electrophysical calculation of TFE as a whole [7].

1.3. Causes of Fuel Element Failures and Methods for Eliminating Typical Failures

The thermionic nuclear power system is a complex system operating under conditions of high temperatures and irradiation. In the face of strict weight/size limitations and reactor criticality requirements, ensuring reliability using traditional design decisions and materials often turns out to be impossible. The primary path to securing long operability is, in this case, the development of new design solutions and structural materials. This discussion will encompass only those failures that are immediately linked to the fuel element. The major failure mode connected with the fuel element is the emitter-to-collector short circuit. The short circuit occurs when radial deformation of the emitter is comparable to the IEG value, usually not exceeding 0.5 mm.

The second malfunction type may be failure in the cladding integrity provoked by a chemical reaction with fuel, fission products, and cesium.

The third TFE malfunction type immediately linked to fuel-element operation is degradation of voltage/current characteristics under the effect of fuel components, i.e., impurities contained in fuel and fission products. Such a malfunction may develop when the fuel element cladding becomes permeable to harmful components or when the fuel-element and IEG cavities communicate with each other.

1.3.1. Fuel Element Deformation under the Effect of Pressure Loading of GFP Released by Fuel

Axial and radial temperature non-uniformity along the fuel stack cause fuel-material transfer, which tends to form a central cavity with an isothermal surface. Release of GFPs into the cavity formed leads to internal pressures building up to levels that result in deformation of the cladding, even when high-temperature materials are used for the cladding [1, 11, 12, 13]. Traditional ways of solving this problem by using a compensation space, increasing the cladding thickness, or reducing the cladding temperature prove to be inefficient because of the high cladding temperature requirements and rigid restrictions on free volume and structural-material volume. These circumstances, as noted in Section 1.1.2., bring about a need to ventilate the fuel element's inner space. Creation of a gas-exhaust system, however, substantially complicates the fuel-element design. An important portion of the following sections is dedicated to design choice and substantiation of the gas vent device, because as a practical matter the trouble-free operation time of the fuel element coincides with the operation time of the gas-exhaust system.

1.3.2. Fuel-Element Deformation under the Influence of Fuel Swelling

Fuel-element deformation because of fuel swelling has been characterized as the most serious reason for fuel-element geometric instability [1]. Fuel swelling under the effect of solid and gaseous fission products leads to fuel-volume expansion, causing cladding deformation if free space is not available. Even if free space is present, cladding deformation can occur if the fuel stack's resistance to creep exceeds the cladding creep resistance. Unlike power reactor fuel elements, a gap between the fuel and the cladding does not function as a compensating space, because at high fuel temperatures the gap fills quickly with fuel condensate. The most efficient technique for reducing the cladding deformation induced by fuel swelling is expansion of the free volume within a fuel element up to maximum permissible values and simultaneous strengthening of the fuel-element cladding. In aggregate these measures can redistribute the fuel swelling into the fuel-element free space. Fuel-element deformation under the effect of swelling is considered in Chapters 3 and 4.

1.3.3. Non-Irradiation Deformation of Emitter

Some known emitter-deformation mechanisms are not connected with fuel irradiation. Several investigators described the emitter-deformation mechanisms resulting from reactor power cycling [1, 13, 14, 15]. These deformations are caused by the difference in thermal expansion between fuel and cladding. In thermionic fuel elements, because of the high temperature, the gap between fuel and cladding fills with fuel condensate, and the cladding is in contact with the fuel stack. Raising the power increases the fuel-stack/cladding temperature. Due to a higher coefficient of UO_2 expansion, as well as to higher fuel temperatures, cladding deformation occurs, including inelastic deformation. When returning to a previous power, a gap may form, which during the next period of steady-state operation fills again with fuel condensate. Repeated power cycling will bring about permanent accumulation of cladding radial deformation by this mechanism. The deformation can also take place under thermocycling with a small amplitude, during which the fuel stack does not detach from the cladding [14, 15]. This question is considered in Chapter 5.

1.3.4. The Compatibility of Structural Materials with Fuel

The compatability of structural materials with fuel composition is necessary for securing a long life of the fuel element. As long ago as the early 1970s, investigations at RI SIA "Lutch" showed that, for practically all fuel types, single-crystal molybdenum and tungsten and a number of single-crystal alloys based on these metals are the best cladding materials [1].

Tungsten possesses higher strength and emission characteristics. When molybdenum is used, the emitter surface is applied with a single-crystal tungsten coating to improve its emission parameters. However, because of a large cross-section for thermal-neutron capture by natural tungsten, the W^{184} isotope, which has a small thermal-neutron-capture cross-section, must be used as the cladding material. As a result of the investigations, an emitter was built for the TOPAZ-2 single-cell TFE on the basis of a single-crystal alloy of molybdenum, coated with single-crystal tungsten. An emitter based on single-crystal tungsten alloys was created for the multi-cell TFE. These TFE tests did not reveal any interaction between the oxide fuel and the emitter.

Still more rigid conditions relate to structural elements located within a fuel element, e.g., the gas-exhaust system, for which tungsten and its alloys are used. Free oxygen is always present in the gaseous phase over the oxide fuel. Tungsten oxidation on the open surface and tungsten oxide's quick evaporation may induce rapid failure of the gas-exhaust system. Gontar et al. [17] studied the influence of uranium-dioxide composition on gas-exhaust-system workability. They inferred that a hypostoichiometric fuel of $UO_{1.995}$ composition at a 2000°C temperature does not significantly enhance the tungsten evaporation rate. Under the same conditions, in a gas environment over $UO_{2.005}$ fuel, the tungsten evaporation rate grows by almost six orders of magnitude, which can cause rapid failure of the gas-exhaust system. Thus, use of the hypostoichiometric fuel is expedient to provide long gas-exhaust system operability.

1.3.5. Influence of Fuel and Fission Products on Electrical Parameters of the Converter

A reactor-converter contains several sources of IEG contamination. The most important of these is the fuel element, which generates in the course of operation a wide spectrum of uranium fission products; the fuel element also appears to be a source of contaminants from fuel materials and impurities contained in fuel. In thermal neutron reactors, the IEG may contain a significant amount of hydrogen released from the moderator. Koryukin and Obrezumov [18] noted that the impurities' greatest effect on TFE parameters is the transfer and deposition of the impurities and emitter material onto the collector, causing a tangible change in the latter's characteristics. Given substantial thickness of the deposited layer, an additional resistor joins the electric circuit, deteriorating the converter parameters. In addition, flaking of the coating can lead to a short circuit between the emitter and the collector. In reviewing the mass transfer into the IEG in Chapter 3, it will be shown that intensity of the mass transfer in the IEG is mainly connected with its content of oxygen, hydrogen, and cesium.

Another important factor is the negative influence of some impurities on the electrodes' emission characteristics. As a rule, the presence of impurities results in

collector work-function increase and output-voltage reduction. It is known that some electronegative additions such as oxygen or fluorine exert a positive effect on the voltage-current characteristics of the converter [19]. But as previously noted, these additions also cause the chemical transport reaction. Baksht et al. [19] also examined the influence of a large number of both electronegative and electropositive additives on converter operation.

Among the additives adversely affecting the electrodes' work function is carbon, which is present in a considerable amount as an impurity of uranium dioxide. Carbon is a gas-forming impurity and is present as CO and CO_2 in a substantial concentration in gaseous phase. Nikolaev et al. [2] emphasized a particular role of carbon, i.e., if deposited on the insulators it can provoke electrical leakage and even short circuits.

The inert gases hydrogen and nitrogen contained in the IEG in significant amounts may exert an effect on electrical current in plasma [21, 22], but an unfavorable influence only results under appreciable pressure of these gases. With hydrogen pressure increase, the output voltage decreases linearly by 0.11 V/gPa [20].

The gaseous impurities within the IEG alter the gap's thermal conductivity and can bring about extra heat losses, thus decreasing the converter's efficiency. The effect of the inert gases He, Ar, and Xe on the IEG thermal conductivity has been studied by Modin et al. [22], who pointed out that under ~100 Pa gas pressure and constant heat flux delivery, the emitter temperature decreased by some tens of degrees.

The data given confirm the necessity for undertaking measures to reduce IEG contamination. In the course of creating the reactor-converter, RI SIA "Lutch" had developed and put into practice a number of measures aimed at the reduction of impurities in the IEG.

One way to lower the gaseous hydrogen concentration in the reactor is by applying a coating with low hydrogen permeability to zirconium hydride [16]. The release rate for hydrogen was reduced by 4 to 6 orders of magnitude. Encapsulation of the hydride in an oxidizing medium additionally decreased hydrogen evolution by 4 to 5 times.

A drastic measure to restrict the penetration of fuel components, fission products, and fuel impurities to the IEG had been transition from polycrystal to single-crystal cladding of a fuel element. The transition from the polycrystal cladding materials to single-crystal reduces uranium release into the IEG by 2 to 3 orders of magnitude [16].

As long-term tests in experimental nuclear cores showed, the above measures provided stability of the single-cell TFE's current voltage characteristics. A similar situation exists for the multi-cell TFE with isolated cavities of the fuel element and IEG. Nikolaev et al. [2] expressed the opinion that a long operability may be achieved for a TFE with communicating cavities when using oxide fuel, because

oxygen in small amounts is not hazardous to the converter operation and, by actively oxidizing the fission products to their less volatile state, aids in their retention within the fuel-element cavity. A key problem in this case is the oxide fuel purification of the carbon impurities. Questions concerning degassing of the oxide fuel are reviewed in Section 2. Continuous cesium pumping through the IEG, efficient removal of gaseous products from the IEG using diffusional processes, and magnetic pressure influencing the cesium plasma under TFE conditions, have also been suggested for use of TFE with communicating cavities [2].

1.4. References

1. Degaltsev, Yu.G., Ponomarev-Stepnoy, N.N., and Kuznetsov, V.F. *Behaviour High-Temperature Nuclear Fuel under Irradiation.* Moscow: Energo-atomizdat, 1987, 208 p.
2. Nikolaev, Yu.V., Kucherov, R.Ya., Gontar, A.S., et al. "Comparative Analysis of Concepts of Single-cell and Multi-cell TFE of Thermionic NPS." *Proc. 10th Symp. on Space Nuclear Power and Propulsion.* Albuquerque, 1993, part 3, pp. 1347-1353.
3. Griaznov, G.M, Zhabotinsky, E.E., Zrodnikov, A.Y., Nikolaev, Yu.V., et al. "Thermionic Reactors-Converters for Space NPP." *Atomnaya Energy,* 1989, v. 66, iss. 6, pp. 347-377.
4. Kuznetsov, V.A. *Nuclear Reactors for Space Power Plants.* Moscow: Atomizdat, 1977, 240 p.
5. Ponomarev-Stepnoy, N.N. "Nuclear Power in the Space." *Atomnaya Energia,* 1989, v. 66., iss. 6, pp. 371-374.
6. Brovalsky, Yu.A., and Sinyavsky, V.V. "Multi-Parametric Optimization of a Thermionic Electrogenerating Element." *Jour. Engin. Phys.*, 1972, v. 42, iss. 9, p. 1909.
7. Sinyavsky,V.V., Berzhaty, V.N., Maevsky, V.A., and Petrovsky V.G. *Designing and Testing of Thermionic Fuel Elements.* Moscow: Atomizdat, 1981, 96 p.
8. Andreev, P.V., Galkin, A.Ya., and Zhabotinski, E.E. "Optimal Dimensions of Thermionic Fuel Elements for In-core Thermionic Reactor." *Proc. 10th Symp. on Space Nuclear Power and Propulsion.* Albuquerque, 1993, part 3, pp. 1529-1533.
9. Nikolaev, Yu.V., Eremin, S.A., Gontar, A.S., et al. "A Single-cell TFE Mock-up of the Thermionic Nuclear Power System "Space-R"." *Proc. 12th Symp. on Space Nuclear Power and Propulsion.* Albuquerque, 1995, part 2, pp. 815-820.

10. Lee, H.H., and Klein, A.C. "Analysis of Topaz-II Reactor Performance Using MCNP and TFEHX." *Proc. 28th Intersociety Energy Conversion Engineering Conf.* Atlanta, 1993, v. 1.
11. Yang, L., Hudson, R.G., Johnson, H., et al. "Material Development of Thermionic Fuel-Cladding Systems." *Proc. 3rd Intern. Conf. on Thermionic Electrical Power Generation.* Juelich, 1972, v. 2, pp. 873-893.
12. Gontar, A.S., Kucherov, R.Ya., Nelidov, M.V., et al. "Some Questions of Uranium Dioxide Mass Transfer Influence on High-temperature Fuel Element Behaviour." *Proc. 24th Intersociety Energy Conversion Engineering Conf.* New York, 1989, v. 6, pp. 2803-2808.
13. Begg, L.L., Wetch, J.R., and Nelin, C.J. "Thermionic Fuel Element Endurance Enhancement." *Proc. 19th Intersociety Energy Conversion Engineering Conf.* San Francisco, 1984, v. 3, pp. 2276-2281.
14. Gontar, A.S., Nelidov, M.V., Nikolaev, Yu.V., et al. "Problems of Development of the Thermionic Fuel Elements." Report at the Branch Jubilee Conference "Nuclear Power in the Space." Obninsk, 1990.
15. Nikolaev, Yu.V., Gontar, A.S., Vedenyapin, G.A., et al. "Out-of-pile Simulation of Deformation Behaviour of a Thermionic Fuel Elements under Thermocycling Conditions." *Proc. 29th Intersociety Energy Conversion Engineering Conf. Monterey,* 1994, v. 2, pp. 1027-1031.
16. Nikolaev, Yu.V. "RI SIA "Lutch" R&D in the Area of Direct Conversion NPP Materials." Report at the 4th Branch Conference "Nuclear Power in the Space. Materials. Fuel." Podolsk, 1993.
17. Gontar, A.S., Sotnikov, V.N., and Shulepov, L.N. "Influence of Uranium Dioxide Mass Transfer on Workability of Thermionic Fuel Element Gas Venting System." Report at the Branch Jubilee Conference "Nuclear Power in the Space." Obninsk, 1990.
18. Koryukin, V.A., and Obrezumov, V.P. "Oxygen and Carbon Monoxide Adsorption Influence on the Emissional Parameters of TFE Electrodes." Report at the Branch Jubilee Conference "Nuclear Power in the Space." Obninsk, 1990.
19. Baksht, F.G., Dyuzhev, G.A., Martsinovsky, A.M, et al. *Thermionic Converters and Low Temperature Plasma.* Moscow: Nauka, 1973, 480 p.
20. Zherebtsov, V.A., Kiryushchenko, A.I., Kononova, Z.N., et al. "Influence of Hydrogen Impurity within the IEG on TEC Operation." Report at the Branch Jubilee Conference "Nuclear Power in the Space." Obninsk, 1990.
21. Zherebtsov, V.A., Lebedev, M.A., Sobolev, A.A., and Galanova, V.D. "The Diatomic Gas Impurity Influence on Power Loss in TEC." Report at the Branch Jubilee Conference "Nuclear Power in the Space." Obninsk, 1990.
22. Modin, V.A., Nikolaev,Yu.V., and Izhvanov, O.L. "The TEC's IEG Heat Conductivity Induced by Inert Gases under Low Pressures." Report at the Branch Jubilee Conference "Nuclear Power in the Space." Obninsk, 1990.

CHAPTER 2

DATA ON PROPERTIES OF MATERIALS USED AND RELATED FABRICATION PROCESSES

The creation of highly efficient TFEs with long life and stable output parameters (e.g., TOPAZ-2 NPS [1]) was to a significant extent feasible only as a result of development and implementation of fabrication processes for producing a number of new materials. These materials meet a wide domain of comprehensive and strict requirements specified for their properties; the materials include new high-temperature emitter materials, new modifications of nuclear fuels optimized for structure and composition, electroinsulating materials, and others. The results of work dedicated to creating the materials and investigating their properties are considered below in more detail.

2.1. Emitter Materials

2.1.1. Emitter Material Requirements

Among the diverse materials applied to thermionic electrogenerating channels of the "in-core" type, the strictest requirements are specified for the emitter material. These requirements are determined by the functional purpose and operating conditions of a given TFE unit. The primary requirements are these:

- high vacuum work function, to optimize the TFE electrical parameters;
- low emissivity, specifically under low current density, to reduce heat losses onto the collector and heighten TFE efficiency;
- small cross-section of thermal neutron capture, to minimize the size and mass parameters of a thermal reactor, or, if strict restrictions to this NPS parameter are absent, for fuel-element design optimization feasibility;
- compatibility with cesium vapor and fuel material and its low diffusional permeability in relation to fuel and fission products, to ensure the stability of emission and strength parameters in time;
- low saturated vapor pressure and resistance to chemical transport reactions, to reduce material transfer to the anode;
- high mechanical resistance to loads exerted by fuel, and especially a low creep rate under mechanical stresses arising in the emitter because of interaction with the swelling fuel stack;
- low temperature of brittle-ductile transition point and ease of manufacture; i.e., the plasticity margin, at operating temperatures, must be adequate to provide a maximum tolerable emitter deformation with no destruction of it;
- resistance to the vacancies-induced swelling in fast neutron flux; and

- low electrical resistance.

2.1.2. Emitter Material Properties

Because of the high temperatures (see Chapter 1), only molybdenum, tungsten, and their alloys were adopted in practice as emitter materials for thermionic electrogenerating channels in Russia and the United States. But, unlike the United States, where most development and study has been on polycrystal materials and age-hardened alloys, RI SIA "Lutch" developed a fundamentally different approach to creating the refractory emitter materials. The organization has developed single-crystal molybdenum and tungsten alloys that are unique in their properties. The chronology of the development of emitter single-crystal materials at RI SIA "Lutch" is given in Table 2.1.

The single-crystal materials were preferred even at early stages of development, and molybdenum emitters with tungsten coating were already used in the early phase of the single-cell TFE work. A single-crystal alloy based on molybdenum with 3% mass niobium had found its application to TOPAZ-2 TFEs and successfully withstood land-based tests in a reactor-thermionic converter assembly for ~1.5 years. For higher temperature and power systems with much longer life, high-temperature tungsten single-crystal alloys had been developed and introduced into practice.

The single crystal materials were preferred for the following reasons [1]:

- absence of re-crystallization, which provides structural and property stability in the entire range of TFE operating temperatures;
- low temperature of brittle-ductile transition point and, consequently, better fabrication properties;
- anisotropy of electron work function and mechanical properties, which enables use of the material's best parameters.

Let us now compare material properties for single and polycrystal emitters.

The definition of "single-crystal material" is an issue of discussion in the literature, which necessitates an explanation of the criteria for single crystallinity accepted at RI SIA "Lutch." There exists for molybdenum, tungsten, and their alloys a crucial value of disorientation angle, at which a sharp transition of the material from the ductile to brittle condition occurs [2]. Figure 2.1 shows the influence of disorientation angle at the molybdenum bicrystal interface on its impact ductility and bending angle. The value of "critical" disorientation depends slightly on the crystallographic orientation and is ~6 to 9 degrees. The critical disorientation angle values obtained were accepted as the criterion for material monocrystallinity. Investigations had ascertained that some other materials' characteristics are linked to the disorientation level in the subgrain boundaries.

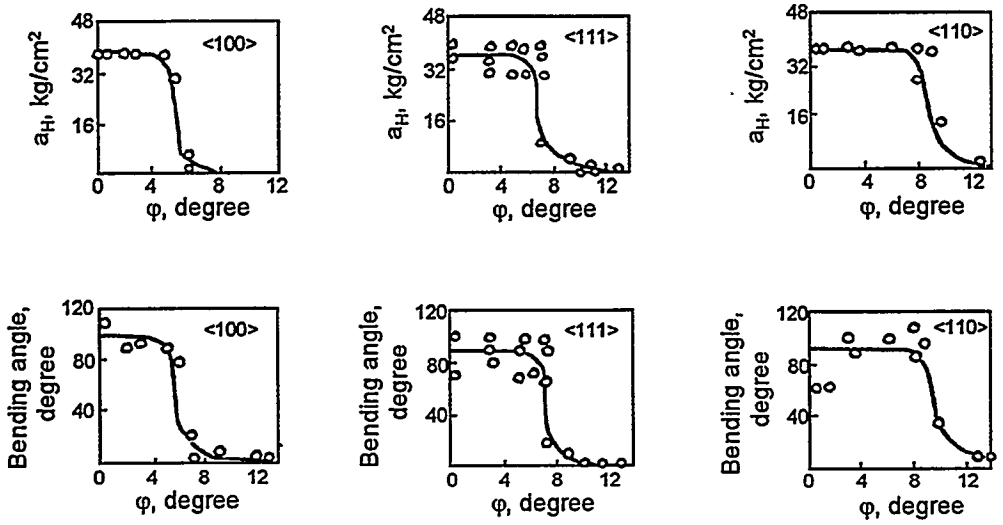

Figure 2.1. Influence of disorientation angle (φ) on impact ductility (a_H) and bending angle for Mo bicrystals of various orientations [2].

Table 2.1. Emitter-materials development chronology at RI SIA "Lutch" [1]

No.	Emitter Material	Years of Development
1	Molybdenum single crystal alloy	1968-1970
2	[111] single crystal molybdenum	1970-1972
3	Molybdenum single crystal coated by W^{184} polycrystal	1973-1976
4	Molybdenum single crystal coated by W^{184} single crystal	1976-1977
5	Single crystal molybdenum alloy (MN3) coated by W^{184} single crystal	1977-1982
6	Single crystal tungsten isotope W^{184}	1982-1985
7	W^{184} single crystal alloy	1985 to date

Figure 2.2 and Table 2.2 contain data characterizing the uranium penetration into a cladding of poly- and single-crystal molybdenum [1]. As shown, uranium penetration into single-crystal molybdenum is not less than two orders of magnitude lower than into polycrystal material.

Table 2.3 provides the work function values for poly- and single-crystal molybdenum and tungsten. Maximum work function (both for molybdenum and tungsten) is related to (110)-faces, i.e., to surfaces with the densest atomic packing. In this case, the work function of single crystals is higher than that of polycrystals by ~0.5 eV. The single-crystal molybdenum work function for the most efficient (110)-face is higher by almost 17% than that of a polycrystal of the same chemical composition [4]. Pursuant to diverse data, the work function for the single-crystal molybdenum (110)-face is 4.9 to 5.1 eV, and for single-crystal tungsten, ~5.3 eV [4].

Table 2.2. Amount of uranium having passed through 1 mm-thick molybdenum cladding at 1650°C [1]

Material	3 years (experiment)	10 years (forecast)
Single Crystal	$3 \cdot 10^{-8}$ g-at/cm^2	$1 \cdot 10^{-7}$ g-at/cm^2
Polycrystal	$6 \cdot 10^{-6}$ g-at/cm^2	$2 \cdot 10^{-5}$ g-at/cm^2

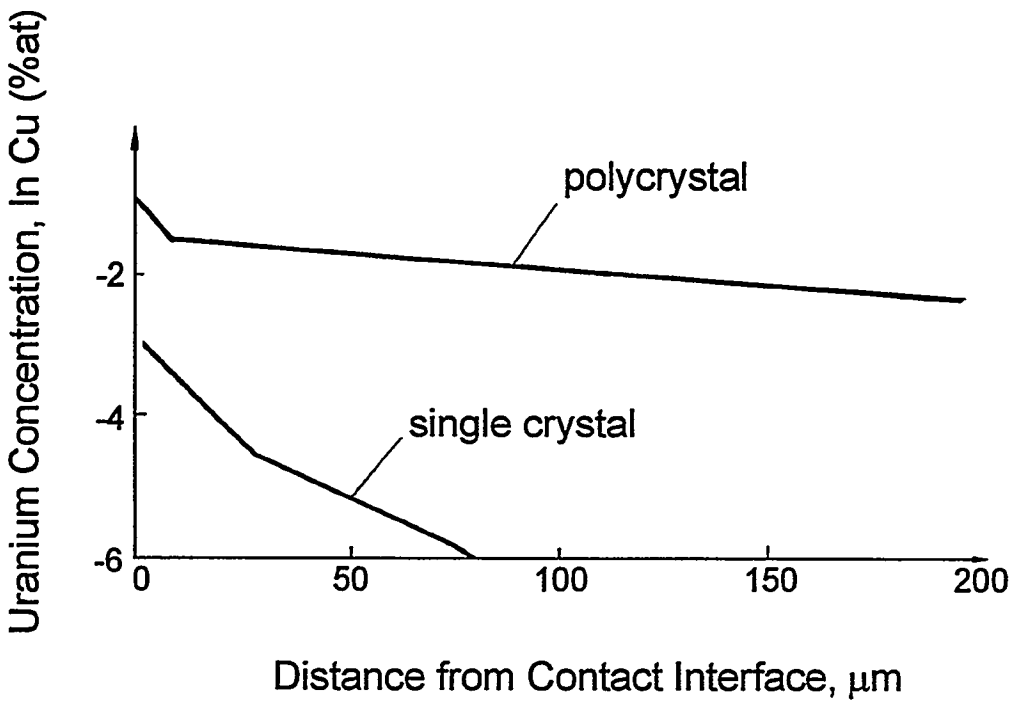

Figure 2.2. Uranium distribution in single and polycrystal molybdenum after tests in contact with $UO_{2.002}$ at 1650°C for 1.5 years [1].

Table 2.3. Work function of poly/single crystal molybdenum and tungsten [3]

No.	Emitter Material	Work function, eV
1	Polycrystal Molybdenum	4.4
2	Molybdenum (100)-face	4.35
3	Molybdenum (110)-face	4.9
4	Polycrystal Tungsten	4.55
5	Tungsten (100)-face	4.5
6	Tungsten (110)-face	4.9

To guarantee long lifetime and minimum heat losses, the emitter material must also have a minimum evaporation rate and low emissivity. These parameters for single and polycrystal molybdenum have been compared [4]. The absence of grain boundaries in single crystals, where the interatomic bonds are weakened, provides a lower rate of material evaporation. Mikhailov et al. [5] showed experimentally that the single-crystal molybdenum evaporation rate at 2073 K in a $7 \cdot 10^{-4}$-Pa vacuum is about two times lower than for polycrystal. The values of emissivity almost coincide for single and polycrystal molybdenum [4].

Ismailov [6] compared some of the mechanical characteristics of single-crystal molybdenum to those of high-purity polycrystal molybdenum. For single-crystal molybdenum, the orientation impact on the short-time strength parameters had also been studied. Tensile-test results are provided in Figure 2.3 and Table 2.4.

The results allow several inferences. First, the single-crystal molybdenum's maximum strength is associated with the <111>-direction (see Table 2.4). Second, as to the short-time strength parameters (yield strength, see Figure 2.3), the single/polycrystal difference is insignificant. However, an essential difference in the materials' destruction behavior is noted. The single-crystal specimens had a

Table 2.4. Mechanical characteristics of single-crystal molybdenum at 20°C (sample loading rate $\varepsilon = 2.38 \cdot 10^{-4}$ c^{-1}) [6]

Orientation	Yield Strength σ_T, MPa	Strength, σ_B, MPa	Relative Constriction, ψ %	Relative Elongation, δ, %
<110>	275	360	100	39
<111>	285	380	68	20.5

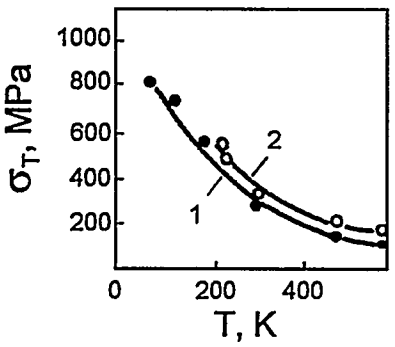

Figure 2.3. Temperature dependence of yield strength for single and polycrystal molybdenum [6]:
1 - <111>-oriented single crystal;
2 - polycrystal.

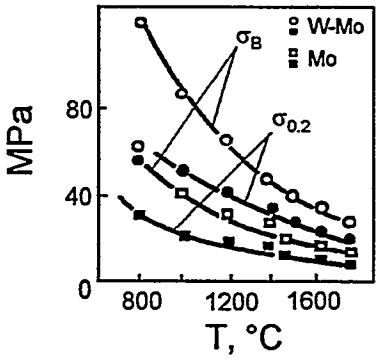

Figure 2.4. Tensile test results on bimetallic specimens of (Mo_{mono}-W_{mono}) and Mo_{mono} [8].

Table 2.5. Properties of Mo single crystals fabricated through RI SIA "Lutch" technology [1]

No.	Parameter	Value
1	Subgrains Disorientation Angle, °	< 2
2	Specific Electric Resistance at 20°C, Ohm·m	$(5.0\text{-}5.5)\cdot10^{-8}$
3	Thermal Conductivity at 20°C, W/m·K	160 to 170
4	Workfunction at (110)-Face, eV	5.0
5	Conventional Yield Strength, MPa - at 20°C - at 160°C	 250 to 400 10 to 12
6	Temperature of Brittle-Ductile Transition Point, °C	< -100

plastic character of the destruction over the entire range of temperatures under study, 573 K to 77 K, but over the temperature change from 573 K to 200 K, the polycrystal molybdenum destruction behavior changed from plastic to brittle type.

The comparison of thermal conductivity and specific electric resistance for poly- and single-crystal molybdenum samples fabricated at RI SIA "Lutch" shows these characteristics to coincide with each other [7].

Thus, on the aggregate of the data considered above, the single-crystal molybdenum is obviously preferred to the polycrystal material.

The primary thermal and mechanical characteristics obtained for the single-crystal molybdenum specimens fabricated at RI SIA "Lutch" are given in Table 2.5 [1].

However, single-crystal molybdenum is notable for its comparatively low high-temperature strength. Its creep rate is inferior to polycrystal molybdenum by about one order of magnitude [1]. In this connection, RI SIA "Lutch" reviewed various ways to strengthen this material, e.g., application of a tungsten coating to the single-crystal molybdenum surface [8, 9]. Figure 2.4 contains data on tensile tests of annular specimens made from a Mo_{mono}-W_{mono} bimetallic tube [8]. The overall tube wall thickness was 1.55 mm; the single-crystal tungsten coating thickness reached 0.15 mm. As shown, the short-time strength parameters of the bimetallic specimens are about 2 times higher than those of single-crystal molybdenum. The dependence of these parameters on the tungsten coating thickness and test results on the effect of this characteristic upon the creep rate are shown in Figures 2.5 and 2.6.

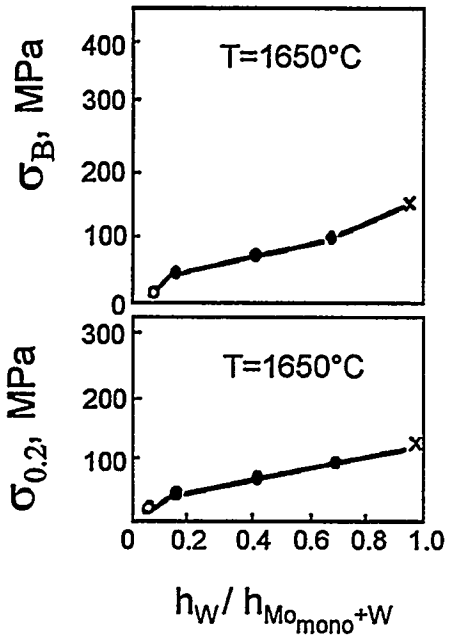

Figure 2.5. Strength (σ_B) and yield strength ($\sigma_{0.2}$) vs. relative thickness of tungsten coating.

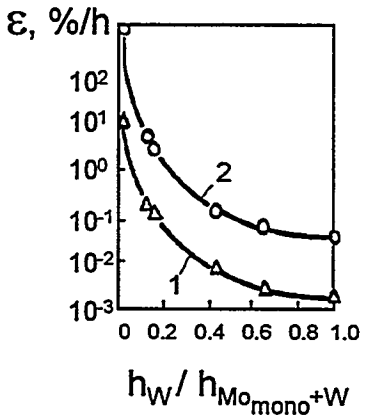

Figure 2.6. Bimetallic tube steady-state creep rate vs. relative thickness of tungsten coating [9]:
1 - σ = 10 MPa;
2 - σ = 20 Mpa.

The strength substantially increases with an increase of the relative thickness of the tungsten coating ($h_{W\text{-poly}}/h_{Mo\text{-mono+W-poly}}$). A sharp reduction of the samples' creep rate is also observed; e.g., in the 1650 to 1800°C temperature range and under 10 to 20 MPa stresses, the creep rate decreases by ~2 to 4 orders of magnitude.

However, the most effective solution to the problem of strengthening the single-crystal molybdenum was found to be alloying. The technique is based on solid-solution alloying combined with a single-crystal matrix. This provides high stability of the alloys' mechanical properties over time, while maintaining the above-mentioned merits of the single crystal. The resulting single-crystal alloys are basically equivalent, in their resistance to creep over a wide temperature range, to the best of the known polycrystal alloys [10].

Let us now consider some of the parameters of short-time strength and endurance of a single-crystal alloy of molybdenum with niobium dopants, used in the TOPAZ-2 fuel element (Mo+3% mass Nb[11]). Figures 2.7 and 2.8 represent dependencies of yield strength ($\sigma_{0.2}$) on temperature and niobium content. The tests were performed at a rate of active clamp movement of ~2mm/min.

Yield strength increases almost linearly with niobium concentration (for a concentration range of 3 to 12% mass Nb) and is, for (Mo+3% mass Nb) <110>-oriented alloy at T=1600°C, ~ 60 MPa (see Figure 2.8).

The ultimate strength (σ_B) value for the single-crystal alloys of the (Mo-Nb) system with niobium content ≥3% mass, at the test temperatures of 1500 to 1800°C, are given in Table 2.6. Values of σ_B for non-alloyed single crystal tungsten are also provided.

A comparison reveals that, from the viewpoint of the short-term strength, "Lutch"'s (Mo-Nb) molybdenum alloys are considerably superior not only to the non-alloyed single crystal molybdenum (see, e.g., Table 2.4) but also to a stronger high-temperature material such as non-alloyed single-crystal tungsten.

A substantial increase in the material creep resistance is achieved as a result of alloying the single-crystal molybdenum. Figures 2.9 and 2.10 contain the creep curves for the single crystal molybdenum and its alloys [13].

Table 2.6. Comparison of material strengths [12]

Alloy		Mo-3% Nb	Mo-6.5% Nb	W
Strength, σ_B, MPa	T=1500°C	75	140	50
	T=1800°C	60	-	37
	T=2000°C	40	90	25

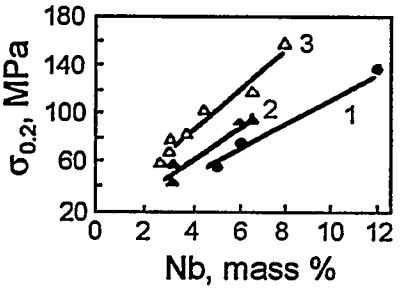

Figure 2.7. $\sigma_{0.2}$ versus niobium concentration at 1600°C [12]:

1 - Mo-Nb, <100>;
2 - Mo-Nb, <110>;
3 - Mo-Nb, <111>.

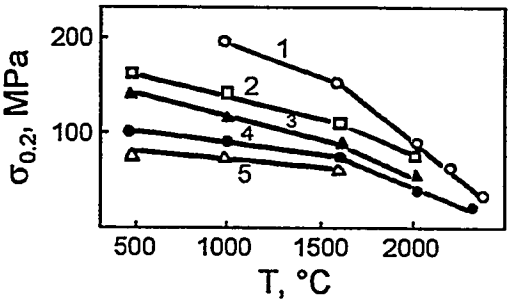

Figure 2.8. Temperature dependence of $\sigma_{0.2}$ for molybdenum niobium single crystal [12]:

1 - Mo-7, 8Nb, <111>;
2 - Mo-6, 5Nb, <111>;
3 - Mo-6, 5Nb, <110>;
4 - Mo-3Nb, <111>;
5 - Mo-3Nb, <110>.

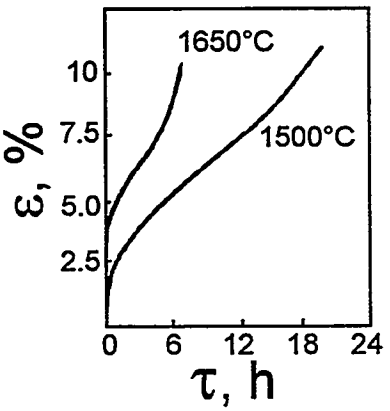

Figure 2.9. Creep curves for single-crystal <111>-oriented molybdenum under 6 MPa stress [13].

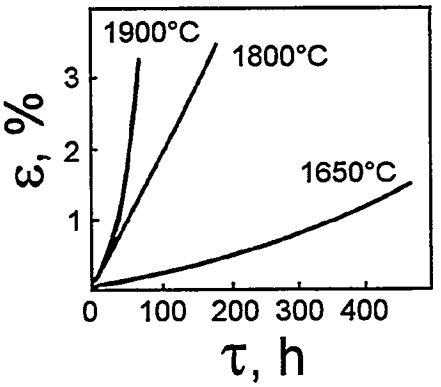

Figure 2.10. Creep curves for single-crystal alloy Mo-3%Nb <111>-oriented under 10 MPa Stress [13].

The creep of single-crystal molybdenum is characterized by appreciable instant deformation and presence of a transient stage. For the alloy, the creep deformation in these stages constitutes only an insignificant part of total deformation. A considerable reduction of the creep rate in the phase of steady-state material creep is also achieved by alloying.

The comparison of steady-state creep for the single-crystal molybdenum and (Mo+3% mass Nb) alloy is given in Figure 2.11 [13]. The single-crystal alloy's steady-state creep rate is 3 to 3.5 orders of magnitude lower than that of the non-alloyed molybdenum.

Molybdenum single-crystal alloys obtained through solid-solution hardening are effective over a wide temperature range. They are, as for their creep resistance at 1600 to 1900°C, competitive not only with molybdenum polycrystal alloys but also with tungsten and its traditional alloys. For example, the non-alloyed tungsten and W-Re, W-Re-Mo alloys are usually used in the USA as thermionic fuel-element cladding at temperatures in excess of 1500°C. There is also the possibility of using other high-temperature alloys such as W-23.4%Re-HfC, W-HfC, W-2%ThO_2, and W-4%Re-HfC. Of molybdenum alloys, TZM (Mo-0.5%Ti-0.09%Zr-0.03%C), Mo-Re, Mo-10%W-2%Re-HfC, and others are under consideration.

A comparison [10] had shown, for the single-crystal alloys of molybdenum developed at RI SIA "Lutch", that the creep rate is lower by about one order of magnitude than that of Mo-Re, TZM, as well as Mo-0.5 HfC (see e.g. [13, 14]). But it is especially interesting to compare molybdenum single-crystal alloys to tungsten materials having about twice the density and less workability. Figure 2.12 shows stresses causing a 1% deformation during 1000 hrs at T=1650°C for a number of tungsten materials and Mo_{mono1} and Mo_{mono2} single-crystal alloys [10].

The molybdenum single-crystal alloys possess superior creep characteristics compared with tungsten polycrystal and with a number of alloys based on it (e.g., W-5Re, W-26Re). At temperatures in excess of ~1700°C, the molybdenum single-crystal alloys also withstand comparison to some age-strengthened tungsten alloys, e.g., to W-23.4%Re-HfC [10]. So, for example, at 1650°C, the stress causing a $10^{-6}s^{-1}$ creep rate is ~46 MPa for MN3 [13] and ~53 MPa for W-23%Re-0.27HfC [15]. When niobium concentration increases to, e.g., 6 to 8% mass, the single-crystal molybdenum alloy is already superior to the considered tungsten alloy for this parameter.

As already noted, for high-power TFEs with a lifespan of 7 to 10 years, RI SIA "Lutch" has developed single-crystal tungsten alloys. To date, they are included in a group of materials with the highest creep resistance. Figure 2.12 shows that, given stresses that generate a 1% deformation at 1650°C for 10^3 hrs, the single-crystal tungsten alloys are 3 to 5 times superior to non-alloyed tungsten and its alloys with rhenium. Use of the single-crystal tungsten alloys instead of

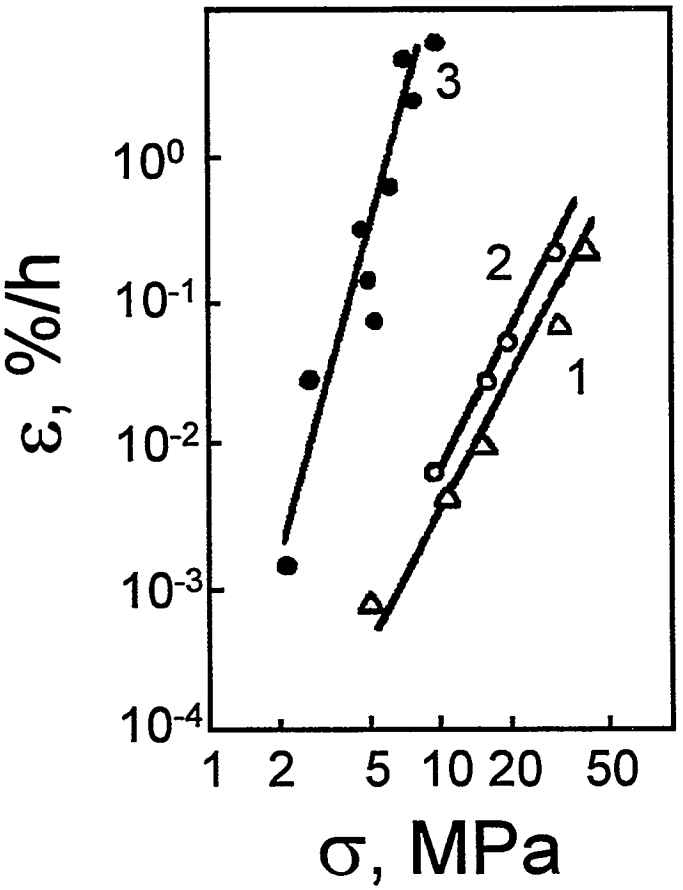

Figure 2.11. Stress dependence of steady-state creep rate at 1650°C for single-crystal molybdenum and (Mo-3% mass Nb) alloy [13]:

1 - Mo-3%Nb, <111>;
2 - Mo-3%Nb, <110>;
3 - Mo, <111>.

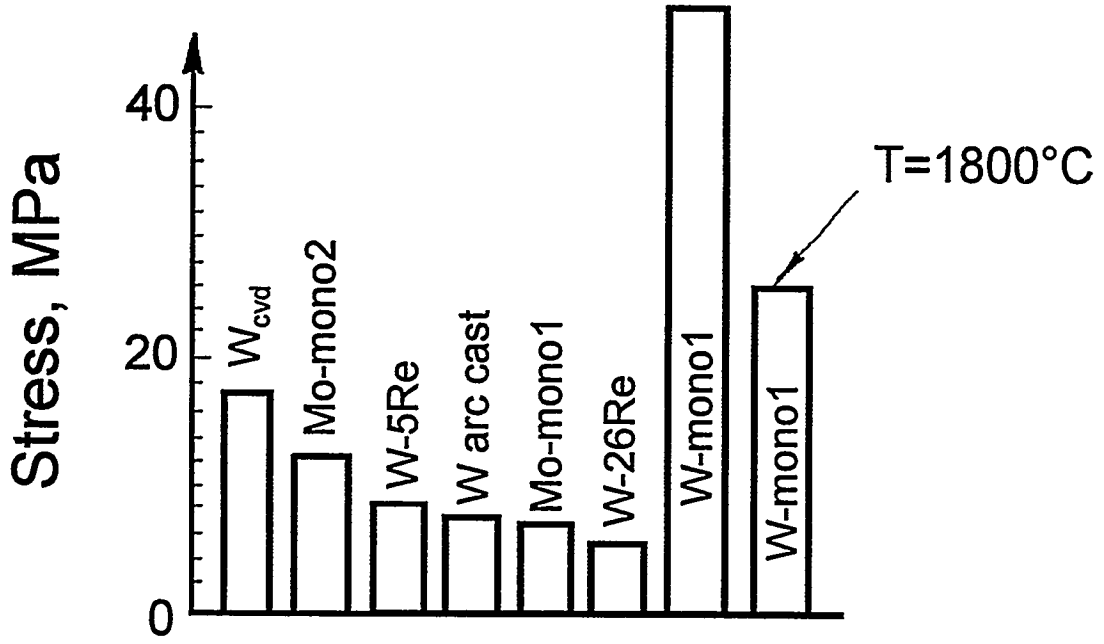

Figure 2.12. Stresses causing 1% deformation for 1000 hrs at 1650°C [10].
W_{cvd} - Tungsten produced by chemical vapor deposition

polycrystal tungsten allows either prolongation of the TFE life or, at the same lifetime, significant elevation of the emitter temperature, by ~200 to 250°C [10]. Such temperature elevation, pursuant to our American colleagues' estimates, should allow a reduction of reactor-plant weight by ~40% [10]. Moreover, the single-crystal tungsten alloys are much stronger at high temperatures than the age-hardened polycrystal alloys. As an example, Figure 2.13 contains the creep curves for polycrystal alloys of W-2ThO_2 and W-0.5HfC-0.05C and single-crystal tungsten alloys at 1650°C [10].

The single-crystal alloys also are basically equivalent to W-4%Re-HfC, currently deemed the best high-temperature material. For comparison, RI SIA "Lutch" had conducted tests of one of the tungsten alloys under conditions similar to those for W-4%Re-HfC [17]. Figure 2.14 [2] contains creep curves for both materials at T=1682°C.

The single-crystal tungsten alloys' merits also hold at higher temperatures. Figure 2.15 compares the steady-state creep rates for these materials at the test temperature T=1800°C [10].

Several thermal properties of tungsten single-crystal alloys developed at RI SIA "Lutch" are presented in Table 2.7 [1].

In discussing the properties of tungsten and molybdenum single-crystal alloys, it is expedient to include questions concerning workability and plasticity of the materials. The brittle-ductile transition point (T_{bd}) may serve to some extent as the fabrication criterion.

Nikolaev et al. [10] compared the above value for our single-crystal alloys to polycrystal tungsten and its alloys with rhenium. The latter is used as a plasticizer. For the correctness of this comparison, our alloys' T_{bd} was measured using a procedure used in the USA. A flat specimen was bent with a 4H bending radius (H=specimen thickness) under three-point loading. The clamp movement rate was one inch (2.54 cm) per minute. A temperature at which a 90° bending angle was reached without specimen destruction was accepted as the brittle-ductile transition point. Comparative data on T_{bd} are provided in Figure 2.16.

It was found that for a single-crystal molybdenum alloy T_{bd} does not rise above room temperature. The single-crystal molybdenum alloys are inferior, in their low-temperature plasticity, only to alloys with a high content of rhenium, e.g., W-26%Re. The tungsten single-crystal alloys' brittle-ductile transition point is much lower than that of the polycrystal alloys (see Figure 2.16).

Another advantage of the single-crystal alloys is the absence of recrystallization [10]. For the polycrystal materials, the recrystallization point lies in the range from 1300°C (for non-alloyed tungsten) to 1850°C (for W-4%Re-HfC). As a result of recrystallization of the polycrystal materials, their plasticity is reduced over the course of time. This is manifested through an increase of the brittle-ductile transition point of the polycrystals after a high-temperature hold.

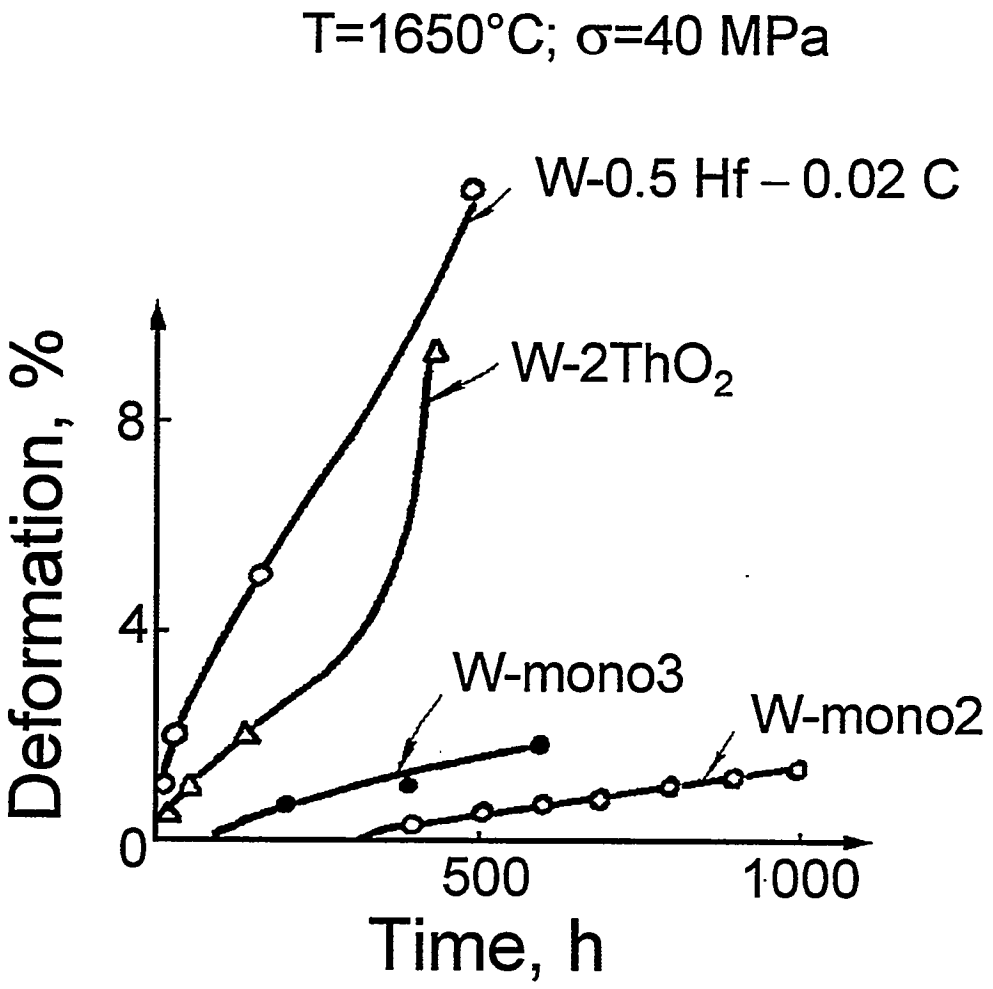

Figure 2.13. Comparison of creep curves for some poly- and single crystal tungsten alloys [10].

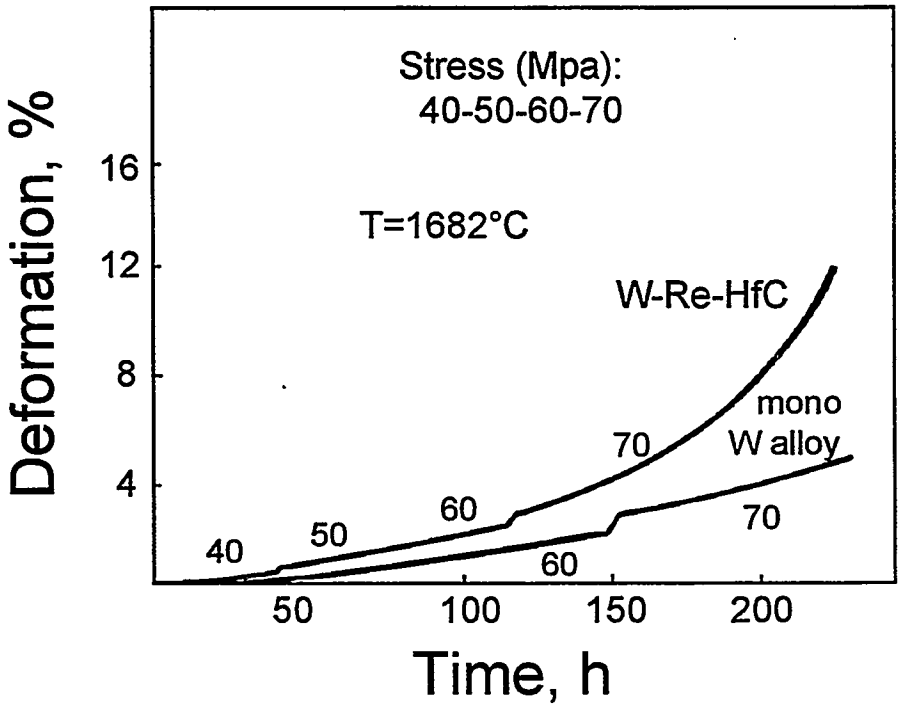

Figure 2.14. Creep deformation of W-4Re-0.33HfC polycrystal alloy and single-crystal tungsten alloy [2].

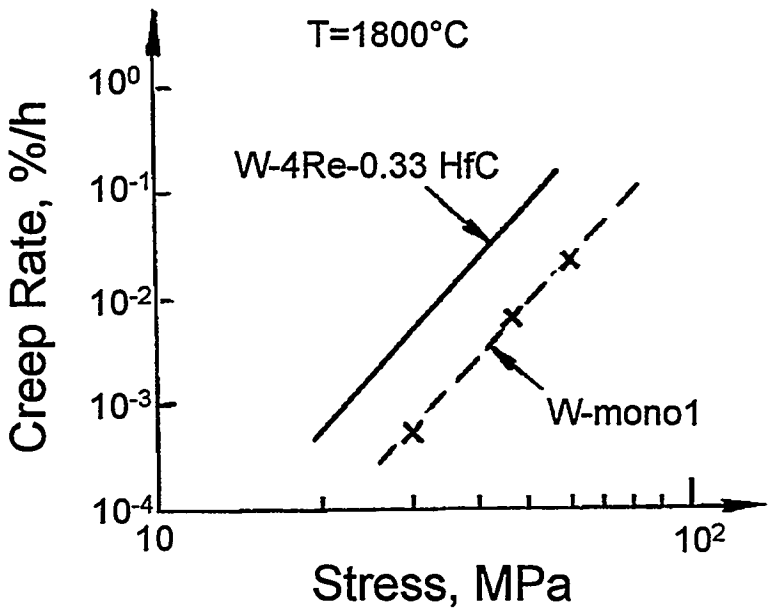

Figure 2.15. Comparison of steady-state creep rates for W-4Re-0.33HfC and tungsten single-crystal alloy [10].

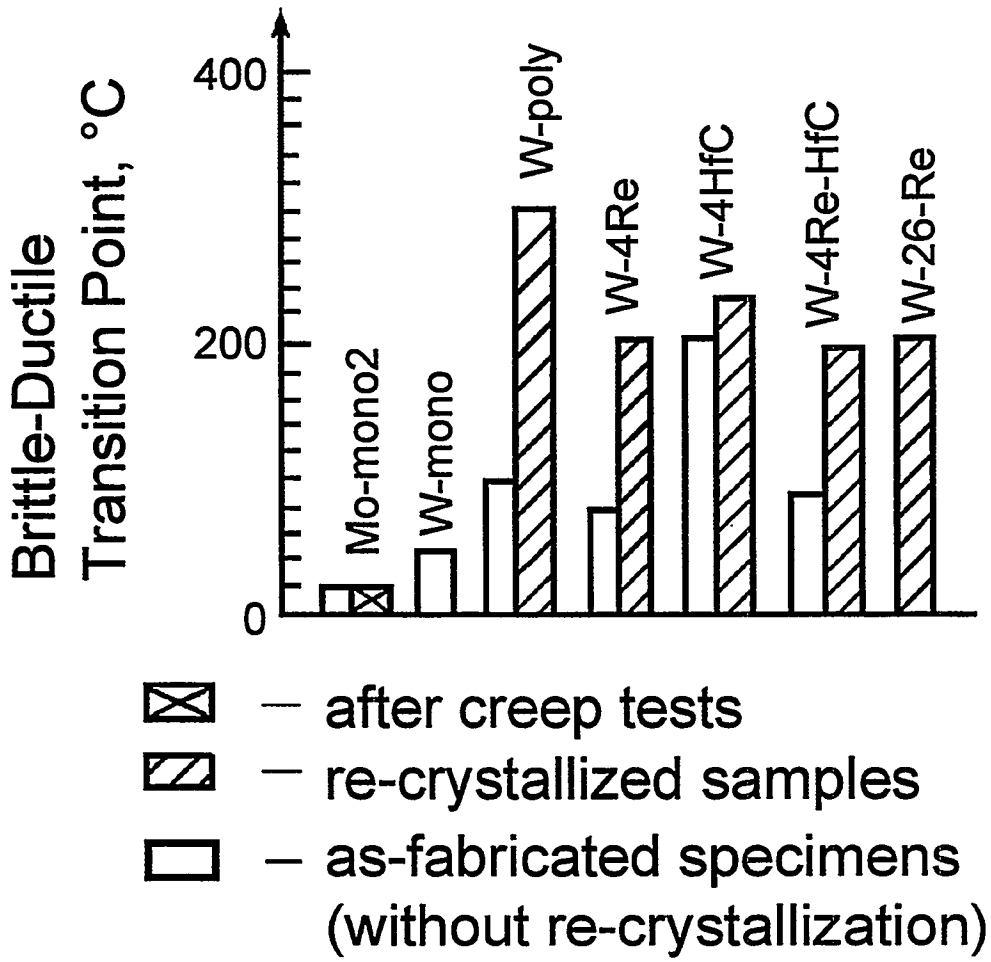

Figure 2.16. Comparison of brittle-ductile transition point for various single and polycrystal alloys [10].

Table 2.7. Properties of single-crystal tungsten alloys fabricated at RI SIA "Lutch" [1]

No.	Parameter	Value
1	Subgrain disorientation angle, °	< 2
2	Specific Electric Resistance at 20°C, Ohm·m	$(7.5\text{-}8.0)\cdot10^{-8}$
3	Thermal Conductivity at 20°C, W/(m·K)	100 to 120
4	Work function for (110)Facet, eV	5.2
5	Yield strength, MPa at 20°C at 1600°C	 800 to 1000 80 to 120
6	Brittle-Ductile Transition Point, °C	<20

For single crystals the increase is not observed. This was verified under more rigid conditions than mere annealing. Figure 2.16 also contains T_{bd} levels for specimens of molybdenum single-crystal alloy that has undergone high-temperature creep tests and accumulated a 12% deformation. Deformation and high-temperature hold did not reduce the material plasticity margin.

2.1.3. Fabrication Process for Emitter Materials

The use of single-crystal molybdenum, tungsten, and related alloys as emitter claddings called for the development of a large complex of new technologies for single-crystal production, treatment, welding, etc.

At RI SIA "Lutch", a fabrication process for single-crystal emitter materials is based mainly on two methods [2]: electron-beam zone fusion and chemical transport reactions. The former method produces single-crystal materials as rods, tubes, and flat ingots. The second method gives tubular and flat articles and allows the application of coatings while preserving the single crystal, to obtain capillaries, foils, etc. The processing principles for production of single-crystal molybdenum and tungsten using these techniques have been considered widely enough in both Russian and foreign literature (see, e.g., [8, 18-21]) that there is no need for a detailed discussion here.

In electron-beam zone fusing, the crystals are grown, as a rule, using a seed crystal. Therefore, the single crystal's perfection is largely governed, at least near the seed, by the latter's quality [22].

When obtaining single-crystal products or coatings by the chemical transport reaction method, the structural perfection of a deposit is mainly controlled by the

degree of perfection of the substrate single crystal [21, 22]. To obtain single-crystal deposits with a minimum number of defects, it is necessary to optimize the fabrication process parameters, such as temperature of the substrate, raw materials, or vaporizer. Evstyukhin et al. [21] reviewed these parameters' influence on the growth rate for large single-crystal deposits of tungsten. The cylindrical deposits were fabricated in a quartz reactor with "pseudo-closed" volume (Figure 2.17).

The process-adjusted parameters were the substrate temperature and vaporizer temperature; the raw material tube is heated by radiation, and its temperature depends on the substrate temperature. The obtained growth rate for the (110) and (112) faces and total tungsten mass transfer as functions of these parameters are shown in Figures 2.18 to 2.20.

In the development of stronger refractory single-crystal alloys, as compared to the non-alloyed tungsten and molybdenum, RI SIA "Lutch" had made a choice relating to solid-solution hardening of these materials. This technique is not efficient at high temperatures in polycrystals, and given abundant alloying, the catastrophic fall of polycrystal plasticity is observed. Nevertheless, solid-solution hardening, as shown above, is extremely effective in alloying single-crystal materials. Additionally, the method produces superior crystal structures, achieving disorientation of the blocks (i.e., subgrains) of less than several angular minutes. This is more difficult to implement for single-crystal refractory metals [2].

2.2. Fuel Materials

As a rule, uranium dioxide of high density (≥95% of theoretical) and enrichment on U^{235} in excess of 90% is used as the fuel material for "in-core"-type TFEs [23]. This type fuel is used also in the Russian TFEs for TOPAZ-1 [24] and TOPAZ-2 [25] NPSs.

2.2.1. Uranium Dioxide Properties

Uranium dioxide properties are well known. Its basic thermal and strength parameters, subsequently required to compare it to alternative fuel compositions, are provided in Table 2.8. These characteristics, to a greater or lesser extent, depend on UO_2 structure, which in turn depends on the manufacturing process used in producing the UO_2. UO_2 strength parameters are the most sensitive characteristics [26], which explains the differences in their values observed in the literature. The most important of the characteristics is the creep rate of the fuel, which affects the pressure exerted by a swelling fuel upon the emitter. This value also characterizes the swelling fuel's ability to be redistributed into the fuel-stack

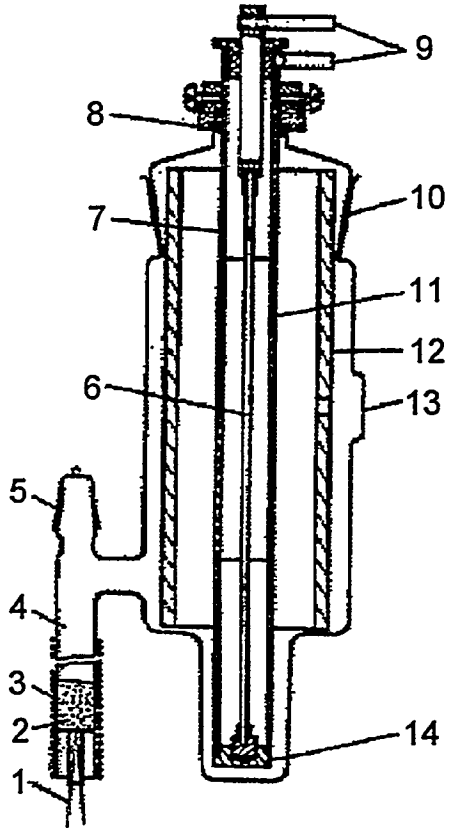

Figure 2.17. Quartz reactor with pseudo-closed volume [21]:

1 - thermocouple;
2 - powder of tungsten hexachloride;
3 - heater;
4 - vaporizer;
5 - valve;
6 - rod-shaped heater;
7, 14 - technological extension-piece and plug;
8 - sealing joint;
9 - current supplies;
10 - ground-in joint (quartz);
11 - substrate;
12 - raw material;
13 - sight hole (optical grade quartz).

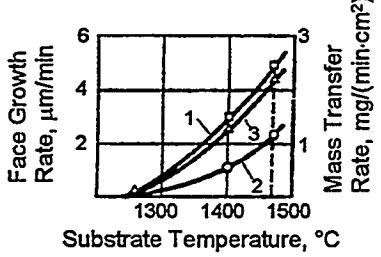

Figure 2.18. (110)- and (112)-face growth rate and overall mass transfer vs. substrate temperature at vaporizer constant temperature (T_{vap}=120°C) [21]:
1 - (110)-face;
2 - (112)-face;
3 - tungsten overall mass transfer.

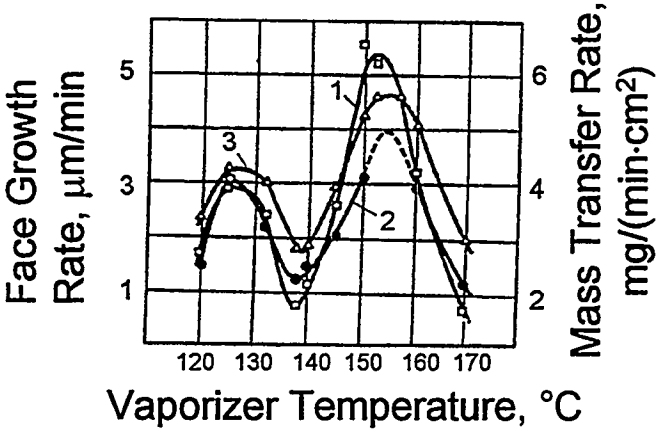

Figure 2.19. (110)- and (112)-face growth rate and overall mass transfer vs. vaporizer temperature at substrate (1640°C) and raw material (1110°C) constant temperatures [21]:
1 - (110)-face;
2 - (112)-face;
3 - tungsten overall mass transfer.

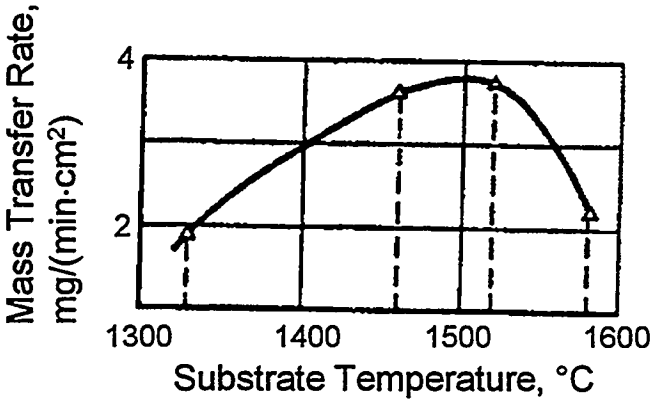

Figure 2.20. Tungsten overall mass transfer dependence on substrate temperature (T_{vap}=150°C) [21].

central channel. Thus, the fuel creep rate determines, to a considerable extent, TFE lifetime and choice of the emitter material.

As noted in Chapter 1, a feature of thermionic fuel-element operation conditions is a high temperature (T≥1400°C) at a relatively low power density ($q_V \leq 300$ W/cm^3), as compared to terrestrial power-reactor fuel elements. Under these conditions (i.e., at T≥0.5 melting point and burnup rate $\leq 1 \cdot 10^{13}$ fiss. cm^{-3} s^{-1}), UO_2 in-pile creep is governed by the thermal constituent, since the irradiation effect is very slight (e.g., [27, 28]). For this reason, the subsequent discussion is restricted to out-of-pile data on UO_2 creep.

Investigations reveal (e.g., [28]) that UO_2 creep is substantially affected by its structure and composition: grain size, density, oxygen coefficient (O/U), etc. The structural transformations occuring within the fuel under irradiation at high temperature (change in grain size/configuration, density, oxygen coefficient) are able to essentially alter the as-fabricated UO_2 creep parameters.

The effect of these factors is widely enough studied for the fuel stack structure zone, characterized by a growth of initial equiaxial grains in the course of operation (e.g., [28]). The investigation of the oxygen coefficient influence has been performed, as a rule, at O/U≥2.0., since for the power-reactor fuel elements, use of a hypostoichiometric uranium dioxide is problematic because of its narrow range of homogeneity at low temperatures. For thermionic fuel elements, use of hypostoichiometric uranium dioxide is promising and currently widely discussed

Table 2.8. Uranium dioxide characteristics

No.	Parameter	Value	Reference
1	Theoretical density, g/cm^3	10.97	[29]
2	Fissile element content, g/cm^3	9.67	[29]
3	Melting point, °C	2805	[29]
4	Mean coefficient of linear expansion from 25 to 1600°C, 1/deg	12,15·10^{-6}	[27]
5	Thermal conductivity at 1600°C and relative density of 95% TD, W/(m·K)	2.6 (2.1)	[29] [30]
6	Evaporation rate at 1600°C, g/(cm^2·s)	4·10^{-7} (1·10^{-7})	[1] [29]
7	Elasticity Modulus at 1600°C and relative density of 95% TD, MPa	1.66·10^5	[31]
8	Bending strength, MPa - at 20°C - at 1600°C	 100 to 170 90	[31]

[32-35]. As compared to power reactor fuel elements, there is a more substantial structural transformation of fuel in thermionic fuel elements—a considerable extension of a zone with elongated or so-called "column" grains is observed. In light of this, let us consider in more detail only the data on hypostoichiometric uranium-dioxide creep and test results for column-structure coarse-grained UO_2.

RI SIA "Lutch" performed investigations on coarse-grained uranium dioxide [36]. In the fuel samples, the column structure observed in fuel elements after irradiation tests was reproduced under out-of-pile conditions. The samples were fabricated through re-condensation, and they had almost stoichiometric composition (O/U=1.9999). The column grains had diameters of 150 to 250 μm and lengths of 500 to 3500 μm. Sample density was 81 to 99% TD. During the tests, the load was applied both along and across the <111> texture. The compression tests were conducted in $\sim 2 \cdot 10^{-3}$ Pa vacuum.

Analogous investigations of fine-grained (5 to 10 μm) uranium dioxide with a composition close to stoichiometric (O/U≈2.001) and a density of 96 to 99% TD were performed for comparison.

Typical creep curves for the coarse-grained uranium dioxide with various porosities are displayed in Figure 2.21.

A short (≤2 hr) transient creep stage is characteristic of the curves. Sample porosity has a considerable effect on the creep rate. The steady-state creep rate ε depends on the porosity P following a power type expression: $\varepsilon \sim P^{1.9}$.

The influence of stress (σ) on the steady-state creep rate is shown in Figure 2.22. Within the range of stresses examined (5 to 40 MPa), the steady-state creep follows the $\varepsilon \sim \sigma^{4.2}$ law, i.e., the creep occurs pursuant to the dislocation-diffusion mechanism. Grain size, ranging from 150 to 3500 μm, does not affect the creep rate. Samples were loaded both along and across the <111> texture. As seen in Figure 2.22, the creep rate essentially did not change.

For the coarse-grained uranium dioxide with elongated grains, within the range of stresses σ=5 to 40 MPa and temperatures of T=1500 to 1900°C, the steady-state creep rate may described by the relationship

$$\varepsilon = A \cdot \sigma^{4.2} \cdot \exp(-41000/(R \cdot T)),$$

where:
- ε - steady-state creep rate, %/hr;
- A - coefficient;
- σ - stress, MPa;
- R - universal gas constant, J/(mole·K);
- T - temperature, K.

For comparison, Figure 2.22 also contains ε =f(σ) dependence for a fine-grained uranium dioxide. In this case, under stresses lower than the dioxide linear

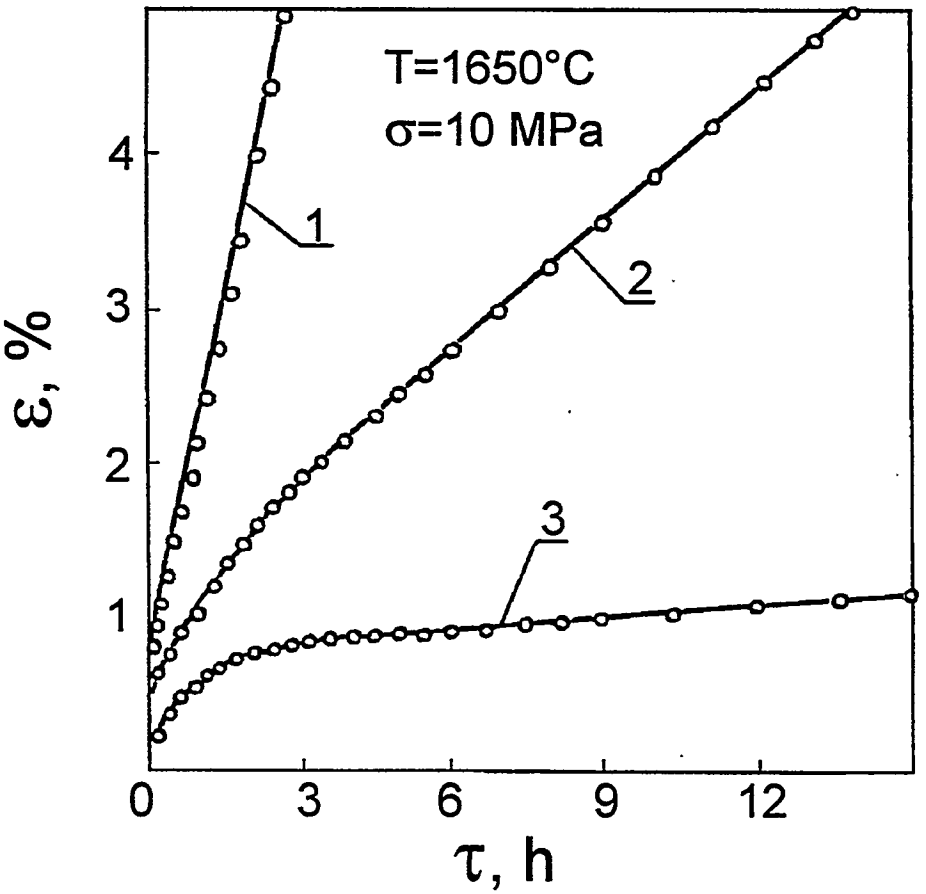

Figure 2.21. Creep curves for coarse-grained UO_2 of various densities [36]:
1 - ρ=81-87% TD;
2 - ρ=91-92% TD;
3 - ρ=94-99 % TD.

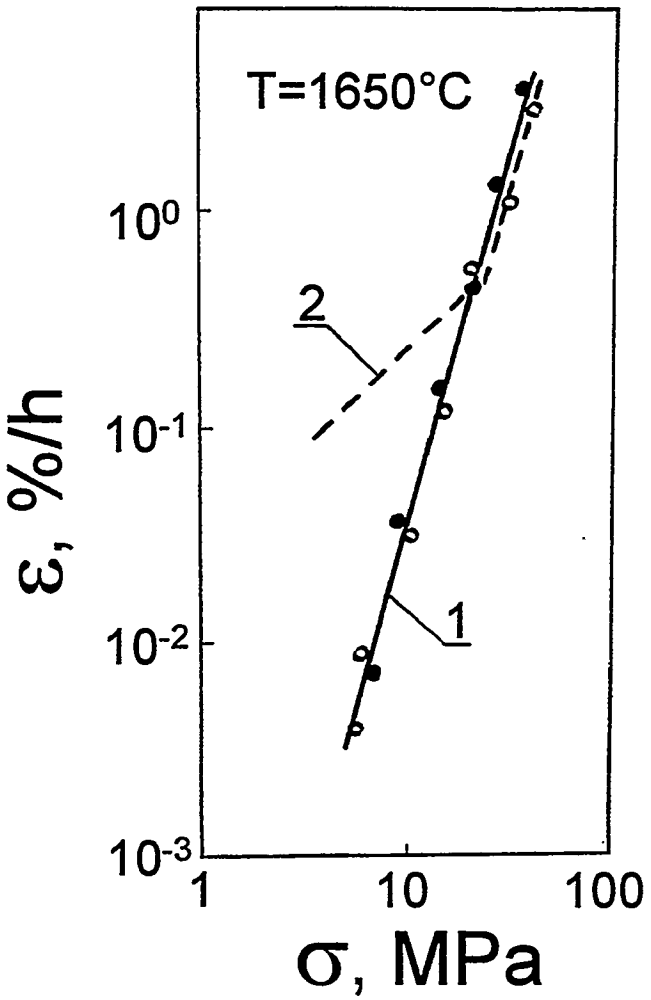

Figure 2.22. Stress dependence of uranium dioxide steady-state creep rate [30]:
1 - coarse-grained uranium dioxide
• - loading across <111>, d=150-250μm;
o - loading along <111>, d=500-3500μm
2 - sintered fine-grained UO_2 (d=5-10μm).

creep limit (σ>20 MPa), the creep rate is linear with stress ($\varepsilon \sim \sigma^{1.0}$), which points to the Nabarro-Hering vacancy-diffusion mechanism.

It follows from comparison of the curves that re-arrangement of the dioxide's initial fine-grained structure to column-type structure leads to reduction of the linear creep limit. The latter's level constitutes, for UO_2 with grain size d=5 to 10 μm, $\sigma_t \approx 20$ MPa; for the coarse-grained uranium dioxide with the column grain width of ~200μm -$\sigma_t \approx 2.6$ MPa [36]. As a result, a substantial reduction of UO_2 creep rate (by over two orders of magnitude) takes place under low stresses, characteristic of high-temperature thermionic fuel elements ($\sigma \leq 1$ to 2 MPa).

Gontar et al. [35] reviewed the results of the hypostoichiometric uranium-dioxide creep-rate investigation. Figure 2.23 provides a typical microstructure of the samples examined.

The hypostoichiometric uranium-dioxide sample structure was characterized by equiaxial grains and uniform porosity distribution. Metallic uranium inclusions, the size of which did not exceed 1 μm, were observed in as-fabricated samples. However, the investigations showed that upon heating such samples to T≥1100°C, the uranium dioxide transition to the single phase area takes place. For this study, samples with O/U=1.983 were used. The samples were heated in a 10^{-3} torr vacuum. The heating rate reached ~15°C/min. During heating, the samples' lattice spacing was measured at different temperatures. Measurement results are listed in Table 2.9.

The data show that as soon as TFEs experience operational conditions, the hypostoichiometric uranium dioxide transition to the single phase area occurs.

Hypostoichiometric $UO_{1.965}$ creep rate vs. stress is displayed in Figure 2.24 [35]. Data on $UO_{2.004}$ are included for comparison. The creep rates do not vary by more than a factor of two.

Table 2.9. UO_{2-x} lattice spacing vs. temperature [35]

	Lattice Spacing, A°		Phase Composition
T, °C	UO_2	Another Phase	
25	5.4695	4.940	UO_2+second phase
125	5.4771	4.946	UO_2+second phase
400	5.4995	4.960	UO_2+second phase
600	5.5100	4.980	UO_2+second phase
1000	5.5330	4.998	UO_2+second phase
1400	5.5525	-	UO_2
1800	5.5772	-	UO_2
25	5.4697	4940	UO_2+second phase

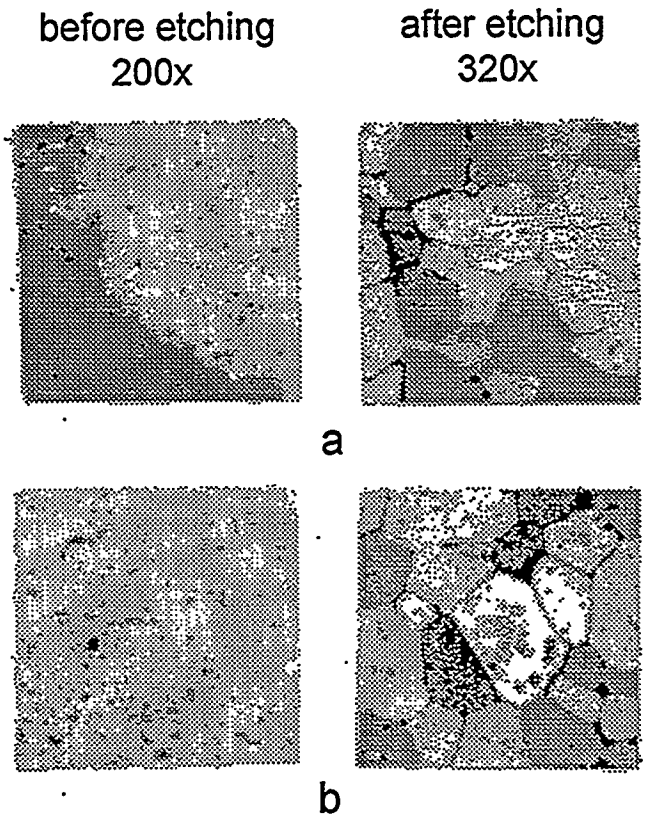

Figure 2.23. Microstructure of UO_{2-x} samples:
a. Uranium precipitates as a network along grain boundaries;
b. Uranium point inclusions near pores.

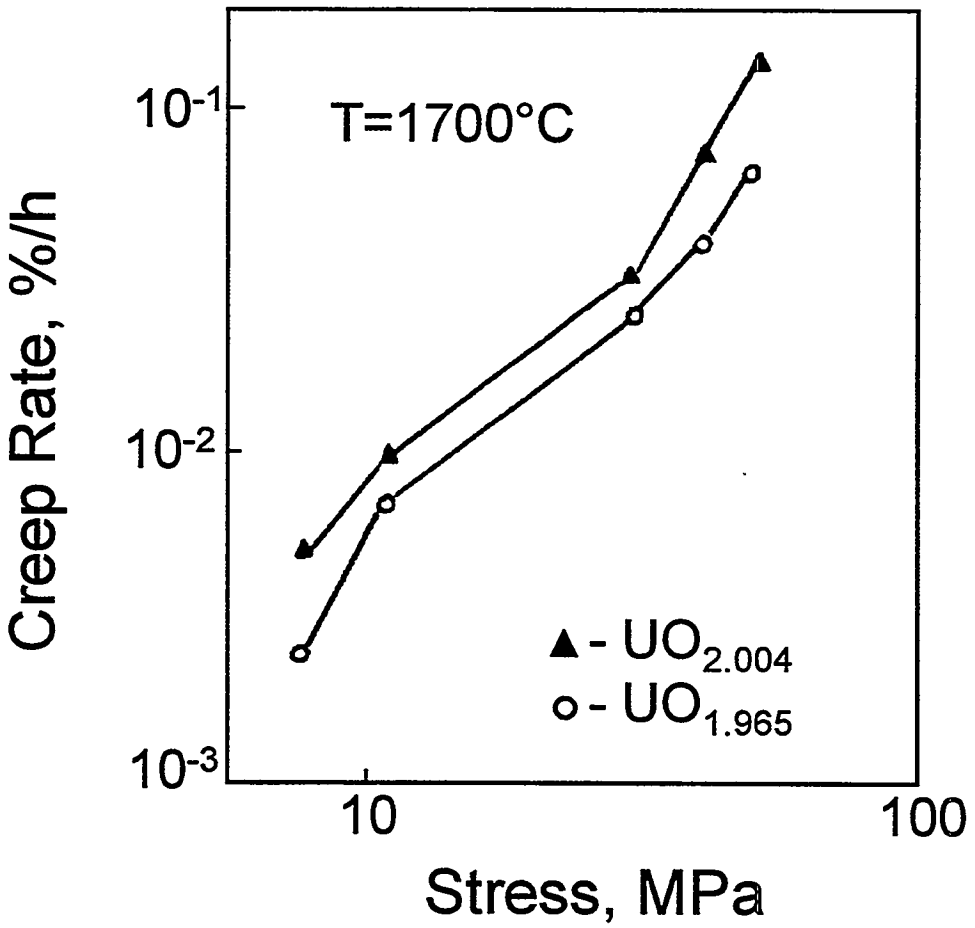

Figure 2.24. Stress dependence of hypo- and hyperstoichiometric uranium dioxide creep rate [35].

An optimal value of the oxygen coefficient for thermionic fuel elements is O/U≈1.995 to 1.975 [35, 37]. The results indicate that the use of hypostoichiometric uranium dioxide does not appreciably change the fuel creep rate.

2.2.2. Fuel Pellet Fabrication. Pellet Quality.

Pellets for TOPAZ-2 TFE fuel stacks are manufactured using methods of powder metallurgy. The process includes, after molding, sintering, and subsequent machining of fuel pellets, a visual inspection of the pellet surface and control of dimensions and density. Parameters to be checked include content of impurities, oxygen coefficient, and fuel structure parameters [38, 39].

The pellet-fabrication process had been developed and adopted at RI SIA "Lutch". The process had been put into practice on a semicommercial scale with output of series-produced sets of pellets for TFE tests in NPS land-based prototypes. The process provides a high stability of structural parameters and physical/chemical and strength characteristics of the pellets. Property stability is guaranteed both within each batch and for the series-produced sets of fuel pellets, i.e., from batch to batch [38].

The UO_2-pellet properties and their stability are to a considerable extent governed by the initial uranium dioxide powder. This powder fabrication process enables the manufacture of strong molded products under comparatively low molding pressure. Use of powders with favorable moldability and a binder, separable at low temperatures, sharply reduces the number of internal defects in finished products [40].

The stability of fuel parameters had been confirmed in the course of a joint test performed by Russian and American experts [39, 41]. Fuel pellets fabricated for TFE tests in NPS land-based prototypes were subjected to random inspection. The following characteristics were determined: pellet dimensions, impurity content, and macro- and microstructure. Tables 2.10 to 2.13 provide some of the fuel-pellet parameters being checked in the course of this joint Russian/American inspection [39, 41].

Fuel Pellet Dimension Deviation. The outer diameter of fuel pellets lies within a zone of manufacturing tolerance of 0.00 to 0.05 mm. The major portion of pellets (~60 to 70%) have the outer diameter deviation from its rated value of ~ 0.03 mm.

Density (Porosity). Pellet porosity was measured using mercuric porosimetry. The data are given in Table 2.10. About 90% of the pellets have a density in excess of 96% TD. Pellet-density stability is ensured both by the initial powder parameters and by sintering runs.

Table 2.10. Porosity of samples [41]

Initial Powder Batch	Sintering Batch	Stack No.	Pellet No.	Sampling label	Porosity, % vol
306	1	1	3	HD-33	1.7
			17	HD-39	1.4
			31	HD-44	1.6
306	2	1	40	HD-51	2.9
			53	HD-57	3.3
306	3	2	5	HD-63	3.3
			17	HD-70	1.9
306	4	2	30	HD-75	3.5
			39	HD-80	4.4
			45	HD-86	1.5
115	5	3	6	HD-93	1.4
76	6		19	HD-101	2.0
54	7		23	HD-108	1.6

Table 2.11. Content of impurities [41]

Element	Impurity Content in Samples, %mass			
	Sample HD-30 Pellet No. 3 Stack No. 1	Sample HD-48 Pellet No. 40 Stack No. 1	Sample HD-67 Pellet No. 17 Stack No. 2	Sample HD-98 Pellet No. 19 Stack No. 3
Fe	$1.2 \cdot 10^{-2}$	$1.5 \cdot 10^{-2}$	$1 \cdot 10^{-2}$	$2 \cdot 10^{-2}$
Si	$<1 \cdot 10^{-1}$	$1 \cdot 10^{-1}$	$1 \cdot 10^{-1}$	$4 \cdot 10^{-2}$
Mn	$2 \cdot 10^{-4}$	$1 \cdot 10^{-4}$	$1.2 \cdot 10^{-4}$	$<1 \cdot 10^{-4}$
Be	$<1 \cdot 10^{-4}$	$<1 \cdot 10^{-4}$	$<1 \cdot 10^{-4}$	$<1 \cdot 10^{-4}$
Cr	$<3 \cdot 10^{-3}$	$<3 \cdot 10^{-3}$	$<3 \cdot 10^{-3}$	$<3 \cdot 10^{-3}$
Mo	$1.7 \cdot 10^{-3}$	$2 \cdot 10^{-3}$	$1 \cdot 10^{-3}$	$1.3 \cdot 10^{-3}$
V	$<3 \cdot 10^{-3}$	$<3 \cdot 10^{-3}$	$<3 \cdot 10^{-3}$	$<3 \cdot 10^{-3}$
Ni	$<3 \cdot 10^{-3}$	$<3 \cdot 10^{-3}$	$<3 \cdot 10^{-3}$	$<3 \cdot 10^{-3}$
B	$<3 \cdot 10^{-5}$	$<3 \cdot 10^{-5}$	$<3 \cdot 10^{-5}$	$<3 \cdot 10^{-5}$
Cu	$5 \cdot 10^{-4}$	$2.5 \cdot 10^{-4}$	$1 \cdot 10^{-4}$	$2.3 \cdot 10^{-4}$

Table 2.12. Isotopic composition of fuel pellets [41]

Sample No./ Stack No.	Sampling Label	Isotope Concentration, % at.			
		U-234	U-235	U-236	U-238
3/1	HD-29	1.10±0.02	95.88±0.05	0.015± 0.005	3.00±0.03
17/2	HD-66	1.02±0.02	95.87±0.05	0.07±0.01	3.04±0.03
6/3	HD-89	1.00±0.02	95.78±0.05	0.48±0.03	2.74±0.03
19/3	HD-96	1.11±0.02	95.86±0.05	0.025±0.03	3.00±0.03
23/3	HD-104	1.11±0.02	95.89±0.05	0.027±0.05	2.97±0.03

Table 2.13. Mean size of pellet grains [39]

No.			
Stack	Pellet	Sampling Label	Mean Grain Size, μm
1	17	HD-36	28
1	31	HD-47	28
1	53	HD-54	28
2	5	HD-60	25
2	45	HD-83	21
3	6	HD-90	33*
3	19	HD-97	21
3	23	HD-105	25

Note: * after thermal tests

Impurity content. Data on impurity content are presented in Table 2.11.

Isotopic Composition. Data on isotopic composition are presented in Table 2.12.

Microstructure. The results of measurements of mean grain size in uranium-dioxide pellets are provided in Table 2.13.

The observed grains are equiaxial with low porosity. Mean grain size lies within the range of 21 to 28 μm (the increase of grain size in pellet No. 6 is caused by previous thermal tests).

The results of the investigation have allowed Los Alamos National Laboratory to state [41] that the procedures currently applied at RI SIA "Lutch" and the pellets' quality control are very similar to those used in the United States. Control data have shown that the pellets manufactured at RI SIA "Lutch" can be successfully applied to the American TOPAZ program [39, 41].

The experience of RI SIA "Lutch" and RSC "Kurchatov Institute" related to the TOPAZ-2 points out that uranium-dioxide pellets with properties that were optimized during TFE development are essential to achieving a long life (over 3 years) and stable parameters for electrical output from a TFE.

2.3. Materials for Spacers and Electroinsulation

Figure 2.25 outlines the arrangement and some design features of the single-cell TFE. The purpose of the spacers is to ensure a guaranteed interelectrode gap between TFE electrodes. The electroinsulating materials separate the emitter from the collector and the electrodes from the TFE case.

In the course of operation these components are subjected to the effects of the aggressive environments of high temperature, radiation, and mechanical and thermal loadings. Therefore, reliability of these elements is determined by high corrosion and radiation resistance and stability of thermal and strength parameters during operation.

At present, ceramic materials based on oxides such as Al_2O_3, Sc_2O_3, and others are usually used for spacers and electronsulating parts. The materials used at RI SIA "Lutch" for TFE spacers and electroinsulation parts, as well as their basic characteristics, are presented in Table 2.14.

2.3.1. Thermal and Electric Properties

The study of the properties of these materials was aimed mainly at investigations of their thermal conductivity, thermal expansion, electric resistance, and electric strength. Results for alumina are presented in Tables 2.15 to 2.18. The properties of scandia at low temperatures (up to 473 K) are given in Table 2.19.

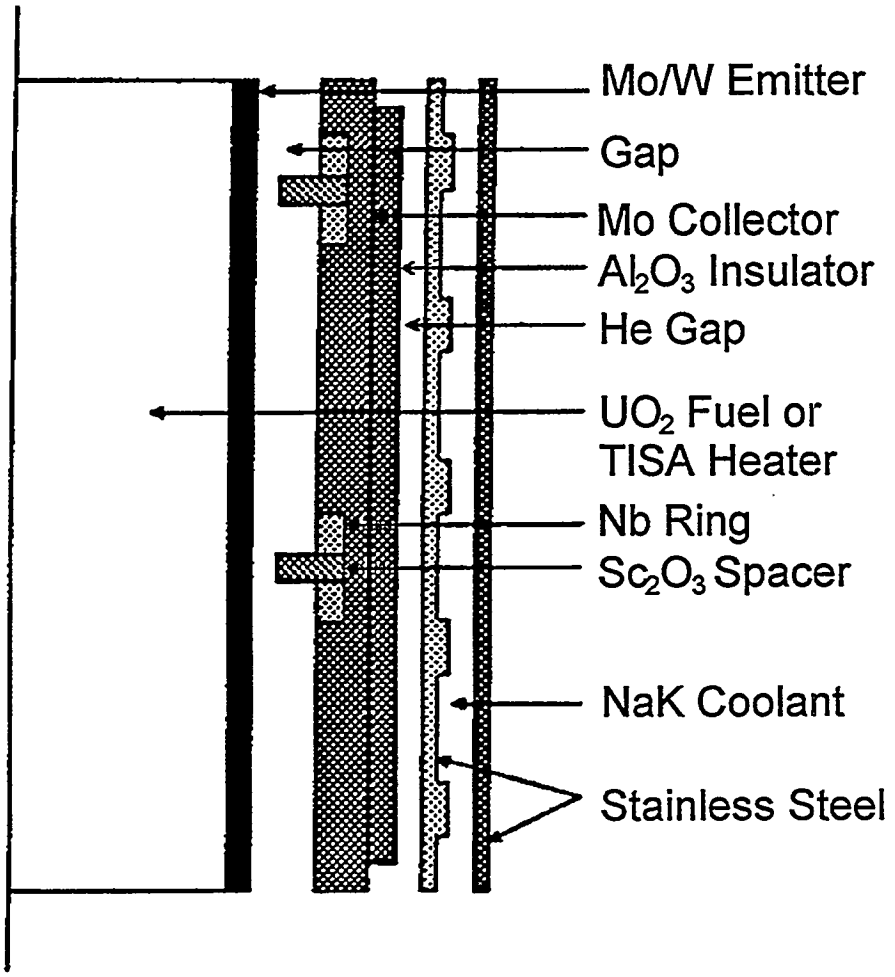

Figure 2.25. TOPAZ-II TFE working section.

Table 2.14. Main characteristics of materials for spacers and electroinsulating elements [4]

Material	Polycrystal Alumina		Single Crystal Alumina	Polycrystal Scandia
Designation	99.7 Al_2O_3	98.7Al_2O_3	mono-Al_2O_3	Sc_2O_3
Structural Element	Spacer	Insulator	Insulator	Spacer
Content of Basic Oxide	99.7	98.7	100	100
Alloying Dopants	MgO	MgO, Y_2O_3	-	-
Density, %TD	98 to 99	96 to 98	100	98 to 99
Grain Size, microns	20 to 40	40 to 60	-	1 to 3
Fabrication Process	Sintering	Sintering	Drawing out of Melt	Isostatic Molding

Table 2.15. Thermal conductivity of Al_2O_3 electroinsulating materials, W/(m·K) [4]

Temperature, K	98.7 Al_2O_3	mono-Al_2O_3	
		Along "C"-axis	Across "C"-axis
293	-	26	23.1
373	-	22.4	20
473	22	17.5	18
573	18	-	16.5
873	10	-	10.5
1273	5.5	-	6.5
1873	6.0	-	7

Table 2.16. Mean coefficient of linear heat expansion of Al_2O_3 electroinsulating materials, $\alpha \cdot 10^6$, K^{-1} [4]

Temperature, K	98.7 Al_3O_3	monoAl_2O_3	
		Along "C"-axis	Across "C"-axis
373	6.35	7.15	5.60
473	6.80	7.50	6.10
573	7.18	7.78	6.60
673	7.45	7.96	6.90
773	7.62	8.10	7.10
873	7.74	8.23	7.22
1273	8.15	8.60	7.62
1873	8.60	8.96	8.06

Table 2.17. Specific volume electrical resistance of Al_2O_3 electroinsulating materials, Ohm·cm [4]

Temperature, K	98.7 Al_2O_3	monoAl_2O_3
293	$(1\text{-}10)\cdot 10^{14}$	$(1\text{-}29)\cdot 10^{18}$
873	$9\cdot 10^4$	$5\cdot 10^8$
1273	$1.5\cdot 10^3$	$9\cdot 10^4$
1873	95	100

Table 2.18. Breakdown voltage for Al_2O_3 electroinsulating materials, kV/mm [4]

Temperature, K	98.7 Al_2O_3	monoAl_2O_3
293	30 to 40	50 to 52

Table 2.19. Scandia properties [4]

Thermal Conductivity,W/(m·K)	Coefficient of Linear Heat Expansion, $\alpha \cdot 10^6$, K^{-1}	Specific Electrical Resistance, Ohm·cm
4.0	7.8	$(5\text{-}15) \cdot 10^{14}$

2.3.2. Mechanical Properties

Under standard test conditions, the strength for 98.7 Al_2O_3 from various batches has the following ranges [4]:

- bending: 150 to 300 MPa;
- tensile: up to 250 MPa;
- compressive: up to 2500 MPa.

The strength for 99.7 Al_2O_3 has the following ranges [4]:

- bending: 240 to 400 MPa;
- tensile: up to 300 MPa;
- compressive: up to 3000 MPa.

The temperature dependencies of the bending strength for polycrystal alumina and scandia are displayed in Figure 2.26. Figures 2.27 and 2.28 contain data on the single-crystal Al_2O_3 bending and tensile tests.

Investigations of these material properties at RI SIA "Lutch" reveal that they are strongly affected by treatment runs and the surface condition of samples [4].

2.3.3. Irradiation Influence

The influence of irradiation on the spacers and electroinsulation materials are reviewed in the work of the Institute of Physics and Power Engineering (Obninsk) [43]. The alumina, baria, yttria, scandia, and zirconia samples studied were manufactured from high-purity powders. Total impurities in the finished samples ranged from 0.05 to 0.1% mass.

The samples possessed polycrystal structures and were molded by the method of hot casting with subsequent two-step annealing. In addition to the polycrystal samples of Al_2O_3, single crystals obtained from a melt by the Stepanoff method were studied. Physical and mechanical characteristics of as-fabricated samples are provided in Table 2.20.

The samples were irradiated at temperatures of 523 to 723 K and fluences of $5 \cdot 10^{21}$, $2.1 \cdot 10^{22}$, and $6 \cdot 10^{22}$ n/cm^2.

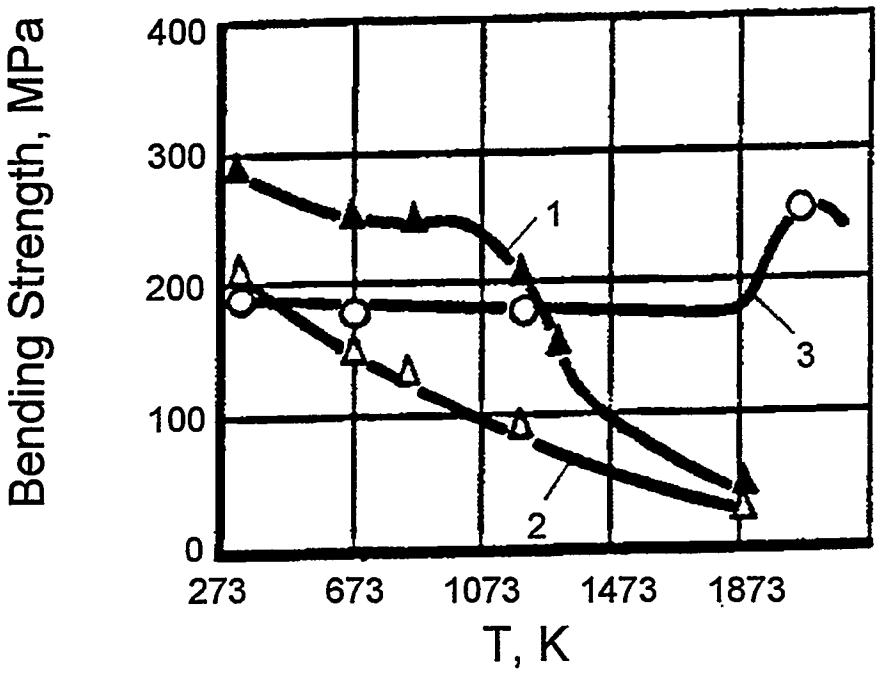

Figure 2.26. Bending strength of polycrystal alumina and scandia vs. temperature [4]:

1 - 99.7% Al_2O_3;
2 - 98.7% Al_2O_3;
3 - Sc_2O_3.

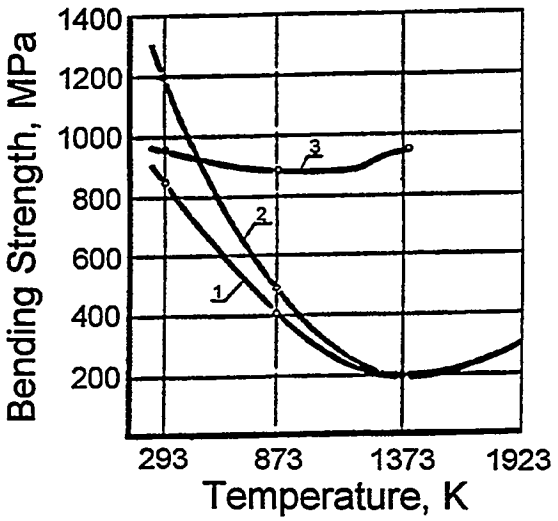

Figure 2.27. Temperature dependence of bending strength for mono-Al_2O_3 [4]:
1, 2 - sample axis <0001>;
3 - at 60° to <0001>;
1 - grinding;
2 - polishing.

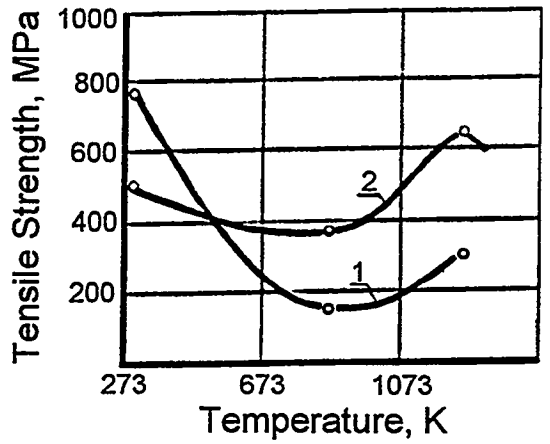

Figure 2.28. Temperature dependence of tensile strength for polished mono-Al_2O_3 [4]:
1 - along <0001>-axis;
2 - at 45° to <0001>-axis.

Swelling of Samples. The swelling of samples was measured through changes in sample density after irradiation. The density was measured using hydrostatic weighing. Apparently yttria, scandia, and zirconia initially swell under the influence of irradiation, but at some point they stop swelling, even with continued irradiation (cf. [43]).

Minimum swelling was found in yttrium oxide. Its swelling level is maintained after irradiation by a $1.89 \cdot 10^{22}$ and $6 \cdot 10^{22}$ n/cm^2 fluence. Scandia and zirconia were characterized by swelling a factor of 2 higher than that of yttria. These oxides hold their swelling value after irradiation by a $4.6 \cdot 10^{21}$ and $2.1 \cdot 10^{22}$ n/cm^2 fluence.

As to the polycrystal alumina, swelling under irradiation by $4.9 \cdot 10^{21}$ n/cm^2 fluence was 5 times greater than that of yttria swelling; single-crystal alumina underwent swelling 2.5 times lower than polycrystal. After irradiation by $6 \cdot 10^{22}$ n/cm^2, the polycrystal aluminum oxide, notwithstanding its considerable swelling—17 times that of yttria—maintained its structural integrity.

Beryllia samples after irradiation by a $4.7 \cdot 10^{21}$ n/cm^2 fluence underwent a 9.2±0.5% swelling. After $6.6 \cdot 10^{22}$ n/cm^2 fluence irradiation, the beryllium oxide samples lost structural integrity.

Table 2.20. Characteristics of ceramic samples

Characteristic	Material Composition					
	mono-Al_2O_3	BeO	Y_2O_3	Al_2O_3+MgO	Sc_2O_3+ +ZrO_2	ZrO_2+ +Y_2O_3
Density, kg/m^3	3.98	2.92 to 2.95	5.01 to 5.04	3.84 to 3.93	4.05 to 4.09	5.59 to 5.63
Open Porosity,%	<0.1	<0.1 to 0.17	<0.1	<0.1	<0.1 to 0.4	<0.01 to 0.12
Bending Strength, MPa, T_{test}=293K	1000	266	55	225	-	140
Compressive Strength, MPa, T_{test}=293K	1450	1550	680	2200	900	1180
Moduls of Elasticity, GPa	462	323	150	390	200	195
LTEC, $10^{-6}K^{-1}$ T_{test}=293 to 1073 K	8.6	8.4	7.95	8.1	8.7	10.1

Microstructure and Microhardness. In the as-fabricated condition, the grain size for the materials tested ranged from 20 μm (alumina and yttria) to 55 μm (zirconia). After irradiation, the grain size did not alter. No appreciable changes in the structure of alumina, yittria, or zirconia were found.

For all but zirconia, the oxides' microhardness changed slightly. The microhardness of zirconia, after $2 \cdot 10^{22}$ n/cm^2 fluence irradiation, increased by 60%.

Thermal Conductivity. Thermal conductivity was measured at 373 K using the method of heat flux.

The greatest change in thermal conductivity, 98%, was observed on beryllium oxide; the least for zirconium and scandium oxides. The highest absolute value of thermal conductivity after irradiation by a $1.34 \cdot 10^{22}$ n/cm^2 fluence was found in the alumina sample.

Electric Strength. Measurements of electric strength (the maximum electric field intensity within a sample at which the electroinsulating properties are maintained) were performed on samples of alumina and beryllia.

In the as-fabricated conditions, the alumina samples had a breakdown strength of 32±1 kV/mm, and beryllia, 25±1 kV/mm. After irradiation by a $3.5 \cdot 10^{21}$n/cm^2 fluence, the alumina breakdown strength was reduced to 17 kV/mm and beryllia's to 3 kV/mm.

Change in Crystal Lattice Parameters. Experimentally obtained values of changes in lattice parameters are presented in Table 2.21.

The greatest change in the crystal lattice parameters occurred in alumina and beryllia after irradiations of 3 to $4 \cdot 10^{21}$ n/cm^2.

The data allow several conclusions [43]. Lattice type plays an important role in irradiation stability: oxides with the more symmetrical cubic lattice are less prone to irradiation swelling. Swelling of the ceramics with a hexagonal lattice (alumina, beryllia) considerably exceeded swelling of other oxides subjected to irradiation under the same conditions.

Study of thermal and electric properties shows that alumina conserves its thermal conductivity and breakdown strength at a level acceptable for this material to be used in space NPSs. Scandium and yttrium oxides are also promising for use in space NPSs.

2.3.4. Spacer Resistance to Cesium Plasma

Investigations RI SIA "Lutch" and SPTI (Sukhumi) previously revealed that alumina is prone to react strongly with cesium plasma [1, 44, 45]. This process

Table 2.21. Change in lattice parameters after irradiation [41]

Material	Fluence, 10^{21}n/cm^2 E>0.1MeV	Irradiation Temperature, K	Lattice Type	Change in Parameters, %	
				Δa/a	Δc/c
Single Crystal Al_2O_3	2.2	540	hexagonal	0.32±0.02	0.42±0.04
Polycrystal Al_2O_3	3.0	540	hexagonal	0.53±0.17	0.34±0.05
Polycrystal Al_2O_3	18.7	723	hexagonal	0.02±0.08	0.08±0.06
BeO	3.2	600	hexagonal	0.14±0.03	3.08±0.22
Sc_2O_3	3.0	583	cubic	0.19±0.01	-
Sc_2O_3	19.1	723	cubic	0.18±0.02	-
ZrO_2	3.4	330	cubic	0.13±0.01	-
ZrO_2	18.7	723	cubic	0.10±0.01	-
Y_2O_3	17.0	723	cubic	0.18±0.02	-

considerably restricts the life of Al_2O_3 spacers used in the first phase of work on TOPAZ-2 TFEs [2].

Based on thermodynamic analysis, the alumina is stable in a vacuum and cesium vapor up to 2000 K [44], but in TEC cesium plasma (P_{Cs}=2.5 gPa, $P_{Cs+}=0.1P_{Cs}$, $P_{O_2}=2\cdot10^{-6}$Pa), the upper threshold of alumina stability does not exceed 1550 K.

To forecast spacer lifetimes, their corrosion in a TFE interelectrode gap medium was experimentally investigated [44, 45]. The experimental device for this investigation comprised a TEC with a parallel-plate electrode configuration. A specimen was placed in a longitudinal slot in the emitter isothermic section, which was heated using a resistor heater. Heat was removed from the collector through a helium gap to a water jacket. The residual gas composition within the device operating space after degassing was measured by mass spectrometer. Operating conditions were altered and the TEC output parameters registered using a device that measures and plots current-voltage characteristics.

To study the corrosion, the sample was held at a fixed temperature for 300 to 500 hrs within the IEG of the experimental TEC under vacuum, diffusion, and ignited modes. Before and after the hold, sample weight was measured. The sample mass-loss rate (W) was estimated using the formula

$$W = \Delta G / (S \cdot \tau),$$

where: ΔG - change in mass of sample;
S - open portion of sample side surface;
τ - hold time.

Samples of alumina with a 3.989 g/cm^3 density and 3 to 5 μm grain size were examined.

Temperature dependencies of the mass loss for different TEC operation conditions are shown in Figure 2.29. The mass-loss rate in cesium vapor under diffusional TEC operation conditions is about one order of magnitude lower than the vacuum conditions. This is explained by the effect of a diffusion barrier formed by Cs atoms to the evaporated particles.

In cesium plasma (ignited TEC operation conditions), the mass-loss rate for alumina grows by 1.5 to 2 orders of magnitude as compared to this parameter in cesium vapor. The samples' structure and their surface relief are considerably changed [44, 45].

Al_2O_3 mass-loss rate dependence on the TEC operation conditions is shown in Figure 2.30. The mass-loss rate increases stepwise (by about two orders of magnitude) when the transition from the diffusion regime to the ignited mode occurs, which is linked to Al_2O_3 reacting with cesium plasma [44, 45].

A strong interaction between alumina oxide and cesium plasma considerably limits spacer life, but RI SIA "Lutch," in the course of work on TOPAZ-2 TFE, had successfully substituted new scandia spacers, stable under TFE operation, for those of alumina.

The stability of a number of refractory oxides (Y_2O_3, BeO, ZrO_2, HfO_2, Sc_2O_3, MgO, ThO_2, Al_2O_3) under various IEG-atmosphere conditions was analytically assessed using methods of thermodynamics. It was ascertained that in cesium plasma only yttria and scandia are stable up to a maximum temperature of 2000 K [43].

Kozlov et al. [46] provided comparative experimental data on Sc_2O_3 and Al_2O_3 spacer stability. Material chemical composition of the investigated samples is given in Table 2.22.

Table 2.22. Chemical composition of sample materials under investigation

	Element										
Material	Cr	Fe	Ni	V	Mg	Al	Si	Ca	Sc	Ba	Ti
Al_2O_3	0.01	0.01	0.01	0.01	0.04	99.39	0.01	0.06	0.00	0.06	0.00
Sc_2O_3	0.01	0.00	0.01	0.00	0.00	0.04	0.00	0.00	99.57	0.06	0.01

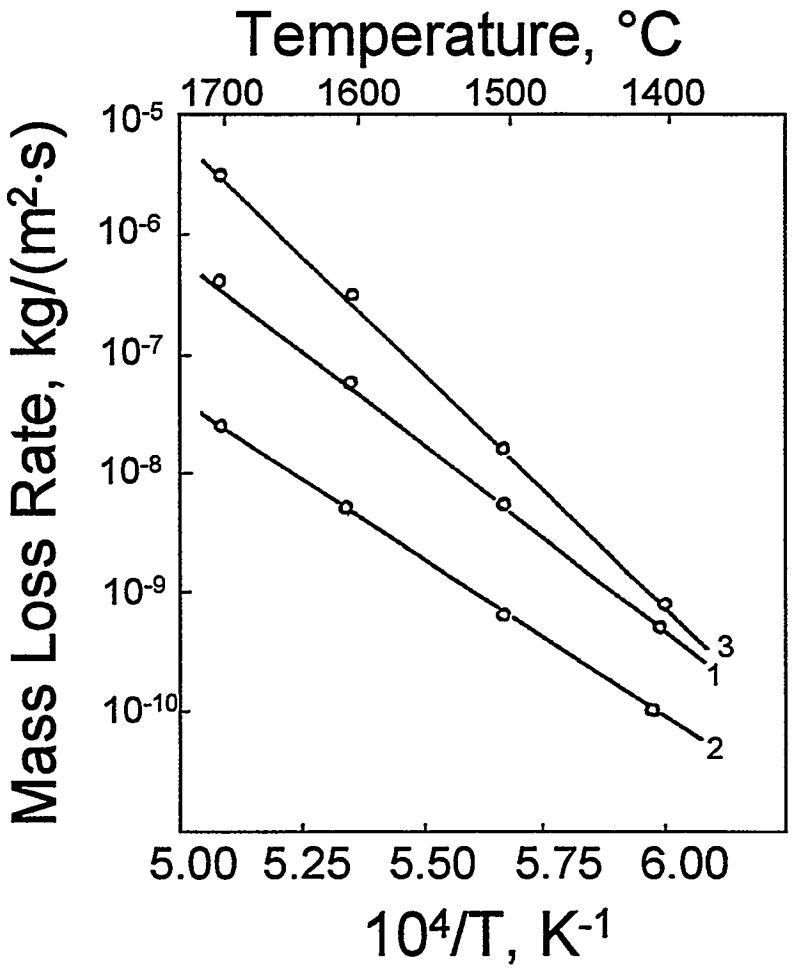

Figure 2.29. Temperature dependence of Al_2O_3 mass-loss rate [44]:
1 - in vacuum ($P_{res}<1\cdot10^{-3}$ Pa);
2 - in cesium vapor (P_{Cs}=2.5 gPa);
3 - in cesium plasma (P_{Cs}=2.5 gPa, J_k=3 A/cm^2).

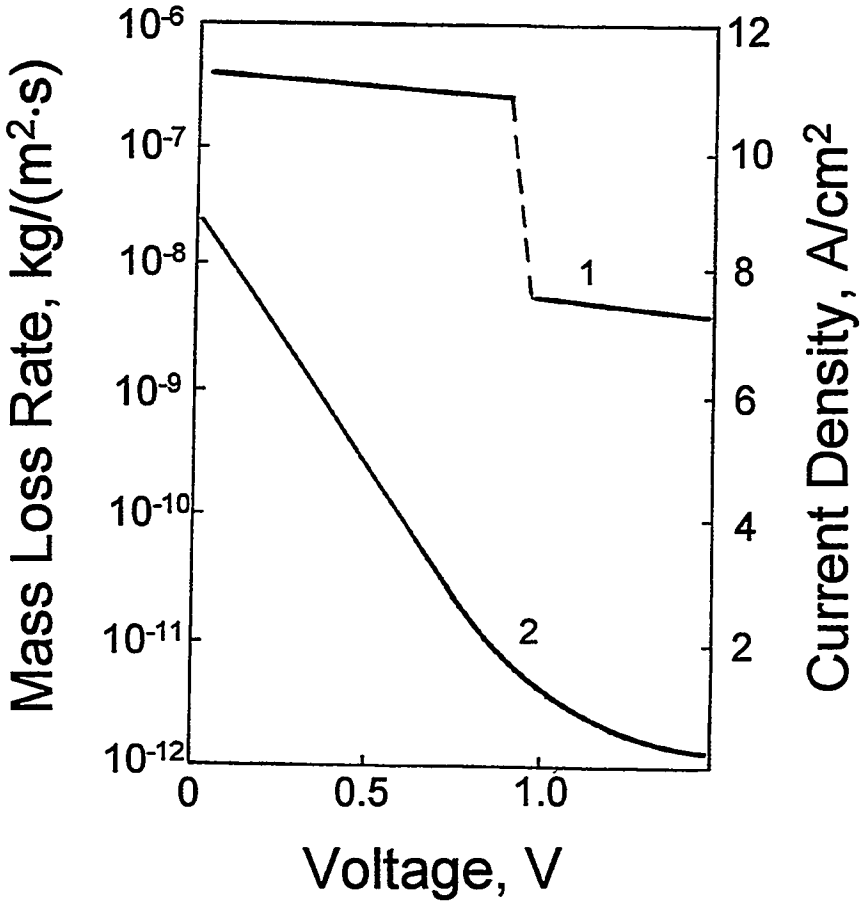

Figure 2.30. Al_2O_3 mass-loss rate dependence on TEC operating conditions (T_{Sample}=1870 K, P_{Cs}=2.5 gPa) [44]:
1 - mass loss rate;
2 - voltage-current characteristics of TEC.

Table 2.23. Lifetime of TFE spacers with 0.4 mm interelectrode gap [46]

Spacer Material	Parameter	
	Mass Loss Rate, kg/(m^2·s)	Lifetime, hrs
Al_2O_3	$3.9 \cdot 10^{-8}$	$2.077 \cdot 10^3$
Sc_2O_3	$8.0 \cdot 10^{-11}$	$1.013 \cdot 10^6$

Figure 2.31 presents the above materials' mass-loss rates under various TEC operating conditions. The mass-loss rate of Sc_2O_3 does not change appreciably in cesium plasma (ignited mode of TEC operation) and is about the same as in Cs vapor (diffusion conditions). The Sc_2O_3 surface profile and structure, unlike Al_2O_3 samples, did not change during these tests. As shown, the Sc_2O_3 mass-loss rate is lower by at least three orders of magnitude than that of alumina under the ignited TEC operating conditions, which is of the greatest practical importance.

The lifetime for TOPAZ-2 TFE spacers from these materials was estimated from these experimental results (Table 2.23). At an emitter temperature of ~1800°C, Al_2O_3 spacer life does not exceed 2500 hrs, while Sc_2O_3 spacer lifetime reaches $\sim 1 \cdot 10^6$ hrs.

At present Sc_2O_3 spacers are used in the TOPAZ-2 single-cell TFE, improving operation lifetimes.

Scandia ceramics are manufactured using the method of powder metallurgy, which encompasses the following basic steps: fabrication of blanks through hydrostatic molding; encasing blanks in niobium shells; hot isostatic molding of blanks; finishing spacers by diamond-tool machining; and control of spacers [47]. Specially developed processing techniques allow the production of scandia ceramics with a fine-grained structure (grain size of 2 to 3 μm) and high density at comparatively low temperatures of the isostatic molding. The scandia ceramic possesses high strength over a wide temperature range, combined with a high melting point, low evaporation rate, and good chemical resistance to aggressive media characteristic of TEC operation [44].

2.4. Vacuum Preparation of Fuel Pellets

A TFE is a high-temperature gas-discharge device whose operational performance is substantially influenced by some of the constituents of the interelectrode gap gas medium. Residual gases in the IEG typically contain H_2, N_2, O_2, H_2O, CO, and CO_2 in substantial amounts. The most detrimental

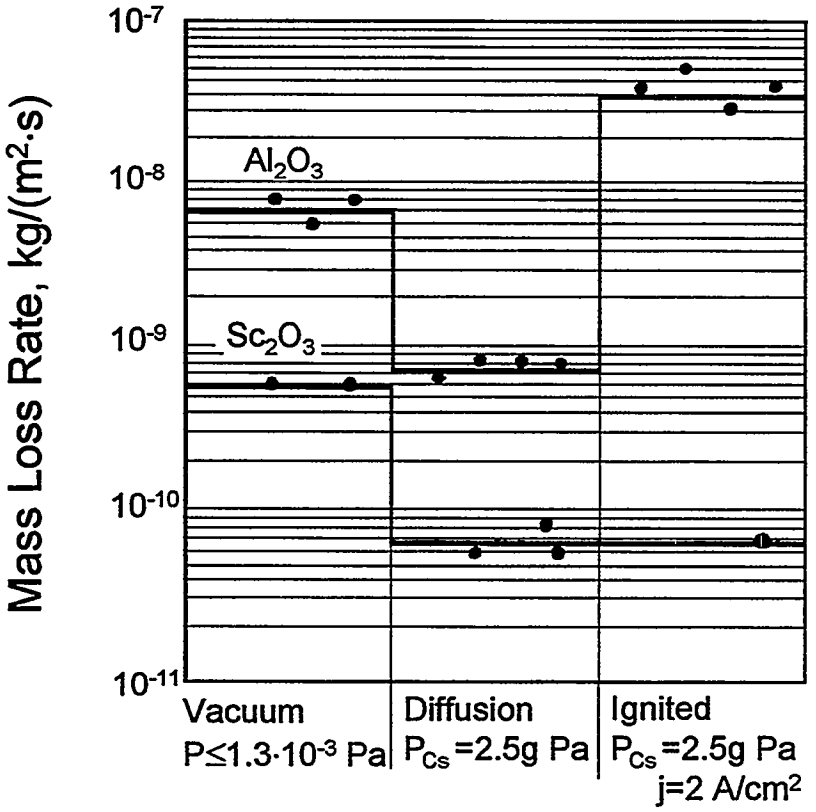

Figure 2.31. Al_2O_3 and Sc_2O_3 mass-loss rate at 1770 K vs. TFE operating conditions [46].

effect of the complex gas medium is the mass transfer of emitter material onto the collector surface, which considerably changes the latter's properties [48]. This factor will be considered in detail in Chapter 3. In addition, chemically active gases such as O_2 and CO exert an essential effect upon the emitter and collector emission parameters already under ~10^{-5} torr pressure [48]. Oxygen appreciably improves the emitter emission characteristics, but CO, reacting slightly with the emitter, sharply spoils the collector's parameters. As for the diatomic gases N_2 and H_2, the literature contains data suggesting that, under low pressures at the residual gases' level, these gases do not exert any essential influence on converter performance. Thus, for example, Zherebtsov et al. [49] reported that output voltage linearly decreased by 0.11 V/gPa with hydrogen pressure increase.

The major gas source, specifically in TFEs with communicating IEG and fuel-element cavities, is fuel. Therefore, the key task in the study of gas evolution was to reveal the laws governing fuel outgassing relative to gas-forming impurities and temperature. Since under NPS conditions, degassing occurs through a long exhaust-channel system, it is important to determine the possibility of fuel pre-degassing and the effect on gas evolution by a subsequent long hold of the fuel in air.

Gas release from uranium dioxide was investigated by heating, in a 10^{-4} to 10^{-6} Pa vacuum, cylindrical pellets of 97 to 98% TD density fabricated by routine methods of powder metallurgy [50, 51]. Evolution of gases from UO_2 was studied in a high-vacuum, high-temperature installation with mass-spectrometer monitoring of gas composition. Figure 2.32 shows the time dependence of the gas evolution specific rate (q) for $UO_{2.005}$ samples, uniformly heated to 2200 K [50]. The temperature rise with time in the process of outgassing is represented by the dotted line. As one can see, hydrogen evolution begins at an early stage of outgassing at comparatively low temperature. At ~60 min, when the rate of hydrogen evolution is at a maximum, the fuel temperature is ~750 K. With a further temperature rise, the hydrogen-evolution rate decreases abruptly. Thus below 1250 K the main gas evolved by UO2.005 is hydrogen. Evolution of CO_2 and water vapor entirely ceases at 1200 K. At higher temperatures, the main gas evolved has a molecular mass of 28, including a mixture of CO and N_2.

Andrievsky et al. and Galkin et al. [50, 51] did not discriminate the above constituents' contributions. The non-monotonic behavior of gas release was explained by different sites of gas-forming impurities in the fuel [50]. So, the first maximum at 670 K is related to surface-gas desorption. The maximum at 1550 K is explained by removal of gases dissolved in the fuel bulk. Increase of the gas-evolution rate at a high temperature (1700 to 2300 K) is apparently linked to the release of gases being formed by decomposition of uranium oxycarbonitrides [50]. Total content of nitrogen and carbon after high temperature annealing (2300 K, hold 3 to 5 hrs) was reduced to 10^{-4} to 10^{-3}% mass.

Figure 2.33 presents results of a study of the evolution of gases from $UO_{2.005}$ with various nitrogen and carbon contents [50]. Data are also presented for the effect on gas evolution of the time that uranium dioxide degassed at 2300 K is held in air. The study involved only H_2 and (N_2 + CO), since they comprise the major contribution to gas evolution in the investigated temperature range (500 to 2300 K). It follows from Figure 2.33 that hydrogen evolution depends on the duration of the degassed $UO_{2.005}$ hold in air; however, gas sorption practically terminates within several hours.

The total amount of hydrogen released does not exceed 1 to $2 \cdot 10^{-3}$ stand.cm^3/g; the main fraction is evolved during heating to 750 K.

(CO+N_2) evolution is strongly affected by the temperature and C and N contents in uranium dioxide. A change in the content of these impurities from $2 \cdot 10^{-2}$ to $1.7 \cdot 10^{-1}$% enhances the gas release from fuel by about a factor of 20. Thus to remove nitrogen and carbon, high degassing temperatures of 2200 to 2300 K are required. Degassing at such temperatures unavoidably brings about UO_2 loss by evaporation.

A considerable file of data relating to degassing a number of UO_2 pellet batches is contained in the work of Rakitskaya et al. [52]. The pellets tested had significant variation in density, 96 to 81% TD, but the impurity content was about the same through all the batches: ~20 ppm carbon and not over 50 ppm nitrogen. Gas release from hyperstoichiometric uranium dioxide $UO_{2.004}$ and hypostoichiometric $UO_{1.995}$ was studied separately. The residual pressure of gases in the unfueled installation was 10^{-4} to 10^{-5} Pa.

Figure 2.34 presents change in gas partial pressures within the installation in the course of heating to 1800°C and 10 hrs annealing at the same temperature for a batch of $UO_{1.995}$ pellets. Here the relative contributions of CO and N_2 were discriminated, in contrast to previous work [48, 49]. As seen from Figure 2.34, the residual gases contain CO in considerable amounts. Comparison of Figures 2.31 and 2.34 confirms the conclusions of Koryukin et al. [48]. The key problem is oxide fuel purification from carbon impurities.

Since uranium-carbide-based fuels are considered as alternative fuel compositions, gas evolution from uranium-carbide alloyed compounds was studied [51]. As for uranium dioxide, the major gas exerting an adverse effect on TEC behavior at high temperatures is carbon monoxide. The gas release level for carbide materials is determined by the initial concentration of oxygen in the fuel.

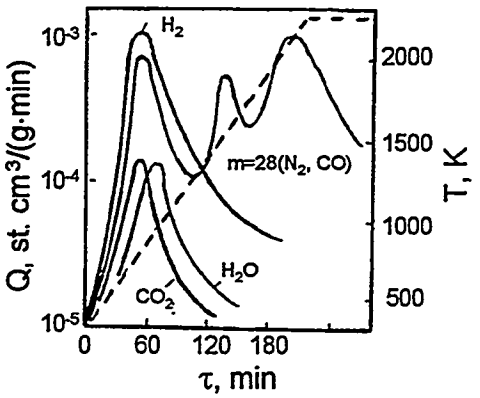

Figure 2.32. Composition of gases released from UO_2:
- - - - change in sample temperature when heating;
—— specific rate of gas release.

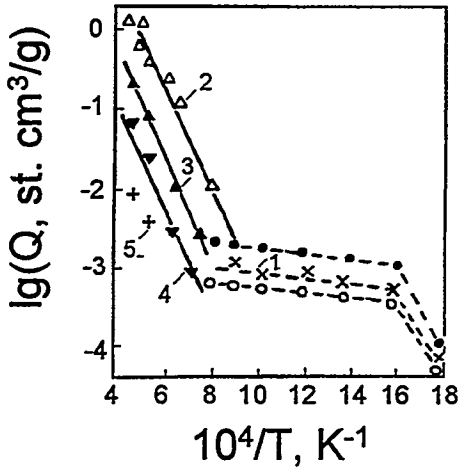

Figure 2.33. Temperature dependence of gas release:
- - - hydrogen;
— gas with mass m=28 (N_2, CO);
• - as-fabricated UO_2;
° - UO_2 after 6 and 46 hrs hold in air;
1 - UO_2 after 360 hrs hold in air;
2 - C + N =$1.7 \cdot 10^{-1}$% mass;
3 - C + N =$5 \cdot 10^{-2}$% mass;
4 - C + N =$2 \cdot 10^{-2}$% mass;
5 - C + N =$7 \cdot 10^{-3}$% mass.

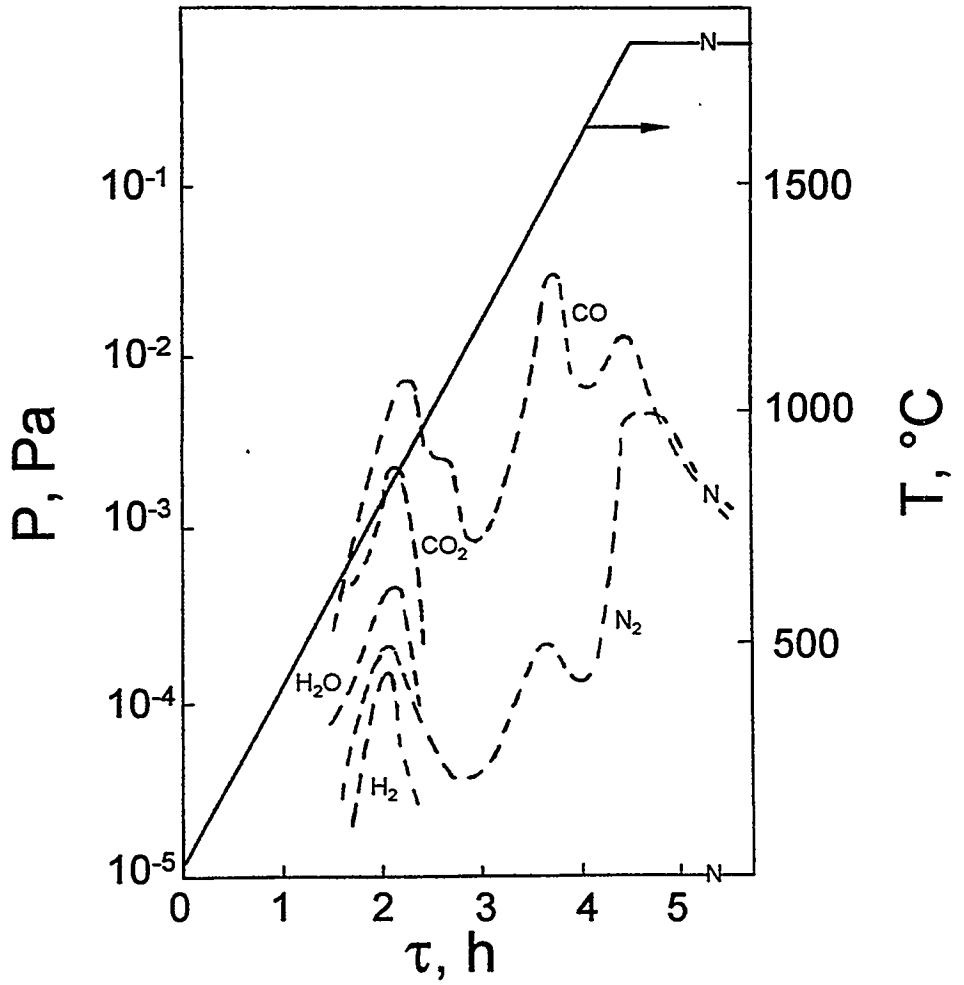

Figure 2.34. Partial pressures of gases over pellets [52]:
—— change in temperature with heating;
- - - partial pressure of gas over pellets.

2.5. References

1. Nikolaev, Yu.V. "R&D RI SIA Lutch in the Area of Materials for Direct Conversion NPP." Report at the 4th Branch Conference "Nuclear Power in the Space. Materials. Fuel." Podolsk, 1993.
2. Nikolaev, Yu.V., Yastrebkov, A.A., et al. "Structural Materials on Base of Refractory Metals." Report at the 4th Branch Conference "Nuclear Power in the Space. Materials. Fuel." Podolsk, 1993.
3. Langhape, R. "Thermionische Energiewandler." *Elektrotechnik und Machinenbau.* 1969, v. 86, No. 11, pp.480-487.
4. "The Materials for Thermionic Converters." Review on Contract#1-209 between UEKI Corporation (Japan) and STC "Istok" RI SIA "Lutch" (Russia). Podolsk, 1995, 73 p.
5. Mikhailov, S.N., Chechentsev, V.N., and Shmakov, A.M. "A Practice of Production Non-Porous Single Crystal Molybdenum of Enlarged Diameter." *Growing of Refractory and Rare Metal Single Crystal.* Moscow: Nauka, 1973, p. 165.
6. Ismailov, A.I. "Temperature and Deformation Rate Impact on Molybdenum Single Crystal Mechanical Properties." *Rare Metals and Single Crystal Structure Alloys.* Moscow: Nauka, 1981, pp. 85-89.
7. Peletsky, V.E., Druzhinin, V.P., and Sobol, Ya.G. "Thermal Properties of Single Crystal Molybdenum at High Temperatures." *Single Crystal of Refractory and Rare Metals.* Moscow: Nauka, 1971, pp. 85-89.
8. Evstyukhin, A.I., Gavrilov, I.I., Levin, S.V., Smirnov, V.P., Ryabenko, A.V., and Yanchur, V.P. "Production Single Crystal Deposits of Tungsten from Chlorides Using Transport Reactions." *Single Crystals of Refractory and Rare Metals, Alloys and Compounds.* Moscow: Nauka, 1977, pp. 27-32.
9. Korolev, Yu.M., and Stolyarov, V.I. *Hydrogen Reduction of Refractory Metal Fluorides.* Moscow: Metallurgia, 1981, 184 p.
10. Nikolaev, Yu.V., Kolesov, V.S., et al. "Molybdenum and tungsten single crystal alloys with abnormally high creep strength for space nuclear power and propulsion systems." *Proc. 10th Symp. on Space Nuclear Power and Propulsion.* Albuquerque, 1993, part 1, pp. 267-274.
11. Abdrakhmanov, R.K., Belenov, V.S, et al. "Summarization of Materials Study for TFE and TOPAZ-2 Reactor's Moderator, Undergone Nuclear Power Tests in Ya-81 Experimental Plant." Completed on the contract with JV "Inertek", 1994, NoC -15/203, suppl. 4., 76 p.
12. Yastrebkov, A.A., Afanasiev, N.G., Repiy, V.A., et al. "Niobium/Rutenium Impact on High Temperature Strength Parameters of Single Crystal Molybdenum." *Single Crystal Refractory Metals, Alloys and Compounds.* Moscow: Nauka, 1984, pp. 201-207.

13. Tachkowa, N.G., Zubarev, P.V., et al. "A Study of High-Temperature Creep of Mo-3% Nb Single Crystal Alloy under Long-Time Loading." Single Crystal Refractory Metals, Alloys and Compounds. Moscow: Nauka, 1984, pp. 196-201.
14. Luo, A., Park, J.J., and Jacobson, D.L. "Creep Behavior of Molybdenum-0.5% Hafnium Carbide at Temperatures above 0.5 Tm." *Proc. Thermionic Energy Conversion Specialist Conference.* Goteborg, 1993, pp. 119-126.
15. Tsaoo, B.H., Ramalingam, M.L., and Donovan, B.D. "Creep Considerations of a W-Re-HfC Alloy for Thermionic Fuel Element Application." *Proc. 25th Intersociety Energy Conversion Engineering Conf.*, Reno, 1990, v.2, pp. 326-331.
16. Begg, L.L. "The Thermionic Fuel Clad/Emitter with Long Life Potential." *Proc. 7th Symposium on Space Nuclear Power and Propulsion.* Albuquerque, 1990.
17. Tsaoo, B.H., Ramalingam, M.L., Donovan, B.D., and Lamp, T.R. "W-Re-HfC as an Emitter Material with Long Life for Thermionic Fuel Element Application." *Proc. 26th Intersociety Energy Conversion Engineering Conf.* Boston, 1991, v.3, pp. 154-159.
18. Smirnov, V.P., Sidorov, Yu.I., and Yanchur, V.P. "Epitaxial Growing of Single Crystal Tungsten Using Chemical Transport Reactions." *The Surface, Physics, Chemistry, Strength.* 1986, pp. 123-128
19. Evstyukhin, A.I., Djalandinov, D.N., Dementiev, L.N., et al. "Production CVD Single Crystal Tungsten and Study of Its High Temperature Creep." *Rare Metals and Single Crystal Structure Alloys.* Moscow: Nauka, 1981, pp. 252-256.
20. Belomytsev, Yu.S., Savitsky, E.M., et al. "Production, Investigation of Structure and Mechanical Parameters of Some Single Crystal Tungsten - Based Alloys." *Single Crystals of Refractory and Rare Metals and Compounds.* Moscow: Nauka, 1977, pp. 98-99.
21. Evstyukhin, A.I., Gavrilov, I.I., Smirnov, V.P., and Yanchur, V.P. "Deposition Parameters Influence on Growth Rate and Morphology of Large Deposits of Single Crystal Tungsten." *Metallurgy and Science of Pure Metals.* Moscow: Atomizdat, 1980, pp.21-28.
22. Yastrebkov, A.A., Repiy, V.A., et al. "Structural Features of Single Crystal Refractory Metals, Obtained by Electron-Beam Zone Fusion and Chemical Transport Reactions." Report at the 4th Branch Conference "Nuclear Power in the Space. Materials. Fuel." Podolsk, 1993.
23. Degaltsev, Yu.G., Ponomarev-Stepnoy, N.N., and Kuznetsov, V.F. *High Temperature Nuclear Fuel Irradiation Behavior.* Moscow: Energoatomizdat, 1987, 208 p.
24. Rizhkov, A.N., Bologov, P.M., et al. "Experience of Development TFE Design and Fuel Materials for Thermionic Reactor-Converters in IPPE."

Report at the 4th Branch Conference "Nuclear power in the Space. Materials. Fuel." Podolsk, 1993.
25. Hoth, W, Degaltsev, Yu., Gontar, A., and Rakitskaya, E. "Design and performance of the UO_2 fuel for the "Topaz-2" reactor." *Proc. 11th Symposium on Space Nuclear Power and Propulsion.* Albuquerque, 1994, part 1, pp.55-61.
26. Kotelnikov, R.B., Bashlykov, S.N., et al. *High Temperature Nuclear Fuel.* Moscow: Atomizdat, 1969, 368 p.
27. Olander, D.R. "Fundamental Aspects of Nuclear Reactor Fuel Elements." Published by Technical Information Center Energy Research and Development Administration, 1976, 614 p.
28. Seltzer, M.S., Perrin, J.S., Clauer, A.H., and Wilcox, B.A. "Review of creep behavior of ceramic nuclear fuels." *Reactor Technology*, 1971, v. 14, No. 2, pp. 99-135.
29. Kotelnikov, R.B., Bashlykov, S.N., et al. *High Temperature Nuclear Fuel. 2nd edition.* Moscow: Atomizdat, 1978, 432 p.
30. Fink, J.K., Chasanov, M.G., and Leibowitz. "Thermophysical properties of uranium dioxide." *J. Nucl. Mater.*, 1981, v. 102, No. 1-2, pp. 17-25.
31. Matthews, J.R. *Mechanical properties and diffusion data for carbide and oxide fuels.* AERE-M 2643, 1974.
32. Gontar, A.S., Kucherov, R.Ya, Nelidov, M.V., et al. "Some questions of uranium dioxide mass transfer influence on high-temperature fuel element behaviour." *Proc. 24th Intersociety Energy Conversion Engineering Conf.*, New York, 1989, v. 6, pp. 2803-2808.
33. Kazantsev, G.N., Moseev, L.N., et al. "A Study of Hypostoichiometric Uranium Dioxide." Branch Jubilee Conference "Nuclear Power in the Space" Reports theses. Part 1. Soviet specialists' reports. Obninsk, 1990, p. 502.
34. Kazantzev, G.N., Ovchinnikov, I.Ya., et al. "Some Questions of Hypostoichiometric Uranium Dioxide Application to Reactors in Space." 4th Branch Conference "Nuclear Power in the Space. Materials. Fuel." Report Theses. Podolsk, 1993, p. 312.
35. Gontar, A.S., Gutnik, V.S., et al. "Possibilities of using understoichiometric uranium dioxide in thermionic fuel elements." *Proc. 27th Intersociety Energy Conversion Engineering Conference.* San Diego, 1993.
36. Gridnev, A.A., Djalandinov, D.N.; et al. "Investigation of Creep of Coarse-Grained Uranium Dioxide." *Atomic Energy*, 1985, v. 59, iss. 1, 1985, pp. 27-29
37. Zrodnikov, A.V., Van Hagen, T.H., et al. "Conceptual design of a multi-cell thermionic fuel element for a 40-kW space nuclear power systems." *Proc. 12th Symp. on Space Nuclear Power and Propulsion.* Albuquerque, 1995, pp. 785-789.

38. Ponomarev-Stepnoy, N.N., Nikolaev, Yu.V., et al. "Properties and operation characteristics of fuel pellets for thermionic fuel element of the installation "TOPAZ-2"." Technical Paper, 1994, 17 p., fulfilled by the Contract No VI-077 with Joint Venture "Inertec".
39. Ponomarev-Stepnoy, N.N., Nickolaev, Yu.V., Hoth, C.W., et al. "Selective samples of uranium dioxide fuel pellets for the "TOPAZ-2"." Technical Information, 1984, 31 p., fulfilled by the Contract No I-077 with Joint Venture "Inertec".
40. Gutnik, V.S., Rakitskaya, E.M., and Tsiplenkova, V.L. "High Density Uranium Dioxide: Some of Properties." Report at the 4th Branch Conference "Nuclear Power in the Space. Materials. Fuel", Podolsk, 1993.
41. Hoth, Ñ.W., Blair, H.T., Degaltsev, Yu.G., Rakitskaya, E.M., Gontar, A.S., et al. "Characteristics of prototype TOPAZ-2 fuel." *Proc. 12th Symposium on Space Nuclear Power and Propulsion.* Albuquerque, 1995, part 1, pp.265-270.
42. Morris, D.B. "The thermionic system evaluation test (TSET): descriptions, limitations, and the involvment of the space nuclear power community." *Proc. 10th Space Nuclear Power and Propulsion.* Albuquerque, 1993, part 3, pp.1251-1256.
43. Ievleva, J.I., Pinchuk, A.P., et al. "Comparative Parameters of Irradiation Stability of Oxide Electroinsulating Materials." Report at the 4th Branch Conference "Nuclear Power in the Space. Materials. Fuel." Podolsk, 1993.
44. Kozlov, O.F., Uvarov, V.I., and Tsetskhladze, D.L. "Alumina Corrosion in Thermionic Converter Interelectrode Gap Environment." Report at the 2nd Branch Conference "Nuclear Power in the Space. Physics of Thermionic Power Convertors." Sukhumi, 1991, pp. 406-416.
45. Kozlov, O.F., Uvarov, V.I., and Tsetskhladze, D.L. "Alumina Corrosion in Thermionic Converter Interelectrode Space Environment." *Physics of High Temperatures*, 1992, v. 30, No. 2, pp. 400-405
46. Kozlov, O.F., Nikolaev, Yu.V., Olson, D., et al. "Research of ceramic materials stability in thermionic converter interelectrode gap." *Proc. 12th Symposium on Space Nuclear Power and Propulsion.* Albuquerque, 1995, pp. 271-276.
47. Belousenko, A.P., Serov, V.M., and Nikolaev, Yu. V. "High Strength Oxide Ceramic in the Thermionic Convertor." Report at the 4th Branch Conference "Nuclear Power in the Space. Materials. Fuel." Podolsk, 1993.
48. Koryukin, V.A., and Obrezumov, V.P. "Oxygen and Carbon Dioxide Adsorption Influence on the Emission Parameters of TFE Electrodes." Report at the Branch Jubilee Conference "Nuclear Power in the Space." Obninsk, 1990.

49. Zherebtsov, V.A., Kiryushchenko, A.I., Kononova, Z.N., et al. "Influence of Hydrogen Impurity in IEG on TEC Operation." Report at the Branch Jubilee Conference "Nuclear power in the Space." Obninsk, 1990
50. Andrievsky, R.A., Galkin, E.A., Makeev, A.V., and Khromonozhkin, V.V. "Outgassing of Uranium Dioxide under Vacuum Heating." *Atomic Energy*, 1981, v. 51, iss. 2, pp. 129-130.
51. Galkin, E.A., Gagarin, A.S., Makeev, A.V., et al. "Outgassing of Uranium Dioxide under Vacuum Heating." Report at the 4th Branch Conference "Nuclear power in the Space. Materials. Fuel." Podolsk, 1993.
52. Rakitskaya, E.M., Galkin, E.A., and Gontar, A.S. "Advanced Uranium Dioxide Thermionic Fuel." Report No RDD:93:62411-001:01, 1993, prepared on the Contract between "Lutch" (Russia) and Babcock & Wilcox (USA).
53. Galkin, E.A., Gagarin, A.S., Zaitsev, V.A., et al. "Outgassing of Carbides Uranium Compositions under Vacuum Heating." Report at the 4th Branch Conference "Nuclear Power in Space. Materials. Fuel." Podolsk, 1993.

CHAPTER 3

THEORETICAL DESCRIPTION OF PROCESSES DETERMINING THE LIFETIME OF FUEL ELEMENTS

For the required operational life of space systems under development (7 to 10 years), the calculational methods for predicting the behavior of a TFE—the most complex and critical unit of a TRC, governing its electric parameters and lifetime—take on special significance because of the expense of in-pile experiments. Theoretical models and estimation procedures provide vital information for technical decisions made to ensure the required power and life of TFEs.

3.1. Temperature Fields in the Fuel Stack

The rate of the processes determining the fuel-element life behavior depends on temperature. For many processes, such as evaporation or diffusion, this dependence has an exponential form. For others, such as fusion or peritectic reactions, temperature dependence has a threshold form. Under these circumstances, and because of the unavailability of direct measurement and adjustment of the temperature within fuel elements, accurate calculation of temperature fields is required to forecast their lifetime. Because the main goal of the investigations is lifetime prediction, one may, as a rule, neglect the process of reaching operating conditions and use the steady-state equation of heat conduction to calculate temperature fields,

$$\mathrm{div}\,(\lambda \mathrm{grad}\, T) = -\, q_V, \tag{3.1}$$

where λ and q_V, thermal conductivity and power density, depend in the general case on coordinates and material characteristics.

In addition, the characteristic time of change in the fuel-stack geometric parameters, linked to mass transfer and fuel-stack swelling, is usually much longer than the equilibration time for thermal conditions. This allows the set of heat and mass transfer equations to be disconnected and the heat problem to be solved at each point in time with constant geometric parameters.

The institute has paid great attention to calculational methods for the steady-state temperature fields in structural elements of nuclear reactors [1]. Fedik et al. [1] developed a method of boundary integral equations for the calculation of temperature fields. This technique is most convenient in solving parametric two-dimensional boundary-value problems. The method of boundary integral equations decreases dimensionality of the boundary-value problem and reduces two-dimensional problems to one-dimensional problems, significantly improving the possibility of achieving a high-accuracy solution.

In the initial state, the fuel stack usually has the form of a cylinder with a central hole, and cylindrical coordinates are used to describe the processes occurring in the stack. Because of azimuthal non-uniformity of heat release resulting from the fuel elements' different location in relation to the core center, the central channel can shift and its form change somewhat. These processes are essential, for example, in considering bending deformations of the fuel element that arise from different thicknesses of the cylinder walls. However, the radial dependence of the temperature is most important, and most problems need not take into account the azimuthal non-uniformity of heat generation.

Dependence of the power density q_V on the axial coordinate z is usually significant and must be taken into account in solving Equation 3.1. Accounting for this dependence may be different for single and multi-cell TFEs. Calculational practice shows that for the single-cell TFE, due to a slow temperature change along the axial coordinate, the z-derivative in the left side of Equation 3.1 may be neglected; i.e., in this case, as for the power reactor fuel elements, a one-dimensional equation of heat conductivity can be used to determine the temperature distribution. The z-dependence enters parametrically through q_V (r, z), as well as through boundary conditions at the external surface of the fuel stack. In this event, the values of the conductivity integral may be applied for determining the temperature [2]. For any arbitrary dependence of the volumetric heat release on the radial coordinate, the conductivity integral is expressed as a function of q_V as

$$\int_{T_s}^{T(r)} \lambda(T)dT = -\int_{R^V}^{r_1^V} \int_{r_o} u \cdot q_V \cdot (u,r)dudv, \qquad (3.2)$$

here: r_0 - radius of fuel stack central channel;
R - outer radius of stack;
T_S - temperature at the stack outer surface.

The temperature drop along the thermionic fuel element's radius, specifically in the single-cell TFE, is substantially lower than in power-reactor fuel elements. In addition, the operating temperature range lies in the vicinity of a minimum in the temperature dependence of the thermal conductivity coefficient. Due to these circumstances, the thermal conductivity change along the stack radius is slight, and a reasonable accuracy is reached when using a constant magnitude of the thermal conductivity coefficient equal to its value in the minimum.

Equation 3.2 is presented as

$$T(r) = T_s + \frac{1}{\lambda_{min}} \int_{R^V}^{R_1^V} \int_{r_o} u \cdot q_V \cdot (u,r)dudv. \qquad (3.3)$$

For the multi-cell TFE, the length of which is routinely only several times their diameter, the axial spreading of heat contributes tangibly to the temperature distribution. In this case, Equation 3.1 must be solved numerically. Depending on the fuel element version under consideration, several versions of the boundary conditions were used. The boundary conditions for the heat conduction equation have been stated in detail, e.g., by Lykov and Mikhailov [3].

Let us consider a boundary condition at the stack outer surface. Because of variations in the value of the fuel pellet outer diameter and emitter inner diameter, the fuel/cladding contact behavior may also vary. In the course of time as a result of fuel condensation onto the cladding, the contact improves and transforms to an ideal contact. Accordingly, three versions of the boundary condition at the stack outer surface are used.

1. Given the ideal contact, the stack outer surface temperature equals the cladding temperature:

$$T(R,z) = T_{Cl}(z). \tag{3.4}$$

2. Given a gap between the fuel and cladding, heat is transferred through radiation:

$$-\lambda \frac{dT}{dr}\Big|_{r=R} = -\varepsilon_r \sigma \left[T^4(r,z) - T_{Cl}^4(z)\right], \tag{3.5}$$

where: ε_r - reduced emissivity;
σ - Stefan-Boltzmann constant.

3. In the presence of a stack/cladding contact thermal resistance with a known level of thermal conductivity α on the contact sites, the following boundary condition is used:

$$-\lambda \frac{dT}{dr}\Big|_{r=R} = \varepsilon_r \sigma \left[T^4(R,z) - T_{Cl}^4(z)\right] + \alpha \left[T(R,z) - T_{Cl}(z)\right]. \tag{3.6}$$

At the inner surface of the fuel pellets the following boundary condition is used:

$$\frac{dT}{dr}\Big|_{r=r_o} = 0. \tag{3.7}$$

This condition is usually well satisfied for long single-cell TFEs and has been used to obtain Equations 3.2 and 3.3.

Radiation heat transfer in the central channel is taken into consideration using methods described by Siegel and Howell [4]. The heat flux transferred by radiation is assumed to be equal to the heat flux on the fuel stack surface.

$$\lambda \frac{dT}{dr}\bigg|_{r=r_o} = -q_s \tag{3.8}$$

where q_s is the resultant density of heat flux removed by radiation from the central channel surface and is defined from the following set of heat balance equations in the central channel:

$$\begin{aligned} q_s(z) &= q_i(z) - q_o(z) \\ q_o(z) &= \varepsilon(z)\sigma T^4(r_o, z) + (1-\varepsilon(z)) \cdot q_i(z), \\ q_i(z) &= \int_s q_o(z) dF_{z-dS'} \end{aligned} \tag{3.9}$$

where: q_i - density of heat flux falling onto an element of central channel surface;
q_o - density of heat flux removed from the fuel surface;
ε - surface emissivity;
$F_{Z\text{-}dS}$ - angular coefficient determining probability of radiation getting from channel surface element dS to a point of z-coordinate in the central channel surface [4].

Integration in Equation 3.9 is performed on the entire surface from which radiation can reach z-point, including surfaces of the end caps.

In that part of the stack where a gas-exhaust system is located within the central channel, a boundary condition of Equation 3.5 type is used, describing the radiation heat exchange between the gas-exhaust device and fuel with appropriate reduced emissivity.

For the end part of the stack, depending on its design, boundary conditions from the same set as for the fuel/cladding interface are used.

3.2. Theoretical Foundations for Description of Mass Transfer in Fuel Elements

Under steady-state operation of a fuel element, after completion of degassing of the fuel and structural materials, the gaseous phase within the fuel element contains fuel vapor, gaseous fission products, and (for a design with communicating fuel-element cavity and interelectrode gap) cesium vapor at a pressure of ~1 torr. Estimates show that GFP pressure in the ventilated fuel elements is not high. For the TOPAZ-2 single-cell TFE with removal of all inert

gases generated within the fuel element through a tip with a 0.02-cm-diameter capillary channel, GFP pressure is ~0.01 torr under steady-state conditions. For the multi-cell TFE, because of its short length as compared to the TOPAZ-2 single-cell TFE, the amount of inert gas evolving in each of the fuel elements will be significantly smaller and, hence, the steady-state pressure of the inert gases will be still lower.

Figure 3.1 presents the dependence of UO_2-molecular free path length on the temperature, plotted using, for the free path l, the expression [5]

$$l = \frac{1}{\sqrt{2}\ \pi n \sigma^2}$$

where: n - quantity of molecules in unit volume;

σ - molecule diameter.

Curve 1 represents the free path length in its own vapor. In this event, vapor pressure grows with temperature, leading to a sharp decrease of the free path length with temperature. Curve 2 represents the UO_2 molecular free path length in xenon under its pressure of 10^{-2} torr. Curve 3 shows the UO_2 molecular free path length in cesium vapor under its pressure of ~2 torr. In the latter two cases, the free path length grows proportionally to the temperature. As seen from Figure 3.1, the free path length in xenon covers several centimeters. Characteristic cross dimensions of the channels and gaps are, as a rule, much shorter than the above value. Thus, the presence of xenon within the fuel element does not exert any appreciable influence on the conditions of UO_2 vapor flow and, at lower temperatures (<2100°C), uranium dioxide vapor flow behaves much like the free-molecular mode (Knudsen number $Kn = l/d \gg 1$). At higher temperatures, the UO_2-molecular free path length in its own vapor becomes comparable to or shorter than the characteristic cross dimension of the channel d, i.e., vapor flow occurs under transient conditions (Kn~1).

In the event of the fuel-element cavity communicating with the IEG, at a 2-torr cesium vapor pressure, the UO_2 molecular free path length is ~0.02 cm. For this case, the dioxide flow in the free central channel has a nature of uranium dioxide molecular diffusion in cesium vapor. However, in the capillary channel of the gas-exhaust device and in other narrow gaps, UO_2 vapor flows under conditions close to those of free-molecular.

The available studies of vapor flow with evaporation and condensation on channel walls were mostly performed in applications to thermal tubes, where the main interest relates to the flow conditions at $Kn \ll 1$ and a gasodynamic description of vapor flow is used. In view of the above, RI SIA "Lutch" had conducted a complex of theoretical studies on vapor flow with evaporation and condensation on the channel walls under transient and free-molecular flow.

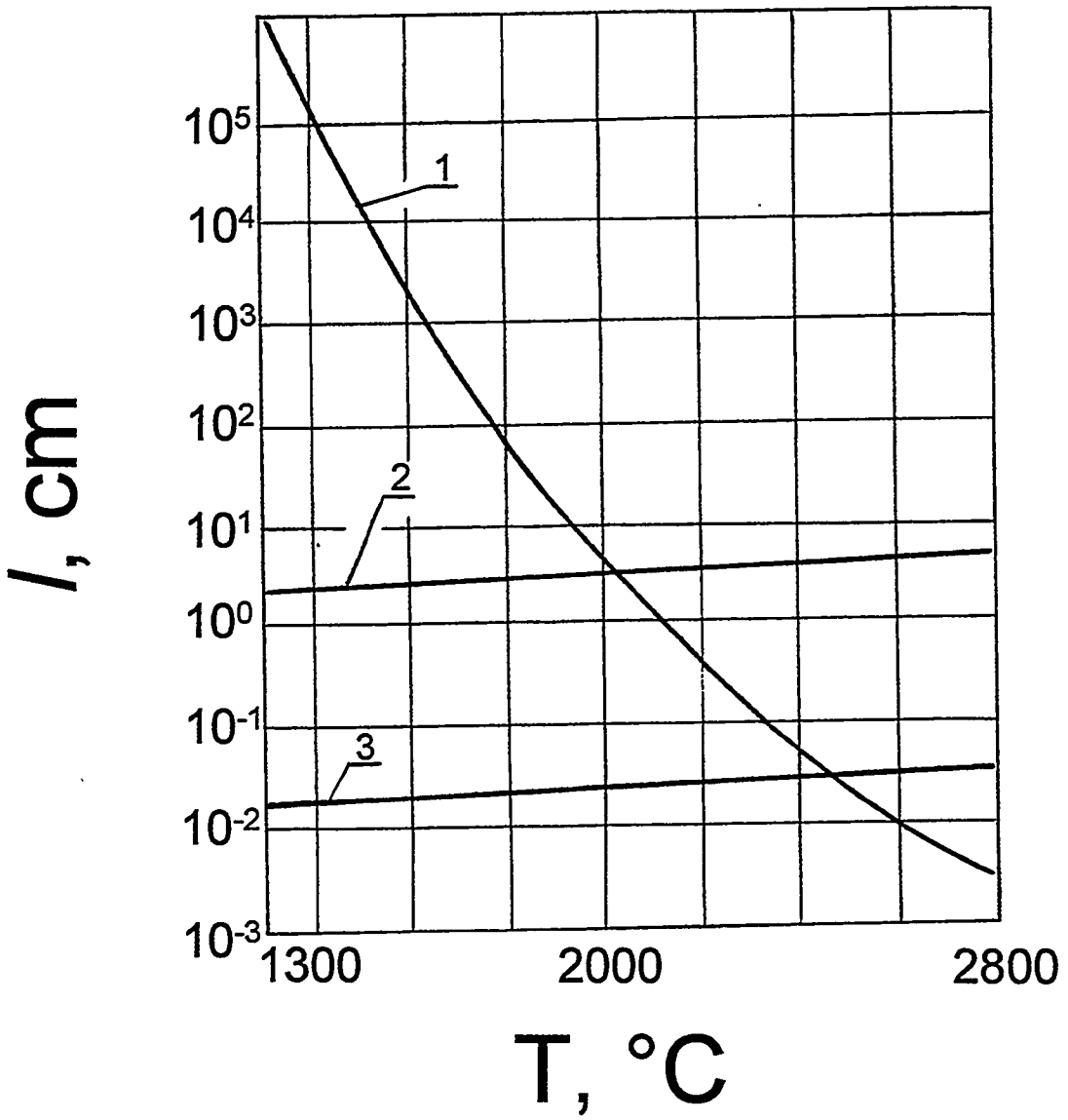

Figure 3.1. UO_2 molecular free path length vs. temperature:
1 - in UO_2 vapor;
2 - in xenon at $P_{Xe}=10^{-2}$ torr;
3 - in Cs at $P_{Cs}=2$ torr.

In work based on the Boltzmann's kinetic equation with BGK-model collision integral [6], a description of the cylindrical channel walls' material transfer, caused by a temperature gradient along the channel walls, was obtained. The expression for the mass flux passing through the channel section obtained [6] is applicable to the entire range of Knudsen number at an arbitrary value of the condensation coefficient.

In a particular case, with condensation coefficient equal to 1, this solution coincides in appearance with an expression describing nonisothermal flow of non-condensing gas in a cylindrical channel. However, the pressure gradient, determined for the case of the non-condensing gas flow by conditions at the channel ends, is replaced by a local value of the gradient of the wall material's saturated vapor. In the limiting case Kn>>1 at the condensation factor equaling 1, the solution appears as

$$G(z) = -\frac{8}{3} R^3 \sqrt{\frac{\pi m}{2k}} \cdot \frac{d}{dz} \cdot \frac{P_{eq}}{\sqrt{T}}, \tag{3.10}$$

where: P_{eq} - equilibrium vapor pressure at temperature K;
R - channel radius;
m - molecule mass;
k - Boltzmann constant.

In the opposite limiting case Kn<< 1

$$G(z) = -\frac{\pi R^4}{8\mu} \cdot \rho \cdot \frac{dP_{eq}}{dz}. \tag{3.11}$$

where: μ - vapor viscosity.

With the condensation coefficient β differing from 1, mass flux in the channel G(z) is connected with the flux at β=1 through the equation

$$\frac{d^2 G_\beta}{dz^2} - \alpha^2 G_\beta = -\alpha^2 G, \tag{3.12}$$

the solution of which, limited far from a point considered, can be presented as

$$G_\beta = \sum_{i=0}^{\infty} \frac{1}{\alpha^{2i}} \cdot \frac{d^{2i} G}{dz^{2i}} \tag{3.13}$$

The first term of this series expansion represents the mass flux at β=1 and does not depend on the condensation coefficient. The dependence on the condensation coefficient enters via coefficient α of Equation 3.13, which is

proportional to $\sqrt{\frac{\beta}{\beta-1}}$. Vapor flux onto and from the channel wall $q_{r(z)}$ is found using the continuity equation:

$$q_r(z) = -\frac{1}{2\pi R} \cdot \frac{dG}{dz} . \tag{3.14}$$

One solution is applicable to analysis of the initial phase of fuel transfer in the free central channel [6]. This allows the position of evaporation and condensation zones and the distribution of evaporation/condensation rates in these zones to be found.

However, use of the initial rates of condensation for estimating the time to overlap the central channel provides only a rough estimate of channel lifetime. First, fuel re-distribution throughout the channel leads to temperature equilibration between the evaporation and condensation zones and to lowering the mass flow density. Second, in the narrowing channel section, more intense condensation will take place, and the area of maximum condensation rate will shift from its initial site.

To draw a more realistic picture of the channel profile change, Shulepov [7] considered the mass transfer in a conic channel. His consideration [7] was restricted to free-molecular flow; the condensation coefficient was deemed to be 1. Moreover, it was assumed that molecules evaporated from a wall have a Maxwellian distribution of velocities at the wall temperature. Under these assumptions, mass transfer is governed by equations analogous to radiation transfer in an appropriate channel with walls made of an ideal black body.

Shulepov [7] provided expressions for mass flows using angular coefficients. The angular coefficients are geometric interrelations determining angles at which surface elements see each other. The mass or radiation flux from one surface to another is proportional to the value of the angular coefficient. Expressions for fluxes in terms of the angular coefficients and also, apparently, the most complete reference material on the expressions available in the literature for the angular coefficients are contained in the work of Siegel and Howell [4].

In the general case, expressions using angular coefficients for mass fluxes are very awkward, but for small temperature gradients the expression for mass flux far from the channel ends takes the following form:

$$G(z) = -\frac{8}{3} r^3(z) \sqrt{\frac{\pi m}{2k}} \cdot \frac{d}{dz} \cdot \frac{P_{eq}}{\sqrt{T}} \tag{3.15}$$

Equation 3.15 coincides in appearance with Equation 3.10 for mass flow in a cylindrical channel under free-molecular conditions, but a constant value of the cylindrical channel radius is replaced by the current value of the conic channel radius r(z). It is seen from Equation 3.15 that if a sharp change in radius takes

place in some section of the channel, restructuring of the flow must occur from one to another radius value in the vicinity of this point, and, depending on the direction of the temperature gradient, a zone of intense evaporation or condensation appears around the point.

In addition to the problems of longitudinal flow in channels, mass transfer caused by temperature gradients and drops on the channel section was also considered. In many cases, fuel may not touch the surface of various structural elements. Temperature drop between the fuel and the structural parts brings about fuel condensation onto these parts. If a gap is small, it may be deemed flat. A strict consideration of this problem for a single-component system was first performed by Kucherov et al. [8]. Zhdanov and Shulepov [9] reviewed the problem of re-condensation within a flat gap for a binary gas mixture. Either both components of the gaseous phase can evaporate from the hot surface, or one of the components is a non-condensing gas filling the gap between the evaporation and condensation surfaces. The problem is solved by the method of moment using a model of "Maxwell" molecules. For a small relative difference in the surface temperatures, analytical expressions are obtained for the mass and heat fluxes, valid in the entire range of Knudsen numbers at arbitrary values of evaporation and condensation coefficients for both components. Specifically, at the rate of one of the components equal to zero, there is a solution describing the re-condensation through a gap filled with non-condensing gas.

Kucherov and Shulepov [10], using a rigorous approach, examined radiation and mass transfer in a vacuum spherical cavity. Strict expressions were obtained for the distribution of mass and radiation fluxes at arbitrary distribution of the cavity walls' temperature.

For a specific case, when a constant temperature gradient exists far from the cavity, the solution predicts more exactly the walls' temperature distribution and the cavity migration rate. For fuel pores, when the temperature drop on a pore cross-section is small, the solution is expanded in a series. The first term of the expansion describes pore migration without a change in form. The second term of the expansion describes change of pore shape in the temperature gradient field. Kucherov and Shulepov's analysis [10] revealed that the pores extend along the temperature gradient, and here the pores' relative deformation is proportional to their volume.

Their work [10] also involved radiation and wall-material transfer in a cylindrical channel with a temperature distribution $T(\varphi)$. An integral equation describing fluxes of heat transferred by radiation and mass flows is derived, and the related solution is achieved for an arbitrary function $T(\varphi)$. This solution describes a shift and profile change of the central channel in a fuel element, given azimuthal non-uniformity of the heat release. The case when a constant temperature gradient across the channel axis exists far from the channel is also considered. For this case, the channel-wall temperature distribution is defined

more accurately due to precise consideration of heat transfer by radiation. The value of the cylindrical pore migration velocity is defined more exactly, and its shape modification is considered. The cylindrical pore cross-section takes an oval form, extended along the temperature gradient.

If the fuel-element cavity communicates with the IEG, the following equation, describing uranium dioxide diffusion in cesium vapor, is used to find the fuel pressure distribution along the central channel [11]:

$$\frac{d^2P}{dz^2}+\left(\frac{2}{r_z}\cdot\frac{dr_z}{dz}+\frac{1}{2T}\cdot\frac{dT}{dz}\right)\cdot\frac{dP}{dz}-\frac{2}{r_z D_z \cos\Theta_z}\sqrt{\frac{kT}{2\pi m}}(P-P_{eq})=0, \quad (3.16)$$

where: Θ_Z - angle of channel generatrix tilt to channel axis at z-coordinate point;

r_Z - channel radius at z-coordinate point.

The choice of boundary conditions for Equation 3.16 is governed by design of and temperature conditions at the fuel element end parts. If at a distance d from the fuel stack end, with reference to z=0, fuel condensation may occur on structural elements having temperature T_O, the following boundary condition is applied:

$$\left.\frac{dP}{dz}\right|_{z=0}=\frac{1}{d+\sqrt{\frac{2\pi m}{kT_o}}\cdot D_o}\left[P(0)-P_{eq}(T_o)\right]. \quad (3.17)$$

An analogous condition at another end of the fuel element differs in the derivative sign. As a result of fuel condensation, d reduces and, at d=0, central-channel-length shortening begins. Here at the channel end the boundary condition Equation 3.17 is used, with d=0 and estimated temperatures at the channel ends.

In the case of an overheated end of the fuel element, when fuel is not condensed on the end structural parts, the following boundary condition was used:

$$\left.\frac{dP}{dz}\right|_{\substack{z=0\\z=L}}=0 \quad (3.18)$$

In some structural elements, specifically in the capillary channel of the gas-exhaust device, temperature conditions are set such that uranium dioxide vapor flows with no condensation on walls. To estimate the flow for this case, known expressions for non-condensing gas flow in tubes and channels are used. As noted in the beginning of this section, flow conditions in fuel elements may range from free-molecular to diffusion in cesium vapor; therefore, in describing vapor flow it

is advisable to use expressions applicable to the entire range of flow conditions realized within a fuel element.

An approximate description of gas flow under transient conditions was developed by Present and de Bethune [12]. Strictly speaking, they developed a theory for transient flows adjacent to the free-molecular flow; however, comparison to results obtained for viscous slip flow [13] reveals that their equations [12] are valid within the entire transient area with accuracy up to the barodiffusion factor in viscous flow. To obtain a uniform description of flow, it is convenient to introduce the coefficient of Knudsen diffusion, D_{Kn}, which allows an expression for the free-molecular flow to be represented in the same form as for diffusion in non-condensing gas:

$$G = S \cdot \frac{m}{kT} \cdot D_{Kn} \cdot \frac{dP}{dz}, \tag{3.19}$$

where S is the cross-sectional area of the channel.

For a cylindrical channel with radius R, the Knudsen diffusion coefficient equals

$$D_{Kn} = \frac{2}{3} \cdot R \cdot \bar{v} \tag{3.20}$$

where: $\bar{v}$ is the mean velocity for Maxwell distribution of molecular speeds,
$\bar{v} = \sqrt{8kT / \pi m}$.

To describe flow under transient conditions, an effective diffusion coefficient is introduced:

$$D_{eff} = \frac{D_{Kn} \cdot D_{12}}{D_{Kn} + D_{12}}. \tag{3.21}$$

D_{12} is the coefficient of diffusion in a binary gas mixture, for which an expression obtained in a first approximation of distribution function expansion on Sonin polynomes is used:

$$D_{12} = 0.002628 \cdot \frac{1}{P\sigma_{12}^2 \Omega_{12}^{(11)*}(T^*_{12})} \sqrt{\frac{T^3 (M_1 + M_2)}{2M_1 \cdot M_2}}, \tag{3.22}$$

where: P - gas pressure in atm;
T - temperature in K;
M_1 and M_2 - molecular weights of components 1 and 2;
T^*_{12} - kT/ε_{12};

σ_{12} and ε_{12}/k - parameters of potential energy of molecular interaction, in Å and K respectively;

$\Omega_{12}^{(11)*}$ - integrals incorporated in equations for kinetic coefficients related to respective values for the model of solid spheres.

Their definition and tabulated values for most often used potentials of interaction are available (e.g., in [14]).

Using the effective coefficient of diffusion, an expression for flow within the entire range of Knudsen numbers can be written as Equation 3.19. Here it is assumed that non-condensing gas filling the fuel element cavity (Cs) is motionless.

Calculations were performed in several stages to find the condensation-zone boundaries when uranium dioxide vapor flows in the gas-exhaust lines. In the first stage, uranium dioxide vapor flow as a non-condensing gas was estimated, and zones where vapor pressure exceeds saturated vapor pressure at the channel-wall temperature were found. In subsequent stages, for the condensation zones found at the previous calculational stage, expressions were applied describing gas flow, given evaporation and condensation on walls. Then the condensation-zone boundaries were corrected.

It was assumed that in the condensation-zone boundaries, vapor pressure was equivalent to saturation pressure at the wall temperature. It was also assumed as a boundary condition that the fluxes in the condensation zone and the zone where flow occurs without condensation were equal.

3.3. Joint Description of Mass Transfer, Change in Channel Geometry, and Transformation of Temperature Fields within a Fuel Element

Fuel transfer from the hottest stack zones to pellets in the cold zone leads to a change in the stack geometric parameters, and as a result, to re-distribution of heat release and transformation of temperature fields. In addition, recondensation of fuel on structural parts alters the contact behavior, which also results in a significant change of the temperature fields. On the other hand, the fuel evaporation rate depends exponentially on temperature. These circumstances necessitate joint consideration of the temperature fields and fuel transfer. Some of the mass transfer processes occur throughout operation, but several processes are short compared to operational lifetime. A detailed description is not needed for such rapid processes; only a final state and estimate of the time at which this state is reached are important. Transition of the actual initial contact in the fuel/emitter interface to a condition similar to an ideal contact is one such quickly completing process. The time for condensation of a fuel layer as thick as the order of microroughness comb height in the contacting surfaces is adopted as the time of transition from the actual initial to ideal contact. The calculation takes into account temperature reduction on the evaporation surface during condensation. Another relatively quick process is the formation of a closed isothermal cavity

within the fuel stack of a multi-cell TFE. Kornilov et al. [15] described a computer program and provided calculational data on temperature fields in fuel and on the steady-state configuration of the isothermal cavity in fuel elements with a gas-exhaust device as a pipe located along the fuel element axis. A similar program, PIKVIK, had been developed at RI SIA "Lutch" [16], but PIKVIK uses a different method of solving the equation set and a different algorithm of the isothermal cavity formation in the fuel stack, which reduces the degree of the calculated cavity nonisothermality and shortens the calculational time.

At the first step, PIKVIK considers heat release and the temperature distribution within a stack having no free volume. The isothermal cavity is formed by removal from the zone occupied by fuel of the several hottest nodal points at each calculation step. After each step, heat release and temperature distribution is re-calculated. The number of nodes from which the fuel is removed at each step is determined on the basis of a compromise between calculational time and achieved isothermality of the cavity. The procedure is over when the value of free volume in the fuel-element cavity becomes equal to an actual free volume in the fuel element considered. The program envisages the possibility of considering various types of gas-exhaust device (GED) attachment by setting different boundary conditions at the point of GED attachment.

Unlike the above-mentioned quick processes, mass transfer in the central channel of the single-cell TFEs continues for a time comparable to the operational life, which allows the free central channel to remove GFPs from the fuel elements. Long duration of mass transfer is, in this case, linked to lower maximum fuel temperatures, much lower temperature gradients along the channel axis, and low temperatures at the ends of fuel elements. The possibility of using the free central channel to exhaust GFPs requires a reliable prediction of its operability, including all the key factors affecting the mass transfer. Gontar et al. [11] reviewed the main processes to be taken into account in predicting free central channel workability.

3.3.1. Equations Describing Uranium-Containing Components Transfer

In single-cell TFEs with separated fuel-element and IEG cavities, the inner fuel-element cavity communicates with vacuum; therefore vapor flow occurs under free-molecular conditions. In deriving the mass-transfer equations, it was assumed that molecular evaporation from a wall has equilibrium behavior, corresponding to the oxygen coefficient value and to the temperature at the current point on the channel surface. The evaporation and condensation coefficients are assumed to be 1. We considered a channel with origin at z=0 and end at z=L and assumed that, at the channel ends, the pressure of a gaseous phase component equals P_0 and P_L, respectively. This component mass flux may be described using the angular coefficient $F_{\xi z}$, representing the probability that a particle, having passed through

the channel section at ξ-point, will then pass through the channel section at z-point, undergoing no collisions with the channel walls [11].

$$Q(\xi) = \sqrt{\frac{\pi m}{2k}} r_z^2 \left\{ \left(\frac{P_o}{\sqrt{T_o}} - \frac{P_{eq}(0)}{\sqrt{T(0)}} \right) F_{\xi_0} - \left(\frac{P_L}{\sqrt{T_L}} - \frac{P_{eq}(L)}{\sqrt{T(L)}} \right) F_{\xi_L} - \int_o^L \frac{d}{dz} \cdot \frac{P_{eq}(z)}{\sqrt{T(z)}} \cdot F_{\xi_Z} dz \right\}, \tag{3.23}$$

where: r_ξ and r_Z - channel radius at points with ξ- and z-coordinate;
$P_{eq}(T)$ - the considered component equilibrium vapor pressure at the central-channel surface temperature T.

For a convex-walled channel the probability $F_{\xi Z}$ is described as [4]

$$F_{\xi z} = \frac{(z-\xi)^2 + r_z^2 + r_\xi^2 - \left\{ \left[(z-\xi)^2 + r_z^2 + r_\xi^2 \right]^2 - 4 r_z^2 r_\xi^2 \right\}^{1/2}}{2 r_\xi^2}. \tag{3.24}$$

Expressions for the mass flux are also similar for a non-convex-walled channel, but in this case, $F_{\xi Z}$ is not described by Equation 3.24. At present, an accurate consideration of shading effects has not been realized even for the simplest configurations, so an approximate method to account for shading is used. A limiting configuration for the convex-walled channel on a length between ξ and z-points constitutes a conic channel passing through these sections. To account for shading, the angular coefficient (Equation 3.24) is multiplied by the ratio of the minimum cross-sectional area on the channel segment length of a real channel to the cone passing through cross-sections at ξ and z-points.

3.3.2. Vapor Pressure in the Gaseous Phase over $UO_{2\pm x}$

It is known that the gaseous phase over $UO_{2\pm x}$ contains a number of components, primarily UO_2, UO_3, UO, and O_2. The relative content of these components depends on fuel composition and temperature. Figure 3.2 presents the dependence of the saturated vapor pressure of uranium-containing component on fuel composition at 2000 K. The calculation was performed using the thermo-chemical model of actinide oxides, and model parameters of Olander [2]. As seen from Figure 3.2, within the hypostoichiometric area at $-0.005 \le x < 0$, UO_2 is the main constituent of the gaseous phase, and its vapor pressure does not depend on fuel composition. For the hyperstoichiometric fuel with $x > 0.001$, UO_3 becomes the major component in the gaseous phase, and UO_3 pressure grows with the departure of the fuel composition from stoichiometry.

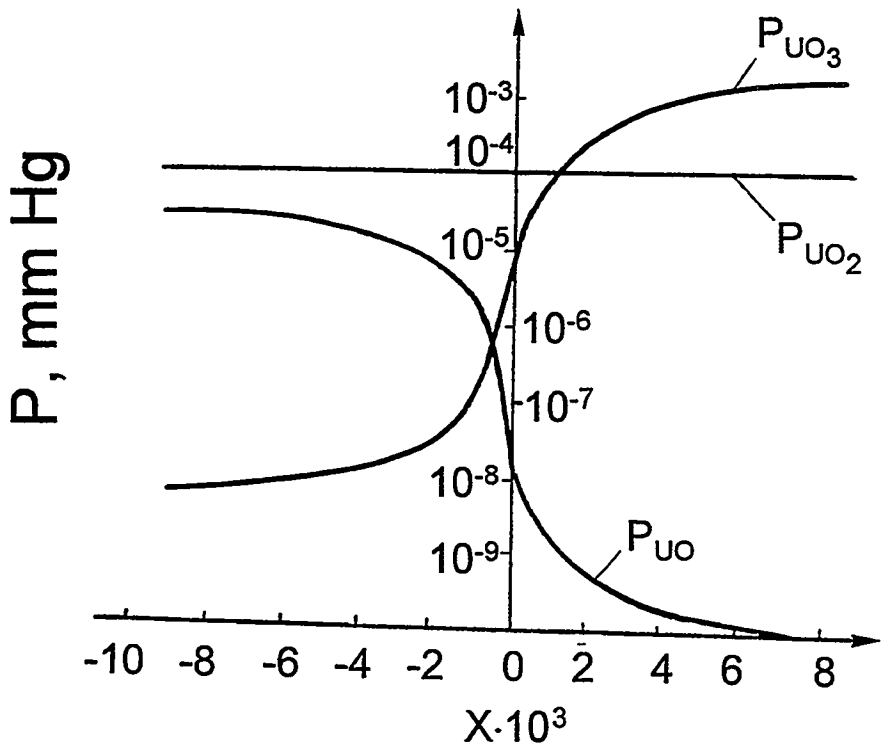

Figure 3.2. Pressure of uranium-containing components in the gaseous phase over $UO_{2\pm x}$, T=2000 K.

3.3.3. Redistribution of Fuel Components

Fuel transfer in the gaseous phase as UO_3 molecules is accompanied by reduction of oxygen content in the evaporation zone and rise in its concentration in the condensation zone. By virtue of that, the overall content of excess oxygen is not high in the fuel, and only a negligible amount of fuel can be transferred to a cold zone as UO_3, if there is no back transfer of oxygen to a hot zone. The available experimental data show that within the fuel volume, oxygen is redistributed in such a way that fuel composition in the cold region shifts to the stoichiometric composition. Thus, in the hyperstoichiometric fuel, the hot zone is enriched with oxygen, i.e., within the fuel volume, oxygen is redistributed in the opposite direction to its redistribution direction in the central channel gaseous phase. The excess oxygen, migrating as UO_3 through the central channel from the hot to cold zone, can then return through the fuel to the hot zone and is able to take part repeatedly in the fuel transfer. For a strict consideration of oxygen redistribution within the fuel, a joint solution is required for problems of mass transfer in the central channel and oxygen diffusion in uranium dioxide. The available literature data on the oxygen diffusion coefficient for uranium dioxide have a considerable spread; nevertheless, in aggregate the data show that the diffusion coefficient values are very high. According to Breitung [17], in the temperature range of most interest, 1800 to 1200°C, the oxygen diffusion coefficient ranges from 10^{-4} to 10^{-5} cm^2/s. Sari [18] provided still higher levels of the diffusion coefficient over a wide temperature range, 900 to 1550°C, for experiments of durations up to 20 min that studied the kinetics of oxygen redistribution in a sample.

Thus oxygen redistribution in fuel is rapid, and estimates made using the above-cited values of the coefficient of oxygen diffusion within uranium dioxide suggest that the excess oxygen can indeed participate many times in the fuel transfer, as UO_3 through the central channel. This circumstance allows oxygen redistribution within fuel to be neglected and its steady-state distribution corresponding to temperature distribution at the current time to be used, which in compliance with the work of Sari [18] appears as

$$x = c \cdot \exp\left(-\frac{Q^*}{RT}\right). \qquad (3.25)$$

For the heat of transfer, Q*, the value of Q*=142 kJ/mole [19] was used in the calculations. The constant C is determined from Equation 3.25 by normalizing overall oxygen content within the fuel element. In calculating the mass transfer in the channel, the change in oxygen content in the fuel as a result of its escape from the fuel elements in molecular form and as UO_3 and as a result of fuel burnup is also considered. Part of the oxygen, released in uranium fission, is spent to

oxidize fission products; the remainder alters the fuel oxygen coefficient. Oxygen pressure over the fuel and the fuel's oxygen potential change in the course of burnup were estimated through a procedure described by Olander [2].

3.3.4. Spacer Effect on Temperature Fields in Fuel Element and on Fuel Mass Transfer in Central Channel of Fuel Element

Removal of heat from fuel elements through the spacers can cause the appearance of a local minimum in temperature distribution along the emitter length and, consequently, also along the central channel length. As a result, in the central channel near a spacer, a local zone of intense condensation may appear. Examination of the central channel profile in fuel elements tested within experimental nuclear reactors confirms the existence of local minima in the central channel around spacer sites [20]. Thus, the spacers' cooling effect must be considered in predicting central-channel operability.

As underlying data, we assumed the undisturbed distribution of the emitter temperature that was obtained in TFE thermal and electrophysical calculations without considering heat transfer over the spacers.

To find the contacting area, a thermomechanical problem of interaction between spacers, emitter, and collector was solved using the results of Ponomarev [21]. The dependence of the contacting area on emitter deformation, spacer parameters, and materials properties was obtained.

The thermal analysis considered a solid ring of spacer material, the width of which was determined based on the condition of equality between the contact area for the ring and overall contacting area for all spacers of the involved collar.

Constant values for the emitter deformation rate were preset for each spacer collar. The values of the deformation rate were derived from examination of emitter deformation in experimental nuclear reactors.

3.4. Investigation of Gas-Exhaust Device Operability

The main purpose of the gas-exhaust system is to remove GFPs from the fuel element during its life and to restrict fuel loss to a permissible level. The most severe requirements on the fuel-loss restriction are derived from the small bore of the gas-exhaust channels; at a considerable temperature drop along the gas-exhaust line, all the fuel will be condensed within these channels, so that they overlap with the fuel condensate. Fuel loss is restricted using a capillary channel at the inlet of the gas-exhaust device (GED). The channel diameter is governed by the fuel temperature in the fuel element and by the gas-exhaust channel design. Estimates show that usually the capillary diameter must be $\sim 10^{-2}$ cm; therefore even a thin layer of fuel condensate on the GED surface may cause capillary channel blockage and gas-exhaust system failure. Estimates of the central isothermal cavity steady-

state configuration, described in Section 3.3, allow a choice of GED length such that the capillary channel outlet location would be free from fuel condensate under steady-state conditions. But choosing the GED length using only data on the steady-state configuration of the isothermal cavity does not guarantee GED operability throughout the required lifetime. During the early operation period, when the GED pipe is not coupled with the fuel, because of high metallic-pipe heat conductivity, the temperature near the outlet site can be lower than the surrounding fuel temperature, which will lead to condensate appearing on the pipe and potentially overlapping the outlet. As a result, the fuel element is sealed during early operation, when there is a heightened temperature and fuel can release a significant amount of gas, contained in the closed pores of as-fabricated fuel. With a substantial rise of gas pressure within the fuel-element cavity, gas flow converts to a diffusional mode that essentially inhibits mass transfer; as a result, a condensate layer on the GED surface is maintained for a long time. Therefore, it is necessary to choose GED parameters in such a way that the outlet site is overheated in relation to surrounding fuel for the early operational period.

Gontar et al. [11] reviewed the possibility of overheating the GED inlet during the early operational period by increasing the GED pipe length, so that the inlet capillary would be behind the point of maximum fuel temperature. For a fuel-temperature profile along the central channel, approximated by a square parabola

$$T(z) = T_{max.} - a(l_o - z)^2, \tag{3.26}$$

an analytical expression was obtained for the temperature difference between the fuel and GED inlet, which expression for long enough GED pipes ($\exp(\beta L >> 1)$ appears as

$$\Delta T = \frac{2a}{\beta}\left(L - l_o - \frac{1}{\beta}\right). \tag{3.27}$$

In this expression, the parameter β determines a ratio between heat spreading on the GED pipe and radiation heat exchange between the GED and fuel:

$$\beta^2 = \frac{8R\varepsilon\sigma T^3}{\lambda(R^2 - r^2)} \tag{3.28}$$

where: L - GED length
l_o - distance from GED attachment point to a point with maximum fuel temperature;
R - outer radius of GED pipe;
r - inner radius of GED pipe;
ε - reduced emissivity between GED pipe and fuel;

σ - Stefan-Boltzmann constant;

λ - thermal conductivity of GED pipe material.

$T=T_{max}-1/3\cdot a l_0^2$ is the temperature averaged throughout the fuel-element length, given that the temperature profile used in calculations is determined by Equation 3.26.

It follows from Equation 3.27 that GED overheating is achieved when the GED extends beyond a maximum temperature point by a distance

$$L - l_0 = 1/\beta.$$

Naturally, in lengthening the GED pipe, the pipe's free end must remain inside the central isothermal cavity.

The above procedure permits the selection of a GED length that ensures the absence of condensate at the GED inlet. However, in the event of a considerable departure from standard operating conditions, which often takes place in testing fuel elements in loop channels, the GED surface may be coated by a fuel layer sufficient to cover the capillary channel inlet. This does not necessarily indicate a complete breakdown of the GED. Gontar et al. [11] considered a mechanism for restoring GED operation, arising from the fact that when the fuel blocks the inlet, fuel escape through the GED does not decrease. Here, the condensate layer over the inlet becomes the uranium dioxide vapor source.

As a result of fuel migration via the GED, a cavity over the inlet and eventually a hole through the condensate layer is formed. Gontar et al. [11] studied the dependence of time of formation of the through-channel in the condensate layer on layer thickness, capillary channel geometric dimensions, and temperature. It is assumed that under initial conditions, a fuel layer of thickness h is present on the pipe surface and over the capillary inlet. The problem is diagrammed in Figure 3.3. Temperatures of the tip and the fuel on it are assumed to be constant. The following equation is obtained for time τ of through-channel formation in the fuel layer [11]:

$$\tau = 3\frac{\rho r_c}{P_{eq}}\sqrt{\frac{2\pi kT}{m}}\cdot L\left[H+\frac{2}{3}H^3+\frac{2}{3}\left(1+H^2\right)^{3/2}-\frac{2}{3}\right], \qquad (3.29)$$

where: ρ - fuel density;

m - mass of fuel molecule;

P_{eq} - fuel vapor equilibrium pressure at a temperature T near GED inlet;

L and H - dimensionless length of capillary channel and thickness of condensate layer (in units of capillary-channel diameter);

r_c - radius of capillary channel.

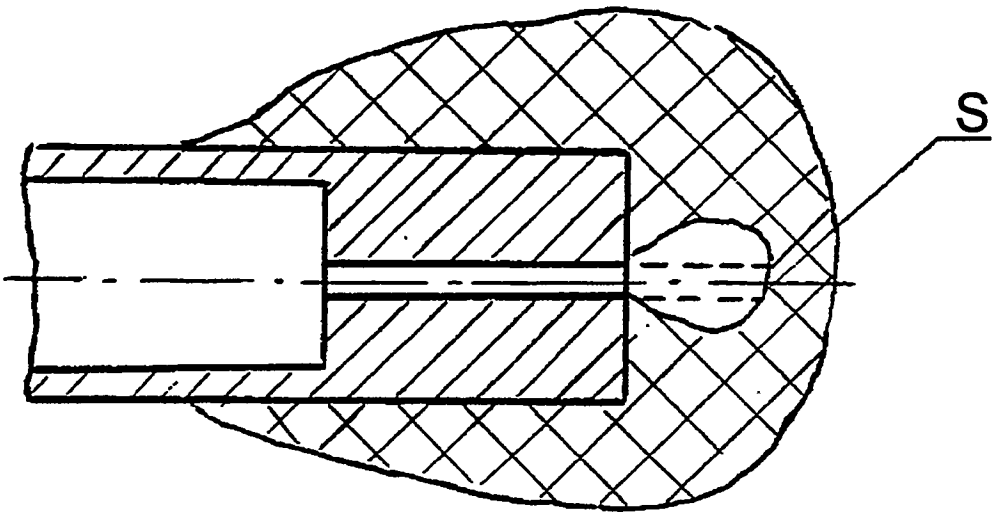

Figure 3.3. Formation of a hole in condensate layer.

The case of practical interest is when the condensate layer thickness is large compared to the capillary diameter, i.e., H>>l. In this case Equation 3.29 becomes

$$\tau = 4\frac{\rho r_c}{P_{eq}}\sqrt{\frac{2\pi kT}{m}}\cdot L\cdot H^3 \qquad (3.30)$$

Thus, the time of through-channel formation in the fuel layer is proportional to capillary-channel length and the cube of dimensionless thickness of the condensate layer. With changing GED pipe temperature, the time of through-channel formation in the fuel layer changes following the temperature dependence of fuel vapor equilibrium pressure. Channel-formation times at T_1 and T temperatures are linked through the relation

$$\tau(T_1) = \tau(T)\frac{P_{eq}(T)}{P_{eq}(T_1)}\sqrt{\frac{T_1}{T}} \qquad (3.31)$$

Blockages in the gas-exhaust channels can take place not only within a fuel element, but also beyond it, where the temperature ranges from ~2000 K to 700 K. In fuel elements containing carbonitride and carbosulphide fuel and not including systems for fuel-loss restriction, the chemical transfer and condensation within the gas-exhaust lines may become limiting factors on fuel-element life. Lyubimov et al. [22] analyzed the quantitative ratio between precipitated phases and showed that their most abundant fractions are Cs_2CO_3 and C, i.e., they are the most dangerous from the viewpoint of clogging the gas-exhaust channel. The analysis revealed conditions for the precipitation of Cs_2CO_3 and C phases on an inert substrate, depending on partial pressure of carbon monoxide. It was ascertained that precipitation of the condensed phases can be prevented through a reduction of oxygen content in the carbonitride fuel to level of 0.1 to 0.4% at.

3.5. Physical and Chemical Changes in Fuel and Fuel Components Released into the Interelectrode Gap

The physical and chemical changes in uranium dioxide during burnup aroused considerable interest during fuel-element development. Olander [2] summarized the available experimental data, theoretical concepts, and models used in describing oxide fuel behavior, but in creating high-temperature fuel elements for thermionic converters, a number of features characteristic of these fuel elements became apparent. First, the high cladding temperature and presence of structural materials within a fuel element (gas-exhaust system and heat-conducting and fuel-fixing elements) raised the problem of long-term compatibility between fuel and structural materials at ~2000°C. Second, the voltage-current characteristics of

thermionic converters are extremely susceptible to emitter and collector surface conditions and to gas phase composition within the interelectrode gap; therefore the possibility of fuel-component and fission-product penetration to the IEG and their interaction with structural materials must be analyzed.

The most important parameter determining the chemical properties of an oxide fuel and its interaction with structural materials is oxygen pressure in the gaseous phase within the fuel element, i.e., the fuel's oxygen potential. In the course of fuel burnup, the oxygen potential changes. Olander [2] considered a change in the oxygen potential of oxide fuel and accounted for the degree of oxidation of the products formed in uranium-atom fission. Lyubimov et al. [23] also took into account the change in fuel oxygen potential within the TFE as a result of oxygen release into the interelectrode gap. The oxide fuel composition change due to burnup and oxygen migration into IEG through the emitter cladding is described using a simple differential equation [23]:

$$\frac{dx}{dt} = \frac{(2+x_0)f(1-k_2) - k_1 \cdot f}{(1+f(1-k_2)t)^2} - G\sqrt{P_{O_2}}, \qquad (3.32)$$

where: x=(O/Me - 2) - deviation from uranium dioxide stoichiometric composition (Me=U+metallic fission products in solid solution of fluorite phase);

x_0 - initial deviation from uranium dioxide stoichiometric composition;

t - time, s;

f - burnup rate, at.fraction/s;

k_1 - oxygen mole fraction consumed to form barium/strontium zirconates;

k_2 - sum of fractional yield of yttrium, rare earth metals, and zirconium, which do not form zirconates;

P_{O2} - oxygen partial pressure over uranium dioxide, atm.

$$G = \frac{F_G \cdot p}{V_f \cdot \alpha \cdot h_{Cl}}$$

where: F_G - area of gap cross section, m^2;

V_f - volume of oxide nuclear fuel, m^3;

h_{Cl} - thickness of emitter cladding, m;

α - a coefficient equal to $4 \cdot 10^4$ mole/m^3

p - emitter cladding permeability to oxygen, mole/(m·s·$atm^{1/2}$).

The interaction between the fuel and the cladding and the migration of fuel components through the cladding into the IEG are determined by local parameter values for the fuel in contact with the cladding. Given significant temperature drops along the oxide fuel-stack length and radius, the fuel composition may vary

in the different parts of the fuel element. Section 3.3 shows that with slow alteration of the fuel composition, a steady-state oxygen distribution in the fuel element, determined by Equation 3.25, can be used. Considering the oxygen coefficient change resulting from uranium decay and oxygen migration beyond the fuel element, the pre-exponential factor in the distribution (Equation 3.25) is a slowly changing time function. Lyubimov and Lovchikov [24] considered the change in oxide fuel's oxygen coefficient jointly with oxygen transport into the IEG through the cladding and interaction of the diffused oxygen with the IEG gas medium.

For fuel elements in which the inner cavity communicates with the IEG space, oxygen penetration into the IEG is possible over the gas-exhaust channels. To reduce the rate of mass transfer into the IEG, oxygen getters located on a segment between the fuel-element and IEG cavities may be used. Bobkov et al. [25] examined the possible use of a niobium getter and noted that previously it was erroneously assumed that the limiting phase for the gettering is oxygen diffusion within the oxide fuel or getter. They [25] showed, however, that for uranium dioxide of a composition close to stoichiometric, the slower stages are oxygen desorption from the fuel surface and niobium chemosorption of oxygen. Assuming the chemosorption of oxygen by a getter as the limiting stage for the gettering, Bobkov et al. [25] obtained an expression determining a time for which uranium dioxide composition changes from UO_{2+X_0} to UO_{2+X}. Such a transition time depends on the thermodynamic parameters of the fuel, the coefficient of oxygen adhesion to niobium, the oxygen molecule dissociation equilibrium constant, and the overall amount of fuel and the ratio of fuel to getter surfaces. It was assumed here that the getter is available in adequate amounts and its saturation by oxygen is not reached (oxygen solubility in niobium is ~1% at.).

Experimental study [25] of gettering the uranium dioxide samples in sealed containers of (Nb+1%Zr) alloy revealed that the calculational results show good consistency with the experimental data. Bobkov et al. [25] assumed that the fuel oxygen immediately reaches the getter surface, i.e., the phase of oxygen transfer from fuel to getter is not limiting. These conditions were realized in the experiments, but if getters are placed at the ends of fuel elements or in the intermodule space, it is necessary to make estimates for each particular fuel-element design, since in this case the limiting stage for the gettering may be oxygen transfer in the gaseous phase.

If carbide fuel compositions are used, the most detrimental effect on the converter characteristics is exerted by carbon. The transfer, through the fuel-element cladding, of carbon, uranium, zirconium, and tantalum from a fuel comprising a carbide solid solution is considered in the work of Lyubimov et al. [26].

3.6. Mass Transfer within the Interelectrode Gap of the Thermionic Converter

The presence of a gas medium of complex composition within the IEG has the result that chemical transport of the emitter material to the collector considerably exceeds the sublimation rate of the emitter material. The chemical transport of a substance can occur in one of three modes: diffusion, diffusion-kinetic, and kinetic. The diffusional regime, for which a process rate is governed by reactant delivery or removal of reaction products, is well-studied [27]. It is not necessary to consider the kinetics of the reaction in the diffusional regime. In contrast to the kinetic mode, the chemical transport rate is governed by the chemical reaction rate; therefore a detailed investigation of the reactions becomes necessary. Under TFE conditions, especially if the TFE contains communicating fuel-element and IEG cavities, the main participants in the reactions may be present in considerable amounts. The fuel is, in fact, an infinite source of oxygen and carbon oxides and, the moderator, of hydrogen. In addition, the IEG contains cesium under ~1 torr pressure, which can also take part in the reactions. The absence of any essential transport restriction means that the mass transfer into the IEG occurs under conditions close to kinetic. Cesium in the IEG under ~1 torr pressure does not bring about any appreciable inhibition of the mass transfer. As shown in Figure 3.1, under actual conditions with ~0.5 mm IEG width, the uncharged particle free path length is close to the interelectrode gap value.

In light of the above-mentioned circumstances, RI SIA "Lutch" paid great attention to examination of substance transfer in kinetic and diffusion-kinetic modes, where the governing role is performed by adsorption and surface reactions. Bobkov et al. and Lubimov et al. [28, 29] stated a set of equations to find the degree of surface coverage with gas-phase components. Those equations are the mass balance equations for each atom type in the steady-state transport of a substance between two surfaces of equal area:

$$\sum_j l_{ij} \cdot \frac{S_j^{(1)}\mu_j^{(2)} - S_j^{(2)}\mu_j^{(1)}}{1-(1-S_j^{(1)})(1-S_j^{(2)})} \cdot R_j = 0 \qquad (3.33)$$

where: l_{ij} - i-atoms number in j-molecule;

$S^{(r)}_j$ - coefficient of adhesion of j-molecules to r-surface;

$\mu^{(r)}_j$ - rate of j-molecule desorption from r-surface;

R_j - transport ratio for j-molecules, considering the diffusional resistance of the gaseous medium filling the gap.

This consideration excludes the processes connected with the molecules' migration into the material volume and supply from it and any chemical reactions in the gaseous phase. As for the rest of the i-equations, equations determining the amount of each component in the system surface and gaseous phase are used.

$$N_i = A\left(n_s^{(1)}\Theta_i^{(1)} + n_s^{(2)}\Theta_i^{(2)}\right), \tag{3.34}$$

$$P_j = \frac{2 - S_j^{(2)}}{S_j^{(1)} + S_j^{(2)} - S_j^{(1)} \cdot S_j^{(2)}}\left[\mu_j^{(1)} + (1 - S_j^{(1)})\mu_j^{(2)}\right]\frac{(2\pi m_j kT_1)^{1/2}}{4} + \mu_j^{(2)}\frac{(2\pi m_j kT_2)^{1/2}}{4} +$$
$$\frac{2 - S_j^{(1)}}{S_j^{(1)} + S_j^{(2)} - S_j^{(1)} \cdot S_j^{(2)}}\left[\mu_j^{(2)} + (1 - S_j^{(2)})\mu_j^{(1)}\right] \cdot \frac{(2\pi m_j kT_2)^{1/2}}{4} + \mu_j^{(1)}\frac{(2\pi m_j kT_1)^{1/2}}{4}, \tag{3.35}$$

where: A - surface area;
T - surface temperature;
n_s - number of adsorption centers on surface,
m_j - mass of j-molecule.

In Equations 3.33 through 3.35, m_j and S_j must be expressed in terms of the degree of coverage. Bobkov et al. and Lubimov et al. [28, 29] used, for the desorption rate, expressions obtained within the framework of the theory of absolute reaction rates; the dependence of degree of coverage on desorption energy is expressed using the model of surface electron gas. They [28, 29] also reviewed the available literature on dependence of the adherence coefficients on degree of coverage; even for diatomic gases these expressions have rather complex configuration. Here it is inferred that, when processing the experimental data, it is advisable to use approximate expressions [31]. Tungsten and molybdenum evaporation in various environments was considered using the approximate expressions. The evaporation in oxygen atmosphere and in hydrogen/water vapor mixture has been examined [28, 29]. Gas pressure/temperature dependences of tungsten evaporation are calculated in these studies. There is good agreement of the calculational data with results of an experimental study of tungsten evaporation under low pressures of hydrogen and water vapor [32], as well with results of literature data on tungsten evaporation at low oxygen pressure.

Lubimov et al. and Grebenshicov et al. [29, 33] reviewed the chemical transport of tungsten in the gaseous phase containing three elements: Cs, O, and H. Thermodynamic estimates showed that, in such a system, oxygen is present mainly in molecules of cesium hydroxide, CsOH. Therefore, tungsten evaporation was considered in a gaseous mixture of CsOH+Cs. A calculated temperature dependence of the tungsten evaporation rate in different gaseous environments is presented in Figure 3.4. A resulting rate of tungsten evaporation is obtained by

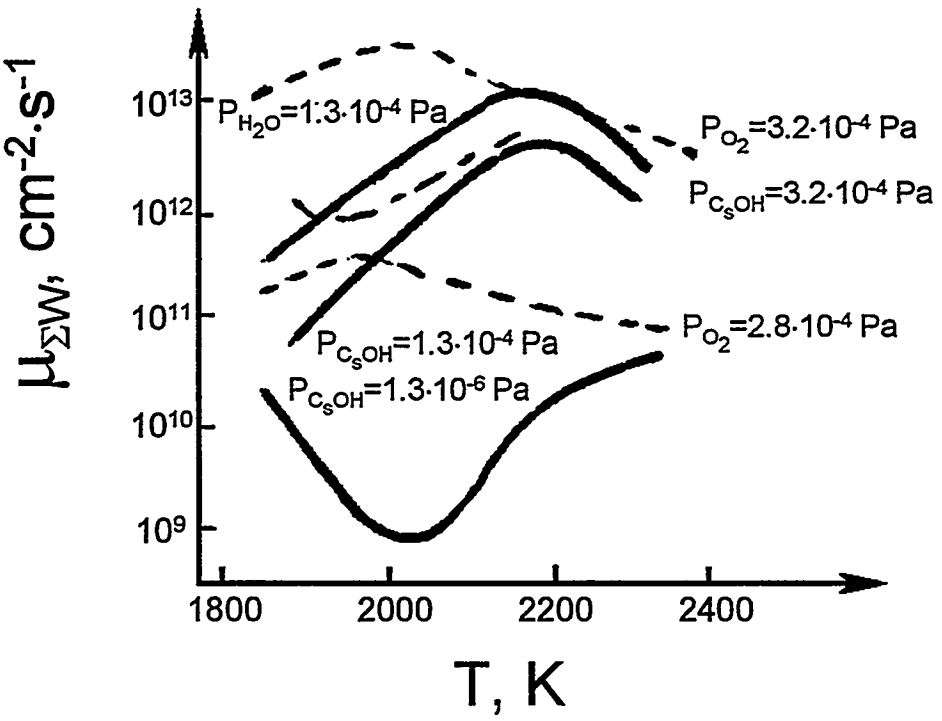

Figure 3.4. Tungsten evaporation rate in oxygen, water vapor, and cesium hydroxide vs. temperature [29].

summation of the main tungsten-containing constituents of the gaseous phase (W, WO, WO_2, WO_3, and Cs_2WO_4).

Grebenshicov et al. [33] studied another aspect of the emitter material mass transfer impact on TEC efficiency. Application of a gold or copper coating to the collector cuts emissivity in half and heightens converter efficiency by 4 to 5%. To maintain a high collector reflectivity, the thickness of the applied layer of tungsten during its lifetime should not exceed 100 to 150 Å. Proceeding from the transfer rate of 10 to 20 Å/year, using the REFNICO computer program, Grebenshicov [33] showed that the oxygen/hydrogen concentration in cesium filling the IEG should not surpass $\sim 2 \cdot 10^{-7}$ mole/kg.

Cesium is able to alter the tungsten oxidation rate as a result of substantial reduction of the tungsten work function with cesium adsorption [34]. The presence of cesium atoms in the surface considerably changes the relation between evaporation rates of diverse oxides in the temperature range where the work function is lower than for the electron affinity of WO_3 [34]. In fact, all oxygen in this case is spent to form the ions WO_3^-, and WO and WO_2 evaporation rates decrease sharply as compared to tungsten oxidation without cesium. As a result, a minimum in the 1700 to 1900 K temperature range in the curve of 1/T dependence on evaporation rate at a surface without cesium, deriving from competition between reactions forming WO, WO_2, and WO_3, is smoothed by considering the reduction in work function.

If uranium dioxide is insufficiently purified of carbon, one of the major gaseous phase components is carbon oxides: monoxide and dioxide. The same ingredients are the main ones over nuclear fuels based on uranium carbide. Lyubimov et al. [35] investigated the tungsten evaporation rate in a ($CO+CO_2$) gaseous mixture. Figure 3.5 represents a calculated temperature dependence of polycrystal tungsten evaporation rate under CO_2 at various pressures [35]. Available experimental data from the related literature are also plotted in this figure. A satisfactory consistency of the calculational results with experimental data is seen.

3.7. Emitter Deformation and Fuel Swelling

One of the key problems in building a long-life TFE is the provision of geometric stability of the emitter to preclude short-circuit of the electrode. Three basic mechanisms of emitter deformation leading to this type of failure are generally accepted [20, 36, 37]:

- fuel swelling;
- fuel element thermocycling;
- emitter loading by inner pressure of GFP released from fuel.

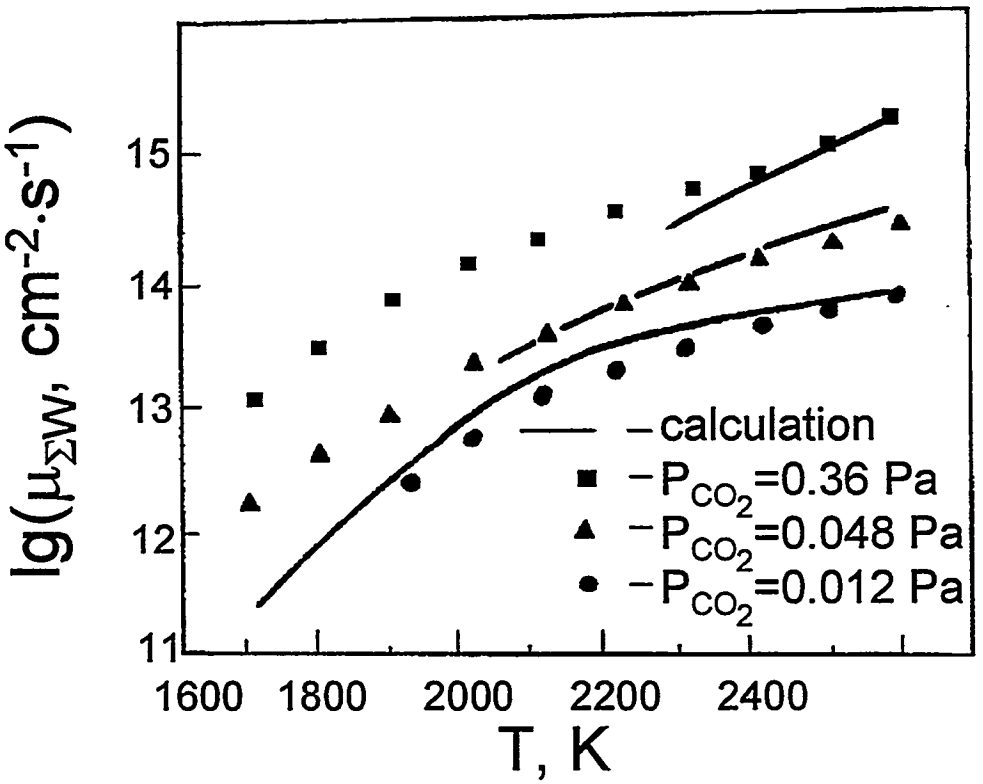

Figure 3.5. Temperature dependence of polycrystal tungsten evaporation rate at various CO_2 pressures [35].

3.7.1. Emitter Creep under Inner Pressure of Released GFPs

Inner pressure is linked to a potential malfunction of the system for GFP removal from the fuel-element cavity. At present, the need for ventilation is commonly accepted [20, 36, 37].

An estimate of the emitter deformation under the effect of GFP pressure in its cavity may be sought from the relationship [11]

$$\Delta D / D = (\sqrt{3}/2)^{m+1} \cdot B \cdot (a/h)^m \cdot \tau^{m+1} / (m+1) \cdot C^m, \qquad (3.36)$$

where: D - outer diameter of the emitter,
$C = q_V/E \cdot Y \cdot k \cdot T \cdot 1/\psi$,
B, m - coefficient and exponent of emitter material creep;
a, h - emitter inner radius and thickness;
q_V - volumetric power density averaged on fuel element;
E - energy released per one fission;
Y - GFP yield per one fission;
T_{GFP} - temperature of gas in fuel-element cavity;
ψ - ratio of gas cavity volume to fuel volume

The relationship is obtained under the assumption that GFP pressure immediately affects the emitter (i.e., the fuel's restrictive influence is neglected). This supposition, first, considerably simplifies the problem solution. Second, the advisability of considering the restrictive effect of the fuel stack (as done in a number of works) is doubtful because of the possibility of cracking, development within the fuel of interlinked porosity in the course of swelling, etc. In addition, investigations [38] show that considering this factor can lead to an appreciable extension of time until short circuit only for "rigid" type fuels. In deriving the relationship it was also assumed that relative GFP leakage from the fuel equals 1, which is permissible because of the high fuel temperature.

3.7.2. Deformation of Ventilated Fuel Element Emitter under Fuel Stack Swelling

For the ventilated fuel-element design (i.e., with GFP removal from its cavity), a key factor limiting TFE operation under steady-state operating conditions is emitter deformation due to fuel-stack swelling.

A problem of theoretical description of emitter deformation is, in this case, connected with the necessity of modelling several interlinked processes: fuel stack swelling, its interaction with the emitter, and fuel structural transformations and their influence on UO_2 mechanical properties.

As analysis shows, the strength-related aspect of this problem is most developed. Facets linked to modelling the processes of UO_2 re-structuring and swelling remain less studied [39].

UO_2 Irradiation Swelling. Uranium dioxide high-temperature swelling, notwithstanding a large scope of published experimental data and theoretical investigations, is to date not studied enough. Analysis of this information [40, 41] revealed that the results of individual works are not in agreement with each other with respect to either values given or qualitative dependence on operational parameters (temperature, burnup). So, for example, findings [36, 42] from calculational investigations of the temperature dependence of swelling predict a maximum in the temperature range of 1500 to 1800 K. A saturation value of the swelling in the course of burnup is also forecasted. At the same time, a number of other calculational and experimental studies point out an increase in swelling with temperature and its practically linear burnup dependence (see, e.g. [43, 44]).

The issues linked to the impact of these parameters are important in predicting the fuel element's lifetime and in optimizing its design.

Use of well-known domestic and foreign mathematical models describing the swelling is also restricted, because most of them were developed only for application to the sintered uranium dioxide with fine-grained equiaxial structure. They cannot be applied to high-temperature fuel elements, where the as-fabricated UO_2 structure converts to column-type with simultaneous change in its irradiation [41, 45] and mechanical [46] properties. For the same reason, there is also limited potential for their application to accelerated tests, where in a number of cases, the test temperature will be high compared to operating conditions.

At present, efforts dedicated to broadening the domain of applicability of both existing and newly developed models of uranium dioxide swelling are conducted at the Institute of Physics and Power Engineering (IPPE) [47], the Russian Scientific Center "Kurchatov Institute" [48], and RI SIA "Lutch" [40, 41].

Thus, application of the theoretical mathematical models describing UO_2 swelling is to date evidently not reliable enough to forecast TFE long life behavior for a wide range of its operating parameters. In connection with this, RI SIA "Lutch" has adopted a comprehensive approach to solving this problem. Within the framework of a theoretical model (computer code BARS), experimental data on UO_2 irradiation behavior are being analyzed and interpreted. Emitter life behavior is estimated using experimental results on UO_2 swelling (computer code SDS) [41].

The computer code BARS (Bubbles Analysis of Radiation Swelling) has been primarily developed proceeding from the BUBL program's model concepts [49], but modifications allow the elimination of a discrepancy in literature data on the impact of operational parameters on UO_2 swelling [41]. BARS computes the value and the rate of change both in UO_2 density, which influences temperature

fields, UO_2 creep, etc., and in the outer dimensions of the fuel to determine emitter loading behavior resulting from UO_2 swelling. Parameters to be computed include size and number of bubbles within the fuel and kinetics of GFP release from UO_2.

In the computer code BARS, as in the known statistical model of swelling BUBL, every bubble is observed from the moment of its formation until its approach to the free fuel surface. The relative volume of bubbles located in the fuel, in contrast to BUBL, is a measure of only irradiation-induced fuel porosity. Also in contrast to BUBL, to find the UO_2 swelling responsible for emitter loading BARS contains an additional subroutine for summing the volume of bubbles located in the fuel and having left it by a given point in time.

Uranium Dioxide Non-Irradiation Swelling Connected with Processing Features of Fuel Pellet Fabrication. Gontar and co-workers [11, 50] reviewed the mechanism of UO_2 non-irradiation-induced swelling. Its manifestation under in-pile conditions may be connected with the processing features of fuel-pellet fabrication, in particular with sintering in a gaseous medium.

The TRC fuel element assembly contains, as a rule, high density uranium dioxide (≥95% of theoretical) to meet strict requirements for the size/mass parameters of a reactor [39]. At the final phase of sintering these pellets, when their density constitutes ~95% of theoretical, all the porosity becomes in fact closed (Figure 3.6 [51]).

At this stage, the pellets' shrinkage ceases and the pressure of the gas within the closed pores—the same gas as the atmosphere in which the sintering occurs—is balanced by Laplace pressure [2, 52, 53]. The closed pores formed in this way are sited both between and within grains, following the distribution achieved at the sintering finish phase. Most of the intragrain pores are smaller than 1 μm in size [54].

Analysis of the represented data [50] indicates that, under thermionic fuel element operation, there is a possible manifestation of an accompanying mechanism of non-irradiation swelling of uranium dioxide along with the irradiation swelling. It is provoked by coalescence of closed equilibrium process-induced pores, which remained motionless within grains during processing operations, but which migrate under in-pile conditions due to temperature gradients.

The scope of this mechanism is based on the following premises. Migration velocity V of the said size pores (d<1 μm), if UO_2 grains do not grow, is controlled by surface diffusion and can be defined using the formula [2]

$$V = \frac{6 \cdot D_s \cdot Q_s \cdot a}{k \cdot T^2 \cdot d} \cdot \text{grad}T, \qquad (3.37)$$

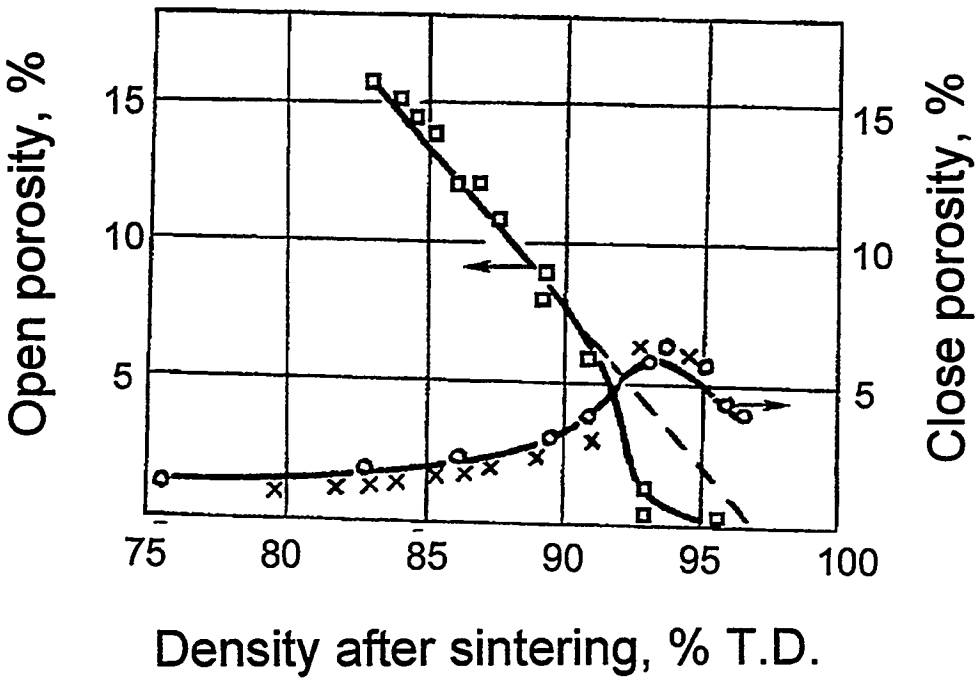

Figure 3.6. Open to closed porosity ratio vs. UO_2 pellet density [51].

where : D_S - coefficient of UO_2 surface self-diffusion;
Q_S - heat of transfer for surface self-diffusion;
d - pore diameter;
a - lattice spacing;
k - Boltzmann constant;
T - temperature.

As a result of a preferred direction of movement, these pores migrate over time to the grain boundaries, where they become fixed under the effect of intergrain surface tension forces, γ_g. In the grain boundaries, related buildup, collisions, coalescence, and size enlargement of as-produced process-induced pores will occur during their migration from the grain volume to its boundary.

The size d of a pore, formed in coalescence of two equilibrium gas-filled pores with diameters d_1 and d_2, is determined from a solution of the in-pore gas state equations and the pores' equilibrium condition [52]:

$$d^2 = d_1^2 + d_2^2 \tag{3.38}$$

In the process, the volume of a pore formed exceeds the sum of the two joined pores' volumes, i.e., the fuel density decreases and it swells.

When a pore reaches d-size, equaling or surpassing the critical d^{cr}, i.e., when

$$d \geq d^{cr} = 2 \cdot \left[\frac{a^3 \cdot \gamma_g \cdot T}{2 \cdot Q_S \cdot \text{grad}T} \right]^{1/2} \tag{3.39}$$

the pore detaches from the grain boundary and migrates to the fuel element center.

To assess the scale of this swelling mechanism, an equiaxial grain was approximated [50] using an equivalent cube, one face of which is perpendicular to the temperature gradient. The site of pores successively reaching this face was determined using the Monte-Carlo method.

Calculational Simulation of Emitter Swelling Deformation Behavior. The SDS computer code (Stress and Deformation under Swelling) has been developed to predict TFE emitter deformation. In this code, the fuel's swelling rate and density, as well as their dependence on operational and structural parameters, are based on statistical, experimentally achieved in-pile test results on fuel samples. This eliminates potential errors linked to the use of mathematical swelling models based on inadequate investigations or inaccurate mathematical descriptions of the processes governing swelling.

For experimental study of fuel-material swelling, i.e., for input data required for the SDS code, RI SIA "Lutch" has developed a technique and irradiation device for gaining these data, depending on burnup [41, 45]. Experimental data have

been collected on the impact of temperature operation conditions for UO_2 of different structural modifications (see Chapter 6).

In this approach, mathematical modelling of the emitter deformation behavior is considerably simplified, because it is reduced to modelling only the mechanical interaction between the swelling fuel stack and the emitter. In this event, only the strength-related facet of the problem is considered, which has been most elaborated to date.

In modelling the interaction between the swelling fuel stack and the emitter, the SDS code assumes them to be coupled by the radial mass transfer of UO_2. Only creep deformation is considered because under this type loading the mechanical stresses are much lower than the materials' yield limit, and the elastic component of total emitter deformation is insignificant.

Calculation of fuel-element deformation under stress is reduced to solving a set of equations of incompressibility, equilibrium, and creep, compiled for the fuel stack and emitter. As the boundary condition, radial stresses in the outer surface of the emitter and fuel-stack central channel are taken to be zero. The joining condition is the equality of the radial stresses and displacement between the stack and emitter.

In estimating the stress-deformed state, no less important a problem is the reliability of the underlying data on fuel-element material creep. The high UO_2 temperature ($T>1650°C$) brings about a strong growth of grains and migration of and release from the fuel by both as-produced and irradiation-induced porosity. Investigations [45] show that these processes lead to an appreciable decrease in the dioxide creep rate. Therefore, in predicting the lifetime and determining the stress-deformed state of the fuel element, the UO_2 creep parameters used are obtained from out-of-pile tests of fuel samples reproducing the intrinsic structural features of UO_2 under operation (grain size and shape, porosity level).

3.7.3. Emitter Deformation under Thermocycling because of TFE Heat and Electric Power Changes

Investigation of emitter deformation under thermocycling because of TFE heat and electric power changes is needed for several reasons.

First, in a number of cases, TFE operation is foreseen at various levels of electric power. Hence, irreversible emitter deformation may build up when shifting from one to another operating condition [36, 39].

Second, research reactor-based loop channel TFE tests, conducted in the phase of the TFE design debugging, are accompanied as a rule by high heat jumps and thermal shocks. They are derived from emergency safety protection responses, scheduled start-ups and shut-downs, or research reactor power lowering. To extrapolate such test results to standard conditions, it is necessary to discriminate the constituent of deformation induced by the thermocycles [55].

Third, TFE operation in a TRC is accompanied by continuous temperature cycles (~10 K), linked to operation of reactor power controls [56].

As applied to thermionic fuel-element operating conditions, the available literature on such investigations is poor. Questions concerning thermomechanical interactions between the fuel stack and cladding have been studied for power-reactor fuel elements (see, e.g., [57, 58]). However, because of an essential difference in operating conditions, these data cannot be extrapolated to the considered TFE operating conditions, mainly because of the much higher temperature of TFE operation. As a consequence of intense UO_2 mass transfer in the thermionic fuel elements, unlike power reactors, their fuel stack is linked to the emitter throughout its lifetime.

Several potential mechanisms for building up irreversible plastic deformation caused by TFE thermocycling have been reviewed [36, 20, 39, 55, 56].

According to Bogush et al. and Degaltsev et al. [36, 39], a major reason for the deformation buildup in TFE power cycling is connected with UO_2 recondensation and fuel cracking or stack/emitter gap formation. Owing to the high TFE operating temperature, the as-assembled fuel stack/emitter gap is entirely filled by fuel condensate formed by UO_2 recondensation. With a power rise, a concomitant elevation of stack and emitter temperatures occurs. Under these conditions, because of the absence of a gap and higher coefficient of UO_2 thermal expansion compared to the emitter material (twice as high), the emitter is deformed by the fuel stack. After the return to a previous power level, a gap (or crack) is formed because of mismatching thermal-expansion factors, given slight coupling or fuel cracking. At the subsequent stage of steady-state operation, the gap fills again with fuel condensate. Thus, iterated power cycling should lead to a permanent accumulation of emitter deformation.

Another mechanism, thermal ratcheting, is connected with deep cooling of the fuel element [20, 55]. The deep cooling of fuel elements, which follows the steady-state operation period, brings about a local (or complete) disconnection of the stack from the emitter. Out-of-pile investigations using electric heating reveal that, after repeated power rises, the thermal conductivity in the disconnection sites is 0.15 to 0.30 $W/cm^2 \cdot K$. For this reason, fuel-element power rise up to its rated level results in local overheating of the fuel stack and local deformation of the emitter up to 0.1% [20].

Such a deformation mechanism is also confirmed by in-pile experimental data. It follows, for example, from analysis of short-term tests of two modules of a multi-cell TFE with tungsten emitter and uranium dioxide stack (Table 3.1). In the first module, a tungsten foil was placed between the stack and emitter to prevent UO_2/emitter coupling. In the second module, the fuel stack was placed within the emitter, with a gap sufficient to accommodate the difference in their heat-induced movement. As seen from Table 3.1, emitter deformation took place only in the

Table 3.1. Conditions and results of TFE module tests [20]

No. module	Emitter Temperature, K	Test time, hrs	Thermocycles number	Maximum change in emitter diameter, %
1 (foil)	1600	3500	38	none
2 (no foil)	1570	1200	12	~1

second module, although it underwent a smaller number of thermocycles in the tests. Here, the emitter became oval in shape.

The "thermal ratcheting" mechanism linked to the thermionic reactor power controls' operation has been examined [20, 56]. Because of TRC controls operation, TFE use, even in the rated operation mode, is accompanied by permanent power oscillation. This leads to small (~10 K) but continuous changes in fuel-element temperature. Under these conditions, as experiments show, emitter/stack coupling is sustained. Manifestation of thermal ratcheting is, in this case, connected with thermocycle asymmetry with respect to heating and cooling rates, as well as with a power stress dependence of the emitter material creep rate ($\xi \sim \sigma^n$).

For all these reasons, changes in fuel-element temperature cause extra creep deformation of the emitter, along with heat-induced movement. Deformation is caused by the stresses arising in the emitter due to mismatching thermal expansion factors of the stack and emitter. Because of the power stress dependence of the emitter creep rate, its deformation per cycle depends on the stress difference arising within the emitter during cooling and heating. If, for example, within one cycle, the cooling rate is higher than the heating rate (with the same temperature change on cycle), emitter creep deformation during cooling will exceed creep deformation during heating, since at a higher cooling rate of the fuel element, a higher stress level is realized in the emitter. As a result of one cycle, the total irreversible creep deformation of the emitter will differ from zero—in the current case, the emitter diameter is reduced. Evidently, for a thermocycle with the opposite ratio of cooling to heating rates, a resulting increment to the emitter diameter will be observed.

Accompanying the thermocycling, continuous under in-pile conditions, unilateral loading of the emitter by swelling enhances the loading asymmetry. This mechanism has been assessed [56] under the following assumptions. A fuel element cross-section sited at a sufficient distance from its ends is considered. Here the flat sections theory is valid. In the given thermocycle range, stresses

within the emitter and stack materials do not reach the yield strength limit. Hence, only creep deformation is taken into account.

Calculational relationships to define deformation rates and stresses on each of thermocycle stages were determined from solution of the following set of equations, compiled both for the stack and emitter:
the incompressibility equation,

$$\xi_r + \xi_t + \xi_z = V, \tag{3.40}$$

where: $\xi_r = dU/dr$, $\xi_t = U/r$

ξ_r, ξ_t, ξ_z - relative deformation rates at radial, circumferential, and axial directions (the solution assumed ξ_z=0),

U - rate of radial displacement,

V - rate of relative volume change;

the equilibrium equation,

$$r \cdot d\sigma/dr = \sigma_t - \sigma_r, \tag{3.41}$$

where: σ_r, σ_t - radial and circumferential stresses, respectively; and

the creep equation,

$$\xi_t - \xi_r = \Psi \cdot \left(\sigma_t - \sigma_r\right), \tag{3.42}$$

where : $\Psi = 1/2 \cdot 3^{(n+1)/2} \cdot B \cdot \overline{T}^{n-1}$

B, n - respectively, creep coefficient and exponent;

$\overline{T}$ - intensity of tangential stresses.

To solve the set of Equations 3.40 through 3.42, we used the boundary conditions

$$\begin{aligned} \sigma_r^T(r_1) &= 0 \\ \sigma_r^{em}(r_3) &= 0 \end{aligned} \tag{3.43}$$

and the conditions of "joining" of the stack and emitter

$$\begin{aligned} \sigma_r^{em}(r_2) &= \sigma_r^T(r_2) \\ U^{em}(r_2) &= U^T(r_2) \end{aligned} \tag{3.44}$$

where: r_1, r_2, r_3 - radius of stack channel, stack/emitter interface, and emitter outer surface, respectively.

Here, the rates of relative change in fuel and emitter volume are determined by the relations

$$\dot{V}_{em} = 3\alpha_{em} \cdot dT / d\tau;$$

$$\dot{V}_f = 3\alpha_f \cdot dT / d\tau + dS / d\tau,$$

where : α_{em}, α_f - thermal expansion coefficients of emitter and stack material, respectively;

$dS / d\tau$ - rate of stack volume change, induced by swelling;

$dT/d\tau$ - rate of fuel element temperature change (hereinafter, v^h when heating and v^c when cooling).

Through the rates of emitter displacement when cooling $\left(U_c^{em}\right)$ and heating (U_h^{em}) found in solving Equations 3.40 through 3.42, the emitter radius change per cycle is sought as

$$\Delta r_3 = U_c^{em} \cdot \tau_c + U_h^{em} \cdot \tau_h,$$

where : τ_c, τ_h - time of cooling and heating, respectively.

Steinar [57] also considered the influence of the fuel stack on the swelling level under a stress state resulting from preset thermocycling.

To assess this effect, the creep of a spherical cell of fuel with a gas pore was examined to predict the swelling in the spherical gaseous pore model [59]. An equation for relative volume change of the spherical cell (swelling), considering UO_2 linear creep dependence of stress (i.e. $\xi \sim \sigma$), is reduced to the following:

$$S_c \approx \varepsilon \cdot \left\{ \exp\left[\frac{9 \cdot K\left(P_{GFP} \cdot \tau_{cyc} + P_{out}^c \cdot \tau_c - P_{out}^h \cdot \tau_h \right)}{4(1-\varepsilon)} \right] - 1 \right\} \qquad (3.45)$$

where: S_c - relative volume change of gas pore per cycle;

ε - process-induced porosity of fuel;

K - fuel creep coefficient;

P_{GFP} - GFP pressure within pore (preset parametrically);

P_{out}^c, P_{out}^h - outer pressure upon the sphere when cooling and heating, respectively;

$\tau_c, \tau_h, \tau_{cyc}$ - time of cooling, heating, and complete thermocycle, respectively.

3.8. Computer Code KATET for Simulation of Fuel Element Lifetime Behavior

Most of the computer codes intended to study fuel-element lifetime behavior involve individual phenomena restricting TFE life, but these phenomena are interlinked in a complex manner. As noted in Section 3.3, the mass transfer and the temperature fields must be described jointly. Change in temperature and geometry of the fuel stack substantially impacts fuel-element deformation. Cladding deformation leads to IEG reduction, which increases emission current and changes the fuel-element cladding temperature. Thus, the thermal, electric, and deformation processes and mass transfer are interlinked, and a separate consideration of these phenomena in predicting a long life may bring about considerable errors.

Kornilov et al. [60] described a procedure and program for self-consistent computation of electric parameters of a multi-cell TFE module and fuel disposition within a fuel element. The calculation is conducted on the final arrangement of uranium dioxide within the fuel element. However, steady-state conditions are reached only in the central, most thermostressed modules for times that are short compared to lifetime. In the single-cell TFEs and outlying multi-cell TFE modules, the fuel steady-state disposition usually is not reached.

In view of this fact, RI SIA "Lutch" has developed a complex computer code, KATET (Complex Analysis of Thermionic Fuel Elements) that simulates single-cell TFE life behavior and considers the interinfluence of life-restricting factors. KATET jointly considers the following questions:

- uranium dioxide mass transfer in the central channel of the fuel-element stack under the effect of temperature gradient;
- time dependence of distribution of heat generation in the fuel stack, deriving from fuel mass transfer;
- fuel swelling induced by gaseous fission products;
- TFE emitter diameter deformation vs. fuel swelling and emitter bending deformation caused by the azimuthal non-uniformity of temperature; and
- time dependence of fuel-element cladding-temperature distribution, deriving from change in heat release distribution in the stack and IEG value change.

Nikolaev et al. [61] summarized the mathematical models used in the code, program structure diagram, computational algorithm, and results. Since the total number of equations solved by numerical methods is very large, the program is built as individual units (subroutines) that characterize the processes considered by the program. The program's main routine alternately calls the units. Because the

processes modeled are of different rates, the time step is chosen equal to the smallest of the steps required to describe the separate phenomena, and to save computer time, subroutines describing less rapid processes may not be called at each time step. One version of the program produces graphical results as output to screen and printer graphs of the emitter temperature distribution along the TFE length and throughout the central channel surface and distribution of diameter deformation of the emitter and stack central channel diameter. These curves are output for instants preset in the underlying data. KATET is compiled in a way that allows the incorporation of additional subroutines considering phenomena which under some conditions may exert an appreciable effect upon the fuel-element life behavior. Such processes may include [61]

- material mass transfer into the IEG;
- deviation of uranium dioxide composition from stoichiometry and change in fuel oxygen coefficient in the course of operation;
- migration of as-obtained porosity within the fuel-element stack in a temperature gradient field;
- material property changes under irradiation;
- pellet cracking; and
- emitter deformation under fuel element thermocycling.

As shown previously in Chapter 3, as well as in Chapter 4, at present, each of the above cited processes has been mathematically described and calculationally studied separately.

3.9. References

1. Fedik, I.I., Kolesov, V.S., Mikhailov, V.N. *Temperature Fields and Thermostresses in Nuclear Reactor.* Moscow: Energoizdat, 1985, 280 p.
2. Olander, D.R. *Fundamental Aspects of Nuclear Reactor Fuel Elements.* Published by Technical Information Center Energy Research and Development Administration. USA, 1976, 613 p.
3. Lykov, A.V., and Mikhailov, Yu.M. *Theory of Heat and Mass Transfer.* Moscow-Leningrad: Gosenergoizdat, 1963, 535 p.
4. Siegel, R., and Howell, J.R. *Thermal Radiation Heat Transfer.* Moscow: Mir, 1975, 934 p.
5. Dushman, S. *Scientific Foundation of Vacuum Technique.* Moscow: Mir, 1964, 715 p.
6. Shulepov, L.N. "Mass Transfer in Cylindrical Channel with Evaporation and Condensation on Channel Walls." *Eng.-Phys. Journ,* 1978, v. XXXV, No. 1, p. 82-86.

7. Shulepov, L.N. "Mass Transfer in Conic Channels with Evaporation and Condensation on Channel Walls." *Eng. Phys. Jour.*, 1978, v. XXXV, No. 2, pp. 284-286.
8. Kucherov, R.Ya., Rikenglaz, L.E., and Tsulaya, T.S. "The Kynetic Theory of Re-Condensation at Small Temperature Difference." *Jour. Tech. Phys.*, 1962, v. 32, No. 11, pp. 1392-1398.
9. Zhdanov, V.M., and Shulepov, L.N. "Of the Kynetic Theory of Re-Condensation in a Binary Gas Mixture at Arbitrary Knudsen Numbers—News of AS USSR." *Mechanics of Liquid and Gas*, 1975, No. 54, pp. 150-155.
10. Kucherov, R.Ya., and Shulepov, L.N. "Motion and Change in Shape of a Pore in Temperature Field as Result of Evaporation and Condensation." *Eng. Phys. Jour.*, 1983, v. XLIV, No. 1, pp. 83-87.
11. Gontar, A.S., Kucherov, R.Ya., Nelidov, M.V., et al. "Some Questions of Uranium Dioxode Mass Transfer Influence on High-Temperature Fuel Element Behaviour." *Proc. 24th Intersociety Energy Conversion Engineering Conf.* New York, 1989, v. 6, pp. 2803-2808.
12. Present, R.B., and de Bethune, A.T. "Separation of a Gas Mixture Flowing through a Long Tube at Low Pressure." *Phys. Rev.*, 1949, v. 75, p. 1050.
13. Zhdanov, V.M. "Of Theory of Slip on Gas Mixture Boundary." *Journ. Tech. Phys.*, 1967, v. 37, pp. 192-197.
14. Hirschfelder, J.O., Curtiss, Ch. F., and Bird, R.B. *The Molecular Theory of Gases and Liquids*. Moscow: Inostrannaya Literature, 1961, 930 p.
15. Kornilov, V.A., Sukhov, Yu.I, and Yuditski, V.D. "A Method for Calculation of Temperature Fields in Heterogeneous Fuel Stack of Thermionic Electrogenerating Element." *Atomic Energy*, 1989, v. 49, iss. 6, pp. 394-394.
16. Gontar, A.S., Sotnikov, V.N., and Shulepov, L.N. "Uranium Dioxide Mass Transfer Influence on Thermionic Fuel Element Gas Exhaust Device Operationability." Report at the Branch Jubilee Conference "Nuclear Power in the Space". Obninsk, 1990.
17. Breitung, W. "Oxygen Self and Chemical Diffusion Coefficients in $UO_{2\pm x}$." *Jour. Nucl. Mater.*, 1978, v. 74, No. 1, pp. 10-18.
18. Sari, C. "Oxygen Chemical Diffusion Coefficient of Uranium-Plutonium Oxides." *Jour. Nucl. Mater.*, 1978, v. 78, No. 2, pp. 425-426.
19. Norris, D.J.R. "Solid State Transport as a Mechanism of Oxygen Thermomigration in (U, Pu) $O_{2\pm x}$." *Jour. Nucl. Mater.*, 1979, v. 79, No. 1, pp. 118-127.
20. Gontar, A.S., Nelidov, M.V., Nikolaev, Yu.V., et al. "Problems in Thermionic Fuel Elements Development." Report at the Branch Jubilee Conference "Nuclear popwer in the Space". Obninsk, 1990.
21. *Strength Calculations in Mechanical Engineering.* Ponomarev, S.D., *ed.* Moscow, Mashigiz, 1958.

22. Lybimov, D.Yu., Bolotov, S.V., Kuraeva, E.M, et al. "Thermodynamical Analysis of Condensed Phases Formation in TEC Gas Exhaust Channels." Report at the 4th Branch Conference "Nuclear Power in the Space. Materials. Fuel." Podolsk, 1993.
23. Lyubimov, Yu.D., Bobkov, B.N., Lavrentiev, E.A., and Panov, A.S. "Simulation of Mass Transfer in Thermionic Converter Interelectrode Gap." Report at the Branch Jubilee Conference "Nuclear Power in the Space". Obninsk, 1990.
24. Lyubimov, D.Yu., and Lovchikov, M.B. "Mathematical Simulation of Physical/Chemical Processes in Fuel and TRC IEG." Report at the Branch Jubilee Conference "Nuclear Power in the Space". Obninsk, 1990.
25. Bobkov, B.N., Goryachkina, L.F., Lavrentiev, E.A., et al. "Oxygen Transfer in Niobium-Uranium Dioxide." *Atomic Energy*, 1991, v. 71, iss. 1, pp. 62-64.
26. Lyubimov, D.Yu, Panov, A.S., Fedorov, E.M., Vedenyapin, G.F. "Carbide Fuel Components Transport into Interelectrode Gap of TRC." Report at the 4th Branch Conference "Nuclear Power in the Space. Materials. Fuel." Podolsk, 1993.
27. Frank-Kamenetsky, D.A. *Diffusion and Heat Transfer in the Chemical Kynetics.* Moscow: Nauka, 1967.
28. Bobkov, B.N., Lyubimov D.Yu., Lavrentiev, E.A., Panov, A.S. *A Substance Chemical Transport via Multi-Component Gaseous Phase under Nonisothermal Conditions. Problems of Atomic Science and Engineering. Series: Nuclear Materials Science/Technology.* 1989, iss. 2(25), pp. 13-17
29. Lubimov, D.Yu., Bobkov, B.N., Lavrentyev, E.A., Panov, A.S. "Model of Mass Transfer between Electrodes in a Thermionic Converter." *Proc. Specialist Conf. on Thermionic Energy Conversion.* Eindhoven, The Netherlands, 1989, pp. 167-175.
30. Glesston, S., Leider, K., and Eiring, G. *The Theory of Reactions Absolute Rates.* Moscow: Inostrannaya Literatura, 1948.
31. Tompinks, E.S. *Chemosorption of Gases on Metals.* London: Academic Press, 1978.
32. Andrievsky, R.A., Galkin, E.A., and Khromonozhkin, V.V. "Tungsten Evaporation in Vacuum under Low Pressures of Hydrogen and Water Vapor." *High Temperature Physics*, 1981, v. 19, No. 4, pp. 762-767.
33. Grebenshicov, S.V., Kucherov, R.Ya., Lubimov, D.Yu., and Nikolaev, Yu.V. "Thermionic Converter with Reduced Radiation Loss." *Proc. Specialist Conf. on Thermionic Energy Conversion.* Goteborg, Sweden, 1993, pp. 241-247.
34. Gunko, V.M., and Smirnova, R.V. "The Work Function Influence on High-Temperature Oxidation of Tungsten Surface." *Jour. Phys. Chemistry*, 1983, v. 57, No. 10, pp. 2581-2583.
35. Lyubimov, D.Yu, Soldatova, N.V., Panov, A.S., et al. "Mathematical Modelling of Tungsten Evaporation in CO-CO_2 at High Temperatures."

Report at the 2nd Branch Conference "Nuclear Power in the Space". Sukhumi, 1991, pp. 374-355.

36. Begg, L.L., Wetch, J.R., and Nelin, C.J. "Thermionic Fuel Element Endurance Enhancement." *Proc. 19th Intersociety Energy Conversion Engineering Conf.* San Francisco, 1984, v. 3, pp. 2276-2281.
37. Bogush, V.B., Borodastov, S.V., Devyatchenok, G.S., et al. "Simulation of High-Temperature Emitter Units Deformation Behavior." Report at the Branch Jubilee Conference "Nuclear Power in the Space." Obninsk, 1990.
38. Gontar, A.S., Kukin, E.B., Nelidov, M.V., and Nikolaev, Yu.V. "Possibilities of Using Alternative Fuels in a Thermionic Fuel Element." *Proc. 26th Intersociety Energy Conversion Engineering Conf.*, 1991.
39. Degaltsev, Yu. G., Ponomarev-Stepnoy, N.N., Kuznetsov, V.F. *Irradiation Behavior of High Temperature Nuclear Fuel.* Moscow: Energoatomizdat, 1987, 208 p.
40. Gontar, A.S., and Nelidov, M.V. "A Model and Calculational Study of Uranium Dioxide Swelling under High-Temperature Irradiation." *International Conf. Irradiated Materials Science.* Alushta, 1990. *Theses of reports, part 3.* Kharkow, 1990, p. 45
41. Gontar, A.S., Gutnik, V.S., Nelidov, M.V., and Nikolaev, Yu.V. "Swelling of Uranium Dioxide and Deformation Behaviour of the Fuel Element at High Temperature Irradiation." *Proc. 28th Intersociety Energy Conversion Engineering Conf.* Atlanta, 1993, v. 1, pp. 549-553.
42. Dollins, C.C., and Nichols, F.A. "Swelling and Gas Release in UO_2 at Low and Intermediate Temperature." *Jour. Nucl. Mater.*, 1977, v. 66, pp. 143-147.
43. Zimmerman, H. "Investigations on Swelling and Fission Gas Behaviour in Uranium Dioxide." *Jour. of Nucl. Mater.*, 1978, v. 75, pp. 154-161.
44. Hilbert, R.F., Storhok, V.W., Chubb, W., and Keller, D.L. "Mechanisms of Swelling and Gas Release in Uranium Dioxide." *Jour. Nucl. Mater.*, 1971, v. 38, pp. 26-34.
45. Gontar, A.S., Gutnik, V.S., Zaitsev, V.A., et al. "A Method and Results of Comparative Irradiation Tests of High-Temperature Fuel Materials." Report at the 4th Branch Conference "Nuclear Power in the Space. Materials. Fuel." Podolsk, 1993.
46. Gridnev, A.A., Djalandinov, D.N., Zubarev, P.V., and Panov, A.S. "A Study of Coarse-Grained Uranium Dioxide High Temperature Creep." *Atomic Energy*, v. 59, iss. 1, 1985.
47. Tchkauseli, V.F., Bogush, V.B., Strokova, A.M., and Raskach, V.N. "Simulation of Gas-Induced Swelling and Gas Release in Oxide Fuel Pellet." *Problems of Atomic Science/Engineering. Series: Physics of Irradiation Damage and Irradiated Materials Science/Technology.* 1989, iss. 50, pp. 19-22.

48. Degaltsev, Yu.G., Kuznetsov, V.F., Ponomarev-Stepnoi, N.N., and Slabki, V.D. "Post-reactor Research and TFE Lifetime Prediction for TOPAZ-2 System." *Proc. 12th Symp. Space Nuclear Power and Propulsion.* Albuquerque, 1995, part 1, pp. 523-527.
49. Warner, H.R., and Nichols, F.A. "A Statistical Fuel Swelling and Fission Gas Release Model." *Nuclear Applications and Technology*, 1970, v. 9, pp. 148-166.
50. Gontar, A.S., Kucherov, R.Ya., and Nelidov, M.V. "The Intragrain Pores Influence on UO_2 Swelling." *Atomic Energy*, 1985, v. 58, iss. 1 pp. 54-55.
51. Belle, I., and Lustman, B. In: "Dissertation 408 from Helsinqin Teknillinen Korkeakonln." Helsinki, University of Technology.
52. Gegusin, Ya.E., and Krivoglaz, M.A. *The Macroscopic Inclusions Motion in the Solids*. Moscow: Metallurgia, 1971, 343 p.
53. Gegusin, Ya.E. *Physics of Sintering*. Moscow: Nauka, 1967, 360 p.
54. Kotelnikov, R.B., Bashlykov, S.N., et al. *High Temperature Fuel*. Moscow: Atomizdat, 1978, 432 p.
55. Nikolaev, Yu.V., Gontar, A.S., Vedenyapin, G.A., et al. "Out-of-pile Simulation of Deformation Behaviour of a Thermionic Fuel Element under Thermocycling Conditions." *Proc. 29th Intersociety Energy Conversion Engineering Conf.* Monterey, 1994, v. 2, pp. 1027-1031.
56. Gontar, A.S., Nelidov, M.V., and Nikolaev, Yu.V. "Deformation Behavior of a Thermionic Fuel Element under Conditions of a Thermal Cycling with a Small Temperature Change." *Proc. 25th Intersociety Energy Conversion Engineering Conf.*, 1990, v. 2, pp. 290-293.
57. Steinar, A. "Mechanical Interaction Between Fuel and Cladding." *Nucl. Eng. and Design.* 1972, v. 21, No. 2, pp. 237-253.
58. Nakatsuka, M. "Theoretical and Experimental Analysis of Cladding Strain Produced by Expansion of Cracked Fuel Pellets." *Nucl. Eng. and Des.*, 1981, v. 65, No. 2, pp. 197-204.
59. Likhachov, Yu.I., and Pupko, V.Ya. *The Strength of Nuclear Reactors Fuel Elements*. Moscow: Atomizdat, 1975, 278 p.
60. Kornilov, Rozhkova, N.M., Sinyavsky, V.V., et al. "A Self-Consistent Determination of Heat Fluxes from Fuel Stack and of Emitter Temperature Field in Thermionic Electrogenerating Element with Gas Fission Products Exhaust System. Report theses. In: "Conference on Thermionic Method of Heat to Electric Power Conversion". Obninsk, 1979, pp. 27-30.
61. Nikolaev, Yu.V., Gontar, A.S., Sotnikov, V.N., et al. "Complex Computational Investigation of Single-Element TFE Time-Dependent Behaviour with Consideration for Mutual Influence of Lifetime Limiting Processes." *Proc. 30th Intersociety Energy Conversion Engineering Conf.* Orlando, 1995, v. 1, pp. 637-642.

CHAPTER 4

RESULTS OF CALCULATIONAL STUDY OF FUEL-ELEMENT BEHAVIOR DEPENDING ON ITS MATERIALS AND OPERATING PARAMETERS

4.1. Calculational Studies of Temperature Fields within the Fuel Element and Their Change in Time

As mentioned in Chapter 3, the calculation of temperature fields within fuel elements is closely linked to calculational problems of mass transfer in fuel elements, to their deformation behavior, and to solution of thermal/electric problems for the thermionic converter, which determine the distribution of temperature and heat fluxes within the emitter. So, the strictest solution of the heat problem can be achieved by jointly solving these problems. Use of such integrated programs is specifically convenient for investigating the change of the temperature field in time, since at each step of the calculation, the temperature field is recalculated. Such a solution for the single-cell TFE is provided by KATET [1] or by a program for mass transfer within the fuel element [2]. Figure 4.1 presents calculational results using KATET as applied to the single-cell TFE of a TOPAZ-2-type reactor, with an emitter fabricated from MN3 single-crystal alloy and stoichiometric uranium-dioxide fuel. The data contained in Figure 4.1 relate to a 400 W electric power fuel element. Coordinate x=0 corresponds to the TFE central cross-section.

Figure 4.1a shows that in the course of operation, the maximum emitter temperature (Curves 1 to 5) drops by ~50°C. This temperature reduction is connected with fuel re-distribution by mass transfer in the fuel-stack central channel and, as a consequence, with change in the linear power distribution along the TFE length (Figure 4.1b). The temperature distribution along the central channel length (Curves 6 to 10) changes even more. As shown in Figure 4.1a, the maximum fuel temperature drops by almost 100°C. This comparatively rapid temperature reduction is also caused by fuel redistribution in the course of its transfer in the central channel. Then, however, a rise in the maximum fuel temperature is observed. This rise is linked to the fuel swelling, leading to decrease of the central channel diameter (Figure 4.1d).

An important part of both KATET [1] and the program for calculating mass transfer in the fuel element [2] is a calculation block for the temperature fields within fuel elements. Variants of the calculation block are officially registered and used as individual programs; the temperature-field calculation programs, developed for particular fuel-element designs, are more efficient and call for much less computer time than well-known multi-purpose programs for estimating temperature fields. To analyze the temperature fields in multi-cell TFEs, the

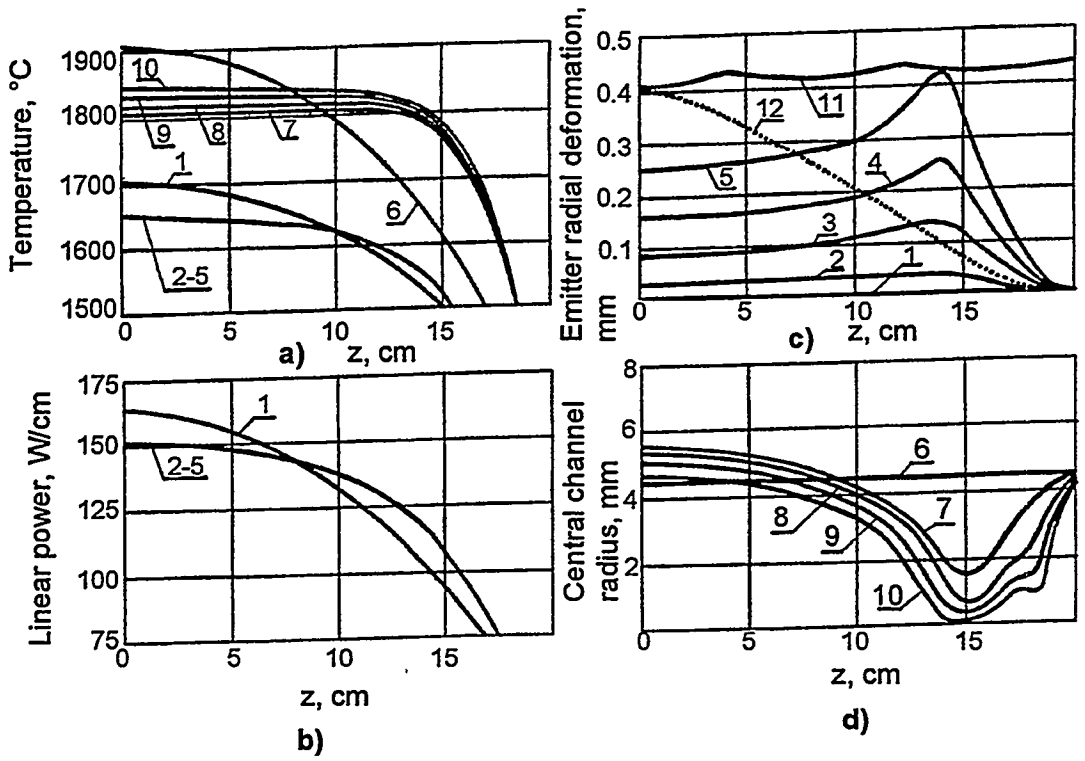

Figure 4.1. Results of calculational investigation of single-cell TFE behavior (p=400 W):

1, 6 - 0 hrs;
2, 7 - 10,000 hrs;
3, 8 - 30,000 hrs;
4, 9 - 50,000 hrs;
11 - ultimate deformation of emitter;
12 - 45,000 hrs, without considering mass transfer;
1-5 - cladding;
6-10 - surface of fuel stack central channel.

program MUTANT [3] is expedient, in the development of which the set of boundary conditions reviewed in Chapter 3 was used. Figure 4.2 presents temperature distributions along the central channel for a fuel element with geometric and operating parameters from the range of values characteristic of the multi-cell TFEs [3]. Solid curves present calculational results that do not consider longitudinal heat transfer due to radiation in the central channel. In calculating the curves represented by dotted lines, radiation-transferred heat in the central channel is taken into account.

As shown in Figure 4.2, at high temperature, the radiation heat-transfer contributes significantly to the temperature distribution, lowering its maximum level by nearly 150 K.

It follows from Figure 4.2 that, depending on contact behavior between pellets and cladding, the difference in the maximum fuel temperature may reach 300 to 400 degrees. Curves 1 and 2, calculated for the case with a gap between fuel and cladding, represent a maximum temperature, which may be realized at the start of operations, if, because of too-small radius of the pellets or their shrinkage, the fuel, in reaching operating conditions, does not contact the cladding. Curves 3 and 4 show the temperature distribution along the central channel length for a case in which there is interface contact thermal resistance between fuel pellets and cladding, i.e., if the outer pellet diameter is correctly chosen and in the course of getting to the operation run, a gap between the fuel and cladding disappears due to mismatching thermal expansion coefficients.

Curves 5 and 6 represent the temperature distribution along the central channel for the case of ideal fuel/cladding contact. These distributions are ultimate steady-state temperature distributions, which can be realized without any significant temperature change when the fuel disconnects with cladding. The time of transition from one contact condition to another is considered in studies of mass transfer leading to a change in contact behavior.

4.1.1. Influence of Spacer Collars, Fuel Enrichment, and Fuel-Element Free Volume on Temperature Fields

Even though spacers are fabricated from oxide ceramics having at high temperature a low thermal conductivity (for Al_2O_3, at 1500 K, $\lambda \approx 5$ W/m·K [4]), nevertheless it is far higher than the thermal conductivity of cesium vapor, which is $\sim 10^{-2}$ W/m·K at 1500 K. Thus the spacer collars can cause appreciable heat leakage over themselves and exert considerable effect on the temperature fields in the fuel element. The question of the spacer collars' influence on voltage-current characteristics and temperature fields was reviewed by Rozhkova and Sinyavsky [5], who showed that local lowering of the emitter temperature near the spacer collars may encompass hundreds of degrees. Profound temperature drops occur only in the immediate vicinity of spacer collars. Far from the collars, the

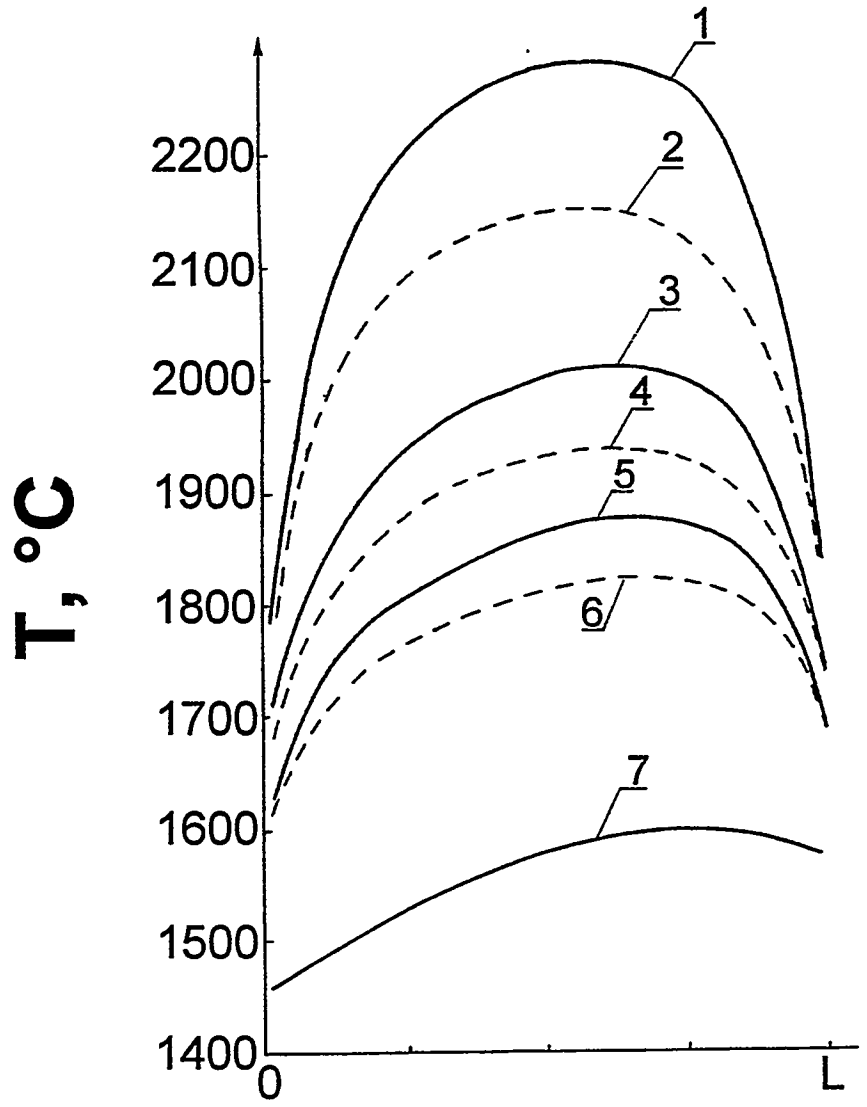

Figure 4.2. Temperature distribution along central channel length:
——not considering radiation;
- - - considering radiation;
1, 2 - fuel/cladding gap;
3, 4 - thermic resistance between fuel and cladding;
7 - cladding temperature.
5, 6 - ideal fuel/cladding contact

temperature reduction is small; if spacing between the collars is over six centimeters, the spacers' influence no longer extends to the entire emitter length, for the fuel elements considered [5].

RI SIA "Lutch" used different approaches to single and multi-cell TFEs in considering spacer influence on fuel-element temperature fields. In the multi-cell TFE, because of the cooling effect of the end caps, free volumes at fuel-element ends fill with fuel. Therefore, additional cooling caused by a spacer collar located at the end of the fuel element cannot lead to a qualitative change in fuel arrangement within the fuel element, but only results in some deformation of the central isothermal cavity. In addition, the spacer's location near the end cap, where cladding deformation is insignificant, means that the pressure exerted by the spacers against the electrodes and, subsequently, the cooling level, changes only slightly during its lifetime. Under these circumstances, spacer influence on the temperature fields in multi-cell fuel elements was taken into account only through boundary conditions on the fuel-element cladding; the temperature distribution throughout the cladding was assumed constant in time.

The situation is different in principle for the single-cell TFE, in which several spacer collars are placed on the emitter length. Some of the collars are located in a zone where, neglecting the spacers' cooling effect in the central channel, fuel evaporation occurs. The presence of spacer collars, in this case, causes the appearance of local condensation zones at the spacer sites and considerable fuel redistribution along the fuel-element length. Gontar and co-workers [6, 2] calculated changes in the central channel diameter, using a subprogram that considers localized heat spreading over the spacers. The temperature distribution along the central channel obtained in this estimate is shown in Figure 4.3. Curve 1 is for a case when the spacers do not contact the emitter. Curve 2 is for the event that one third of the spacers contact the emitter. Curve 3 assumes all the spacers contact emitter. As shown in Figure 4.3, a maximum temperature reduction, about 200 degrees, is reached near spacers when all spacers contact the emitter. Curves 1 to 3 are calculated for the initial instant, i.e., for the as-assembled configuration of the fuel stack. As a result of fuel evaporation in a zone of maximum temperature and its condensation in a zone of lower temperature, the central channel configuration changes, and some equalizing of the fuel-temperature profile occurs along the central channel. The dotted Curve 4 in Figure 4.3 represents the Curve-3 position at $3 \cdot 10^4$ hours.

A question about the effect of neutron spectrum and fuel enrichment on temperature fields is raised by the fact that the neutron spectrum in reactors, where TFE experiments are conducted, differs essentially from the neutron spectrum in the TRC [7]. In a TRC with a hydrogen-containing moderator, highly enriched uranium dioxide (~90%), and structural materials intensely capturing the thermal neutrons (Mo, W, Nb), the neutron spectrum lies mostly in an intermediate zone. But the experiments on the TFE are routinely performed in loop channels of

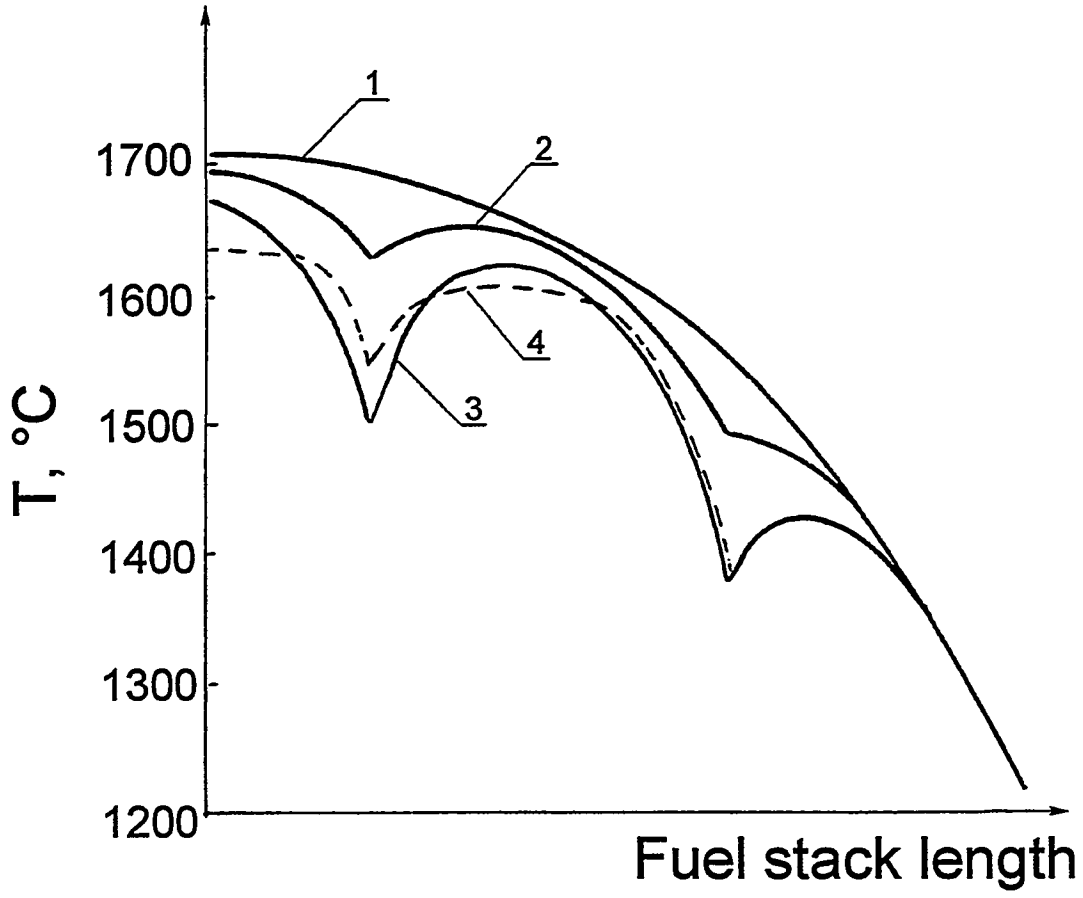

Figure 4.3. Temperature distribution along central channel length for different numbers of spacers in contact with emitter:

1 - spacers not contacting emitter, 0 hr;
2 - one third of spacers contacting emitter, 0 hr;
3 - all spacers contacting emitter, 0 hr;
4 - all spacers contacting emitter, 30,000 hrs.

research reactors having a thermal spectrum of neutrons that can reduce the temperature in the stack center, and some incorrect inferences about fuel-element serviceability become possible. To improve simulation of the power distribution vs. the fuel-element radius and temperature fields within the fuel stack, Gontar et al. [7] reviewed the possibility of simulating, in a thermal research reactor, the radial profile of heat release in the TRC fuel element by altering the fuel enrichment in the U^{235} isotope.

The power distribution vs. fuel-element radius for the thermal spectrum of a research reactor, at several levels of fuel enrichment, is given in Figure 4.4. The dotted curve shows the heat release distribution in the TRC. For 90% enrichment, all the heat in the research reactor is released in a thin surface layer of fuel. Gontar et al. [7] concluded that, for simulation of TRC temperature conditions in a research reactor, uranium dioxide enrichment should be reduced to 20 to 50%.

The TRC fuel-element free volume is determined mainly by the central-channel radius, r_0. For the thermal reactor, power release is localized in the outer layer of fuel, and change in the central-channel radius does not greatly influence the temperature distribution in the fuel element. The free volume impacts maximally on the temperature when power release is constant vs. the fuel-element radius. The temperature distribution in cylindrical fuel pellets, in the one-dimensional case and at constant thermal conductivity, is provided in all the classical guides on heat conduction (e.g., [8]). The temperature drop on a fuel layer, in this case, is

$$T(r_o) - T(R) = \frac{1}{4}\frac{q_v}{\lambda}\left(R^2 - r_o^2\right) + \frac{1}{2}\frac{q_v}{\lambda} r_o^2 \ln\frac{r_o}{R} \quad . \tag{4.1}$$

Figure 4.5 presents the dependence of temperature drop on central-channel radius plotted using Equation 4.1. This dependence is plotted at constant heat power in the pertinent section of the fuel element. Increase of the free volume up to 25% ($r_0/R=0.5$) reduced the temperature drop by almost a factor of 2 as compared to a solid fuel stack. Estimates made for the TRC with the radial heat release distribution (Figure 4.4) reveal that, in this event, the situation is close to that represented in Figure 4.5. Although nearly half the power output is linked to the thermal part of spectrum, the temperature drop on fuel is mainly due to the constant radial heat release constituent.

Nikolaev et al. [9] calculated values of maximum fuel temperature in the single-cell TFE with 300 W power for various free volumes in the fuel element. The results are for a reactor with effective core height of 50 cm and length of 40 cm. Data are given in Table 4.1 for the case when the coefficient of heat release non-uniformity on the reactor radius equals 1 and 1.15.

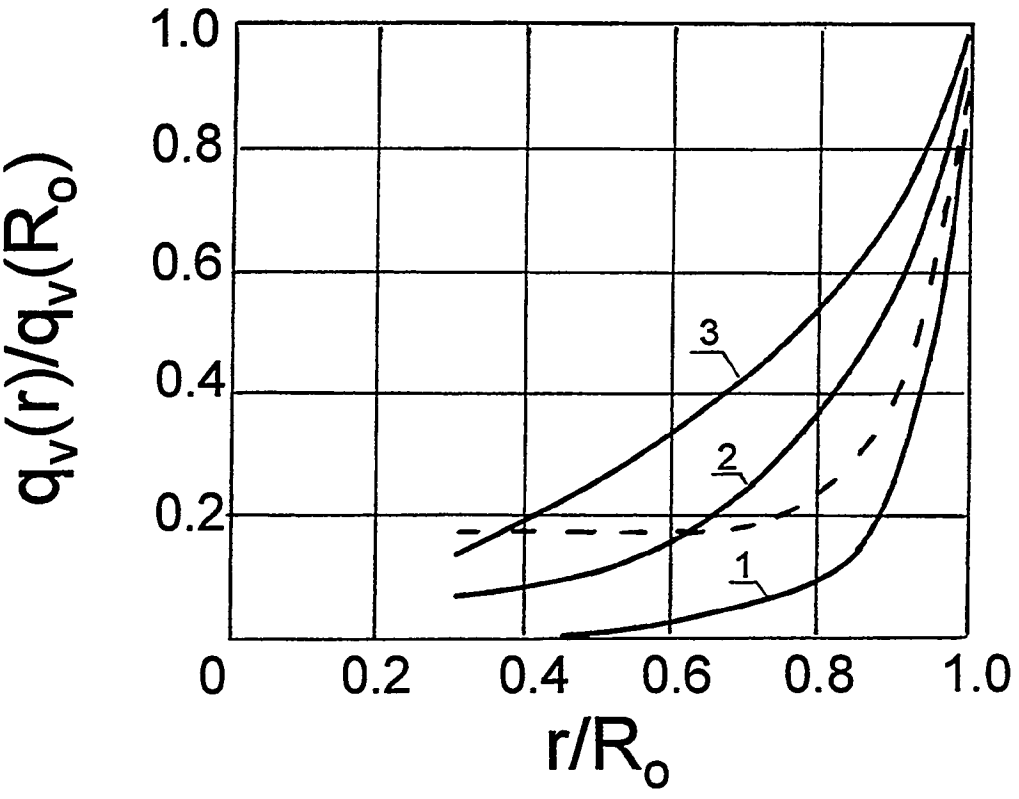

Figure 4.4. Power distribution vs. fuel stack radius [7].
—— thermal spectrum of research reactor, enrichment on U^{235};
1 - 90%;
2 - 50%;
3 - 20%.
- - - intermediate spectrum of TRC, enrichment on U^{235} - 90%.

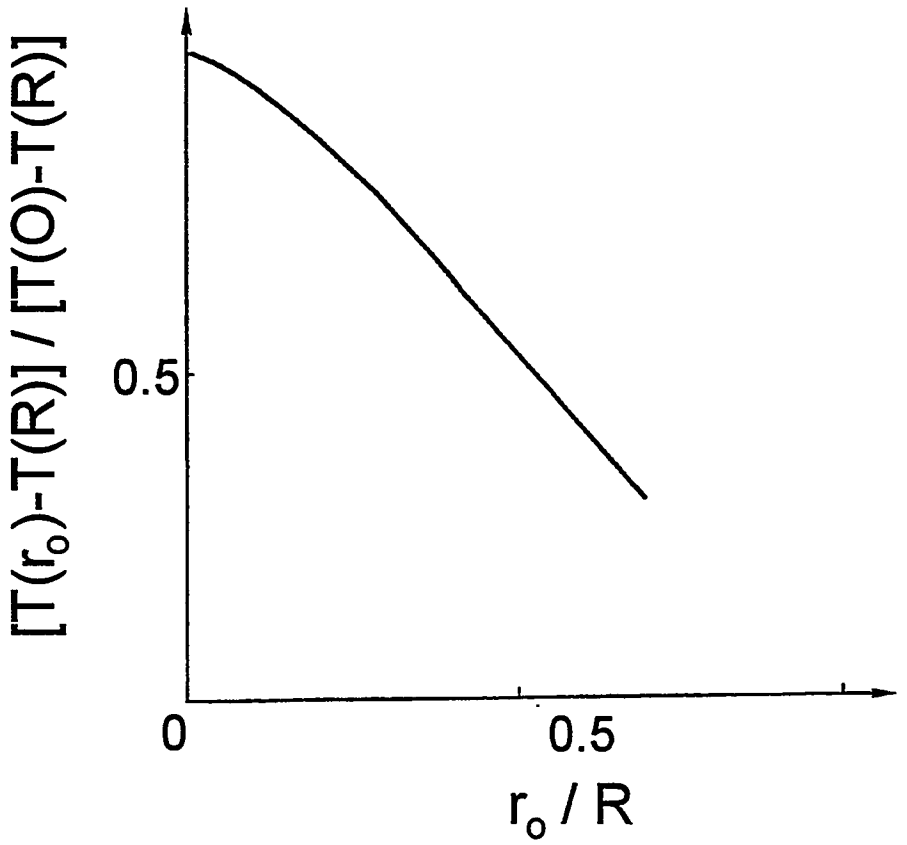

Figure 4.5. Dependence of temperature drop on central-channel radius.

Table 4.1 Maximum temperatures of fuel stack [9]

V_{free}, %	T_f^{max}, K	
	K_r=1	K_r=1.15
20	2110	2220
30	2070	2175
40	2040	2140

4.2. Results of Calculational Study of Fuel Mass Transfer in Fuel Elements

4.2.1. Steady-State Arrangement of Fuel within Fuel Elements and Mass Transfer for Period of Transition to Steady-State Conditions

As a result of the mass transfer processes, the as-fabricated form of the fuel stack is permanently transformed and, with a lapse of some time, a steady-state form can be achieved, characterized by the presence of an isothermal cavity within the fuel element. The arrangement and configuration of the isothermal cavity are estimated using PIKVIC, described in Chapter 3. The program allows the calculation of cavity disposition for a design with a free central channel and a variant with a gas-exhaust device. Calculations [7] have shown that fuel enrichment exerts the greatest effect on the cavity arrangement and configuration. Figure 4.6 shows a calculated [5] configuration of the isothermal cavity for a TRC intermediate spectrum and a research reactor thermal spectrum at different fuel enrichments, for which radial heat release distributions are presented in Figure 4.4. Considerable cavity displacement and change in its configuration take place. This effect is connected with the fact that, in the thermal spectrum, a slight energy release in the inner fuel layers does not offset the axial heat spreading over the structural parts. The gas-exhaust device, operable in the TFE, will be blocked by uranium dioxide condensate in testing the same TFE with unchanged fuel composition in a research reactor. It is obvious from Figure 4.6, for the research reactor-based simulation of TFE conditions, that uranium dioxide enrichment reduction to 20 to 50% is required. PIKVIK gives the steady-state fuel disposition in the fuel element, but it does not illustrate the change in stack geometry in time nor estimate the time required to achieve the steady state. To estimate the time to reach steady-state, it is necessary to apply a program describing the modification of fuel-stack geometry in time [1, 2]. Calculations with the aid of such programs reveal that, for the single-cell TFE, the steady-state fuel arrangement is not reached even during long-term operation (for several years). In this event, the free

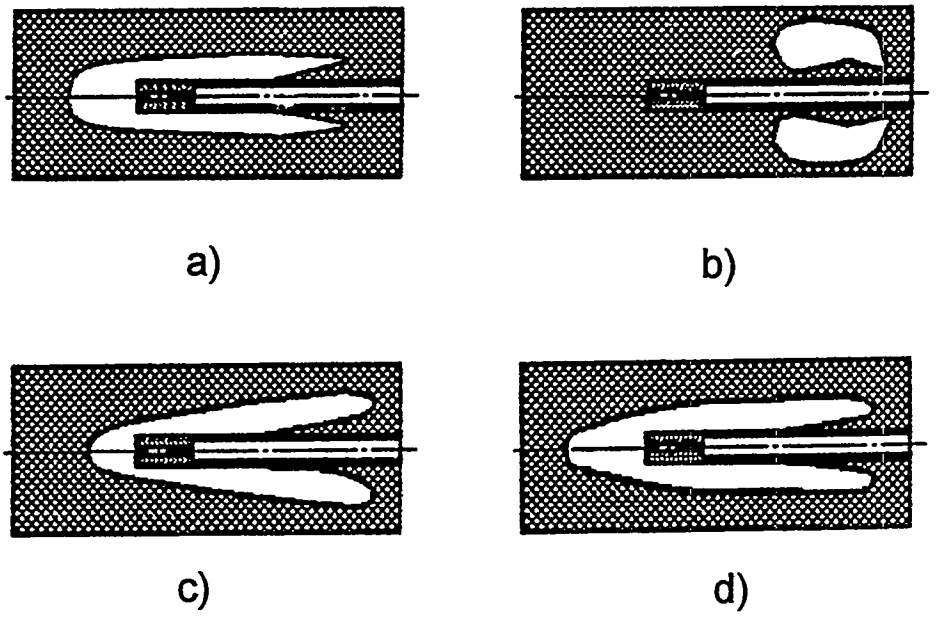

Figure 4.6. Isothermal cavity arrangement in the fuel stack:
a - intermediate spectrum of TRC, enrichment on U^{235}-90%;
b, c, d - thermal spectrum of research reactor, enrichment on U^{235}:
b - 90%;
c - 50%;
d - 20%.

central channel may be used for GFP removal from the fuel element [6]. In the multi-cell TFE center-sited modules, a contrary situation is realized. The steady-state fuel stack configuration is reached for times short in comparison to lifetime; therefore in studying the life behavior there is no necessity to consider details of the transition to the steady-state conditions. For the outermost modules of a multi-cell TFE, the time to reach the steady-state configuration may be comparable to lifetime, so, in this case, like in the case of the single-cell TFE, programs describing the change in fuel-stack condition in time must be applied.

4.2.2. Fuel Loss Beyond the Fuel Element

The problem of fuel lost beyond the fuel element arises most acutely in the multi-cell TFE, where the fuel temperature is high even at the fuel-element ends. As a result, intense fuel evaporation and its transfer in the gaseous phase over the gas-exhaust channels takes place. To restrict fuel loss in this case, a gas-exhaust device with a capillary channel at the inlet [10] is used. Gontar et al. [6] calculated values of maximum permissible diameter of the capillary for various temperatures to guarantee its three-year life.

The initial instant of fuel-element operation, when the fuel is not in contact with cladding, is characterized by a heightened level of temperature and, consequently, enhanced intensity of mass transfer in the fuel element. Gontar et al. [7] calculated the contribution of the transient period to uranium-dioxide vapor transfer over the gas-exhaust device (GED). In solving this problem the following assumptions were used:

- the radial gap between fuel condensed onto cladding and non-condensed fuel remains when the condensation front passes from cladding to the radial channel in the fuel stack;
- the radial gap because of its small size is deemed flat;
- heat is considered to be transferred through the gap only by radiation.

Through integration of mass flux passing through the gap, a current radial gap position was found. For a given gap position, using a solution of the one-dimensional quasi-steady-state equation of heat conduction, a current temperature distribution was defined and, based on it, an extra fuel-mass loss through the capillary of the gas-exhaust device. The ratio of this mass to the mass-loss rate, determined after condensation, comprises a fuel element operation time τ, for which the same fuel mass is lost under steady-state conditions. In the calculation, the fuel element cladding temperature T_{Cl} and the value of mean power release in the most thermostressed section of the fuel element, q_V, were parametrically varied. The lifetime was taken to be $3 \cdot 10^4$ hours. The calculational results [7] are presented in Figure 4.7, which shows that the radial condensation period

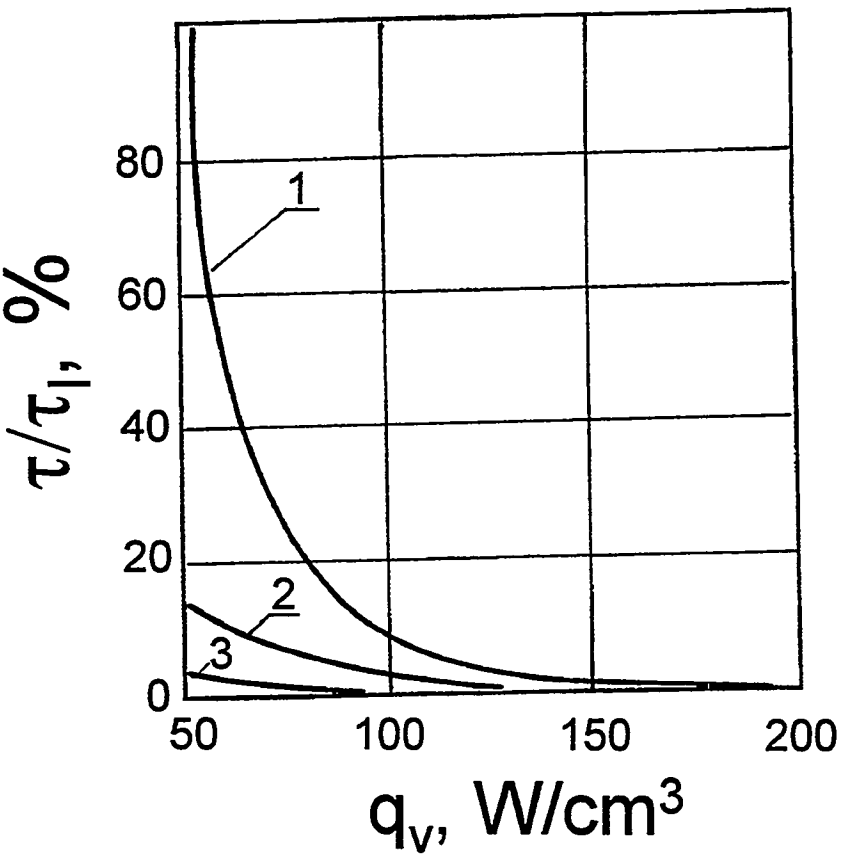

Figure 4.7. Additional contribution to UO_2 vapor loss via the GED for the radial condensation period:

1 - T_{Cl}=1400°C;
2 - T_{Cl}=1500°C;
3 - T_{Cl}=1600°C.

appreciably affects uranium-dioxide loss only at the lower boundary of TFE parameters.

Calculational results are shown in Figure 4.8. The calculation was performed for varying oxygen coefficients. Only stoichiometric and hyperstoichiometric fuel compositions were considered, since it is seen from Figure 3.2 that for hypostoichiometric fuel the overall pressure of uranium-containing components is close to that of stoichiometric fuel. For hyperstoichiometric uranium-dioxide compositions, the vapor pressure grows as the oxygen coefficient increases (Figure 4.8), which brings about considerably stricter requirements for the capillary-channel diameter with an increase in fuel-composition deviation from stoichiometry.

Table 4.2 specifies the maximum permissible diameters of the capillary channel, estimated for single-cell TFEs with 10-year life, vs. a number of free-volume values within the fuel element at equalized and non-equalized power vs. the reactor radius [9]. The effective core height was taken to be 50 cm. The maximum fuel temperatures realized under these conditions are presented in Table 4.1.

As shown in Table 4.2, the minimum capillary diameter, required under the most rigid operating conditions, is 0.15 mm, which can be attained using up-to-date methods of tungsten fabrication.

Figure 4.8 shows that, at a 2200°C, the capillary channel diameter must not exceed 10^{-2} cm for any fuel composition. However, use of the same diameter capillary at lower temperature proves to be inexpedient, since decreasing the capillary diameter impairs the gas-removal system's reliability. GED workability with a condensate layer on its endpiece has been examined [2]. From Equation 3.30, given a thick layer of condensate, the time of through-channel formation in the condensate layer is inversely proportional to the cubed radius of the capillary channel; with small capillary-channel radius and low temperatures, even a relatively thin layer of condensate on the surface of the GED can disable it for a long period. Figure 4.9 shows the calculated [2] dependence of the thickness of the condensate layer on the tip surface, through which a hole is formed for 10^3 hrs, on tip temperature, for a 0.5-cm length, 10^{-2}-cm diameter capillary channel. At the central-cavity operating temperature of 2000 to 2200°C, a fuel layer up to 0.1 cm thick on the capillary tip does not lead to prolonged failure of the gas-exhaust system.

4.2.3. Calculational Investigation of the Possible Use of Free Central Channel for Fuel-Element Ventilation

In the single-cell TFEs, the time of formation of a closed isothermal cavity at moderate operating parameters may be longer than the operating time. In this event, the free central channel can be used for ventilating the fuel element, which

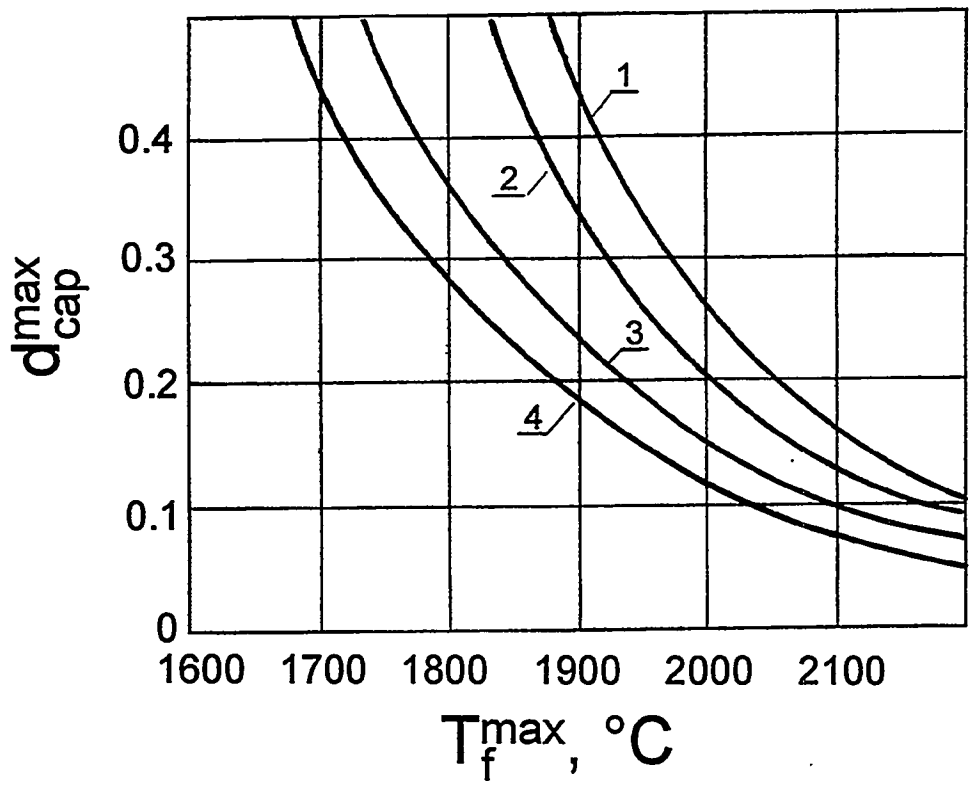

Figure 4.8. Maximum capillary diameter (d_{cap}^{max}) to maintain passage capacity of the GED pipe for 3-year life vs. UO_{2+x} maximum temperature (T_f^{max}):

1 - x=0;
2 - x=0.001;
3 - x=0.005;
4 - x=0.01.

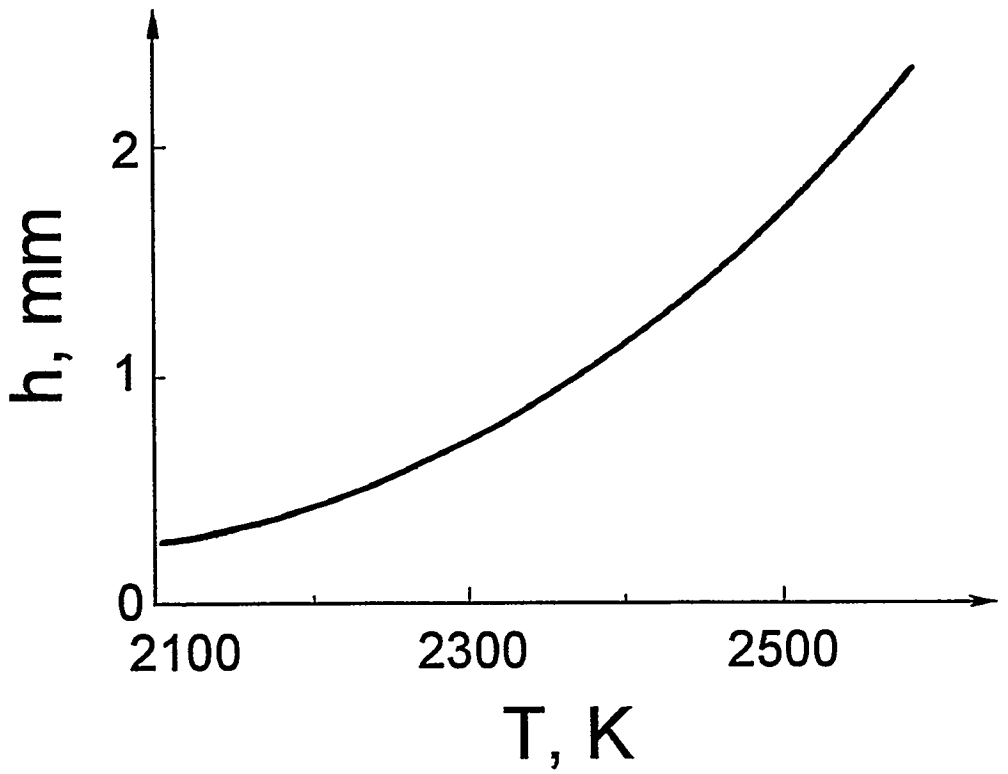

Figure 4.9. Thickness of condensate layer, through which a hole is formed for 1,000 hours.

Table 4.2. Tolerable maximum diameters of capillary in gas-exhaust device [9]

V_{free}, %	d, mm	
	k_r=1	k_r=1.15
20	0.26	0.15
30	0.35	0.20
40	0.40	0.23

simplifies the fuel-element design and improves its reliability. The operability of the free central channel depends on operating conditions and fuel composition [2, 6]. Figure 4.10 presents the calculated configuration of the central channel at 10^4 hours for three initial fuel compositions at the maximum initial fuel temperature of ~2100 K. The initial fuel composition considerably affects the free central channel operability. With an increase in the fuel oxygen coefficient, the time for central closed cavity formation is appreciably shortened. Thus, it is expedient to use a hypostoichiometric fuel in the fuel element with a free central channel. At the same time, at a maximum temperature on the central channel surface in excess of 2100 K and for a lifetime longer than 10^4 hrs, a gas-exhaust device must be used for gaseous-fission-product removal, restricting the fuel transfer also in the single-cell TFE. A calculational study [6] determined the upper limit of applicability for the fuel stack central channel of a 3-year-life single-cell TFE (Figure 4.11). The maximum cladding temperature (T_{Cl}^{max}) is plotted on the Y-axis, and mean density of power release in the stack central section on the X-axis. In the calculation, the volume of the fuel stack central channel occupies ~7% of the fuel-element inner cavity, and uranium-dioxide composition is assumed to be stoichiometric. The procedure was checked by comparing the calculational results to data from experiments on single-cell TFEs, tested in a thermionic reactor convertor for 1.5 years [2]. The results of this comparison for a TFE with a 1550°C maximum temperature of the fuel-element cladding [2] are shown in Figure 4.12. Here, in estimating the temperature, the cooling effect of the spacer collars is taken into account. As seen from Figure 4.12, the calculated results are in good consistency with the experimental data, both in their absolute values and in the occurrence of narrowing of the central channel section at the spacer-collar sites.

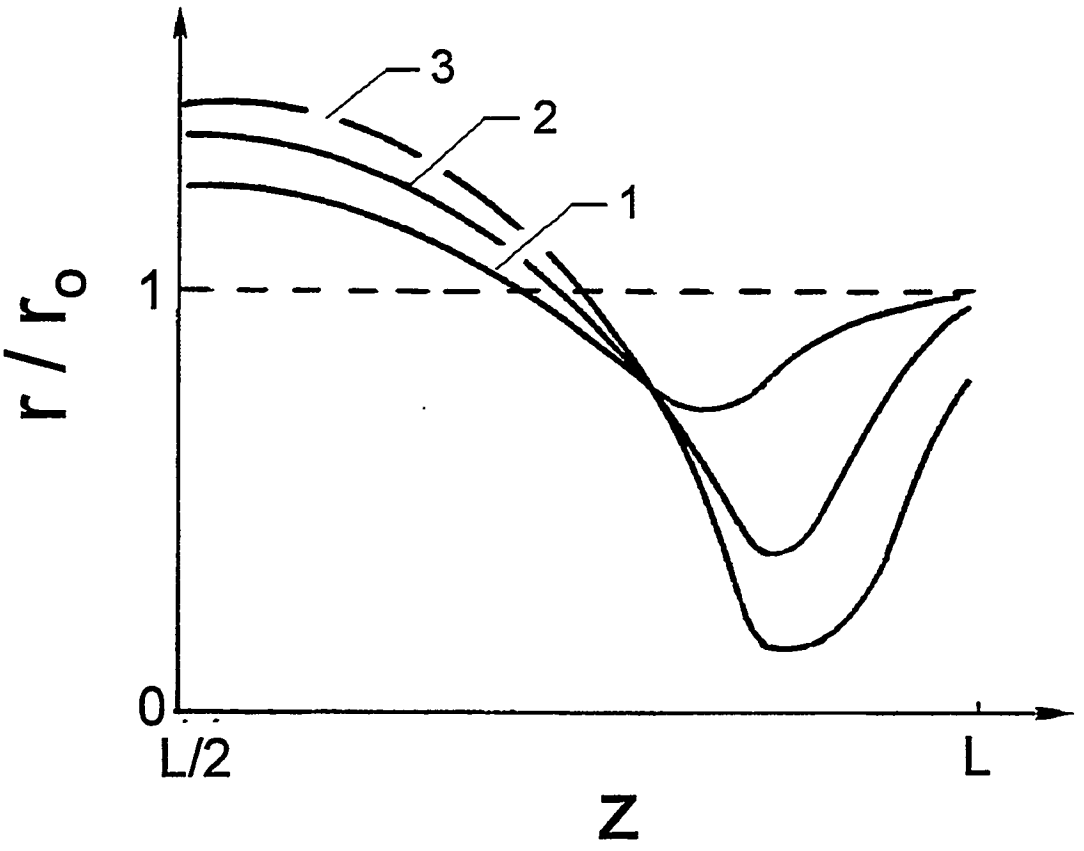

Figure 4.10. Central channel profile at 10^4 hours [2, 6]:
1 - $x_o = 0$;
2 - $x_o = 10^{-3}$;
3 - $x_o = 5 \cdot 10^{-3}$.

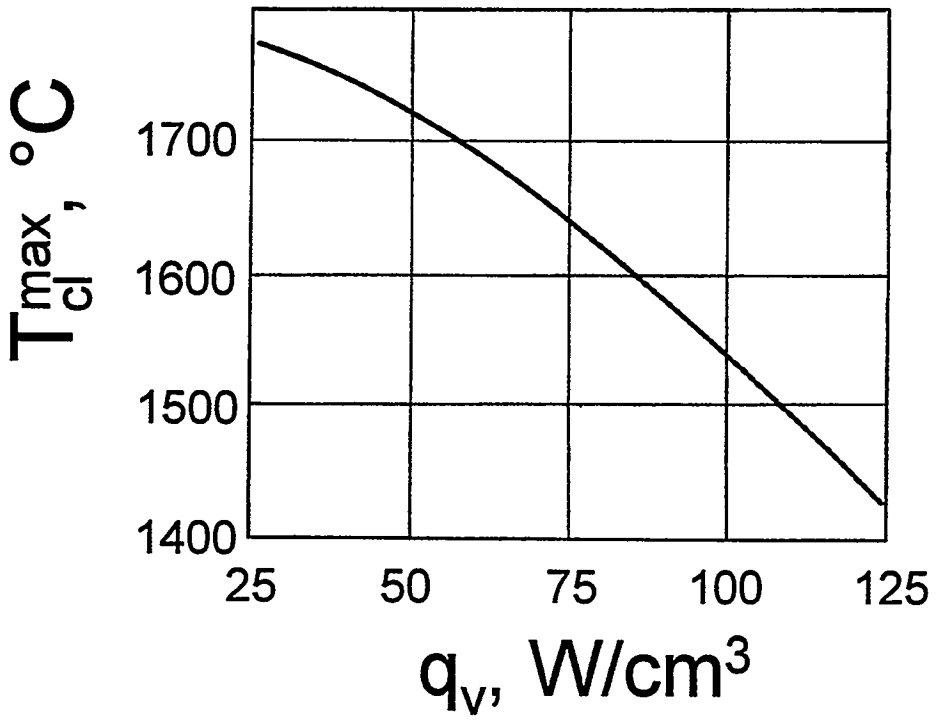

Figure 4.11. Upper boundary of applicability area for fuel-stack central channel.

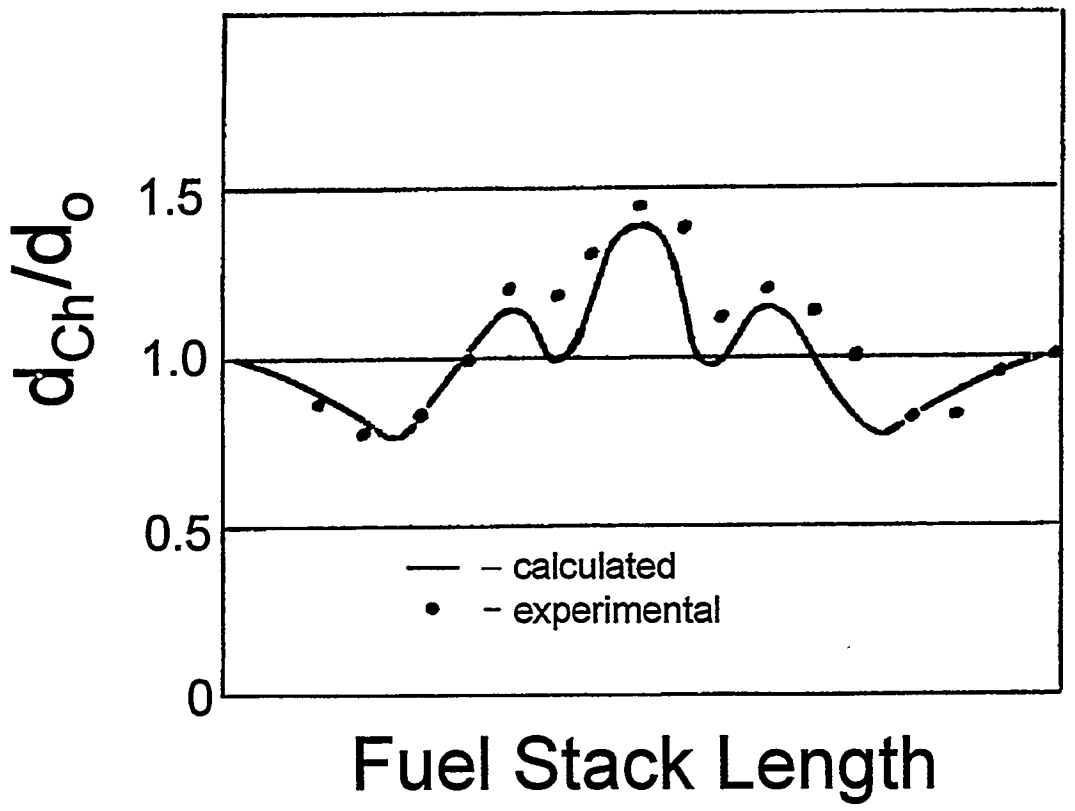

Figure 4.12. Change in central-channel diameter (d_{Ch}) in relation to its initial value (d_o) along $UO_{2.003}$ fuel-stack length.

4.2.4. Impact on Mass Transfer of Cesium in the Fuel Element Central Cavity

In the fuel-element design with communicating fuel element and IEG, the cavity is filled with cesium vapor under ~2 torr pressure. As shown in Figure 3.1, uranium-dioxide vapor-flow conditions convert here from the free-molecular to diffusion type, which may considerably inhibit mass transfer. The description of gas flow in Chapter 3, using the effective diffusion coefficient, allows a simple assessment of the reduction in mass transfer intensity when filling the inner fuel-element cavity with cesium. The reduction in mass transfer intensity equals the ratio of the effective diffusion coefficient in the free-molecular flow to the diffusion coefficient in cesium vapor.

The effective diffusion coefficient in molecular flow is determined by Equation 3.20, and, for diffusion in cesium vapor, is close to the uranium-dioxide diffusion coefficient in cesium, governed by Equation 3.22. For a 0.4-cm radius channel at 2000 K the ratio of the effective diffusion coefficients is $D_{Kn}/D_{12}=35$.

Thus filling the fuel-element inner cavity slows mass transfer in the central channel. To strictly consider mass transfer in the central channel in cesium vapor it is necessary to numerically solve the diffusion equation for uranium dioxide in the central channel [2].

4.3. Results of Calculational Study of Fuel Swelling and Emitter Deformation. Fuel Element Deformation Behavior under Thermocycling

The results of calculational study of emitter deformation should be analyzed with reference to the deformation mechanisms considered above.

4.3.1. Emitter Deformation Induced by GFP Buildup in the Fuel-Element Inner Cavity

Calculational results relating to emitter deformation caused by GFP buildup [2, 11] were obtained for a ~20-mm fuel-element diameter, ~1-mm emitter thickness, and ~20% free volume in the fuel element.

Figure 4.13 displays the time dependence of tungsten emitter deformation at various power densities in the fuel. At a tolerable level of emitter deformation, ~2% for low-power TFEs (q_V=50 W/cm^3), the time until short circuit is about 1 year. With a rise of the power density up to q_V=300 W/cm^3, this time is shortened to $\tau \approx 2 \cdot 10^3$ hrs. Adopting high-temperature strong tungsten alloys for the emitter material does not solve the problem of ensuring long life for UO_2-based gas-tight fuel elements [11]. In this case, at the same emitter temperature, T_{em}=1900 K for q_V=100 W/cm^3, the lifetime is limited to ~1.5 years.

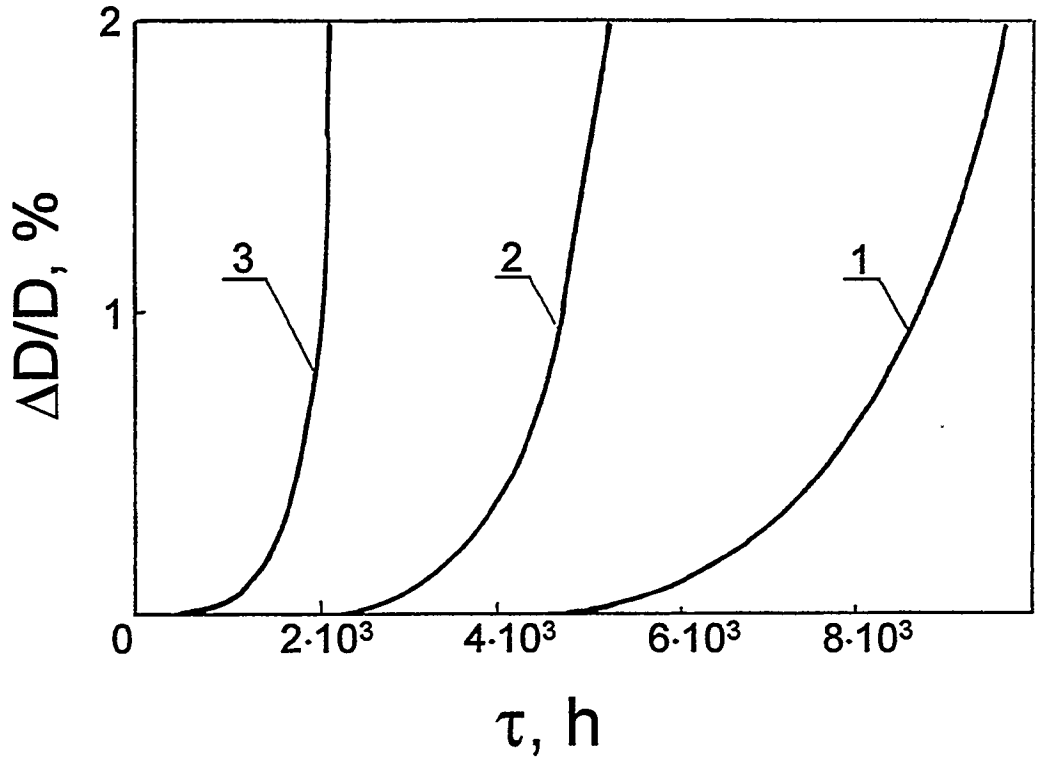

Figure 4.13. Time dependence of tungsten emitter deformation with no GFP removal from the fuel-element cavity (T_{em}=1900 K, T_{GFP} =2100 K) [2]:

1 - q_V=50 W/cm^3;
2 - q_V=100 W/cm^3;
3 - q_V=300 W/cm^3.

Thus the calculational results show that an emitter-unit design with GFP removal is necessary to achieve favorable life/power parameters of the TFE.

4.3.2. UO_2 Swelling and Induced Emitter Deformation

UO_2 Swelling. Analyses [12, 13] have revealed that discrepancies in the literature on the question of the influence of operating parameters on swelling is connected with the use and identification of diverse quantitative characteristics for this process. The common term "swelling" encompasses both UO_2 density changes and changes in the outer dimensions of fuel.

BARS [12, 13] simultaneously considers both these characteristics, allowing a better understanding of UO_2 swelling and eliminating the above-mentioned disagreement of the literature data. This approach also permits complete characterization of UO_2 irradiation behavior.

UO_2 irradiation parameters depending on burnup at two temperature levels are presented in Figure 4.14. At relatively low irradiation temperature ($T \leq 1600$ K), both UO_2 porosity generated under irradiation and UO_2 swelling grow with irradiation dose accumulation. Under these conditions (because of the absence of appreciable bubble migration) these parameters essentially coincide with each other. With temperature elevation, their behavior begins to differ: at 1900 K, swelling increases almost linearly with burnup; simultaneously, the porosity reaches a steady-state level that is linked to bubble migration from the fuel.

Figure 4.14 indicates that the burnup rate has little influence on the swelling level, i.e., the latter is governed by the extent of burnup only. At the same time, when bubbles migrate from the fuel ($T \geq 1900$ K), the burnup rate strongly influences the steady-state porosity in UO_2.

It may be inferred in interpreting this result that the in-pile UO_2 tests accelerated with respect to power output at these temperatures can be appropriately conducted only to find a value and rate of UO_2 free swelling, using, e.g., fuel samples encapsulated in thin claddings having low resistance to creep. Accelerated tests of fuel samples with full-scale claddings to determine the deformation behavior of the latter will be non-representative under these conditions, because increasing the power output density increases the steady-state porosity in UO_2 and leads to a change in UO_2 creep rate and, subsequently, in the state of the whole model fuel element under stress.

The temperature dependence of UO_2 irradiation characteristics is shown in Figure 4.15. UO_2 swelling grows monotonically with temperature. At the same time, for temperature dependence of porosity there is a characteristic maximum, as noted in the literature. It follows from the calculational results that the data inconsistency observed in the literature with respect to burnup and temperature dependencies of the swelling value and behavior is explained by differences in the characteristics examined. The effects of changes in density and outer fuel

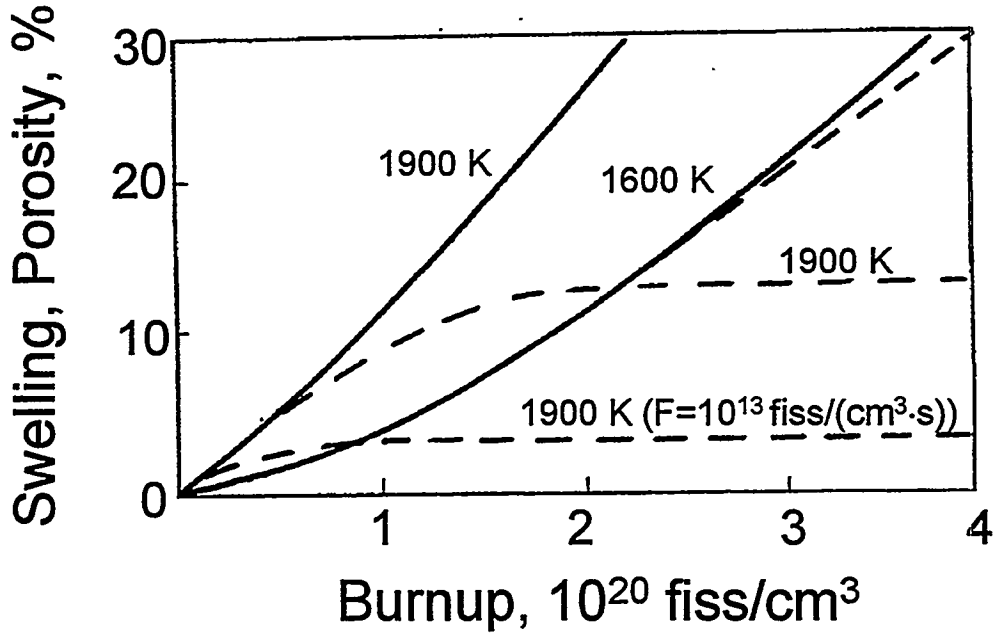

Figure 4.14. Burnup function of swelling and irradiation-induced porosity grad $T=10^3$ K/cm; except as indicated, burnup rate $F=10^{14}$ fiss/(cm^3·s) [13]:

—— swelling;

- - - - porosity.

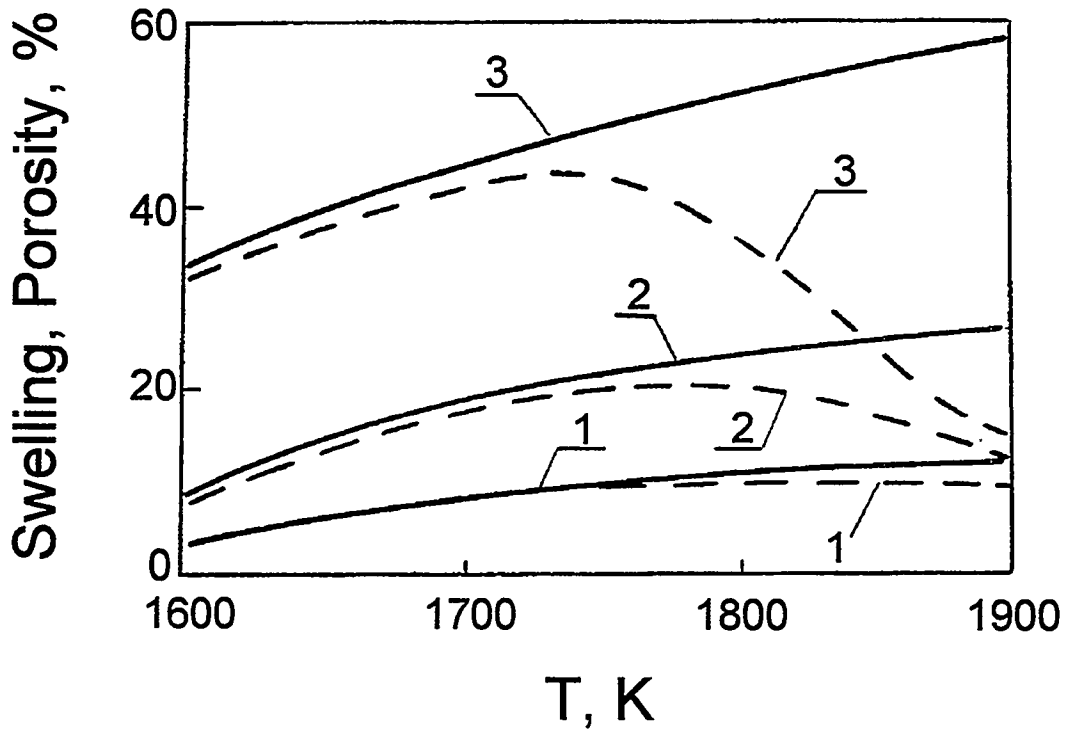

Figure 4.15. Temperature dependence of UO_2 irradiation characteristics (grad $T=10^3$ K/cm; $F=10^{14}$ fiss/(cm^3·s)) [13]:

—— swelling;

- - - - - porosity;

1, 2, 3 - respectively, burnup of $1\cdot10^{20}$, $2\cdot10^{20}$ and $4\cdot10^{20}$ fiss/cm^3.

dimensions, used to define the swelling, are separate at high temperatures. This is connected with bubble migration from UO_2.

BARS produces results useful in planning an experiment and in optimizing operating conditions and fuel structure to minimize the emitter swelling and deformation.

Uranium Dioxide Non-Irradiation Swelling. As noted in Chapter 3, under in-pile conditions, along with the irradiation swelling induced by GFP generation, an additional swelling mechanism is possible, connected with the presence in UO_2 of intragranular fabrication-induced pores. Calculational assessments of this mechanism have been considered by Gontar and co-workers [2, 14].

Times required for pore migration to UO_2 grain boundaries are given in Figure 4.16. The results are obtained for 1800 and 1900 K under varying temperature gradients in the fuel. The grain size was taken to be 6 μm. The dependence of critical pore diameter d^{cr}, at which the pore detaches from the grain boundary, is also presented. Under temperature conditions realized not only in TRC but also in a number of other type reactors, the intragrain pores migrate to grain boundaries as early as the initial period of operation irradiation. The critical pore size, required for their escape from the grain boundaries, may surpass by several times the initial intragranular pore size. The calculational results thus indicate that in-pile conditions provide the necessary prerequisites for the manifestation of non-irradiation swelling.

The value of porosity being generated within uranium dioxide (ε_f) vs. its as-fabricated level (ε_{in}) is represented in Figure 4.17. These results are obtained under the assumption that all the initial pores are intragranular. The effect is enhanced with the growth of as-fabricated porosity and reduction of pore diameter. At ε_{in}=5% and d=0.5 μm, the fuel density change (i.e., swelling) reaches $\Delta\varepsilon=\varepsilon_f-\varepsilon_{in}\approx$7 to 8%.

The results of the calculational analysis correlate with in-pile investigation results [15]. There is an experimentally established adverse effect of porosity formed by isolated small intragrain pores on the high-density UO_2 fuel stack's spatial stability. An increase of UO_2-pellet porosity up to 5% brought about some acceleration of their swelling rate under in-pile conditions. This effect has been explained by fuel-strength reduction without any quantitative substantiation [15].

Emitter Deformation. A considerable number of calculational efforts aimed at emitter deformation have been performed (see, e.g., [1, 2, 9, 11]). The influence on the emitter's dimensional stability of several factors—emitter thickness and material, free volume in fuel element, and TFE operation conditions—have been analyzed.

Results of calculational investigations of the TOPAZ-2 single-cell TFE, operating at T_{em}=1550°C and q_V=45 W/cm^3, are provided in Figure 4.18 [16, 17].

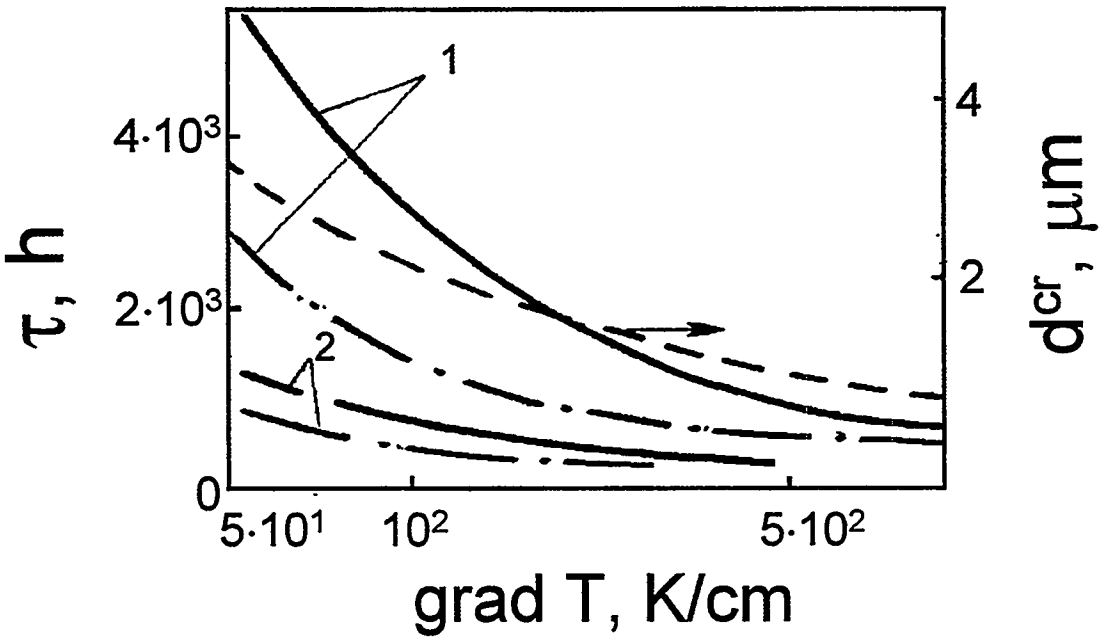

Figure 4.16. Time required for 1-μm-diameter pore (——) and 0.5-μm-diameter pore (-·-) migration by distance equal to grain size and critical pore diameter (- - -) vs. temperature gradient [2]:

1 - T=1800 K;

2 - T=1900 K.

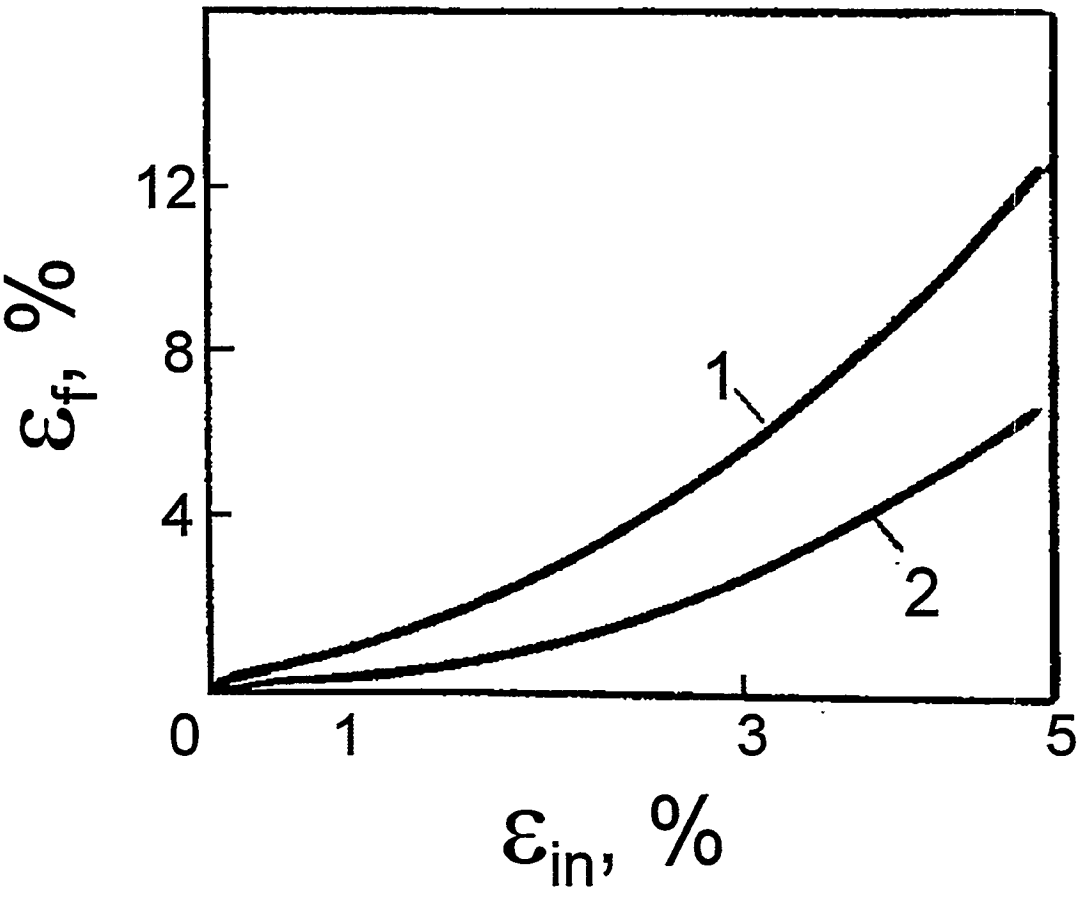

Figure 4.17. Initial intragrain porosity influence on grain boundary porosity generated after migration of all intragrain pores to grain boundary [2]:

1 - d=0.5 μm;

2 - d=1 μm.

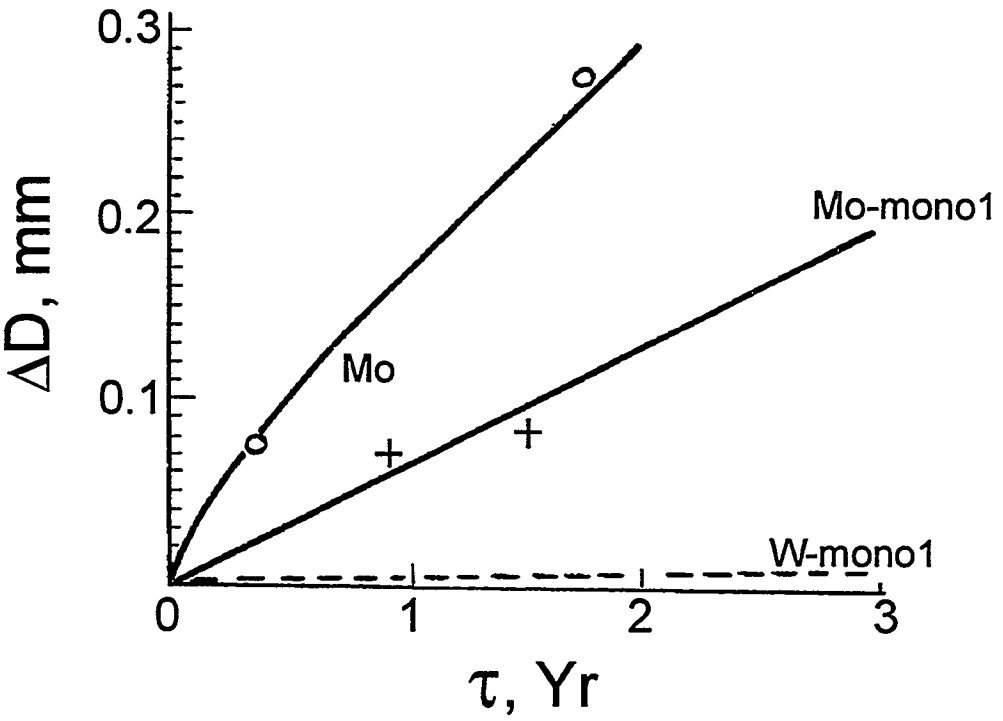

Figure 4.18. Influence of emitter material on its stability (T_{em}=1550°C, q_v=45 W/cm^3) [17].

—— calculations based on experimental data (o, +)

- - - - calculations made in the absence of experimental data

Calculated data are presented with experimental data obtained in tests of single-cell TFEs in trial nuclear power systems (NPSs), i.e., TOPAZ-2 reactor prototypes.

As seen above, TFE life can be prolonged using single-crystal strengthened alloy. In the TOPAZ-2 single-cell TFE, substituting molybdenum alloy for the non-alloyed single-crystal molybdenum as the emitter material reduced its deformation by ~2 to 2.6 times.

Obviously, under conditions of rigidly restricted mass and size in space reactors, the above direction is preferable to thickening the emitter.

The reasonableness of this decision originates from the following calculational assessments. First, molybdenum single-crystal alloy (MN3), applied as the emitter material to the TOPAZ-2 TFE, has a creep rate lower by about 2 to 3 orders of magnitude than non-alloyed molybdenum (see, e.g., Figure 2.11). Second, the emitter creep rate (ξ) is a power function of the mechanical stresses (σ) acting within it, i.e., $\xi \sim \sigma^n$, where n is the material creep exponent. It equals, for Mo, 4 to 5 [17, 18]. Because σ is inversely proportional to emitter thickness ($\sigma \sim 1/h$), $\xi \sim (1/h)^n$ or $\xi_1/\xi_2 = (h_2/h_1)^n$. From this it follows that the same effect, i.e., molybdenum emitter creep-rate reduction by ~2 to 3 orders of magnitude, may be achieved only by a thickening of 2.5 to 5.5 times. This, naturally, would lead to considerable deterioration of the mass/size parameters of the reactor as whole.

The effectiveness of emitter strengthening by use of high-strength alloys is ascertained by direct in-pile tests (see Figure 4.18).

Single-cell TFE emitter deformation, as applied to the Space-R reactor with a 40 kW electric power, has been examined [9] for a reactor with TFE number N=145 to 151 at TFE mean power W≈300 W. SPACE-R single-cell TFE parameters in comparison to data on TOPAZ-2 TFE are listed in Table 4.3 [9].

TFE lifetime was forecasted using a criterion of electrode short circuiting originating under emitter deformation caused by UO_2 swelling. Here, as the tolerable emitter deformation, the accepted value was experimentally determined for the TOPAZ-2 TFE, since the initial TFE interelectrode gaps are the same (δ=0.5 mm).

The calculational results for the influence of the free volume in the fuel element (V_f), of the emitter material (MN3 and MN6), and of the heat release distribution on the lifetime are shown in Figure 4.19 [9]. Variation of the heat release distribution was carried out by changing an effective height of core, H_{eff}. H_{eff} equals the distance from core center to the point where heat release becomes zero. It was assumed that heat release varies along the fuel stack based on the cosine law. A 10-year TFE life is obtained by using an emitter made from MN6 and a free volume in the fuel element of ~25 to 30%.

Nikolaev et al. [1] studied emitter deformation kinetics for a TFE with higher power (W=400 W) and the influence on it of the main processes occurring in the TFE. Results are shown in Figure 4.1, where for different operation times the

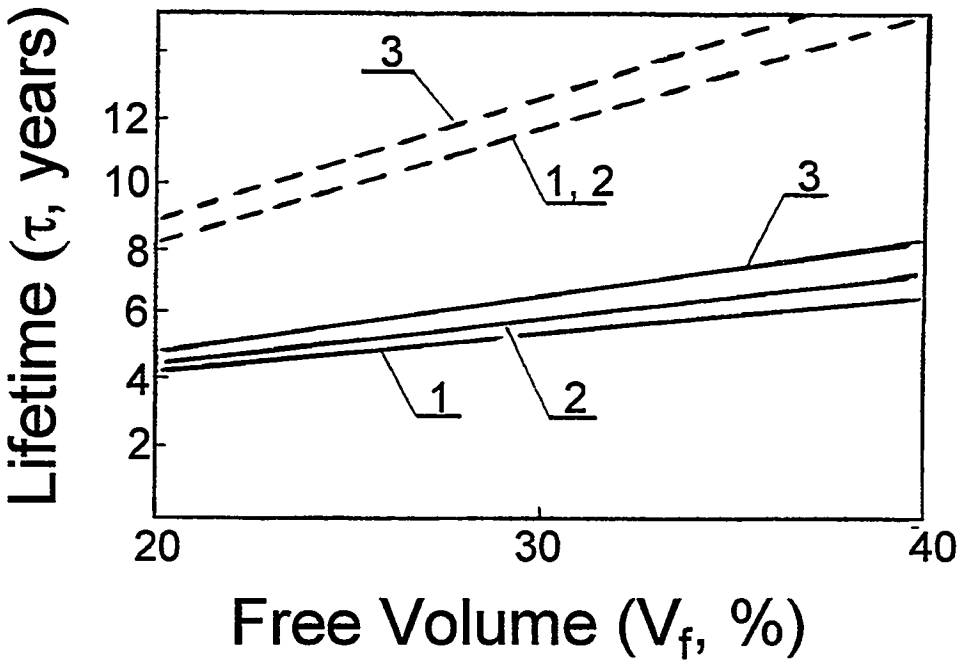

Figure 4.19. Single-cell TFE lifetime forecasted for SPACE-R:
1 - H_{eff}=50 cm;
2 - H_{eff}=65 cm;
3 - $H_{eff} \rightarrow \infty$;
—— MN3;
- - - - MN6.

Table 4.3. TFE characteristics of TOPAZ-2 (experimental values) and Space-R (calculated) [9]

No.	Parameter	TFE	
		TOPAZ-2	Space-R
1	Power, W	132	300
2	Efficiency, %	5	7.3
3	Emitter Thickness, mm	1.15	2.3
4	Emitter Temperature, K	1820	1880

following distributions along TFE length are contained: emitter temperature and stack central channel surface temperature (a), linear power in fuel stack (b), radial deformation of emitter (c), and fuel-stack free central channel (d). The coordinate Z=0 corresponds to the TFE central cross-section.

Over time mass transfer in the central channel changes its geometry (Figure 4.1d). The diameter of the channel increases in the hottest parts of the fuel stack and decreases in the cooler parts. Such a change of the fuel stack form causes equalization of maximum fuel temperature (Figure 4.1a) and linear power (Figure 4.1b) distributions along the fuel element. The joint action of the changes in geometry, temperature, and linear power shifts the position of maximum emitter deformation from the fuel stack center (z=0) to the area of minimum diameter of the central channel, i.e., to the area of the most intense UO_2 condensation (Figure 4.1c). This conclusion from the calculational investigation is confirmed by post-irradiation data on TFEs tested in TOPAZ-2 reactor prototypes [19] (see also Chapter 6).

Emitter deformation in the multi-cell TFE differs from that of the single-cell TFE. In this case, at the modules' end caps, even early in operation, isothermal cavity formation creates zones within the solid fuel stack that can locally enhance deformation of the emitter. However, estimates show that at a fuel-element free volume ≥15%, the length of the solid fuel stack zones is small in comparison with the length in which cladding deformation is limited by the restraining effect of the caps [6].

The maximum rates (U) of radial deformation of the emitter for the multi-cell TFE are presented in Figure 4.20 [13]. The calculation assumed typical dimensions: emitter diameter, 20 mm; emitter temperature in the calculated fuel-element central section, 1900 K; power release density, 145 W/cm^3. These parameters provide TFE output electric power of ~600 W with a core length of 400 mm. Single-crystal non-alloyed tungsten and strengthened single-crystal tungsten alloy were considered as emitter materials.

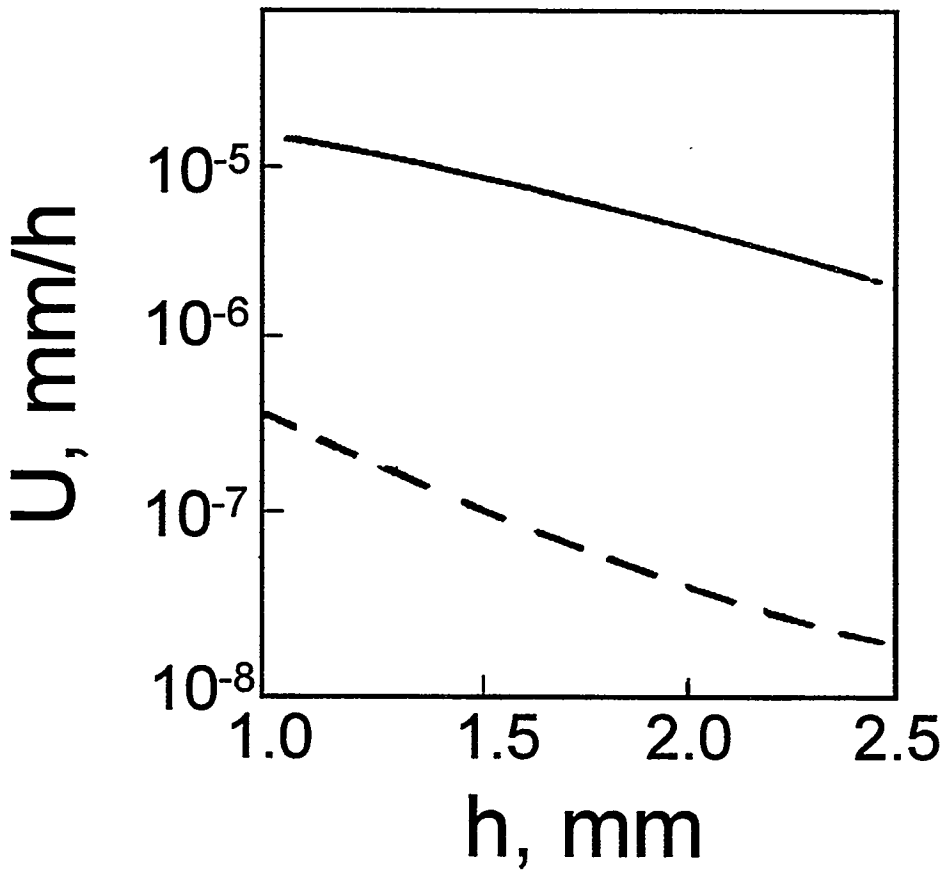

Figure 4.20. Influence of emitter thickness, h, on deformation rate, U [13]:
—— single-crystal W emitter;
- - - - strengthened single-crystal tungsten alloy emitter.

The single-crystal tungsten led to long TFE life (7 to 10 years) only when the emitter thickness h≈2.5 mm. In this case, the radial deformation makes up ~0.15 to 0.2 mm, which is similar to the operating value of the interelectrode gap. Use of the strengthened tungsten alloy, which has a creep rate about three orders of magnitude lower than tungsten, considerably improves the emitter's geometric stability and mitigates requirements relating to its thickness. In this case, even when h=1 mm, radial deformation does not exceed 0.05 mm for 10 years of TFE operation [13]. This effect is connected with redistribution of UO_2 swelling at the fuel-stack central channel direction: when the emitter material is strengthened, fuel swelling is reduced. This is linked to raising the compressive stress within the fuel stack and, as a consequence, decreasing the total volume of GFP bubbles generated. For bubbles fixed to grain boundaries, i.e., the ones that contribute maximally to UO_2 swelling, the latter is lowered 1.5 to 2 times [13].

4.4.3. Fuel-Element Deformation under Thermocycling

As noted in Chapter 3, a fuel element incorporated into a TRC is subjected to continuous thermocycles with small amplitudes. Estimates show the potential influence of such thermocycles on fuel-element deformation behavior and indicate the necessity for subsequent investigations of the mechanism involved [6, 20]. The estimates were carried out for typical dimensions and operating conditions of the thermionic fuel element.

Results are presented in Figures 4.21 to 4.22. Here, both the fuel-element thermocycling conditions during TRC operation and the emitter deformation during simulation of this process under out-of-pile conditions, i.e., without UO_2 swelling ($dS/d\tau=0$), are considered.

Figure 4.21 indicates that for out-of-pile conditions, the cause of change in the emitter dimensions is thermocycle asymmetry with respect to fuel-element heating and cooling rates. Depending on the ratio of these rates either increase (at $\nu^h/\nu^c>1$) or decrease (at $\nu^h/\nu^c<1$) of the emitter size is possible. The emitter deformation per one regular cycle is $\Delta r/r\approx\pm1\cdot10^{-4}\%$ (see Figure 4.21a), but because of the regular fuel-element thermocycling it may reach, even in a 10^3-hr test, ~1% (see Figure 4.21b).

Under in-pile conditions, the zero-deformation point is shifted by unilateral loading of the emitter by the swelling fuel stack to the area of $\nu^h/\nu^c<1$ (Figure 4.22). Thermocycling with small amplitudes under in-pile conditions may also affect porosity development in the fuel stack. Estimates of this effect are presented in Table 4.4.

The fuel-element thermocycling mode at $\nu^h/\nu^c<1$ under low pressure of GFP within a pore (P_{GFP}) leads to reduction of the initial porosity in the fuel stack (Table 4.4). In contrast, at $\nu^h/\nu^c>1$, the thermocycling promotes pore growth (fuel

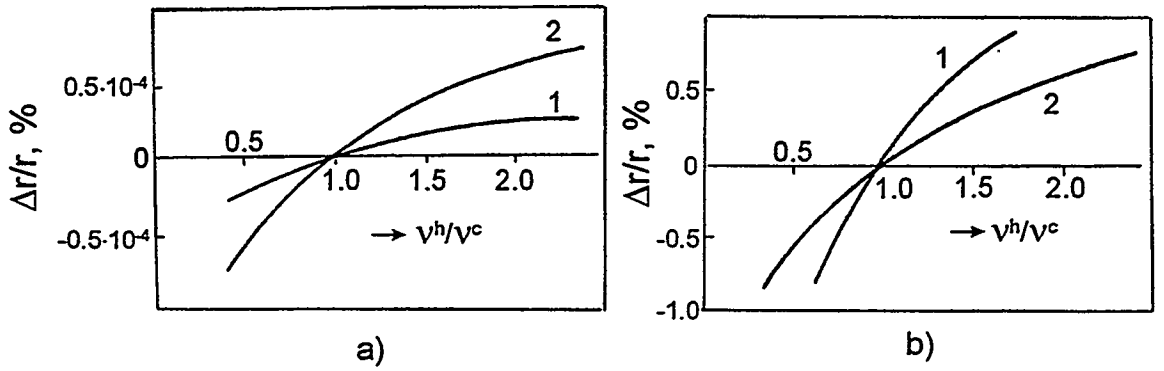

Figure 4.21. Influence of fuel-element heating to cooling rate ratio on Mo-emitter deformation ($dS/d\tau=0$; $\Delta T=10K$) for one cycle (a) and 10^3 Hrs (b):

1, 2 - cycle length, respectively, $\tau_{cyc}=0.02$ hr;

$\tau_{cyc}=0.1$ hr.

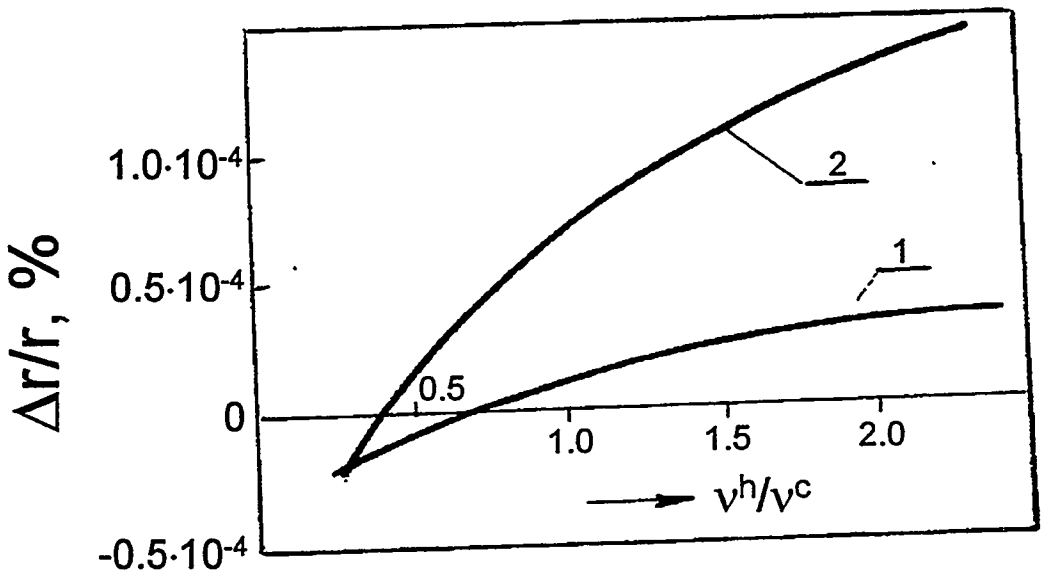

Figure 4.22. Influence of fuel-element heating-to-cooling rate ratio on emitter deformation for one cycle under in-pile conditions (ΔT=10K):

1 - τ_{cyc}=0.2 hr;

2 - τ_{cyc}=0.1 hr.

Table 4.4. Change in gaseous pore volume per cycle (initial porosity ε=0.05; thermocycle length τ^c=0.1 hr; ΔT=10 K) [20]

P_{GFP}, MPa	ν^h/ν^c=0.6	ν^h/ν^c=1.0	ν^h/ν^c=1.4
0.1	$-0.22\cdot10^{-3}$	$0.54\cdot10^{-5}$	$0.15\cdot10^{-3}$
1.0	$-0.17\cdot10^{-3}$	$0.54\cdot10^{-4}$	$0.20\cdot10^{-3}$
10.0	$-0.32\cdot10^{-3}$	$0.54\cdot10^{-3}$	$0.70\cdot10^{-3}$
100.0	$0.52\cdot10^{-2}$	$0.54\cdot10^{-3}$	$0.56\cdot10^{-2}$

swelling). However, with an increase in intrapore gas pressure, the thermocycling effect upon these processes is eased.
These results are preliminary and call for experimental confirmation. Detailed investigations of the emitter/fuel-stack material creep at the unsteady-state stage are necessary in order to build a more representative calculational procedure.

4.5. References

1. Nikolaev, Yu.V., Gontar, A.S., Sotnikov, V.N., et al. "Complex Computational Investigation of Single-Element TFE Time-dependent Behaviour with Consideration for Mutual Influence of Lifetime Limiting Processes." *Proc. 30th Intersociety Energy Conversion Engineering Conf.*, Orlando, 1995, vol. 1, pp. 637-642.
2. Gontar, A.S., Kucherov, R.Ya., Nelidov, M.V., et al. "Some Questions of Uranium Dioxide Mass Transfer Influence on High-temperature Fuel Element Behaviour." *Proc. 24th Intersociety Energy Conversion Engineering Conf.*, New-York, 1989, v. 6, pp. 2803-2808.
3. Shulepov, L.N., Sotnikov, V.N., Anisimova, L.N., *Manual on MUTANT Program Operation for a Calculation of Temperature Fields in Multi-Cell System Fuel Stacks with Free Central Channel or Gas Exhaust Device.* RI SIA "Lutch" I-50-053-89, Podolsk, 1989
4. Chirkin, V.S. *Nuclear Engineering Materials Thermal Properties.* Moscow: Atomizdat, 1968, p. 468.
5. Rozhkova, N.M., and Sinyavsky, V.V. "Spacers Heat Conducting Properties Influence on Thermionic Fuel Element Voltage-Current Parameters and Temperature Fields." *Atomic Energy*, 1980, v. 49, iss. 2, pp. 137-139.
6. Gontar, A.S., Nelidov, M.V., Nikolaev, Yu.V., et al. "Thermionic Fuel Element Development Problems." Report at the Branch Jubilee Conference "Nuclear Power in the Space." Obninsk, 1990.

7. Gontar, A.S., Sotnikov, V.N., Shulepov, L.N., et al. "Uranium Dioxide Mass Transfer Influence on Thermionic Fuel Element Gas Exhaust Device Operationability." Report at the Branch Jubilee Conference "Nuclear Power in the Space." Obninsk, 1990.
8. Carslow, H.S., and Jaeger, J.C. *Conduction of Heat in the Solids.* Moscow: Nauka, 1964, p. 487
9. Nikolaev, Yu.V., Ponomarev-Stepnoi, N.N., Britt, E.J., et al. "A Single-cell TFE Mock-up of the Thermionic Nuclear Power System Space-R." *Proc. 12th Symp. on Space Nuclear Power and Propulsion.* Albuquerque, 1995, part 2, pp. 815-820.
10. Kornilov, V.A., Sukhov, Yu.I., Yuditsky, V.D. "A Method for Calculation of Temperature Fields in Heterogeneous Fuel Stack of Thermionic Electrogenerating Element." *Atomic Energy*, 1980, v. 49, iss. 6, pp. 393-394.
11. Gontar, A.S., Kukin, E.B., Nelidov, M.V., Nikolaev, Yu.V. "Possibilities of Using Alternative Fuels in a Thermionic Fuel Element." *Proc. 26th Intersociety Energy Conversion Engineering Conf.*, 1991.
12. Gontar, A,S., and Nelidov, M.V. "A Model and Calculational Study of Uranium Dioxide Swelling under High-Temperature Irradiation." *The International Conference on Irradiated Materials Science/Technology*, Alushta, 1990. Reports Theses, part 3, Kharkov 1990, p. 95.
13. Gontar, A.S., Gutnik, V.S., Nelidov, M.V., and Nikolaev, Yu.V. "Swelling of Uranium Dioxide and Deformation Behaviour of the Fuel Element at High Temperature Irradiation." *Proc. 28th Intersociety Energy Conversion Engineering Conf.*, Atlanta, 1993, v. 1, pp. 549-553
14. Gontar, A.S., Kucherov, R.Ya., and Nelidov, M.V. "Intragrain Pores Influence on UO_2 Swelling." *Atomic Energy*, 1985, v. 58, pp. 54-55
15. Chabb, U., Storhock, V., and Keller, D. "Factors Affecting the Nuclear Fuel Swelling at High Temperatures." *Nuclear Engineering Abroad*, 1976, no. 2, pp. 8-22.
16. Nikolaev, Yu.V., Kolesov, V.S., et al. "Molybdenum and Tungsten Single Crystal Alloys with Abnormally High Creep Strength for Space Nuclear Power and Propulsion Systems." *Proc. 10th Symposium on Space Nuclear Power and Propulsion.* Albuquerque, 1993, part 1, pp. 267-274.
17. Nikolaev, Yu.V. "SIA "Lutch"'s Development and Study in the Area of Materials for NPPs with Direct Conversion." Report at the 4th Branch Conference "Nuclear Power in the Space. Materials. Fuel." Podolsk, 1993.
18. Tachkova, N.G., Zubarev, P.V., Dementiev, L.N., et al. "A Study of High-Temperature Creep of the Single Crystal Alloy Mo-3%mass Nb under Long-Time Loading." in: "Refractory Metals, Alloys and Compounds with Single Crystal Structure". Moscow: Nauka, 1984, pp. 196-201

19. Degaltsev, Yu.G., Kuznetsov, Yu.F., et al. "Post-Irradiation Study of Processes within Uranium Dioxide Fuel for Single-Cell TEC". Obninsk, 1990.
20. Gontar, A.S., Nelidov, M.V., Nikolaev, Yu.V. "Deformation Behaviour of a Thermionic Fuel Element under Conditions of Thermal Cycling with a Small Temperature Change." *Proc. 25th Intersociety Energy Conversion Engineering Conference*, vol. 2, 1990, pp. 290-293.

CHAPTER 5

RESULTS OF OUT-OF-PILE TESTS OF THERMIONIC FUEL ELEMENTS UNDER DEVELOPMENT

5.1. Results of Out-of-Pile Investigations of Emitter Deformation under Thermocycling

The out-of-pile tests of model fuel elements discriminate the contribution of fuel-element thermocycling to the total emitter deformation observed in the investigation of TFEs after tests in loop channels of research reactors. This allows extrapolation of TFE test results to standard (steady-state) operating conditions in thermionic reactor-converters. Unlike in-pile tests, this technique also permits more detailed study of a fuel element for a larger number of parameters being controlled during the tests, reducing the time and cost of the study.

The thermocycling of a fuel element leads mainly to a change in the interaction between the fuel stack and emitter and to deformation of the latter. The thermocycling also affects structural modifications and fuel-stack integrity.

These results have been discussed by Nikolaev et al. [1].

5.1.1. Test Device and Model Fuel-Element Design

The test device used is diagrammed in Figure 5.1. A model fuel element comprised a stack of 6 or 7 annular pellets of uranium dioxide (1) inserted in a cladding (2) with a gap. The cladding was closed at the top and bottom with caps, which simultaneously insulated and aligned the fuel element in relation to a tungsten rod heater (3). An additional thin-walled cylindrical heater (4) with an autonomous current supply provided the required relation between the cladding temperature and the heat flux from the cladding surface. The cladding thermometry was through tungsten-rhenium thermocouples (5) attached to the cladding and a pyrometer (6) with a window in an outer cylindrical heater (7). The electric power of the central heater was adjusted by a setter (8), and the electrical voltage on the outer heater was changed by a controller (9). The power supplied was measured using the voltmeter-ammeter method with a 2% accuracy.

5.1.2. Testing Conditions

In research-reactor-based tests, some scheduled start-ups and shut-downs precede, as a rule, the first scram protection response. Therefore, the model fuel elements were tested in the following order.

The first series, consisting of 4 thermocycles, for the study of the influence of scheduled start-ups and shut-downs was performed with slow and steady rates of

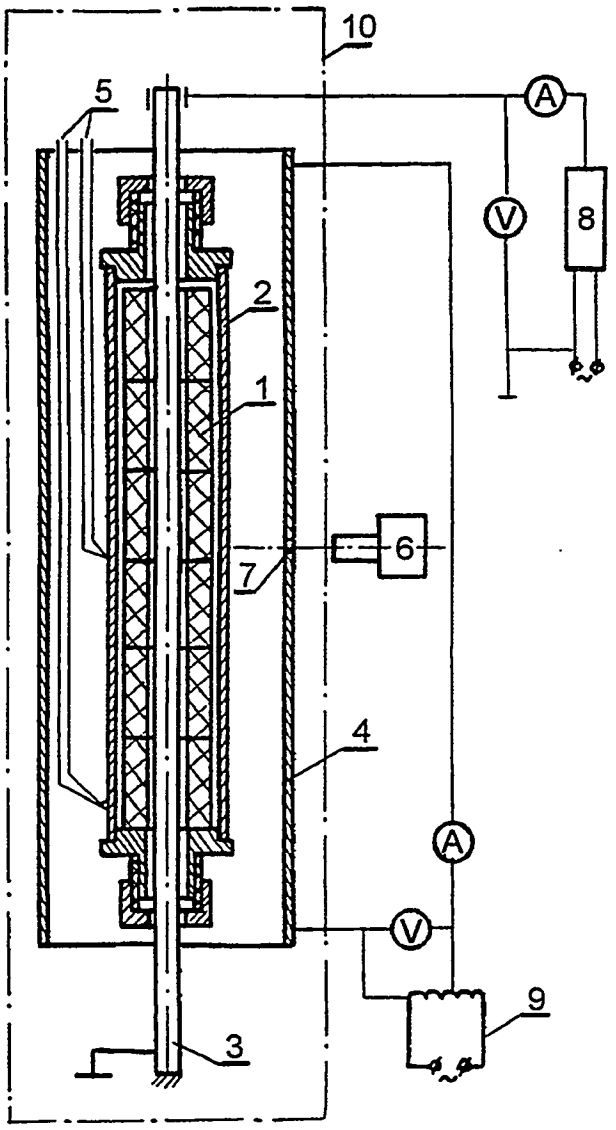

Figure 5.1. Testing device [1] (outline).

heating and cooling (0.16 K/s).

The second series (up to 30 thermocycles) investigated the scram protection response effect, using the same model fuel element but at an increased (up to 2.7 K/s) cooling rate, which corresponded approximately to the condition of the scram response.

The model fuel element was placed in a vacuum chamber (10), within which a 10^{-2} Pa dynamic vacuum was sustained.

To select an optimal time for isothermal holds following each heating, a series of model-fuel-element pretests was executed with successive lengthening of the hold time at a rated power and temperature. After each experiment, UO_2 structure was examined. It was established that the radial recondensation of UO_2 onto the cladding is over within 12 hours under the following conditions, which were realized in subsequent testing: cladding temperature, 2100 K, and heat flux from the cladding, 13 W/cm^2. In testing the model fuel element, the isothermal hold at the upper temperature was the same, 14 hours, in all cases.

5.1.3. Results of the Model Fuel Element Tests

After tests, the cladding diameter was measured with a 2-mm linear spacing in 4 planes, at every other 45°, after the first and each of three subsequent thermocycles. The measurement accuracy was 0.01 mm.

After completion of the tests, metallographical examination of the fuel-stack and cladding materials was conducted.

Figure 5.2 shows the diameters of a 1.0-mm-thick cladding made of single-crystal molybdenum, after the first thermocycle. The cladding becomes oval and its diameter decreases in relation to the initial value for all measurement planes. The greatest effect is seen in the central section on the fuel-element length and reaches $\Delta D/D \approx 1\%$. Experiments showed that the observed diameter behavior along the fuel element axis is caused by a decrease in thickness (from the element center to its ends) of the UO_2 layer re-condensed on the cladding.

Figure 5.2 also shows that cladding deformation is accompanied by formation of annular valleys (waists) with ~0.03-mm depth. Their location corresponds to sites of pellet coupling.

The influence of cladding material and thickness on its deformation as a function of number of thermocycles is shown in Figure 5.3; there is a relative change in averaged diameters along the major and minor axes of the oval in the central section of the fuel element.

Use of the MN3 strengthened alloy for the 1.0-mm thick cladding sharply reduces its susceptibility to the thermocycles. A maximum decrease in the diameter after the first thermocycle was, for this case, only 0.05 mm (0.25%). In subsequent thermocycling, this cladding diameter did not change significantly. Thinning the MN3 cladding to 0.4 mm causes enhancement and building up of the

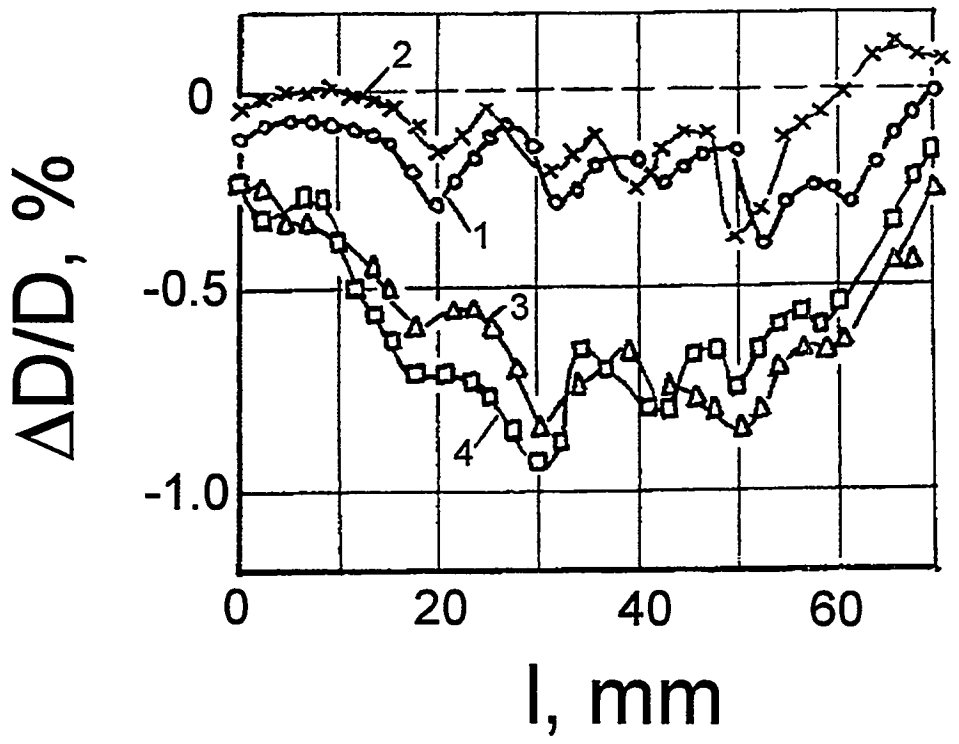

Figure 5.2. Change in single-crystal molybdenum cladding diameter after first thermocycle [1]:

1-4 - planes of 0°, 45°, 90° and 135°, respectively.

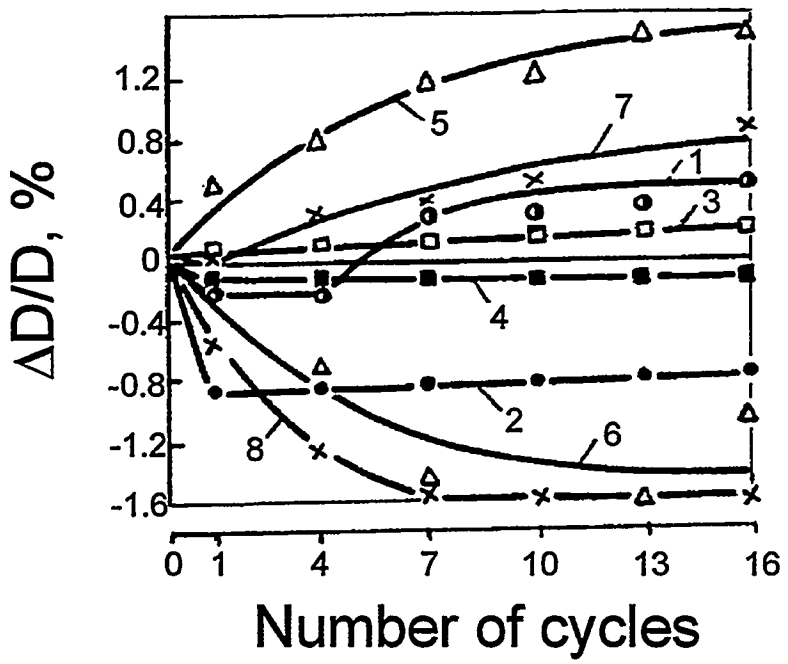

Figure 5.3. Cladding deformation vs. number of thermocycles:
1, 2 - Mo, δ=1.0 mm;
3, 4 - MN3, δ=1.0 mm;
5, 6 - MN3, δ=0.4 mm;
7, 8 - W, δ=0.7 mm.

deformation cycle by cycle. In this case the cladding surface also had waists, analogous to those found on the molybdenum cladding. Additionally, there were observed longitudinal valleys as deep as 0.03 to 0.04 mm and up to 0.5 mm wide, which corresponded to the location of cracks along the fuel stack.

The amount of deformation for the tungsten cladding lay between those of the molybdenum cladding and the thin MN3-alloy cladding.

Raising the cooling rate from the fifth thermocycle did not change the character of the cladding deformation (see Figure 5.3).

The obtained data (Figures 5.2 and 5.3) provide an upper estimate for non-irradiation cladding deformation in research-reactor-based testing: a maximum decrease of the cladding diameter when cooling the fuel element is about 1.0%, and the maximum rate of diameter enlargment, when thermocycling, ~0.1% per cycle.

The appearance of shear lines on the metallographic polished sample of the cladding indicates its plastic deformation behavior for separate periods of loading. Hence, increasing the creep resistance of the cladding material is insufficient to ensure geometric stability of the fuel element; it is necessary to simultaneously reduce stress by thickening the cladding.

The investigation results show that cladding stability in thermocycles can be ensured using strengthened materials (e.g., MN3 alloy) having an acceptable thicknesses of the cladding (~1.0 mm) from the viewpoint of an appropriate design.

5.2. Method and Results of Determining the Fuel Stack/Emitter Interface Heat Conduction

The fuel stack/emitter interface heat conduction depends on the contact pressure between them; this dependence has an exponential nature ($\alpha \sim P^n$, where $n>1$). Under TFE standard (steady) operating conditions (in a TRC), pressure on the emitter and mechanical stresses within it are caused by fuel-stack swelling. Therefore, in defining interface heat conduction under out-of-pile conditions, an indispensable stipulation is simulation of mechanical loading of the emitter by the swelling fuel stack.

A method for doing this in out-of-pile tests was developed at RI SIA "Lutch" [2]. In essence, measurements are conducted under out-of-pile conditions imitating the pressure that the swelling fuel stack puts on the model fuel element's cladding. Fuel/cladding contact is ensured at the temperature under study by the choice of an appropriate value of the initial gap. Later, the fuel element undergoes an isothermal hold for 0.5 to 20 hours. The length of the hold is preset depending on the cladding material, i.e., to relax stresses within it that may arise when the fuel element is put to a rated condition. Subsequently, the fuel stack is heated at a

rate that equalizes the rates of its heat expansion and relative volume enlargement due to its swelling under irradiation.

Results of interface heat conduction experiments and a description of the studied fuel-element design have been presented [3]. The investigations were performed in the device described in Section 5.1 (see Figure 5.1).

The model fuel element had the following design features. A 1.15-mm thick cladding was made of MN3 alloy with an outer diameter of 19.6 mm and length of 63 mm. A corrugated molybdenum foil 0.05 mm thick was placed between the stack and cladding. The corrugations were rectangular with peak and valley azimuthal dimensions of 0.5 mm. The central heater was a 6.0-mm diameter tungsten rod; the fuel-pellet hole diameter was 8 mm. Radial perforations 2 mm in diameter were created within the outer heater and fuel-element cladding.

The tests were executed at the rated cladding temperature, 1660°C. Electrical power was supplied to the central and outer heaters at 0.6 and 1.15 kW, respectively. The hold to relax initial stresses was 1 hour long. The mean rate of alteration of the central heater power was 30 W/hr and was adjusted by the setter (8). The preset cladding temperature was maintained by periodically lowering the outer heater power using the controller (9).

Proceeding from the measurements performed, the interface heat conduction (α) was determined through the relations

$$\alpha = q / \Delta T$$

$$q = \frac{\sigma \cdot \varepsilon_{r1} \cdot F_{Cl} \cdot \left(T_{Cl}^4 - T_{O.h.}^4\right) - \sigma \cdot \varepsilon_{r2} \cdot F_{f_2} \left(T_f^4 - T_{Cl}^4\right)}{F_{f_1}}$$

where: q - density of heat flux from the cladding surface in sites of its contact with the corrugated foil;

$T_{Cl}, T_{O.h.}, T_f$ - temperatures respectively of the cladding; outer heater; and corrugated foil in sites of its contact with the cladding;

ε_{r1} and ε_{r2} - reduced emissivities of materials of respectively, cladding and outer heater; cladding and corrugated foil;

σ - Stefan-Boltzmann constant;

F_{Cl} - area of the cladding outer surface;

F_{f_1} - overall area of the corrugated foil peaks contacting the inner cladding surface;

F_{f_2} - area of the cladding inner surface, having no contact with the corrugated foil.

From 12 measurements, the value of the interface heat conduction was determined to be $\alpha=0.33\pm0.02$ W/cm^2·K [3].

5.3. Results of Out-of-Pile Investigation of Change in Fuel and Emitter-Material Initial Properties

5.3.1. Fuel Structural Change

Structural behavior within the fuel stack was studied not only in the TFE in-pile tests (see Chapter 6), but also in the course of out-of-pile investigation of the model fuel element. The temperature conditions of these tests and the model fuel element design were considered above (see Section 5.1). Nikolaev et al. [1] described the results of the investigations.

Change in grain size and shape. After the tests, the as-fabricated uranium-dioxide equiaxial structure with a 5- to 30-μm grain size gains a characteristic column structure with two zones differing in grain size along the radial direction:

- fine grains (20 to 40 μm width and 100 to 200 μm length) are located near the cladding within 0.3 mm of the fuel-stack outer layer;
- coarser grains (50 to 160 μm width and 1000 to 1500 μm length) occupy a deeper zone, up to the fuel-stack central channel.

UO_2 density change. The fuel density of samples cut from the central section, measured by the hydrostatic method, increased from 10.2 to 10.4 g/cm^3. Fuel microhardness grew from 7000 to 8500 MPa. Cracking in the column structure around the point where the indentor touched the fuel surface shows that the fuel material becomes more brittle. The transition of UO_2 structure from fine-grained to columnar and the fuel density change appreciably reduce the fuel creep rate (see Chapter 2).

Pellet cracking and condition of the fuel stack/cladding interface. In all cases, the fuel stack cracked both in the radial and azimuthal directions. As a rule, 2 to 4 radial cracks were observed. The character of azimuthal cracking was different: a network of azimuthal crazes (~1 μm), extending to depths of 0.3 to 0.5 mm, was observed in fuel elements with claddings having higher deformation (1.0-mm thick molybdenum and 0.4-mm thick MN3-alloy), in the peripheral zones around the entire fuel-stack perimeter (Figure 5.4a). For the strengthened MN3-alloy cladding of 1.0 mm thickness, there was a single main crack around the entire stack perimeter, which was located chiefly between the two structural zones within the fuel (Figure 5.4b). Local separation of the stack from the cladding was observed along with the cracking.

Formation of the azimuthal cracks and fuel-stack exfoliation cause the cladding to become oval in shape during fuel-element thermocycling [1]. The

200x

a)

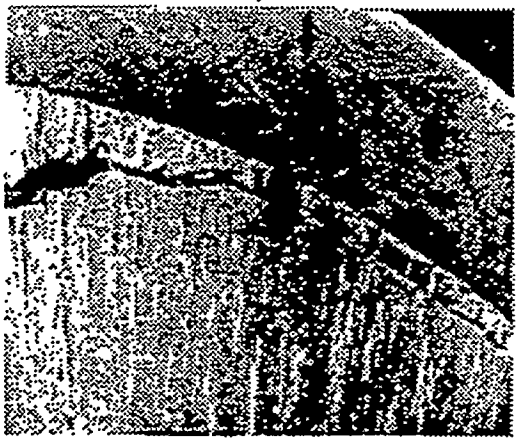

50x

b)

Figure 5.4. Azimuthal cracking of fuel stack with various claddings [1]:
a - MN3, δ=0.4 mm (the same character for Mo, δ =1.0 mm);
b - MN3, δ=1.0 mm.

deformation mechanism linked to such cracking of the fuel stack was considered in Chapter 3.

5.3.2. Simulating the Influence of Irradiation on Emitter-Material Structure and Properties

Under in-pile conditions in the course of neutron irradiation, structural defects are generated in metals (see, e.g., [4]). The influence of such damage of a material on its properties can be studied by simulating this process under out-of-pile conditions. For example, bombarding metals by low-energy ions in glow discharge increases the density of structural defects significantly in these metals [5]. At high temperature, the defects comprise mainly dislocations and dislocation loops.

Irradiation Effect on Creep. Investigations on emitter-material creep under these conditions [6-9] were performed on samples fabricated from single-crystal molybdenum obtained using vacuum zone fusion. The samples' geometric axis coincided with the <111> crystallographical direction. Sample deformation was measured using a cathetometer with ±0.005-mm accuracy.

The tests were carried out in the PV-3012M installation (designed for investigations of material creep and endurance limits), which was partially re-built. A cylindrical molybdenum anode with slots around its circumference, was substituted for a tungsten heater. A test sample served as the cathode.

To conduct the tests, the installation's working chamber was first evacuated to a 0.07-Pa residual pressure. The chamber was filled with a plasma-forming gas such as hydrogen or helium-hydrogen mixture (at 4:1 ratio) up to a pressure of ~8000 Pa. The glow discharge ignited between the test-sample cathode and the cylindrical anode. The sample was loaded after reaching a preset temperature conditions and subsequent 0.5- to 1.5-hr isothermal hold. The temperature was measured using a pyrometer [7]. This test equipment and some features of the sample preparation have been described in more detail by Savvatimova and Tachkova [6].

The test conditions and discharge parameters are presented in Table 5.1.

Creep curves for radiation heating are compared to those for bombarding a sample by hydrogen ions in Figure 5.5a, and to those for helium-hydrogen mixture treatment, in Figure 5.5b (curve numbers correspond to the sample number in Table 5.1).

When testing the samples in glow discharge, their creep rate decreases during the test time (or with irradiation dose accumulation). In Curves 3 and 4 there is a "plateau" indicating successive stages of material strengthening. With loading up to 6.7 MPa, the creep curve for hydrogen-ion bombardment did not significantly change.

Table 5.1. Single-crystal molybdenum creep-test conditions [7]

No. sample	Temperature, °C	Stress, MPa	Heating Technique	Glow Voltage, V	Flux Density, ion/cm^2·s	Irradiation Fluence, ion/cm^2
1	1650	5.7	R	-	-	-
2	1500	5.7	R	-	-	-
3	1650	5.7	IB	470±10	$9.1 \cdot 10^{17}$	$6.2 \cdot 10^{22}$
4	1500	5.7	IB	470±10	$7.5 \cdot 10^{17}$	$1.2 \cdot 10^{22}$
5	1650	6.7	R	-	-	-
6	1500	6.7	R	-	-	-
7	1650	6.7	IB	470±10	$9.6 \cdot 10^{17}$	$1.1 \cdot 10^{22}$
8	1500	6.7	IB	470±10	$7.5 \cdot 10^{17}$	$8.7 \cdot 10^{22}$
9	1500	5.7	IB	400	$5.6 \cdot 10^{17}$	$7.5 \cdot 10^{22}$
10	1500	8.0	IB	400	$5.6 \cdot 10^{17}$	$7.5 \cdot 10^{22}$
11	1500	6.7 to 8.0	IB	400	$5.6 \cdot 10^{17}$	$6 \cdot 10^{22}$

* R - radiation heating;
IB - ionic bombardment heating in glow discharge

Creep resistance under helium/hydrogen mixed-ion irradiation is considerably higher than for the same loading conditions in the hydrogen medium. At T=1500° C and σ=6.7 MPa no deformation was found for 15 hrs of the tests. After the loading stress was raised to 8 MPa, the sample began to deform (Figure 5.5b, curve 11); the deformation behavior was similar to that observed under a loading stress of 8 MPa from the beginning of the test (Figure 5.5b, curve 10).

The steady-state creep rate and time required to accumulate a 1% deformation are provided in Table 5.2 (the sample test conditions are the same as given in Table 5.1). In glow discharge tests, the steady-state creep rate was calculated for the length after the first strengthening at ~10^{22} ions/cm^2 dose was reached.

The experimental data indicate that low-energy ion irradiation does increase material creep resistance. Also, the time needed for accumulating a deformation of ~1% and the time until sample destruction were extended [7].

Further investigations [8] showed that, within the studied range of stresses σ, the steady-state creep curves $\xi=f(\sigma)$ obtained for the irradiation conditions are steeper than the curves relating to the vacuum tests (i.e., irradiation results in an increase of the exponent in the material creep). The curves intersect under stresses $\sigma_0 \approx$ 7.5 to 8.0 MPa, i.e., ionic irradiation lowers the molybdenum creep only at $\sigma < \sigma_0$.

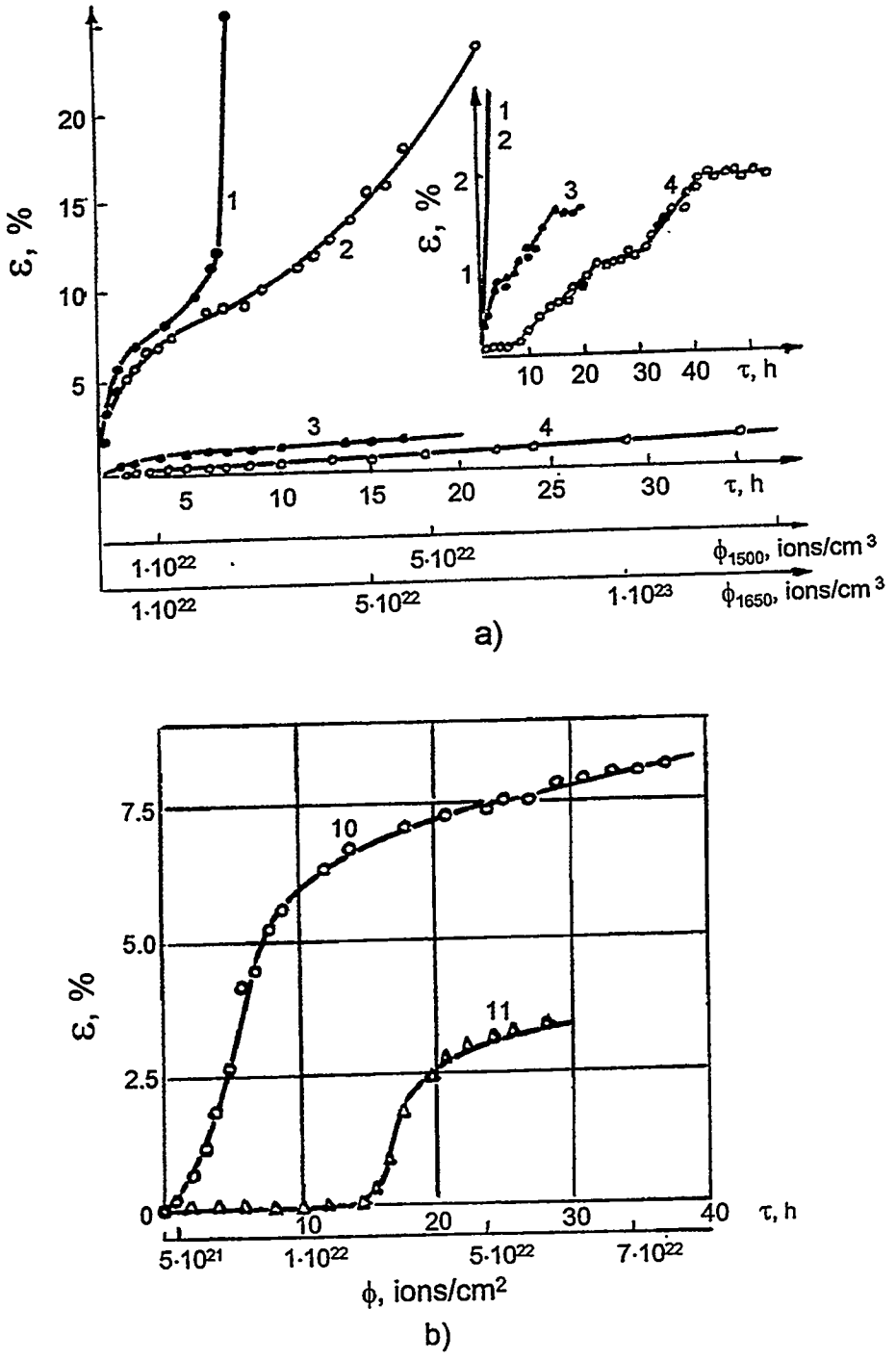

Figure 5.5. Single-crystal molybdenum creep curves [7]
a, b - respectively: irradiation by hydrogen ions and helium-hydrogen mixture.

Table 5.2. Test results on single-crystal molybdenum creep [7]

No. Sample	Sready-state creep rate ξ, %/hr	Time of 1% deformation accumulation, hr
1	0.75	0.3
2	0.39	0.3
3	0.074	7
4	0.056	23
5	0.89	0.3
6	0.48	0.3
7	0.7	2.5
8	0.56	8
9	0	-
10	0.85	3
11	0 to 0.73	-

The treatment by ions in glow discharge up to fluences of 10^{21} to 10^{22} ion/cm^2 at temperatures of 1500 to 1600°C raises the material's yield strength by 10 to 25% [7].

Irradiation Effect on Structure. The volume dislocation structure of the samples tested was examined using methods of high-voltage and analytical transmission electron microscopy [8]. Figure 5.6 contains photomicrographs of the small-angle boundaries in molybdenum after creep testing without (a, b) and with (c, d) irradiation by hydrogen ions.

The dislocation structures of the irradiated samples differ from the structure of samples tested in vacuum. The mean size (~100 μm) and shape of blocks in both samples are roughly similar, but the dislocation structures of their interblock boundaries and the type of these dislocations differ significantly. Within the irradiated sample, the dislocations are very distorted, and within the block boundaries they are interwoven. Near the interblock boundaries there are dislocation loops with a 30 to 80 nm size, the density of which varies widely.

The dislocation structures in a molybdenum single crystal, tested for creep under irradiation in the helium/hydrogen mixture, are shown in Figure 5.7. A large-cell hexagonal dislocation wall and a wall with elements of tetragonal cells formed in the irradiated sample under stress (Figure 5.7a, b). Still larger cell dislocation walls of less regular structure are encountered (Figure 5.7c).

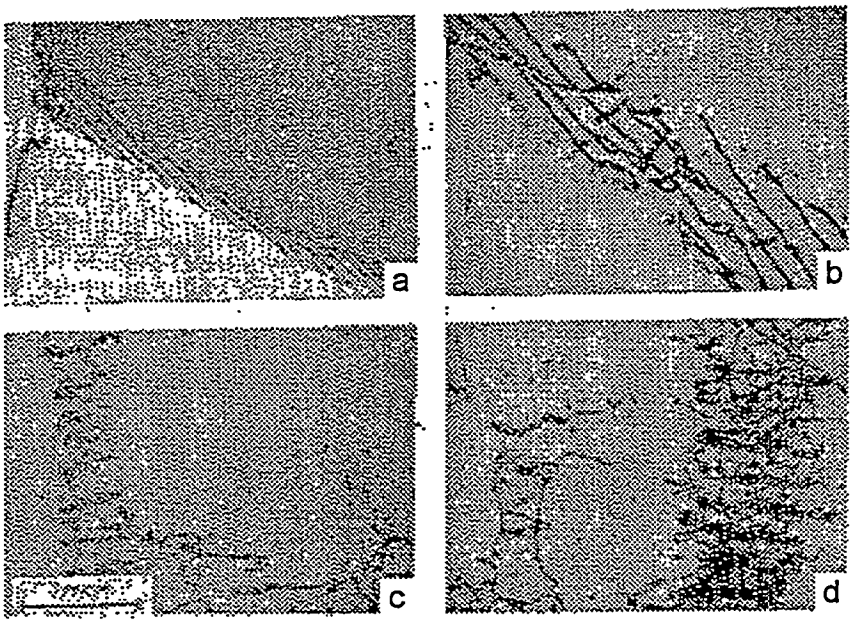

Figure 5.6. Low-angle boundaries in single-crystal molybdenum volume after creep tests (T=1500°C, σ=5.7 MPa) [8]:
a, b - not irradiated;
c, d - irradiated by hydrogen ions.
All photomicrographs have the same scale.

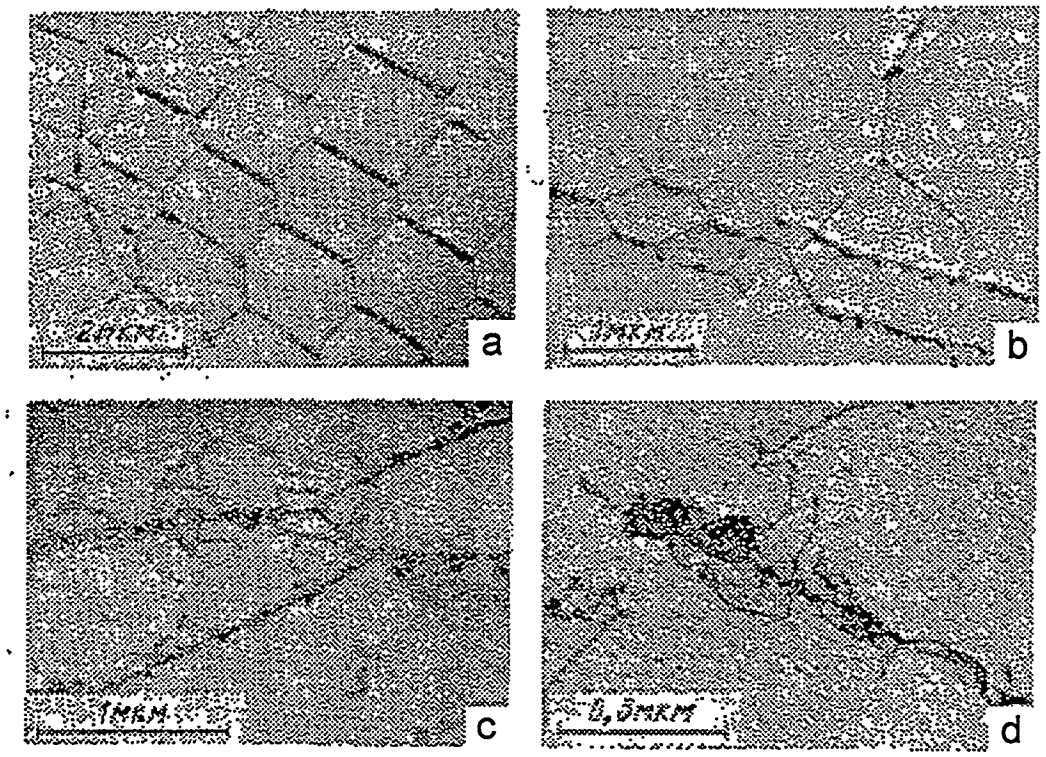

Figure 5.7. Dislocation structures in single-crystal molybdenum tested on creep (T=1500°C, σ=5.7 MPa) under irradiation by glow discharge in helium/hydrogen mixture [8].

The large-cell dislocation walls, characterized by various degrees of perfection, were found in samples that had undergone only high-temperature ionic irradiation without tension (Figure 5.8).

Thus, a general characteristic of all the samples subjected to simulation of irradiation by electron and proton bombardment in a field of electric discharge, both with and without loading, is a heightened dislocation density as compared to unirradiated samples.

Examination of the near-surface (as deep as 10 μm) molybdenum structure after irradiation (1500°C, 1 hr) revealed that when using helium or a helium/hydrogen mixture (unlike hydrogen only) as the plasma-forming medium, a strong gas-induced (helium) swelling ($\Delta V/V \approx 5$ to 10%) with a mean bubble size of 20 to 50 nm develops in the near-surface layer, 300 nm in thickness [8].

Irradiation Effect on the Diffusion Parameters. Defects, continuously generated under material irradiation by plasma ions, promote mass transfer. Some results of these investigations, conducted also on single-crystal molybdenum have been reviewed by Babad-Zakhryapin et al. [9].

Plates of single-crystal molybdenum with ~2-mm thickness, coated by diffusant layers of tungsten and UO_2, were investigated. To reveal the influence of defects, a change in the diffusant concentration was measured both for sections of samples subjected to the discharge effect and for shielded sections. Results were also compared to those obtained for a sample annealed in a vacuum furnace at the same temperature (1600°C) and time.

The irradiation was conducted in glow discharge by hydrogen ion flux of $6.2 \cdot 10^{17}$ ion/cm^2·s. The tungsten-concentration distribution in molybdenum was determined using microroentgenospectrum analysis. The UO_2 distribution in molybdenum was measured by microautoradiography. Results are provided in Table 5.3. The table shows that for the Mo-W couple the interdiffusion coefficients D at high (~50%) diffusant concentration are practically the same both under glow discharge effect and during annealing in a vacuum furnace. At a small diffusant concentration (≤3%), the discharge treatment increases to about 10 times the D value.

For the Mo-UO_2 couple, irradiation slightly affects the volume diffusion coefficient D_V. However, the value of $a^2 \cdot D_{dis}$ (where a is the dislocation tubule diameter, and D_{dis} is the coefficient of diffusion on dislocations) for the irradiated samples is 10 to 100 times higher than for shielded ones. This points to intensification of mass transfer along the dislocations when permanent generation of structural defects takes place.

Figure 5.8. Dislocation network in single-crystal molybdenum irradiated at T=1500°C for 28 hrs in glow discharge, by hydrogen ions.

Table 5.3. Diffusion coefficients in Mo-W and Mo-UO_2 systems [9]

Diffu-sant	Fluence, ion/cm^2	Diffusion coefficient						
		Heating in Discharge				Heating in Vacuum		
		Section on analysis	D, cm^2/s	D_v, cm^2/s	$a^2 \cdot D_{dis}$, cm^4/s	D, cm^2/s	D_v, cm^2/s	$a^2 \cdot D_{dis}$, cm^4/s
W	$3.3 \cdot 10^{23}$	A*	$3.6 \cdot 10^{-14}$					
		B*	$4.0 \cdot 10^{-14}$					
		A**	$6.0 \cdot 10^{-13}$			$4 \cdot 10^{-14}$		
		B**	$4.0 \cdot 10^{-14}$					
UO_2	$1.1 \cdot 10^{24}$	A		$2.8 \cdot 10^{-13}$	$4.6 \cdot 10^{-18}$			
		B		$2.7 \cdot 10^{-13}$	$4.6 \cdot 10^{-20}$		$4 \cdot 10^{-14}$	$1 \cdot 10^{-19}$

A - section that has undergone ionic bombardment;
B - shielded section;
* and ** - W concentration ~50% and ≤3%, respectively.

5.4. Vibration Tests of Uranium-Dioxide Fuel Pellets

A test program for the TOPAZ-2 fuel-element pellets foresees an assessment of their vibration strength. This property is an important fuel feature, because pellet destruction can lead to heightened local stresses within the emitter and adversely affect TFE lifetime [10].

Pellet vibration strength is, to a great extent, governed by the size and shape of random defects, large pores, cavities, and cracks and by the resistance to cracking around a defect. The greatest danger, from dust and spall formation, derives from surface defects, such as cracks and cavities located near a pellet edge [11].

The fuel-pellet vibration tests were performed in a TFE prototype.

Tests carried out at the initial stage of TOPAZ-2 TFE development had shown that the fuel-pellet failure occurred here [10], and the metallographic study revealed that pellet microcracking, arising at the molding and sintering process stage, was responsible.

As a result of fuel improvements, the pellets' vibration strength was significantly increased. This demanded a revision of the fabrication process, especially preparation of raw materials and sintering runs [10].

Selected results of the vibration tests of UO_2 pellets, manufactured in compliance with the adopted process, are given in Table 5.4. Parameters of the pellets tested are presented in Table 5.5.

Table 5.4. Pellet vibration-tests results [11]

Batch No.	D/d*	Test Results				
		Dust Presence	Mass Loss**, g	Defects	Appearance Inconsistent with Reference Sample	Notes
25	5.31	no	no	no	no	
	6.0	no	no	no	no	
35	5.3	no	no	no	no	
26	2.07	no	0.66	in 36% of pellets***	present***	
	2.14	no	1.06	in 19% of pellets***	no	
82	2.14	no	no	no		repeated test
	3.7	local areas	0.03	no	no	
39	3.2	local areas	not measured	no	no	
	3.3	no	no	no	no	

* - D,d - outer and inner pellet diameter;
** - permissible loss - 1 g;
*** - with accounting of spalls when dismantling

Table 5.5. Structure characteristics of pellets (averaged through batch) [11]

Batch No.	Density, % of theoretical	Grain Size, μm
25	96.1	10 to 12
35	96.4	5 to 7
26	97.8	10 to 15
82	97.8	8 to 12
39	96.3	12 to 22

The results testify to a high vibration strength of the pellets: they withstand external mechanical loads corresponding to launch conditions [12]. Pellet strength was also confirmed in the course of multiple vibroloading (at minimum, in 4 to 5 cycles), performed for the TFE as whole in the range of the most hazardous frequencies (40 to 240 Hz), even after storage in argon for 8.5 years and in air for 1 month [12].

5.5 References

1. Nikolaev, Yu.V., Gontar, A.S., Vedenyapin, G.A., Nelidov M.V., and Sotnikov, V.N. "Out-of-pile simulation of deformation behaviour of a thermionic fuel element under thermocycling conditions." *Proc. 29th Intersociety Energy Conversion Engineering Conf.* Monterey, 1994, part 2, pp. 1027-1031.
2. Vedenyapin, G.A., Gontar, A.S., Zaznoba, V.A., Nelidov, M.V., and Podogov, Yu.N., "Technique of Determination of the Contact Heat Conductivity between the Cladding and Fuel Stack of a Model Fuel Element." Authors Certificate No 1785046. USSR. Applicant: Research Institute of Scientific Industrial Association "Lutch" Priority, August, 4, 1989.
3. Invention description to the author's certificate: SU 1785046 A1.
4. Olander, D.R. *Fundamental Aspects of Nuclear Reactor Fuel Elements.* Technical Information Center, Energy Research and Development Administration. 1976, 612 p.
5. Babad-Zakhryapin, A.A., and Lagutkin, M.I. "Structure Defects in Materials Treated in Glow Discharge." *Metal Science and Heat Treatment of Metals*, 1976, No. 7, pp. 70-71.
6. Savvatimova, I.B., and Tachkova, N.G. "Equipment for Study of Metal Creep under Low-Energy Ions Bombardment." *Works Laboratory*, 1980, v. 46, No. 2, pp. 172-173.
7. Babad-Zakhryapin, A.A., Savvatimova, I.B., Zubarev, P.V., and Tachkova, N.G. "The Creep of Single Crystal Molybdenum under Low-Energy Ions Irradiation." *Physics and Chemistry of Metals Treatment*, 1981, No. 6, pp. 155-160.
8. Chernikov, V.N., Savvatimova, I.B., Babad-Zakhriapin, A.A., and Zakharov, A.I. "The Structure of Molybdenum, Irradiated by Hydrogen and Helium Low-Energy Ions, in Creep Tests." *Atomnaya Energia*, 1980, v. 48, iss. 2, pp. 98-99.
9. Babad-Zakhryapin, A.A., Borisov, E.B., Savvatimova, I.B., and Senchukov, A.D. "The Mass-Transfer in Single Crystal Molybdenum and Silicon under Irradiation by Low-Energy Ions of Glow Discharge." *Atomnaya Energia*, 1980, v. 48, iss. 2, pp. 98-99.

10. Gontar, A.S., Rakitskaya, E.M., Degaltsev, Yu.G., and Hoth, C.W. "Design and performance of the UO_2 fuel for the TOPAZ-2 reactor." *Proc. 11th Symposium on Space Nuclear Power and Propulsion.* Albuquerque, 1994, part 1, pp. 55-61.
11. Gutnik, V.S., Rakitskaya, E.M., and Tsiplenkova, V.L. "High Density Uranium Dioxide: Some of Properties." *Report at the 4th Branch Conference "Nuclear Power in the Space. Materials. Fuel".* Podolsk, 1993.
12. Ponomarev-Stepnoy, N.N., Nikolaev, Yu.V., Vibivanets, V.I., Panov, A.S, Gontar, A.S., et al. "Properties and operation characteristics of fuel pellets for TFE of the installation "TOPAZ-2"." Information Paper of the RI SIA "LUTCH". Podolsk, 1994, fulfilled by the Contract N I-077 with Joint Venture "INERTEC."

CHAPTER 6

RESULTS OF MATERIALS AND FUEL-ELEMENT IN-PILE TESTS

In developing the fuel and optimizing the TOPAZ-2 TFE design, a considerable scope of in-pile tests was executed, from irradiation of fuel samples to full-scale fuel elements assembled with prototype nuclear power systems.

6.1. Results of In-Pile Tests of Modified Uranium-Dioxide Fuel Samples

In refining the fuel for the TOPAZ-2 TFE, several different modifications of uranium dioxide were developed and tested; the influence of structural and operational factors on its working characteristics was also studied. In this investigation 85 fuel samples were irradiated; a burnup was reached corresponding to a 5-year lifetime of the TOPAZ-2 reactor [1-5].

Data on irradiation-induced swelling of high-density ($\rho \approx 95$ to 98% TD) uranium dioxide, which depends on burnup, temperature, and as-fabricated UO_2 grain size, are given in Table 6.1 [4].

At the cladding temperature of 1923 K and burnup of ≤1% fissions per initial metal atom (FIMA), the free swelling rate is ~7 to 8%/% FIMA.

With increasing burnup, the UO_2 swelling rate decreases to 5 to 6%/% FIMA, which is connected to the conversion of UO_2 as-fabricated structure to the column-type, which occurs at T_{Clad}>1773 K.

The size and formation time of the columnar grains depend on the power density in the fuel samples: grain width is ~100 to 120 μm at q_V=180 to 200 W/cm^3 and ~60 to 70 μm at a power density of 300 W/cm^3. In addition, the time of formation is shortened by a factor of ~2.5 (from ~1500 hrs to 600 hrs, respectively, at $q_V \approx 200$ and 300 W/cm^3) [4].

The qualitative comparison of swelling of as-fabricated fine-grained and column-type UO_2 vs. irradiation temperature is shown in Figure 6.1 [3]. Data on the irradiation behavior of another modification of UO_2, having a stabilized open porosity, are also presented. This type fuel, developed at RI SIA "Lutch" in the course of efforts aimed at improving the fuel for the TOPAZ-2 TFE, has a number of attractive properties [6], allowing it to be considered as a prospective fuel (see Chapter 8).

Both uranium dioxide with a stabilized open porosity and with the structure rebuilt from fine-grained to column-type have considerably lower swelling level than does dense UO_2. At T_{Clad}=1650°C and q_V=200 W/cm^3 this difference is about two-fold (Figure 6.2). The data show that nearly the same effect is achieved by high-density UO_2 structure optimization.

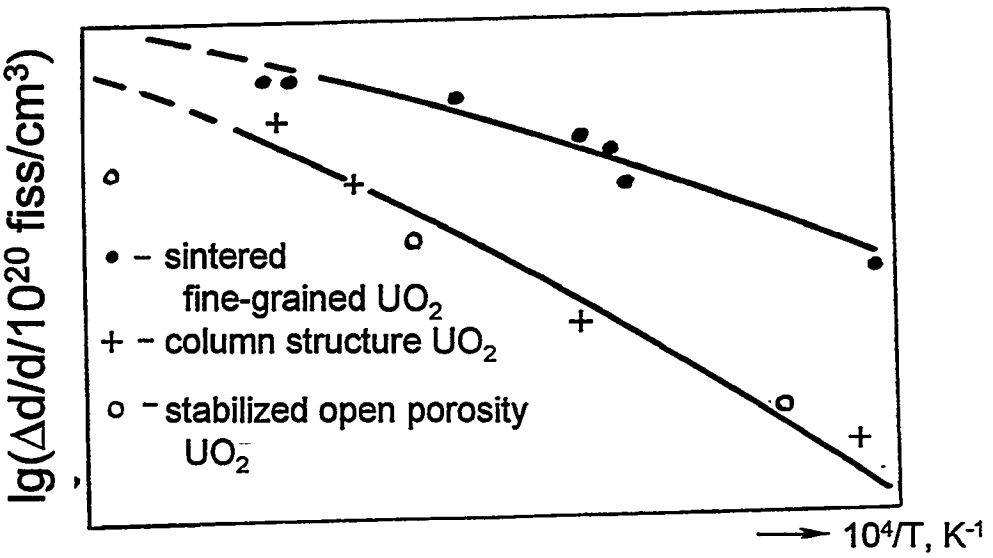

Figure 6.1. Qualitative comparison of swelling rate of modified UO_2 vs. temperature [3].

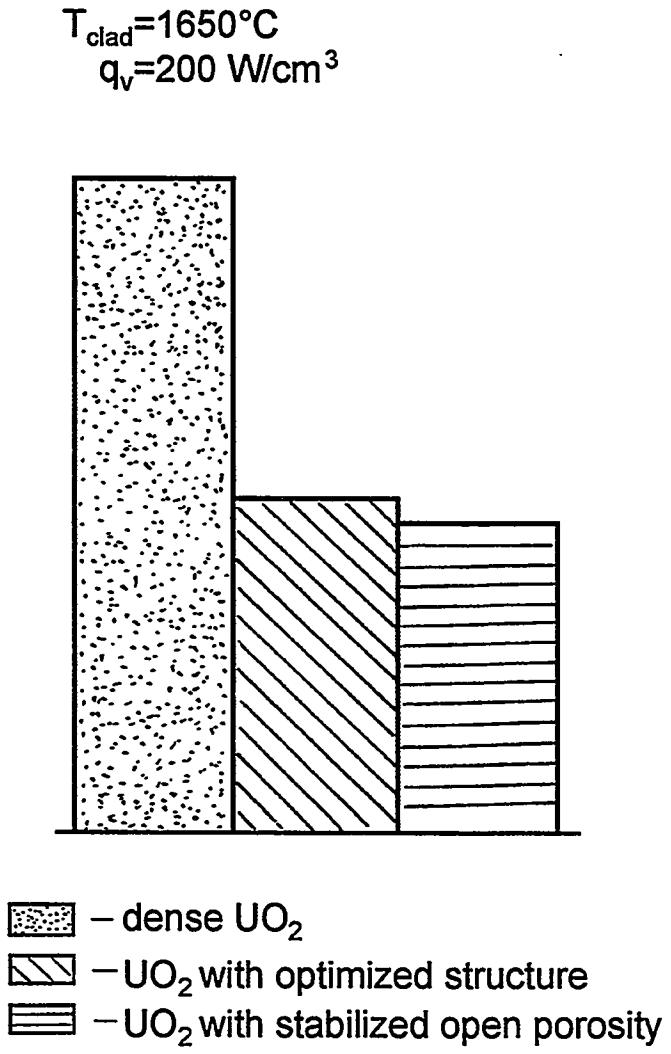

Figure 6.2. Comparison of swelling rates for various UO_2 modifications [5].

Table 6.1. High-density uranium-dioxide irradiation swelling [4]

As-Fabricated Density, %TD	As-Fabricated Grain Size, μm	Irradiation Parameters			Test Results	
		T_{Clad}, K	q_v, W/cm^3	B, % FIMA	Δd/d, %	Δd/d/B, %/% h.at.
94	8	1773±50	180±30	0.60	1.38	3.94
95	8	1923±100	180±30	0.60	3.40	5.67
96	9	1903±100	190±10	0.35	2.58	7.37
97	28	1903±100	190±10	0.35	3.32	10.06
97	8	1873±70	180±30	0.40	3.07	7.68
98	7	1973±50	300±30	1.75	10.40	5.95
98	7	1873±50	250±30	0.96	6.9	7.00

Note: T_{Clad} - cladding temperature;
q_v - heat release density;
B - burnup;
Δd/d - swelling (determined on change in diametric dimensions of fuel pellets, encapsulated into thin-walled shells, i.e., nearly free swelling of UO_2);
Δd/d/B - swelling rate.

The typical structure of irradiated UO_2 samples is presented in Figure 6.3.

An essential difference in the swelling rates is connected to the fact that the swelling of dense UO_2 with equiaxial structure is caused mostly by buildup of GFP bubbles around grain boundaries, but for the columnar structure, by formation of fine intragrain bubbles [3].

A study of the kinetics of GFP release from three UO_2 modifications also reveals a substantial effect of the as-fabricated UO_2 structure on GFP release rate. Figure 6.4 contains data on Kr^{88} relative release, obtained at T=1650±50°C and q_v=200±30 W/cm^3. For the given irradiation parameters, the difference in GFP release for UO_2 with equiaxial and columnar structures is, at an early point in irradiation, a factor of 6. With the as-fabricated structural transformation observed at this temperature, GFP release from the equiaxial dioxide is enhanced, approaching the release from UO_2 with columnar structure and stabilized after ~2000 hrs of irradiation.

6.2. Summary of the Single-Cell TFE Improvements

As a result of in-pile tests, the fuel-element design and fuel for the TOPAZ-2 reactor have undergone significant modifications. The single-crystal molybdenum emitter coated with polycrystal tungsten used in early NPS tests was changed to a

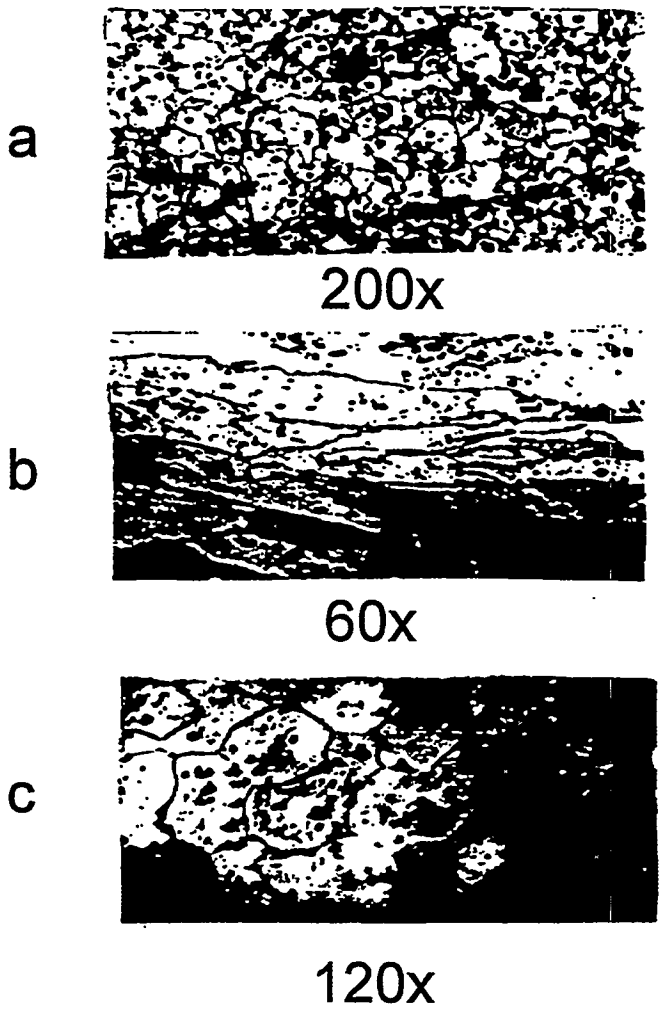

Figure 6.3. Typical structure of irradiated UO_2 samples [3]:
a - equiaxial structure dioxide;
b, c - respectively, transverse and longitudinal polished section of column-structure UO_2.

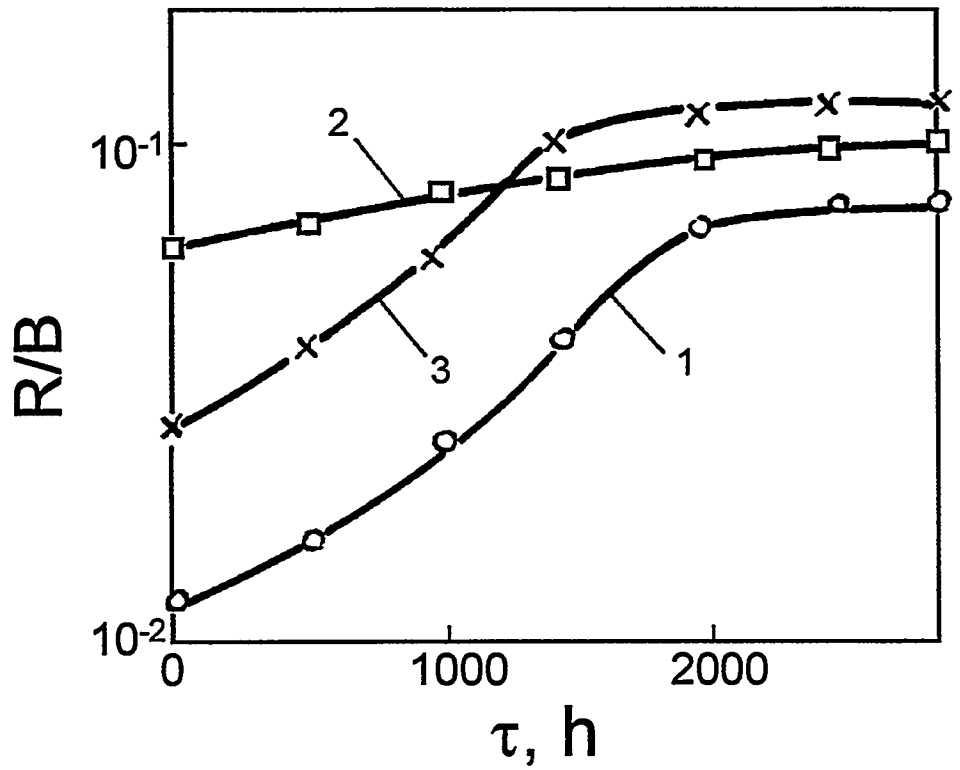

Figure 6.4. Kr^{88} relative release from UO_2 samples [3]:
1 - high-density UO_2 with equiaxial structure;
2 - column-structure UO_2;
3 - stabilized open porosity UO_2.

high-strength refractory alloy MN3 with a W^{184} single-crystal coating. To reduce swelling, the uranium-dioxide structure was optimized. Sc_2O_3 spacers were substituted for the previous Al_2O_3 spacers to improve their electrical resistance (see Chapter 2). These modifications enabled the creation of a fuel-element design with an emitter of high dimensional stability.

In the course of the work, about 20 tests of full-scale fuel elements were performed in research reactors. The maximum length of these tests was ~2 years [1]. In addition, 6 autonomously functioning nuclear power systems were tested [7]; the maximum duration of these tests reached 14,000 hrs [7].

Test results achieved for various design modifications of the TFE [8-11] were summarized by Ponomarev-Stepnoy et al. and Abdrakhmanov et al. [1, 9].

6.2.1. Change in Emitter Dimensions

Figure 6.5 demonstrates the change in time of emitter deformation for various modified TFEs tested in experimental NPSs. The results permit the following conclusions.

- In the fuel elements applied to prototype NPS (Mo emitter, high-density UO_2 fuel), emitter deformation reached significant levels, capable of causing electrode short circuit during tests of duration shorter than one year (Figure 6.5, curve 1).
- Optimizing the UO_2 structure cut molybdenum emitter deformation roughly in half (curve 2).
- Subsequent improvement of the emitter dimensional stability resulted from the use of MN3-strengthened single-crystal molybdenum alloy as the emitter material (curve 3).

Typical curves showing emitter deformation along the TFE length are displayed in Figure 6.6, representing measurements obtained for two TFEs from different rows of the Ya-81 NPS reactor core after tests lasting 12,400 hrs. The results indicate that the deformation along almost the entire emitter length is within the range of processing tolerance specified for emitter fabrication. Only local sections constitute an exception (in the zone of the fifth spacer collar), where deformation is $\Delta D \approx 0.08$ mm (i.e., does not exceed 10% of the IEG width).

6.2.2. Change in Profile of the Fuel-Stack Ventilating Channel

A typical appearance of the central ventilating channel within the fuel stack after TFE tests for 12,400 hrs in the Ya-81 NPS is shown in Figure 6.7. The central ventilating channel maintains its functionality with respect to GFP removal even after test completion. Reduction of the channel diameter caused by UO_2 mass transfer from the central section and fuel condensation near the stack ends does not exceed 25%.

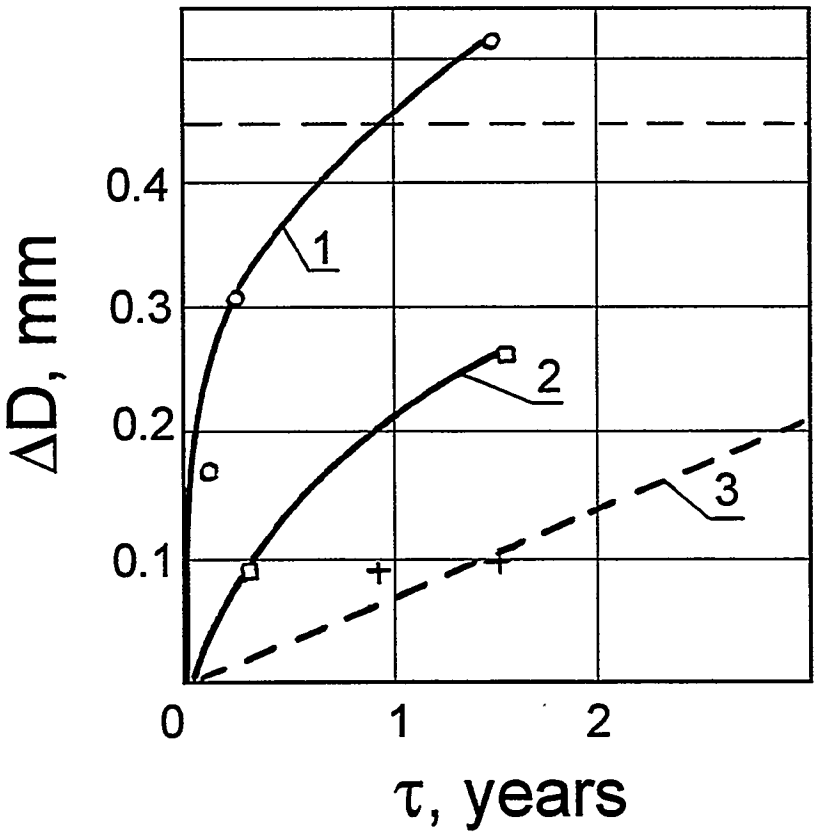

Figure 6.5. Results of TFE tests in experimental NPSs [1]:
1 - molybdenum single-crystal emitter;
2 - molybdenum single-crystal emitter, optimized UO_2 structure;
3 - emitter of strengthened single-crystal alloy (MN3), optimized UO_2 structure;
- - - permissible emitter deformation.

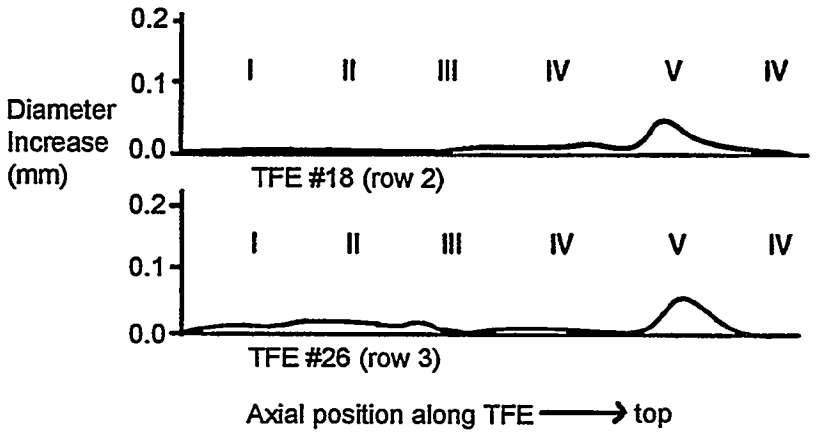

Figure 6.6. Emitter diameter change on TFE length after tests in Ya-81 NPS [8].

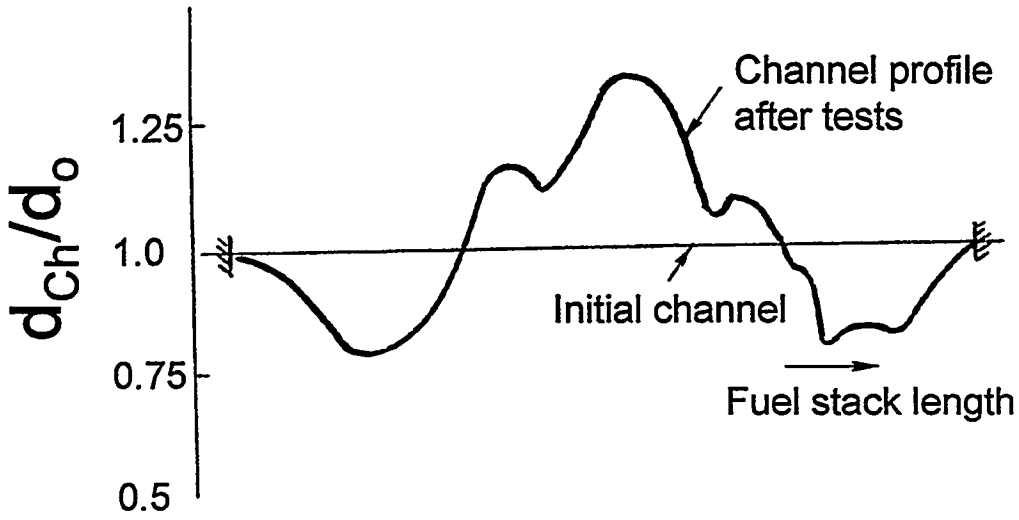

Figure 6.7. Change in fuel-stack channel diameter (d_{Ch}) in relation to its initial value (d_o) [1, 9].

The investigation of changes in UO_2 mass transfer vs. time, which took into account data obtained for different times of TFE testing in other NPSs, revealed that this process rate (and consequently, the channel constriction rate) reduces appreciably with time. The mass transfer rate is $\sim 1 \cdot 10^{-6}$ to $3 \cdot 10^{-6}$ g/s on the time base of $0 \cdot 10^3$ to $3 \cdot 10^3$ hrs and decreases to $\sim 6 \cdot 10^{-8}$ to $10 \cdot 10^{-8}$ g/s for $3 \cdot 10^3$ to $14 \cdot 10^3$ hrs [9]. It follows that the time within which the capability of the central channel to remove GFPs is maintained is greater than the time achieved in the tests and is forecasted to be not less than 3 years.

6.2.3. Structural Transformations in Fuel

UO_2 structural modifications occurring in fuel-element operation exert an appreciable influence on fuel swelling [10]. This process also changes its creep characteristics (see Chapter 2).

Investigations of the structural transformations in the single-cell TFE fuel [8, 10, 11] showed that the degree of structural rebuilding is controlled by time and temperature conditions of TFE operation, as well as by design features of the fuel element.

The typical scheme for arrangement of structural zones throughout the single-cell fuel-element volume after testing is portrayed in Figure 6.8. The microstructures of several of the zones are shown in Figures 6.9 and 6.10. The following features are characteristic of these zones. Within the peripheral layer, the so-called "crown," the grains are elongated in the radial direction. The intergrain porosity is nearly interlinked. Formation of this layer is caused by fuel evaporation from the pellet surface and its condensation on the inner surface of the emitter [10].

Dimensions of the equiaxial grains remaining at the fuel-stack ends grow under irradiation. Their maximum size is ~25 μm. The influence of irradiation on the reduction in growth rate of these grains (as compared to out-of pile tests) was noted [10].

The condensate structure formed on the surface of the ventilating channels as a result of axial mass transfer is notable for its high density ($\rho \approx 99$ to 98% TD) and coarse grains, elongated in the radial direction [10, 8]. Its arrangement along the TFE length corresponds to the emitter temperature range of ~1500 to 1550°C [10].

Elongated or columnar grains form in the middle section of the stack length; around boundaries of the grains, extended pores are located [10]. Some quantitative characteristics for the columnar uranium dioxide have been provided [11]. The metallographical examination was conducted using fuel samples from fuel elements N20 NPS of E-31 and Ya-24, tested respectively for $3 \cdot 10^3$ and $14 \cdot 10^3$ hrs (Tables 6.2 and 6.3).

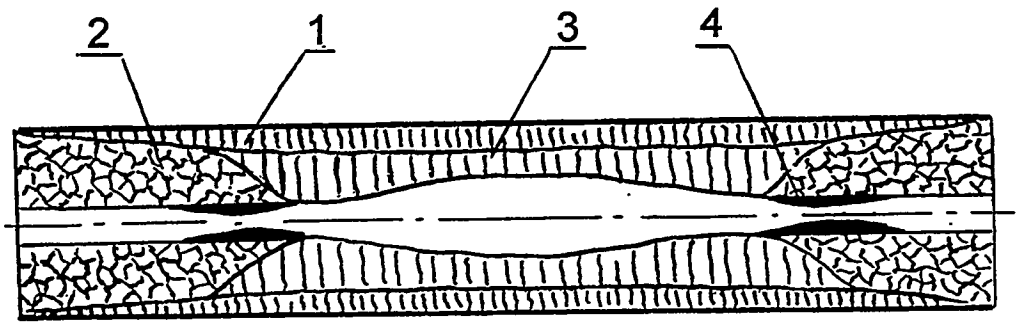

Figure 6.8. Outline of characteristic structural-zones arrangement along single cell TFE Length [10]:

1 - "Crown";
2 - Equiaxial grains;
3 - Elongated or column grains;
4 - UO_2 condensate.

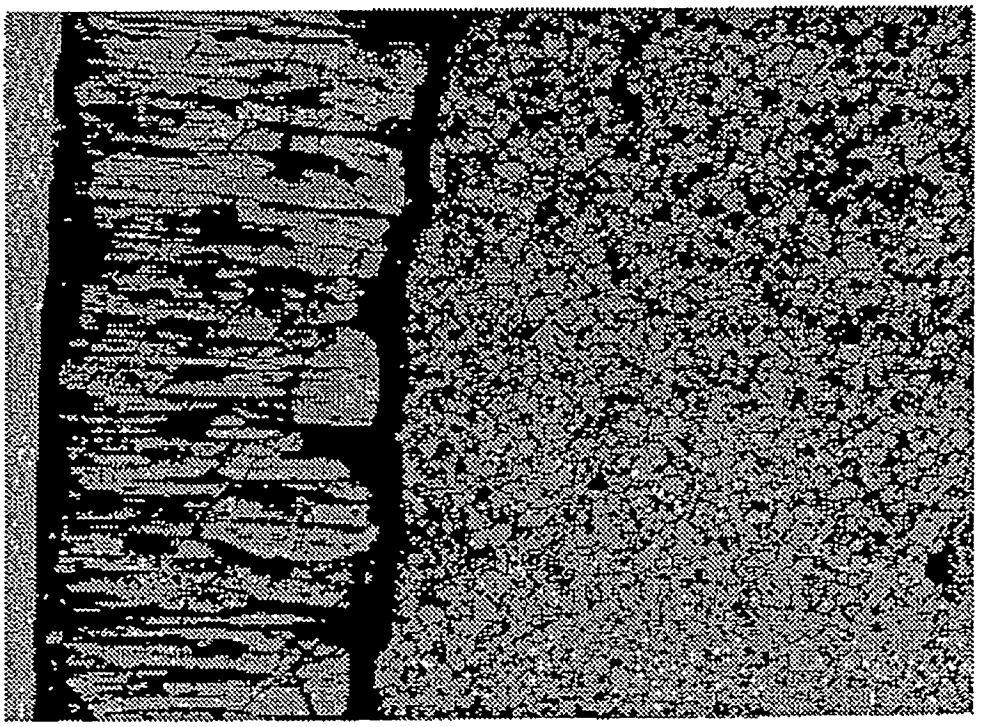

Figure 6.9. Uranium-dioxide condensate ("crown"), formed on the inner surface of the emitter [8].

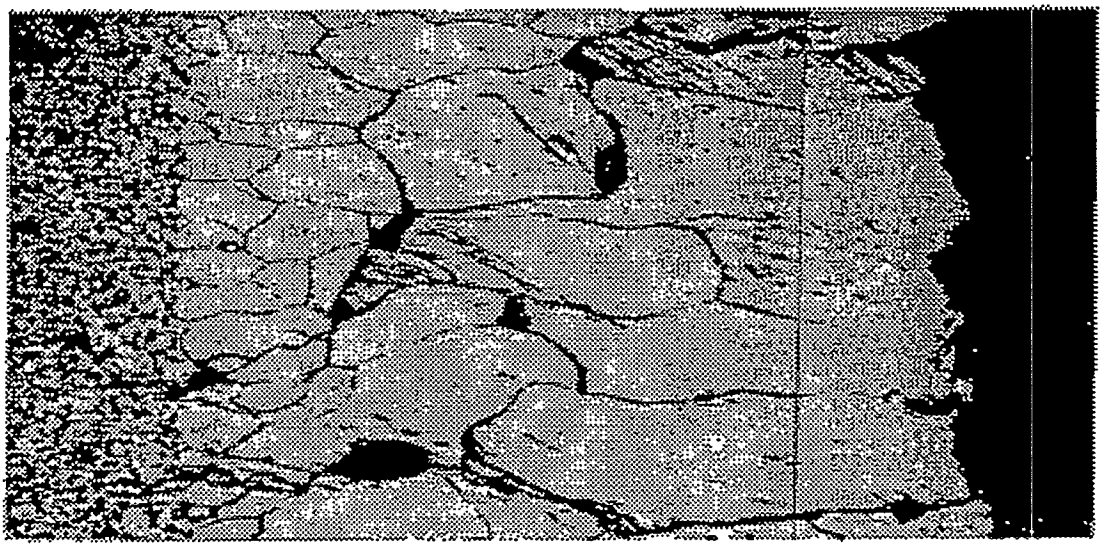

Figure 6.10. Condensate in the fuel-stack central channel surface [8].

Table 6.2. Columnar grain width and temperature conditions of tested samples [11]

NPS No.	Sample No.	Longitudinal Coordinate*, mm	Radial Coordinate**, mm	Grain Width, μm	T_{em}, °C	T_f, °C
E-31	3	140	8.1	176	1560	1599
E-31	3	140	5.85	164	1560	1675
E-31	3	140	3.2	133	1560	1709
E-31	4	180	8.95***	154	1570	1613
E-31	4	180	6.25	62	1570	1675
E-31	4	180	3.85	47	1570	1706
Ya-24	3	60	7.95	85	1460	1493
Ya-24	3	60	5.15	143	1460	1556
Ya-24	3	60	2.95	158	1460	1579
Ya-24	4	185	8.05	133	1545	1586
Ya-24	4	185	6.45	186	1545	1638
Ya-24	4	185	4.85	170	1545	1656

Note: T_{em} - emitter temperature;
T_f - fuel temperature;
* - coordinate, counted from fuel stack open end;
** - coordinate, counted from pellet center;
*** - error in [11] (apparently 8.05)

Table 6.3. Hydrostatic measurements of UO_2 porosity [11]

NPS No.	Sample No.	Total Porosity, P, %	Closed Porosity P_c,%	Open Porosity, P_o, %
Ya-24	3	12.6±0.7	2.7±0.2	9.9±0.5
Ya-24	4	9.0±0.7	3.2±0.2	5.8±0.5
E-31	3	7.3±0.7	1.0±0.2	6.3±0.5

6.2.4. Analysis of Spacer Condition

The spacers' condition and behavior in their interaction with the emitter [9] were investigated for 5 TFEs, tested in different rows of the Ya-81 NPS reactor core for 12,400 hrs. The spacers were made from Sc_2O_3, and the emitter from MN3 alloy coated with single-crystal W^{184}. A short summary of these TFE test conditions is provided in Table 6.4.

Testing performed in "hot" cells at RSC "Kurchatov Institute" revealed mechanical interaction between the spacers and the emitter surface. The number of dents found on each TFE is presented in Table 6.5. Dents were observed only at the second, third, fourth and fifth spacer collars. The length of the dents was ~4 mm, and the width, 0.6 to 1.0 mm. For two TFE (Nos. 17 and 18), the depth of the dents on the emitter surface was measured at the fourth and fifth spacer collars. The measurement had a 2.5-μm accuracy. Results are summarized in Table 6.6.

Table 6.4. Characteristics of TFEs under testing [9]

TFE No.	Row No. in the reactor core	Maximum Emitter Temperature, °C
3	I	1550
17	II	1535
18	II	1545
25	III	1540
26	III	1535

Table 6.5. Number of spacer indentations on emitter surface [9]

	Spacer Collar No.					
TFE No.	I	II	III	IV	V	VI
3	-	3	4	3	6	-
17	-	6	6	6	6	-
18	-	6	6	6	5	-
25	-	6	6	6	6	-
26	-	3	5	3	6	-

Spacer height was measured after disassembly (h_{sp}). The as-fabricated spacer height was $h_0=1^{-0.02}$ mm. The measurement accuracy was ±0.01 mm. Results are listed in Table 6.7. The measurements showed that more than 95% of all the inspected spacers from the five TFEs had heights within the processing tolerance. The height of the rest of the spacers was reduced by ≤0.2 mm.

The results of in-pile study of irradiation influence on the spacers and insulation materials were also reviewed in Section 2.3.

Table 6.6. Depth of spacer indentations on emitter surface [9]

TFE No.	Collar No.	Depth of Indentation, μm					
		1	2	3	4	5	6
17	IV	15	15	15	15	5	-
17	V	15	15	15	15	15	15
18	IV	7.5	15	15	7.5	15	15
18	V	7.5	5	7.5	7.5	7.5	7.5

Table 6.7. Spacer height after tests [9]

TFE No.	Number of Spacers	h_{sp}, mm	$\Delta h=h_o-h_{sp}$, mm
3	25	1.00 to 0.98	0
3	1	0.78	0.2
18	19	1.00 to 0.98	0
18	1	0.79	0.2
17	5	1.00 to 0.98	0
25	14	1.00 to 0.98	0
25	1	0.96	0.02
26	22	1.00 to 0.98	0
26	1	0.96	0.02

6.3. Results of In-Pile Tests of Multi-Cell TFEs

In-pile tests of multi-cell TFEs under development at RI SIA "Lutch," unlike the TOPAZ-2 single-cell TFE, to date have been performed only in the loop channels of research reactors. Over 35 such tests on multi-cell TFEs, differing in both fuel type used and their design features, were conducted during the 20-year period of this work [12]. The distinctive design features and test conditions are specified in Table 6.8. Changes in the electrical parameters during the test are presented in Figure 6.11.

Analysis of these TFE test results allowed the following conclusions. The use of high-density, high-purity uranium dioxide (carbon and nitrogen content up to $1 \cdot 10^{-3}$ to $5 \cdot 10^{-3}$ % mass) as fuel in TFEs with communicating fuel-element and IEG cavities does not lead to changes in the electrical characteristics of the electrode or the TFE output parameters for at least ~4000 hrs of tests.

For module 1 of RM-loop channel, containing uranium-dioxide fuel and operated at $T_{em}^{max} = 1740°C$ and $T_f^{max} = 2050°C$, TFE electrode short circuiting because of emitter deformation was registered and confirmed in subsequent disassembly.

Use of hyperstoichiometric uranium dioxide with O/U≥2.001, brings about chemical reaction between tungsten parts in the internal cavity of the fuel element

Table 6.8. Features of design performance and test conditions of multi-cell TFEs [12]

Loop Channel Label	Design Features of TFE	Temperature Conditions of TFE Testing	Test Duration	Fuel Stack Material (Cell No.)
RM	5 cells, communicating cavities	$T_{em}^{max} = 1750°C$ $T_f^{max} = 2060°C$	4400	$UO_{2.001}$(1,2,5) USC(3,4)
SKAT-1	5 cells, communicating cavities	$T_{em}^{max} = 1510°C$ $T_f^{max} = 1900°C$	2800	$UO_{1.999}$
SKAT-3	7 cells, communicating cavities	$T_{em}^{max} = 1570°C$ $T_f^{max} = 1850°C$	3500	$UO_{1.999}$
SKAT-4	5 cells, separated cavities	$T_{em}^{max} = 1600°C$ $T_f^{max} = 1800°C$	4500	UC-TaC

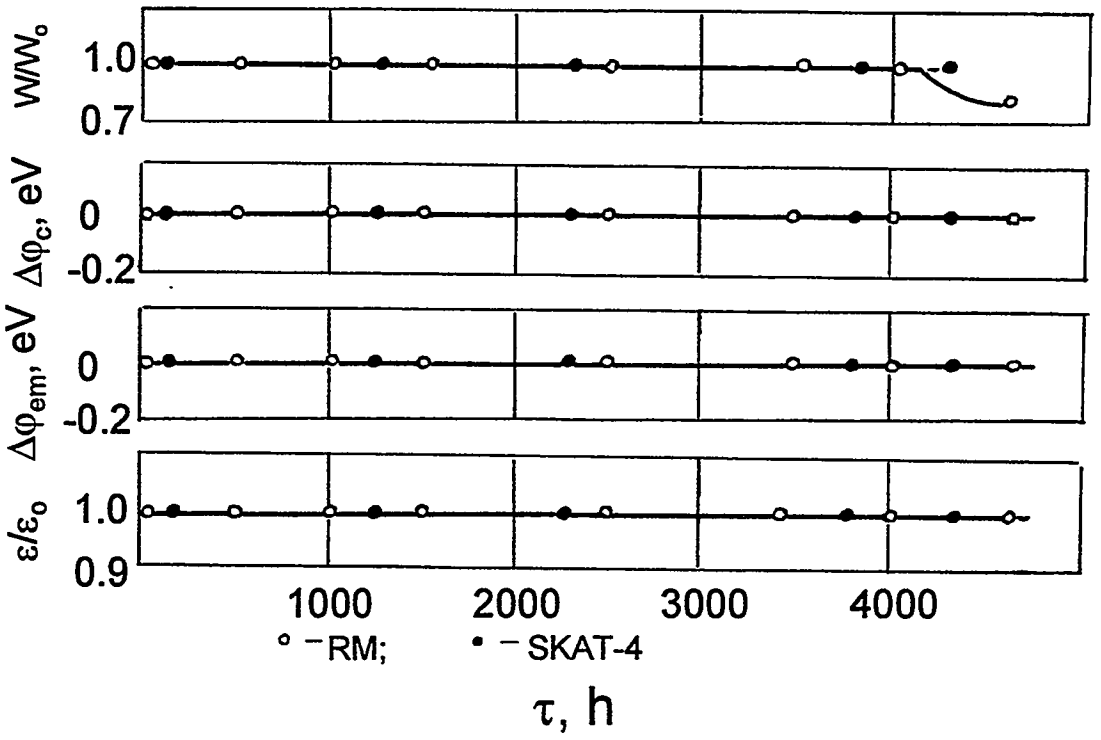

Figure 6.11. In-life change of relative electric power of TFE (W/W_o), work function of collector ($\Delta\varphi_c$) and emitter ($\Delta\varphi_{em}$), and reduced emissivity of electrodes ($\varepsilon/\varepsilon_o$) [12].

(GED, screen, etc.) and the gaseous environment. As a consequence, after disassembling cells Nos. 1, 2, and 5 from the RM-loop channel, partial or complete destruction of the GED pipe and screen was found.

Application of a hypostoichiometric uranium dioxide with O/U=1.9991 to TFEs solves the problem of gas-exhaust system integrity. In post-irradiation investigations of a TFE subjected to testing in the SKAT-3-loop channel with uranium dioxide of the above composition, the gas-exhaust elements (screen and pipe of the GED) remained completely operational. No trace of chemical reaction with the gaseous medium were found on the surface of the tungsten parts of this TFE cell.

Results of multi-cell TFE tests at the Institute of Physics and Power Engineering (IPPE) in Obninsk also point to the necessity for using the hypostoichiometric uranium dioxide [13].

Neither application of uranium carbosulphide of $U(S_{0.78}C_{0.22})$ composition, at a test temperature $T_f \approx 1840°C$, to a TFE with communicating cavities (RM) nor application of carbide solid solution of $U_{0.8}Ta_{0.2}C$, at $T_f \approx 1880°C$, to a TFE with partially separated cavities (SKAT-4), given oxygen content of $\leq 2 \cdot 10^{-2}$ to $5 \cdot 10^{-2}$% mass, results in a change of heat/electrical parameters of the electrodes and TFE power characteristics.

As applied to the multi-cell TFE with uranium-dioxide fuel, design decisions for gas removal similar to those made at RI SIA "Lutch" are also being considered at IPPE. For example, in the recently developed multi-cell TFE designs, GFP removal from the TFE is carried out through the central channel of series-connected emitters, passing by the IEG (i.e., the separated-cavities scheme is used) [13]. The most acceptable design solution for gas exhaust in high-power-density TFEs is also assumed at IPPE to be a gas-exhaust device as a pipe with a capillary endpiece [14]. In parallel, several other design schemes for GFP removal from the fuel stack cavity are under consideration.

Comparative in-pile studies at IPPE of various design solutions for gas exhaust have been reviewed by Sinyavsky et al. [14]. In particular, in testing individual cells, both a pipe with capillary endpiece and tungsten heat-conducting washers were incorporated. Also, a scheme was tested for GFP removal via the central channel in fuel pellets separated by heat-conducting tungsten washers. Four TFEs were tested in a single loop channel. The investigation was performed using the method of neutron radiography in three phases:

- neutronographic examination of the condition of as-fabricated TFE emitter parts;
- neutronographic inspection after "hot" vacuum degassing of the TFE;
- in-pile tests in the TFE power operation mode with cesium and subsequent neutronographic investigation of irradiated TFEs.

A characteristic fuel distribution within the cell volume for the two different designs for GFP exhaust is displayed in Figures 6.12 and 6.13.

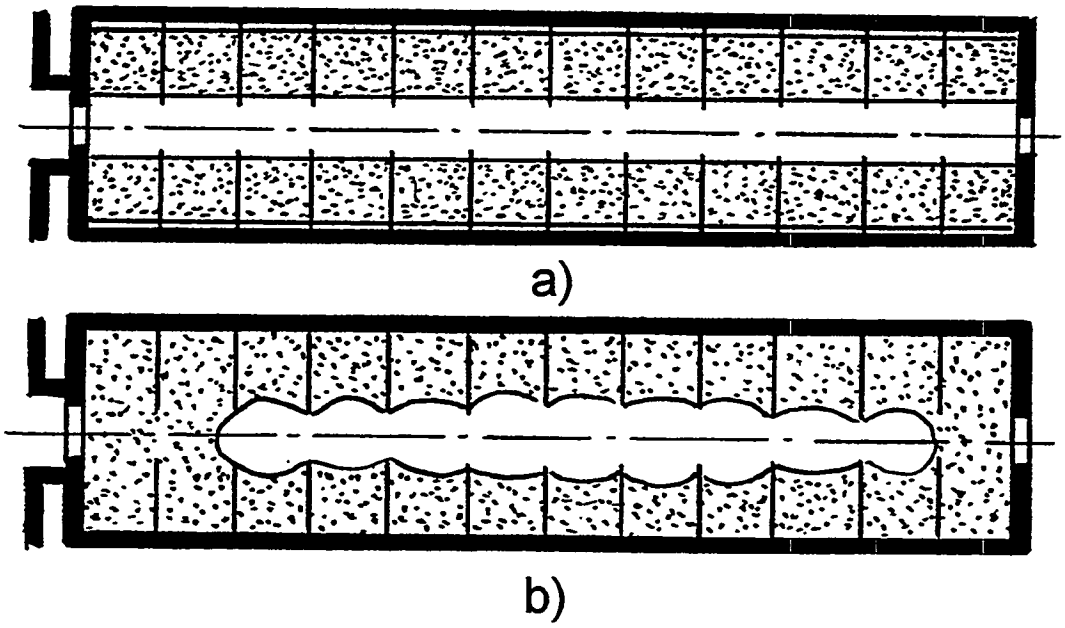

Figure 6.12. Fuel condition before (a) and after (b) tests within cells with GFP removal through a central channel in pellets divided by tungsten washers [14].

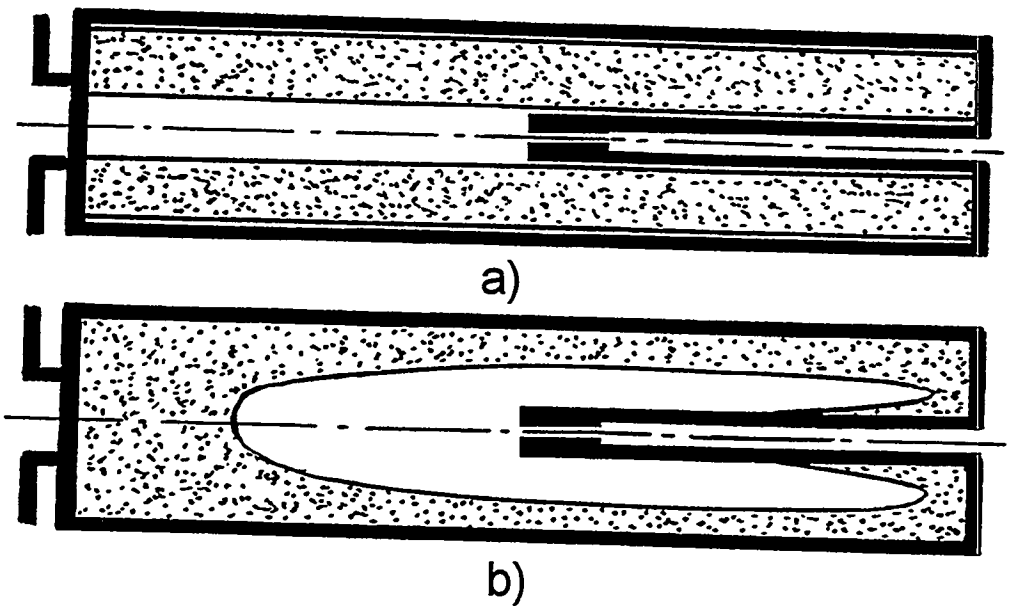

Figure 6.13. Fuel condition before (a) and after (b) tests within cells having GED [14].

The neutronographic investigation results confirmed the workability of a GED as a pipe with a capillary end, given the volume fuel fraction in the cell of ~75 to 80%.

Insertion of heat-conducting washers in the above scheme does not practically affect configuration of the closed central cavity formed in the cell; however, the fuel re-condensation rate is lower than for a cell without washers.

6.4. References

1. Ponomarev-Stepnoy, N.N., Nikolaev, Yu.V., Vibivanets, V.I., Panov, A.S., Gontar, A.S., et al. "Properties and operation characteristics of fuel pellets for thermionic fuel element of the installation "TOPAZ-2"." Information Paper of the RI SIA "Lutch", Podolsk, 1994, 17 p., fulfilled by the Contract No. I-077 with Joint Venture "INERTEC".
2. Gontar, A.S., Gutnik, V.S., Nelidov, M.V., Nikolaev, Yu.V. "Swelling of uranium dioxide and deformation behaviour of the fuel element at high temperature irradiation." *Proc. 28th Intersociety Energy Conversion Engineering Conf.*, 1993, v.1, pp. 549-553.
3. Gontar, A.S., Gutnik, V.S., Nelidov, M.V., Nikolaev, Yu.V., and Rakitskaya, E.M. "A Technique and Results of Comparative Irradiation Tests of High-Temperature Fuel Materials." Report at the 4th Branch Conference "Nuclear Power in the Space. Materials. Fuel.", Podolsk, 1993.
4. Gutnik, V.S., Rakitskaya, E.M., and Tsiplenkova, V.L. High-Density Uranium Dioxide: Some Properties. Report at the 4th Branch Conference "Nuclear Power in the Space. Materials. Fuel.", Podolsk, 1993.
5. Nikolaev, Yu.V. "RI SIA "Lutch"s R&D in the Area of Direct Conversion NPS Materials." Report at the 4th Branch Conference "Nuclear Power in the Space. Materials. Fuel.", Podolsk, 1993.
6. Rakitskaya, E.M., Galkin, E.A., and Gontar, A.S. "Fabrication and Tests of Modified Uranium Dioxide Pellets." Executed under contract between RI SIA "Lutch" (Russia) and Babcock & Wilcox 1993, Advanced Uranium Thermionic Fuel. RDD: 93:62411-001:01.
7. Nikitin, V.P., Ogloblin, B.G., Lutov, Ye.I., et al. "Program on the TOPAZ-2 system preparation for flight test." *Proc. 10th Symposium on Space Nuclear Power and Propulsion.* Albuquerque, 1993, part 2, pp. 741-746.
8. Hoth, C.W., Degaltsev, Yu., Gontar, A., and Rakitskaya, E. "Design and performance of the UO_2 fuel for the TOPAZ-2 reactor." *Proc. 11th Symposium on Space Nuclear Power and Propulsion,* Albuquerque, 1994, part 1, pp. 55-61.
9. Abdrakhmanov, R.K., Belenov, V.S., Volkov, S.P., Gontar, A.S., Degaltsev, Yu.G., et al. "Generalization of TOPAZ-2 TFE/Moderator Materials

Science/Technology Study after Nuclear Power Tests in Ya-81 Prototype Plants." Report of JV "Inertec" No. SP-15/208, suppl. 4, 1994.
10. Degaltsev, Yu.G., Gontar, A.S., Kostochka, N.V. et. al. "Post-Irradiation Investigation of Processes within Uranium Dioxide Fuel of Single-Cell TEC." Report at the Branch Jubilee Conference "Nuclear Power in the Space". Obninsk, 1990.
11. Degaltsev, Yu.G., Kuznetsov, V.F., Ponomarev-Stepnoy, N.N., and Slabki, V.D.. "Post-reactor research and lifetime prediction for TOPAZ-2 system." *Proc. 12th Symposium on Space Nuclear Power and Propulsion.* Albuquerque, 1995, part 1, pp. 523-527.
12. Nikolaev, Yu.V., Vibivanets, V.I., Izhvanov, O.L., Gontar, A.S., et al. "Tests of Structural and Fuel Materials in TFEs in Research Reactor Loop Channels." Report at the 4th Branch Conference "Nuclear Power in the Space. Materials. Fuel". Podolsk. 1993.
13. Ryzhkov, A.N., Bologov, P.M., Vizgalov, A.V., et al. "The Experience in Elaboration of Structural and Fuel Materials for the TFEs of Thermionic Reactors Converters, at Institute of Physics and Power Engineering. Report at the 4th Branch Conference "Nuclear Power in the Space. Materials. Fuel". Podolsk. 1993.
14. Sinyavsky, V.V., Karnaukhov, A.S., Almambetov, A.K., et al. "Comparative In-pile Investigations in a Single Loop Device of Several Multi-Cell TFEs with Different Design Solutions for the Fuel/Emitter and Gas Exhaust Units." Report at the 4th Branch Conference "Nuclear Power in the Space. Materials. Fuel". Podolsk. 1993.

CHAPTER 7

ACCELERATED TESTS OF MATERIALS AND FUEL ELEMENTS: METHODS AND RESULTS

Because of the long life required for the power systems under development, methods and results of accelerated fuel-element tests are especially important. The problem of developing such techniques is considered from two viewpoints at the institute:

- from the standpoint of accelerated debugging of the fuel element design, e.g., the efficacy of decisions made at this stage, aimed at prolonging TFE life, must be analyzed expeditiously and objectively;
- from the standpoint of the necessity to experimentally ascertain, using accelerated tests, TFE operability during the lifetime specified by a given task.

Each of these problems is multifaceted and requires solution of a broad scope of problems, from methods for accelerated study of materials and units to the TFE as a whole. RI SIA "Lutch" has accumulated wide experience in such investigations, many of which are connected to the solution of the major problems in providing a long TFE life, such as prevention of short circuits in the electrodes.

The problems related to accelerated testing may be categorized in two groups:

- methods aimed at immediate study of emitter behavior, measurement of its deformation, and prediction of time until short circuit;
- methods for investigating fuel swelling, i.e., illuminating the root cause of emitter deformation, and determination of quantitative swelling parameters and their changes during operation.

The main problem in developing such methods is that, at present, there is no adequately reliable criterion for correct transfer of data from the accelerated tests, which occur as a rule under the effect of complex changes in the life-controlling processes, to standard operating conditions for fuel elements.

Development of methods for accelerated tests was directed at providing consistency between test and standard conditions, primarily for temperature, since elevated temperature promotes many processes that determine the fuel irradiation behavior and emitter deformation state (structural transformation, mass transfer, gas evolution, creep, etc.) [1-3].

7.1. Accelerated Tests of Fuel Samples

Application of a method for in-pile accelerated tests of fuel samples [1, 2] enables acceleration of the power output level (and, consequently, burnup rate) by several times within the fuel samples. The rated temperature difference on the

sample is maintained in the course of tests. The technique allows discrete values of swelling depending on the burnup to be obtained.

With the goal of maintaining the given temperature conditions, the tests are performed using undersized specimens in relation to the thermionic fuel element's diameter. To encapsulate the test specimens, thin-walled shells of non-strengthened materials are used, providing data on the free swelling of the fuels under study.

To investigate the burnup effect on swelling kinetics, the irradiating device structure allows successive insertion of fuel samples into the irradiating zone in the required time period. To choose an optimal time step for sample insertion into the irradiation zone, a continuous measurement of GFP release from the fuel is performed during testing. The irradiating device is diagrammed in Figure 7.1.

Cylindrical specimens (1), encased in thin-walled shells of single-crystal molybdenum or tungsten (2), are placed within a case (3) in an inert gas medium. The specimen's and case's cavities communicate to relieve the shells of unilateral pressure. A gap between the shells and case is chosen to be wide enough that specimen swelling will not exert any appreciable effect on heat transfer. The case is equipped with an offsetting volume (4), the value of which is chosen to maintain a preset temperature on the specimens under irradiation, notwithstanding the reduction of power output within them (because of U^{235} burnup) and migration of krypton and xenon (inert gases having low thermal conductivity) into the heat-transferring gap. Autonomous capsules (5) contain non-clad fuel samples (6) to measure GFP release. Gas communications (7) connect the capsules (5) with a gamma-spectrometric test stand, analyzing the amount and composition of released krypton and xenon radionuclides. Gages (8) are attached to the samples to control their temperature. The power output within the specimens is monitored using beta-emission gages of neutron flux (9). The specimens (1) are inserted into the irradiating zone by autonomous drives (10). Simultaneous arrangement of several cases (3) and capsules (5) corresponding to them within the device allows comparative tests of various fuel types to be conducted or different irradiation temperatures to be used.

The temperature measurement error is ±25°C. U^{235} burnup is determined using beta-emission neutron-flux gages, taking into account a calculated value of the flux depression on the fuel samples and structural elements of the device. During post-irradiation investigations, the burnup is defined more exactly from the buildup of zirconium, ruthenium, and cerium radionuclides, with a ±12% accuracy. GFP release is determined by gamma-spectrometric methods with a ±25% accuracy.

The irradiation swelling was studied after completion of irradiation by measuring the diameter of both clad specimens and the fuel pellets proper using a shadow microscope with a ±0.005-mm error, as well as by measuring their density by a hydrostatic technique with a ±0.03 g/cm^3 accuracy.

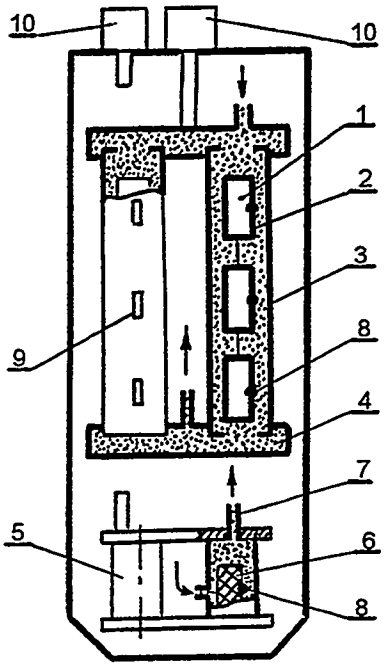

Figure 7.1. Schematic diagram of device for in-pile tests of fuel samples [1].

The structure and phase stability of fuel samples was investigated using metallography and x-ray analysis. The magnification for metallographical polished sections was 50 to 1000x.

Using this method, comparative investigations of free swelling and the kinetics of GFP release from oxide, nitride, and carbide fuel samples were performed. Results are included in Chapters 6 and 8.

7.2. Time-Limited Testing Technique for TFE Life Length Forecast

A technique for predicting TFE lifetime using results of the time-limited tests [3] uses in-TRC-prototype tests of TFEs and results of their subsequent post-irradiation investigation to gain information about kinetics of the change in emitter diameter during operation.

TFE tests using this technique are performed under conditions corresponding to those rated for NPS operation. Therefore, prediction of TFE operability beyond a time reached in testing is feasible by extrapolating the data obtained, without inclusion of any model conceptions or calculational procedures.

Meeting the same goal with traditional TFE test results is difficult. Specifically, TFE loop tests also allow study of the emitter deformation state and IEG change kinetics, e.g., by repeatedly removing the TFEs from the reactor and examining them by neutronographic methods, but in such tests it is impossible to provide temperatures completely corresponding to standard conditions. In addition, the tests are accompanied, as a rule, by significant number of thermal cycles deriving from scheduled startups and shutdowns of the research reactor, alterations of its power, emergency protection system actuation, etc. All this leads to a distortion of the emitter irradiation behavior and complicates the application of the results to standard conditions. On the other hand, in-TRC tests of TFEs occur under conditions consistent with standard conditions. However, TFEs are united within the TRC into a single nondetachable system, which excludes the possibility of studying the development of short-circuit-related malfunctions in time, if such tests are performed in a traditional way.

To investigate emitter deformation under conditions most similar to the operational standard, and to improve, in this way, the fidelity of the lifetime forecast, the following technique has been developed for TFE testing in an experimental TRC [3]. In principle the technique has no restriction with respect to TFE design performance and can be applied to testing both single and multi-cell TFEs.

In designing and fabricating an experimental TRC, individual emitter and collector current terminals are foreseen for the reactor operating section circuit of series-connected TFEs (at least two TFEs).

In preparing the TRC for tests, individual electric loading devices are installed in the test stand systems. Their number equals the number of TFEs having additional current terminals, and electrical resistance must satisfy the relationship

$$\frac{V_{TFE}}{I_{TFE}\left(R_L + R_T\right)} \geq 10-100 \ ,$$

where: V_{TFE}(V) - value of operating output voltage of TFEs having no individual current terminals in TRC;

I_{TFE}(A) - value of operating current of TFEs, having no individual terminals;

R_L(Ohm) - electrical resistance of individual loads;

R_T(Ohm) - electrical resistance of individual terminals.

Bringing the TRC to operational values of output current and voltage and subsequently maintaining these parameters at a preset level is accomplished with the aid of a major loading device, common for all the TFEs in the reactor operating section. In the course of tests, the TFEs with individual terminals are in turn connected to the individual loads. As a result, the output current of the TFE increases to values that reduce emitter temperatures to levels at which deformation practically no longer occurs. The output current of TFEs not connected to the individual loads is restored to a specified level using the main load.

After completion of TRC tests, TFEs both with and without individual terminals are disassembled, and emitter diameters are measured. Measurement results reveal how the increase in emitter diameter depends on irradiation time and allow TFE operability until time of short circuiting to be predicted.

7.3. References

1. Gontar, A.S., Gutnik, V.S., Zaitsev, V.A., et al. "A Method and Results of Comparative Irradiation Tests of High-Temperature Fuel Samples." Report at the 4th Branch Conference "Nuclear Power in the Space. Materials. Fuel." Podolsk, 1993.
2. Gontar, A.S., Gutnik, V.S., Nelidov, M.A., and Nikolaev, Yu.V. "Swelling of uranium dioxide and deformation behaviour of the fuel element at high temperature irradiation." *Proc. 28th Intersociety Energy Conversion Engineering Conf.*, 1993, v.1, pp. 549-553.
3. Gontar, A.S., Karpov, A.A., Korolev, V.U., and Nelidov, M.V. "Method of Tests of TFEs. - Affirmative conclusion on invention application No. 4935901/21/040436 of 15.04.92 (priority of 15.05.91).

CHAPTER 8

PROMISING FUEL COMPOSITIONS: CURRENT DEVELOPMENT STATUS, PROPERTIES, AND POSSIBILITIES OF USE

Most projects using thermionic fuel elements include uranium dioxide as the nuclear fuel. Uranium dioxide has good compatability with molybdenum and tungsten, used in TFE emitters for the entire emitter operating temperature range. The oxide-fuel fabrication process is best developed, as well, and is widely infused into commercial production practice.

A major disadvantage of the oxide fuel is its low thermal conductivity, leading to high temperatures in the central section of the fuel element. The high evaporation rate of uranium dioxide at temperatures reached in the central section of the TFE means that as-fabricated fuel-stack geometry is transformed to a configuration comprising a closed central cavity over periods short in comparison with lifetime. Gaseous fission products accumulate within the closed cavity and bring about fuel-element deformation and its rapid failure. In addition, the high evaporation rate of uranium dioxide can result in an intolerably high level of fuel loss from the fuel element. To avoid these phenomena when using the oxide fuel, a ventilating system is needed, which considerably complicates the fuel element design. Here remains the principle restriction on fuel-element heat power level that is not connected with the fuel melting point, namely: destruction of the gas-exhaust system is possible by its reaction with oxygen contained in the gaseous phase over the oxide fuel. In design decisions made to ensure fuel-element operability, RI SIA "Lutch" intensively studied the possibility of building fuel elements on the basis of alternative fuel materials. Efforts took two directions: improvement of uranium dioxide, and the possible use of high-thermal-conductivity fuels based on uranium nitrides, sulphide, phosphides, and carbides. Results are presented below.

8.1. Development and Study of Hypostoichiometric Oxide Fuel with Stabilized Open Porosity

As known from the theory of free-molecular flow, the intensity of mass flux is enhanced proportionally to a characteristic channel size, e.g., within a long cylindrical channel, the flux is proportional to cubed radius [2], and so the flux density is proportional to the channel radius. The same is true when a substance being evaporated from the channel walls is transferred [3]. Thus if a system of microchannels with a several-micron characteristic transverse size is used for fuel-element ventilation (instead of a single free macroscopic central channel several millimeters in diameter), the intensity of fuel transfer may be lowered by about 3 orders of magnitude. The system of microchannels can be organized as an open

porosity. It is known from the literature (see Figure 3.1) that a porosity of ~10% is already predominantly open, but the usual highly porous uranium dioxide is prone to densification and, if the porosity reduces to ~5%, it is mainly closed. The related literature contains a significant number of works dedicated to the investigation of additional uranium-dioxide sintering under irradiation (e.g., [4-7]). Notwithstanding a wide diversity of initial structures, porosities, pore-size distributions, and irradiation conditions, the investigation results lead to some general conclusions, principally that a rapid additional sintering occurs, mostly due to liquidation of submicron-range pores, with no decrease in the volume of pores with diameters in excess of 3 μm. A study [5] of the irradiation behavior of fuel with ~8% porosity, comprising mainly pores over 10 μm in diameter, showed high dimensional stability of the fuel and maintenance of its initial density under irradiation up to 0.16% at. burnup.

The cited experimental data indicated the feasibility of creating uranium dioxide possessing interlinked porosity resistant to sintering at operating temperatures and under in-pile irradiation. In the 1980s and early 1990s, RI SIA "Lutch" developed a fabrication process for uranium dioxide with a stabilized open porosity [8]. The uranium-dioxide pellets with stabilized open porosity are manufactured by methods of powder metallurgy. The fabrication process includes preparation of powder, molding, sintering, machining, and annealing [8] and produces pellets with a required porosity and preset value of oxygen coefficient O/U. Rakitskaya et al. [9] provided results of investigations of the thermal stability of six batches of uranium-dioxide pellets having various combinations of porosity and O/U values. The tested pellets were heated in high vacuum with a 400 K/hr rate up to temperatures of 1600 and 1800°C and held at these temperatures for 10 hrs. Pellets were cooled at the same rate and examined with respect to their porosity change. Results are given in Table 8.1.

The investigations showed that the closed porosity within the matrix material of pellets with open pores is about the same as the closed porosity within pellets containing no open pores. The open porosity was measured using mercury porosimetry. The measurement error was ±0.5%. As seen from Table 8.1, annealing the hypostoichiometric samples at 1600° appreciably decreases the open porosity, while after annealing at 1800°C, the open porosity remains close to the initial porosity. This unexplained result [9] suggests the need for further investigations. O/U remains close to the initial value. The annealed pellet microstructure did not undergo any essential modification.

The study of the properties of uranium dioxide with stabilized open porosity revealed that it has a number of substantial merits compared with dense uranium dioxide [8]. Uranium dioxide with stabilized open porosity has a swelling rate 2.0 to 2.5 times lower than the dense uranium dioxide's. In addition, the porous uranium dioxide is a "soft" fuel; its creep rate is 3 to 8 times higher than that of high-density uranium dioxide.

Table 8.1. Porosity after heat annealing [9]

Batch No.	O/U	Total Porosity, %	Test Temperature °C	Open Porosity, %	Closed Porosity, %	Deadlock Porosity, %
				2.0	1.8	
1	2.004	3.8	1600	1.8	2.0	
			1800	1.8	2.0	
				7.7	1.8	2.9
2	2.003	12.4	1600	7.7	2.0	3.1
			1800	9.1	2.0	3.1
				14.3	1.8	2.8
3	2.004	18.9	1600	13.1	2.0	3.8
			1800	14.0	2.0	2.9
				1.0	2.1	
4	1.995	3.1	1600	0.9	2.2	
			1800	<0.9	<2.2	
				8.2	2.1	0.1
5	1.997	10.4	1600	6.0	2.2	2.2
			1800	6.7	<2.2	<1.5
				16.2	2.1	0.8
6	1.995	19.1	1600	11.7	2.2	5.2
			1800	15.5	<2.2	1.4

The lack of additional heat-induced or irradiation-induced sintering of uranium dioxide does not, however, mean that as-fabricated open porosity will be maintained in pellets for a long time under any operating conditions. Under operating conditions, significant temperature gradients exist on the pellet radius, and for short fuel elements (multi-cell design), considerable temperature gradients are also present in the axial direction at the ends. Porosity migration in the temperature gradient can lead to loss of pores to the central cavity and the formation of a high-density fuel layer with reduced permeability to gaseous fission products. Thus, the applicability of stabilized-open-porosity fuel is restricted to temperature conditions in which appreciable departure of the initial pores from the fuel does not occur within the required lifetime.

An experimental and calculational study of stabilized-open-porosity uranium-dioxide pellet behavior [10] was carried out using mock-up fuel elements with a central heater. The as-fabricated structure of the fuel under study [10], shown in Figure 8.1a, is characterized by a high-density matrix (density >96% TD). The intramatrix pore size is ~3 μm. Among separate matrix pieces, large pores, inter-linked through pore-channels, are sited fairly uniformly. The maximum diameter of large pores is 30 to 50 μm. The large pores and channel pores constitute the open porosity, the value of which is close to 10%. Figure 8.1b shows the structure

Figure 8.1. Structure of tested uranium dioxide:
a - as-fabricated;
b - after testing.

of uranium dioxide after testing. The pellet's central section has columnar grain structure. The porosity in this section is far lower than the initial porosity and is, to a considerable extent, arranged as microchannels located around the columnar-grain boundaries. In the next zone, a significant extension of large pores along the temperature gradient is observed. Near the pellet's outer surface, uranium dioxide maintains its as-fabricated structure. Figure 8.2 illustrates the kinetics of the uranium-dioxide pellets' integrated porosity change at the pellets' central temperature of 2205°C and outer surface temperature of 1815°C. The sharp reduction in the rate of change in porosity on the initial stage of the curve in Figure 8.2 is mainly connected to the fact that, in the experiment with heating of the pellet's center, in the central region of the fuel not only the maximum temperature, but also a maximum value of the temperature gradient is set (the latter becomes zero on the central channel surface under reactor operating conditions). This circumstance promotes rapid pore migration from the pellets' central zone and subsequently slows the change in porosity. In further testing, within the time period of 30 to 100 hrs, the rate of change of porosity is close to constant. A calculational study of porosity behavior under experimental conditions [10] was performed using the computer code PORA, in which porosity distribution on the fuel-pellet radius was found by solution of the continuity equation for a system of non-interacting spherical equal-size pores. Pore velocity is calculated as the sum of three addends respective to three pore-migration mechanisms. For small pores, the major contribution to the pore velocity is due to fuel diffusion over the pore surface. The pore velocity arising from this mechanism is inversely proportional to the pore radius. For large pores, the main motive mechanism at high temperatures is fuel-vapor transfer via the pore volume. For vacuum pores moving under this mechanism, the velocity is proportional to their radius. A motive mechanism linked to uranium atoms diffusing from the hot to the cold side of a pore within the fuel medium does not significantly contribute to the pore velocity in uranium dioxide at high temperatures. Summation of the two velocities, one of which is proportional to 1/r and another to r, results in the dependence of the vacuum pore velocity on radius, having a minimum at some value of the pore radius.

Calculations [10] show that a minimum migration velocity is associated with pores of several μm radius (the radius of pores having minimum velocity depends on temperature). Figure 8.3 illustrates the relationship between pore radius and pore velocity [10]. Curve 1 relates to the vacuum pores, and Curve 2 to pores filled with helium under 6 MPa pressure. Helium in the pores inhibits mass transfer through the pore volume, and the major mechanism of pore movement in this case is surface diffusion for the entire range of pore sizes.

It follows from the literature [4-7] that pores having, in compliance with Figure 8.3, minimum velocities in the temperature gradient field, also do not significantly contribute to the additional thermal- and irradiation-induced sintering of fuel. Thus in optimizing the fabrication process for fuel with stabilized open

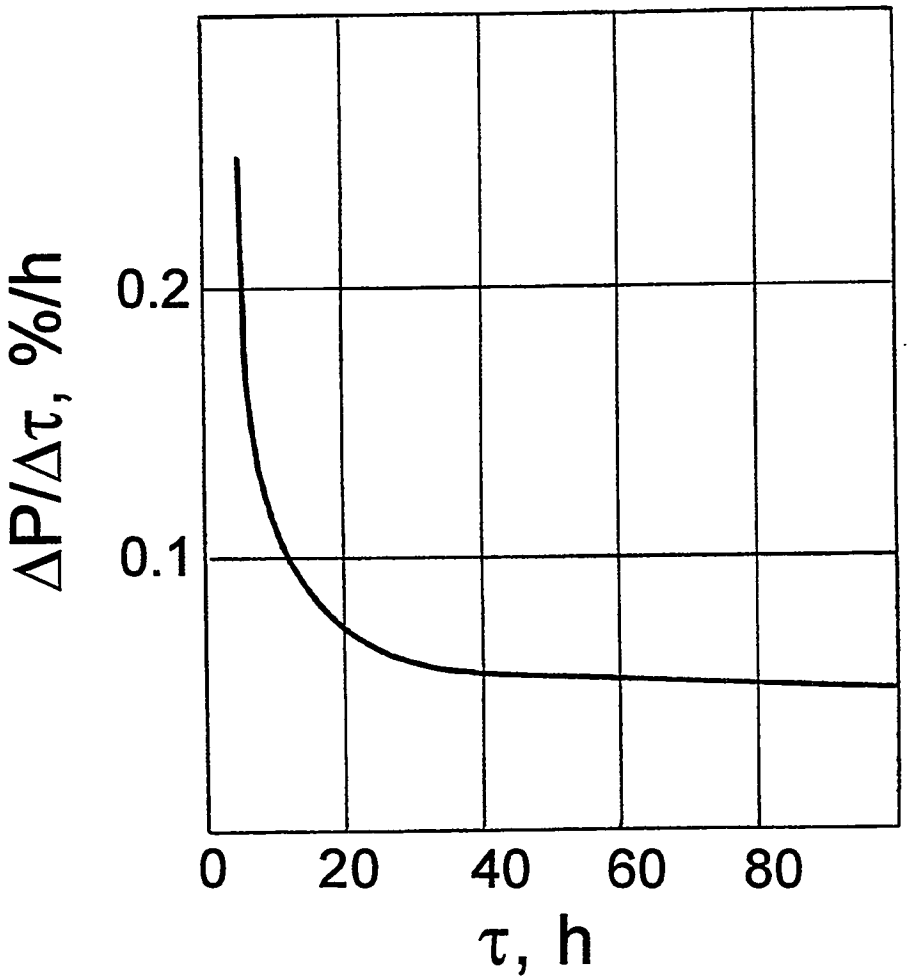

Figure 8.2. Kinetics of porosity change for uranium dioxide with prevailing macropores at 2010°C mean temperature [10].

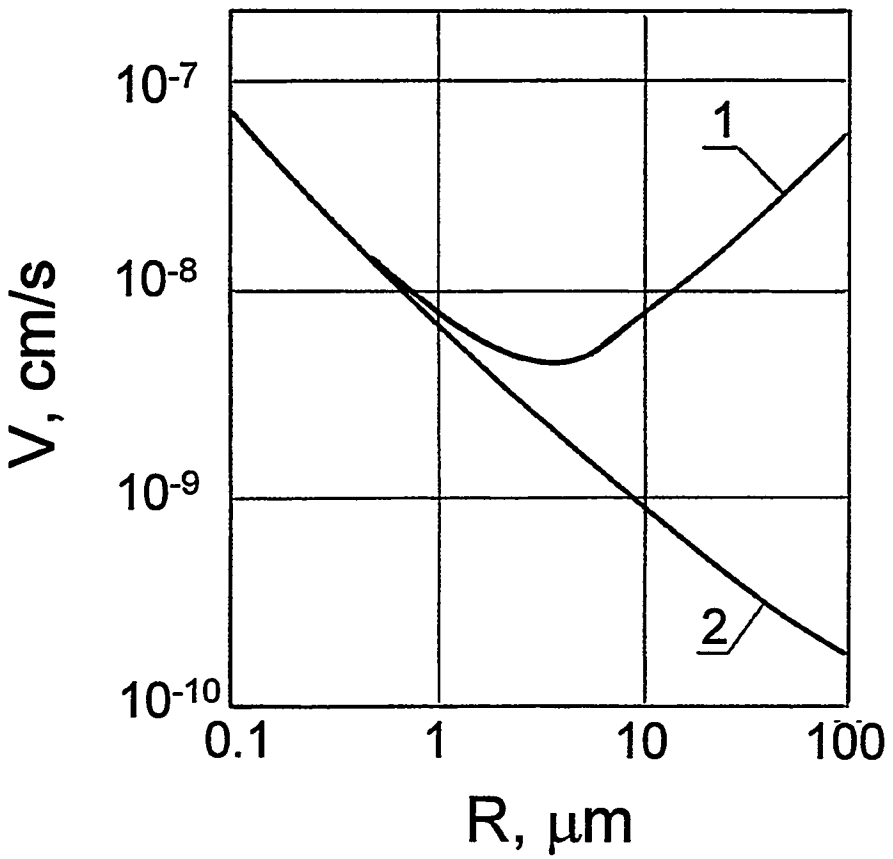

Figure 8.3. Relationship between radius and pore movement velocity:
T=2000 K, ΔT=750 K/cm
1 - P=0;
2 - P_{He}=6Mpa

porosity, the maximum in the pore-size distribution should lie in the range of pores having minimum velocities.

The porosity distribution on the fuel pellet radius [10] is presented in Figure 8.4. The data refer to the same conditions as the experimental results in Figure 8.2. Averaging the porosity distributions shown in Figure 8.4 on pellet radius provides the integrated porosity change, i.e., the value being measured in the experiment. The calculated values of pellet integrated porosity change differ from those experimentally measured by not more than a factor of 2 [10]. Qualitative consistency of the calculated and experimental results under conditions of intense forcing of the temperature justifies the application of the PORA program to lower temperatures, where an experimental study of the porosity change would call for long experiments and prediction of porous-fuel behavior under TFE conditions. A calculation forecasting porosity behavior within uranium-dioxide pellets [11] used the model described above. The area of a heightened uranium-dioxide porosity applicable to cases of 1-year and 3-year lifetime is displayed in Figure 8.5. It is conditionally assumed that the higher-porosity fuel is applicable if power output in the outer annular zone, entirely pore-free, does not exceed half the overall power release and the rest of the fuel-stack medium maintains a porosity not less than ~5%. As seen from Figure 8.5, the area of long-term existence of the initial porosity covers only moderate temperatures and power release densities. Beyond this area, the advantages of the porous fuel are maintained only for a part of the lifetime.

8.2. Promising High-Temperature Fuel Compositions for Thermionic Fuel Elements and Their Properties

In view of the important restrictions on the cladding temperature and heat power of thermionic oxide-fuel elements, RI SIA "Lutch" has performed a great deal of work on the possible application of alternative high-temperature fuel compositions to the thermionic fuel elements.

Among high-temperature uranium monocompositions, its nitride and carbide possess the highest density of uranium and have a number of other merits in comparison with uranium dioxide. They have high thermal conductivity, about an order of magnitude better than uranium dioxide's, and a lower evaporation rate. Each of these compounds has its own disadvantages, however, making their use in the pure state as TFE fuel difficult.

For example, within the operational temperature range of the emitter, uranium carbide reacts appreciably with materials based on tungsten and molybdenum,

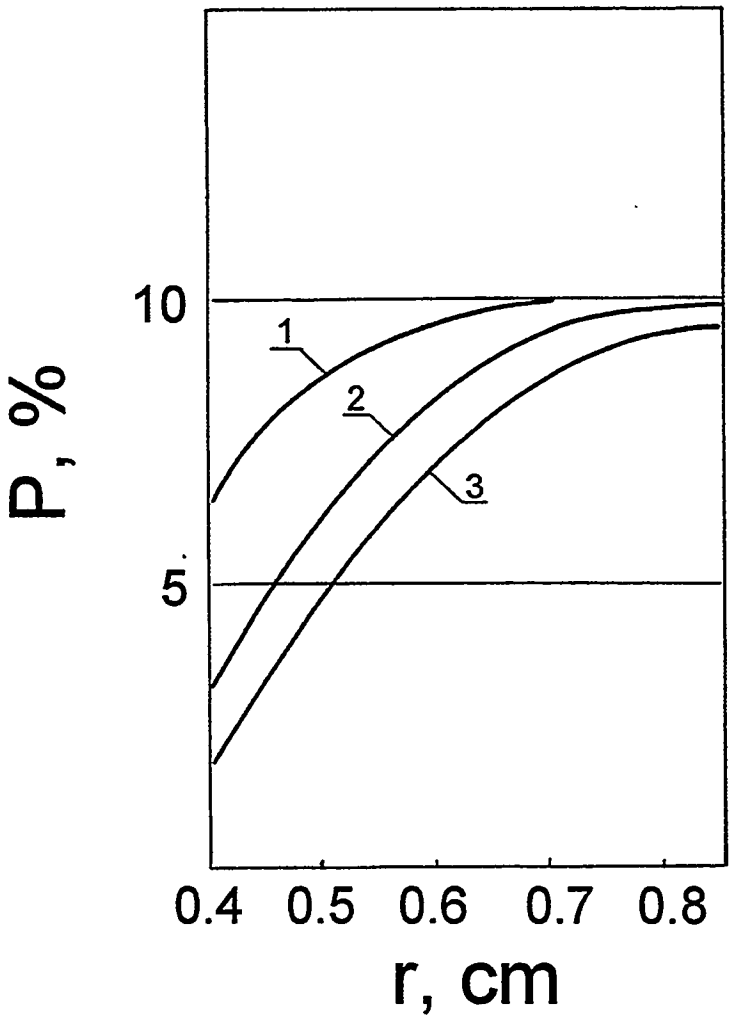

Figure 8.4. Calculated distribution of porosity on fuel pellet radius under experimental conditions at T=2010°C:

1 - τ=10hrs;

2 - τ=50 hrs;

3 - τ=100 hrs.

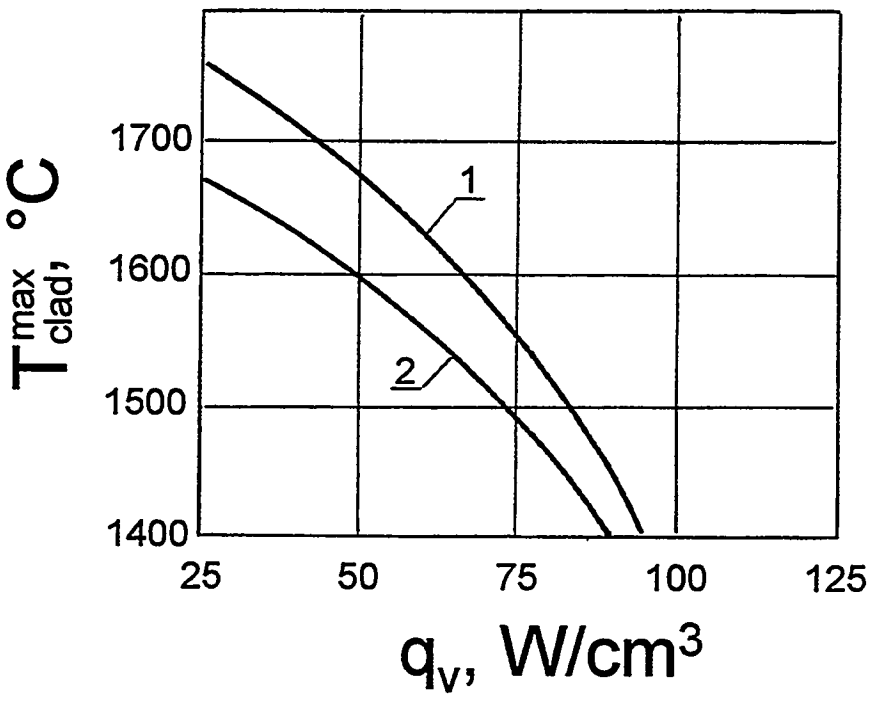

Figure 8.5. Upper boundary of the area of $UO_{2.000}$ with increased initial porosity applicable to fuel stack during 3-year life (Curve 2) and 1-year life (Curve 1).

which serve as the main emitter materials. UC starts carbidizing tungsten even at 1000°C [12]. After a 1300-hr hold, a layer of W_2C 0.5 μm thick was recorded. At high temperatures, the intensity of carbidization is sharply enhanced. At 2000° C for 30 hrs, W_2C-layer thickness grew to 383 μm [13]. The molybdenum carbidization rate is much higher than tungsten's; after a 3600-hr hold at 1200°C, the Mo_2C-layer thickness was 150 μm [14].

In UC-Mo and UC-W systems, peritectics are formed, with melting points of 1850 and 2150°C, respectively [14]. The UC-Mo system's relatively low peritectic temperature, close to the maximum operational temperatures of the emitter, essentially rules molybdenum out of consideration as an emitter material for carbide-based fuel elements. Uranium nitrides' basic disadvantage is their incongruent evaporation behavior and narrow area of homogeneity. In investigations of uranium nitride, $UN_{0.985}$ is accepted as the homogeneity area's lower boundary at temperatures consistent with the level of TFE fuel operating temperatures of ~1700°C [15]. These investigations revealed that for such a composition of uranium nitride, the nitrogen partial pressure exceeds the uranium partial pressure by about four orders of magnitude (in the homogeneity area, this divergence is still broader). These data show that if uranium nitride is applied to ventilated fuel elements of the thermionic convertors, its composition can shift to the lower boundary, and the amount of liquid uranium within the TFE will increase.

In view of the fact that uranium monocompositions do not meet the aggregate of requirements for the fuel material of high-power thermionic fuel elements, the development of promising fuels was aimed at creating complex compositions that conserved the virtues of their constituents. If uranium monocarbide is taken as a basis, the work may be considered to run in two directions. The first direction is partial substitution of niobium, zirconium, and tantalum for the metallic component of the fuel. The unit cell dimensions of the carbides of these metals are close to those of the UC unit cell, which is 4.96 Å for the stoichiometric composition; the difference does not exceed 5 to 10% [16]. Therefore, at high temperatures, formation of a continuous set of solid solutions is observed in U, Nb, Zr, and Ta mixed carbides [14, 16]. Since zirconium, niobium, and tantalum carbides have a wide area of the single phase state, introducing them into uranium monocarbide expands the latter's homogeneity area. Uranium monocarbide crystal lattice constant decreases with increased concentration of the other carbides [14, 16].

The second direction of work relating to improving the compatability of the carbide fuel with cladding materials involves alloying it with uranium mononitride dopants. Because UC and UN have similar type crystal lattices with close geometric dimensions, they form a continuous set of solid solutions [14, 16, 18], but introducing mononitride into uranium monocarbide narrows the homogeneity range further still. Hence, the prospective nuclear fuels are carbonitrides of type $U_{1-y}Me_yC_{1-x}N_x$, in which the homogeneity area expands with substitution of

atoms of the IVA-VA periodical system subgroups (refractory metals) for some of the uranium atoms.

Uranium monosulphide possesses much better compatability with refractory metals than uranium monocarbide [19]. RI SIA "Lutch" has performed a large scope of efforts to advance the fabrication process for and to study properties of uranium carbosulphide [8, 20-25].

8.2.1. Properties of High-Temperature Fuel Compositions

Proceeding from calculational, theoretical, experimental, and processing and materials science-related research, the following requirements have been specified for the high-temperature fuel of thermionic power plants:

- high uranium content per unit volume of fuel;
- high melting points and thermal conductivities;
- low saturated vapor pressures and evaporation rates;
- thermal and thermochemical stability;
- compatability with structural materials of high-temperature fuel elements; and
- dimensional and phase stability under irradiation during a long lifetime (up to 10 years).

For the nitride, carbide, carbonitride, and carbosulphide fuel compositions developed, trial specimens and articles for comprehensive out-of-pile and in-pile tests were fabricated following the available processes. Table 8.2 summarizes data on the developed materials' basic properties [8, 14, 22-27].

Data on structural characteristics and ranges of stable phase existence of high-temperature carbide fuel compositions are given in Table 8.3. All the compositions have face-centered cubic crystal lattice of NaCl-type and exist stably within the entire temperature range from room to melting point.

In the work of Nikolaev [8], some of the important characteristics are presented as diagrams for easy comparison among a number of fuels. Creep rates for a variety of uranium dioxide and alternative fuel compositions are compared in Figure 8.6. Uranium carbosulphide has the highest creep rate, and carbide solid solutions, the lowest.

An important property determining the conservation of the configuration of the fuel stack with time is the fuel evaporation rate. Temperature dependence of the integral evaporation rate from the open fuel surface is shown in Figure 8.7 for uranium dioxide and alternative fuel compositions. Data on dependencies approximating the integral evaporation rate for carbide fuel compositions are contained in Table 8.4.

As seen from Figure 8.7, the (UTa)C carbide solid solution has the lowest evaporation rate. The carbide fuel compositions' low evaporation rate, combined with high thermal conductivity that provides a low temperature in the fuel-stack

Table 8.2. Main properties of fuel materials

Fuel	Uranium Content, g/cm_3	Melting Point, K	Thermal Conductivity at 2270 K, W/m·K	Coefficient of Thermal Expansion 300-1500 K, $\cdot 10^{-6}$, 1/K	Rate of Creep at 40 MPa and 2300 K, %/hr
UC_2	9.67	2770	21.6	13.0	2.5
$U_xZr_{1-x}C$	9.5 to 11.7	3170-3370	17-18	11.8-13	$5\text{-}8\cdot 10^{-2}$
$U_xTa_{1-x}C$	10-11	3170-3270	25-27	9.8-10	$3.6\text{-}7.7\cdot 10^{-1}$
$U_xZr_{1-x}CN$	9.7 to 12.2	3070-3170	30-37 [26] 20 [23]	10.8-11.2	0.7-1.0
UC_xS_{1-x}	10.3 to 10.5	2810	16*		20**
UN	13.63	3120	20*		2.5**

* - at 2170 K;
** - at 1970 K.

Table 8.3. Structural parameters and stable phase existence ranges of high-temperature fuel compositions [26]

Compound	Lattice Spacing, nm	Density of Uranium, g/cm^3	C/Me Ratio in Boundaries of Homogeneity Range at Temperature, K	
			2100	2300
UC	0.49605	12.952	0.92-1.08	0.90-1.15
$U_{0.8}Zr_{0.2}C$	0.4908	10.13	0.86-1.06	0.84-1.12
$U_{0.7}Zr_{0.3}C$	0.4882	8.94	0.83-1.05	0.82-1.11
$U_{0.8}Ta_{0.2}C$	0.4859	10.59	0.89-1.06	0.87-1.12
$U_{0.7}Nb_{0.3}C$	0.4812	9.59	0.87-1.05	0.85-1.11

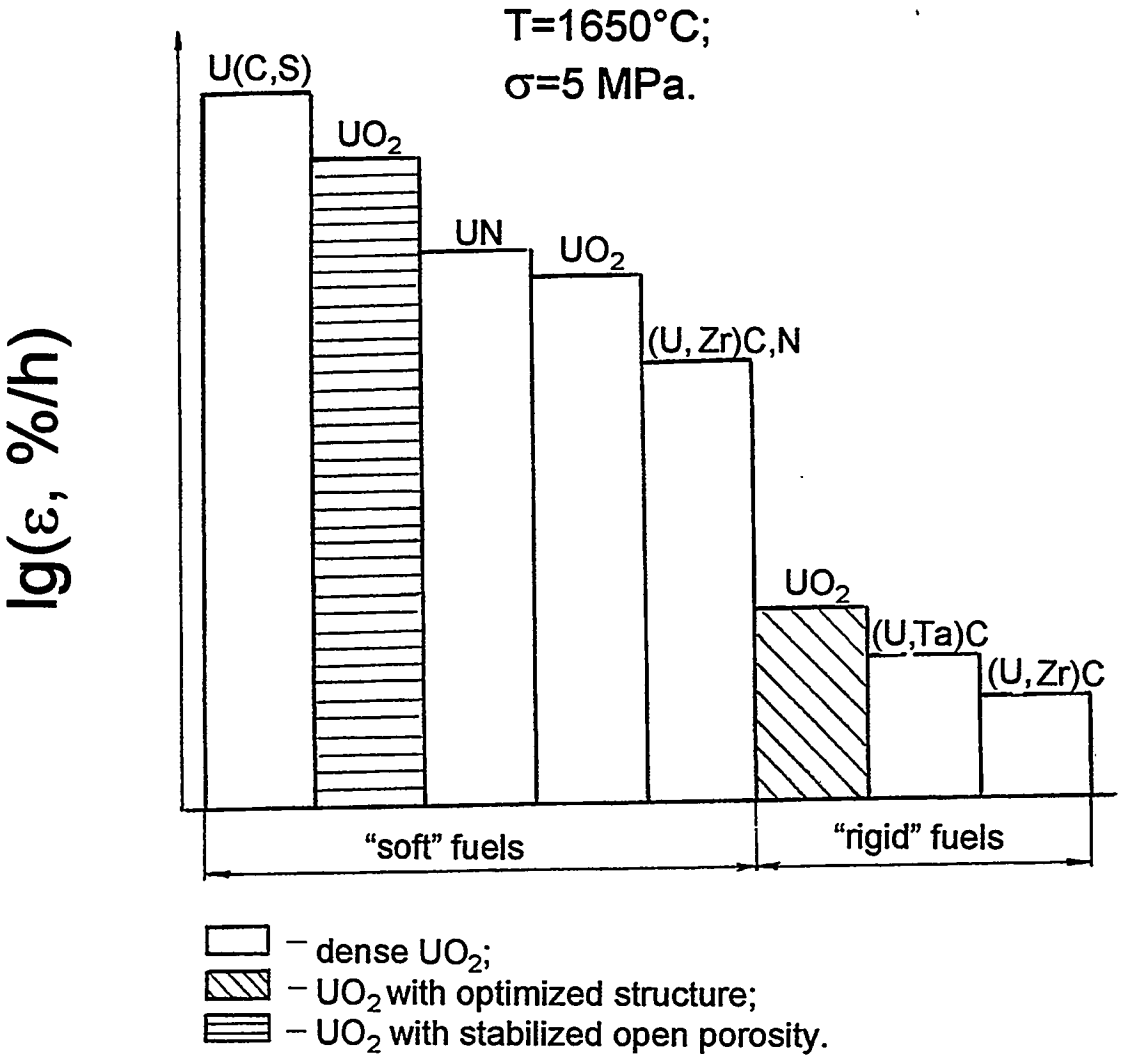

Figure 8.6. Creep rates of UO_2 and alternative fuels.

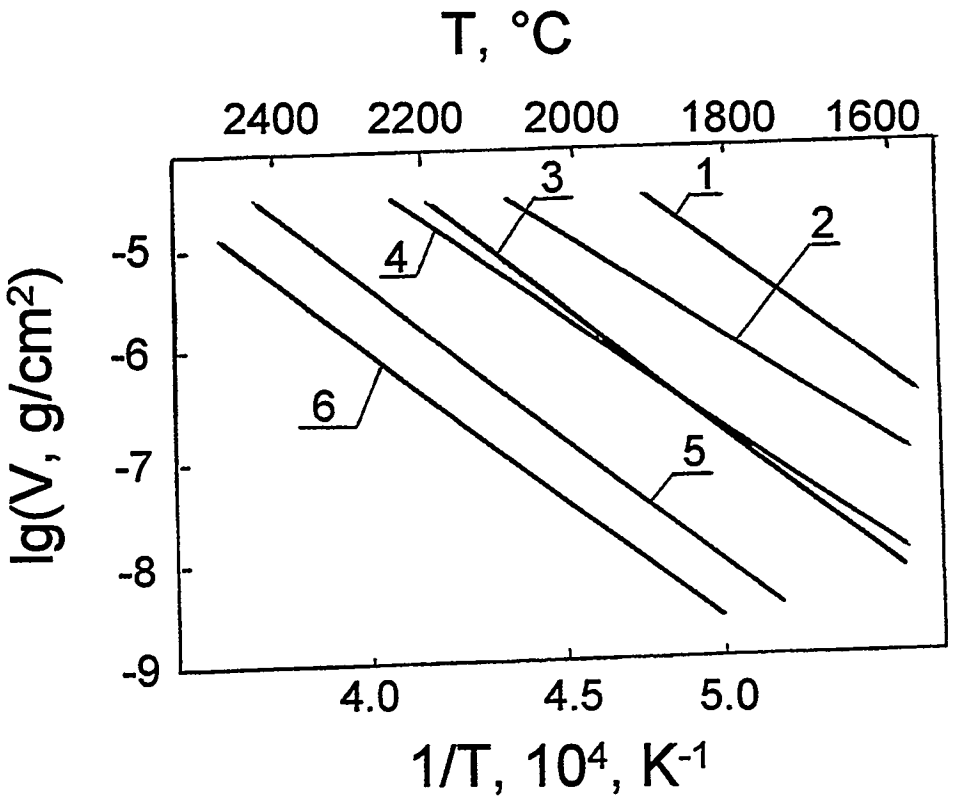

Figure 8.7. Integral rate of evaporation from fuel compositions' open surface [8].

1 - UO_2
2 - UN
3 - (U,Zr)C,N
4 - U(C,S)
5 - (U,Zr)C
6 - (U,TA)C

Table 8.4. Temperature dependence of integrated evaporation rate for carbide composition [26]

Carbide Fuel	$\lg v(g/cm^2 \cdot s)=A+B/T$	
	A	B
$U_{0.8}Nb_{0.2}C$	5.22	-26100
$U_{0.2}Zr_{0.8}C$	5.30	-30300
$U_{0.5}Zr_{0.5}C$	6.71	-31200
$U_{0.9}Zr_{0.1}C$	6.72	-30500
$U_{0.8}Ta_{0.2}C$	6.62	-31100

center as compared to an oxide-fuel-based stack, makes possible the creation, using carbide fuels, of a fuel stack that maintains its configuration near the initial condition for its entire life. Stack-configuration maintenance permits simplification of the related fuel-element design by use of the free central channel for ventilation. For evaporated carbide solutions, the congruently evaporating compositions are absent [20]. Evaporation from the open surface preferentially removes uranium, and as a result, enriches the surface with zirconium and tantalum atoms. At the same time, the condensate, deposited on a cold surface, must have U/Me (where Me is Nb, Ta, or Zr; see Tables 8.3 and 8.4) ratio higher than in the initial carbide. The incongruent evaporation behavior of $U_{1-y}Me_yC$ solid solutions complicate their long-term use at high temperatures in vacuum and must be taken into consideration in developing fuel elements.

8.2.2. Interaction between Fuel and Cladding Materials

If uranium carbide-based fuel compositions are used, tungsten or its alloys are expected to be used as the emitter material. The carbide fuel interaction with tungsten comprises the following processes:

- cladding carbidization caused by development of exchange-type reactions;
- formation of liquid phases at the contact interface;
- appearance of triple and more-complex carbides, $U_xMe_yW_zC_2$;
- diffusion of (UMe)C fuel components into the cladding and their movement toward the outer surface; and
- tungsten diffusion into the carbide fuel.

Generalized experimental data on carbide fuel and tungsten interaction are provided in Table 8.5.

Table 8.5. Interaction between tungsten and $U_{1-y}Me_yC_{1+x}$ solid solutions [26]

Composition	T, K	τ, hrs	Result of Interaction
$U_{0.2}Nb_{0.8}C$	1923	1.0	Very slight interaction
$U_{0.12}Zr_{0.88}C_{0.93}$	2023	973	No interaction
$U_{0.12}Zr_{0.88}C_{0.93}$	2073	50	Slight diffusion U,Zr, C →W
$U_{0.12}Zr_{0.88}C_{0.93}$	2273	10	Slight diffusion U,Zr, C →W
$U_{0.67}Zr_{0.33}C$	2353	18	No interaction
$U_{0.67}Zr_{0.33}C$	2443	0.4	No interaction
$U_{0.67}Zr_{0.33}C$	2513	0.03	Very intense interaction
$U_{0.67}Zr_{0.33}C$	2700	0.2	Very intense interaction
$U_{0.7}Zr_{0.3}C_{0.97}$	1923	6500	Slight diffusion U,Zr, C →W
$U_{0.8}Zr_{0.2}C_{0.97}$	1923	6500	Slight diffusion U,Zr, C →W
$U_{0.8}Zr_{0.2}C_{0.96}$	1923	10000	Slight diffusion U,Zr, C →W
$U_{0.8}Zr_{0.2}C_{0.96}$	2173	2500	Slight diffusion U,Zr, C →W
$U_{0.9}Zr_{0.1}C_{1.07}$	1923	3300	Formation of 100 μm carbide layer
$U_{0.9}Zr_{0.1}C_{1.03}$	1923	10000	Formation of 8 μm carbide layer
$U_{0.9}Zr_{0.1}C_{1.07}$	2073	2500	Formation of 100-250 μm carbide layer
$U_{0.9}Zr_{0.1}C_{1.04}$	2173	2500	Formation of 10 μm carbide layer
$U_{0.9}Zr_{0.1}C_{0.97}$	2173	6500	Slight diffusion U,Zr, C →W
$U_{0.9}Zr_{0.1}C_{0.90}$	1923	2500	Slight diffusion U,Zr, C →W
$U_{0.9}Zr_{0.1}C_{0.96}$	2173	2500	Slight diffusion U,Zr, C →W
$U_{0.68}Ta_{0.32}C_{1.0}$	2023	4000	Slight diffusion U,Ta, C →W
$U_{0.8}Ta_{0.2}C_{1.0}$	2023	4000	Slight diffusion U,Ta, C →W
$U_{0.89}Ta_{0.11}C_{0.98}$	2023	4000	Slight diffusion U,Ta, C →W

It is seen from the table that doping of uranium monocarbide with ZrC, NbC, and TaC improves the fuel/cladding system stability, and formation of interaction layers was observed only at times of ~1 year.

The upper temperature limit on the use of carbide solid solutions, $U_{1-y}Me_yC_{1+x}$, in contact with tungsten, even in short-term tests, should be assumed to be ~2400 K (Table 8.5); exceeding this temperature may bring about intense development of interaction processes, accompanied by the appearance, in the contacting zone, of liquid uranium and complex carbides of UWC_2 or $(U_{1-y}Me_y)WC_2$ type. The peritectic reaction occurring here may be represented as

$$2UC + W \leftrightarrow UWC_2 + U$$

$$2U_{1-y}Me_yC + W \leftrightarrow (U_{1-y}Me_y)WC_2 + \left(U_{1-y}Me_y\right).$$

Other authors' data suggest that the peritectic point may range from 2400 to 2450 K.

It is obvious from Table 8.5 that an essential influence on the behavior and degree of the fuel/tungsten interaction is exerted by the ratio of carbon to metal atoms. If the stoichiometric coefficient is C/(U+Me)≥1, carbidization can occur. The higher the carbon content, the sooner carbidization is observed. So, for instance, in the interaction between $U_{0.9}Zr_{0.1}C_{1.07}$ and tungsten at 1923 K, a W_2C layer built up a 100-μm thickness in 3,300 hrs, but in $U_{0.9}Zr_{0.1}C_{1.03}$ reacting with tungsten at the same 1923 K for 10,000 hrs, only an 8-μm-thick W_2C layer formed (see Table 8.5). If the stoichiometric coefficient C/(U+Me) is below 1, no carbide phases appear in the contact zone. So, for example, the $U_{0.8}Zr_{0.2}C_{0.96}$ solid solution remained stable in contact with tungsten at 1923 K for at least 2,500 hrs.

The values of the temperature of carbidization commencement in tungsten reaction with a carbide fuel were calculated for fuel compositions of $U_{1-y}Me_yC_{1-x}$ (Me=Zr, Ta; y=0.2 and 0.3) having various stoichiometric coefficients x [26]. Equalization of the chemical potentials of the carbide fuel's carbon and W_2C-carbide's carbon at the lower phase boundary of the homogeneity area was accepted as the start of carbidization. Calculation results are given in Table 8.6 [26].

Lowering of the stoichiometric coefficient from 0.99 to 0.97 causes the carbidization start temperature to rise by over 300 degrees. These data agree with the experimental results generalized in Table 8.5.

The hypostoichiometric fuel is notable for its low carbon thermodynamic activity and slow rate of carbon loss via the tungsten single-crystal cladding [26, 29]. The time needed for formation of a carbon monolayer on the anode at a tungsten-cladding temperature of 1900 K and carbon thermodynamic activity in the homogeneity range a_C=0.01 to 0.001 can be several years [28], but at this low

thermodynamic activity of carbon, the thermodynamic activitiy of uranium and its transfer through the cladding are increased, which is also undesirable. Optimization-related estimates of the fuel composition, considering the possibility of cladding carbidization and an optimal ratio between fuel component fluxes through the emitter, led to the recommended application of a carbide fuel with initial composition C/(U+Me)=0.99±0.01 to the thermionic converter fuel elements [26].

8.2.3. Irradiation Behavior of Promising High Temperature Fuel Compositions

To substantiate the operability of the high-temperature fuel materials developed at RI SIA "Lutch," in-pile comparative tests of fuel samples were performed [26]. The tests were carried out using samples with a lessened diameter in relation to the thermionic fuel-element size, which allowed the acceleration of the level of power output while maintaining mean operating temperature. Use of thin-walled non-strengthened shells for the sample casing made it possible to collect data on the free irradiation swelling of the fuel materials. Swelling was examined after irradiation by measuring the diameter both of the clad samples and of the fuel samples proper using a shadow microscope with a ±0.005-mm accuracy and by measuring their density with a ±0.03-g/cm^3 error. The structure and phase stability of the sample materials were studied by metallography and x-ray analysis. Lattice spacing of the irradiated material was determined with an error not

Table 8.6. Calculated temperatures of tungsten carbidization start in its reaction with $U_{1-y}Me_yC_{1-x}$ solid solutions [26]

Carbide	(1-x)	T, K
$U_{0.7}Zr_{0.3}C_{1-x}$	0.99	1920
	0.98	2140
	0.97	2330
$U_{0.8}Zr_{0.2}C_{1-x}$	0.99	2100
	0.98	2230
	0.97	2400
$U_{0.7}Ta_{0.3}C_{1-x}$	0.99	1980
	0.98	2230
	0.97	2420
$U_{0.8}Ta_{0.2}C_{1-x}$	0.99	2120
	0.98	2240
	0.97	2480

exceeding ±0.001 Å. The burnup was defined by determining the buildup of zirconium, ruthenium, and cerium radionuclides with a ±12% accuracy. The in-pile comparative testing procedure has been described by Gontar et al. [24].

A number of fuel modifications were tested to reveal the effect of structure and initial composition on the fuel irradiation behavior. For the uranium/ zirconium carbonitride, 8 modifications were tested, in which the nitrogen-to-carbon ratio, density, and grain size varied. Tests were carried out at 1650±50°C and 180±10 W/cm^3 power density in an inert gas environment, up to a burnup of 0.3% FIMA. The range (Δd/d) of irradiation free swelling associated with these modifications covered 1.6 to 14% per one percent of burnup. Afterwards, representative in-pile tests of an optimized composition/structure modification of the carbonitride were performed: 16 samples up to 0.8% FIMA burnup. The irradiation swelling of the modification optimized in its initial properties did not exceed 2%/% FIMA [23].

X-ray analysis data showed that the samples maintained their phase stability. Grain enlargement of 1.5 to 2 times was detected. The uranium/zirconium carbonitride's thermal stability in vacuum is restricted to a temperature of ~1500°C, however, because of this material's incongruent evaporation. The use of carbonitride at higher temperatures is feasible if the nitrogen pressure within the fuel element is maintained at a level of several torrs [30].

Solid solutions of UC-ZrC and UC-TaC have much higher thermal stability combined with high thermal conductivity and sufficient uranium load (9.5 to 11 g/cm^3). The UC-ZrC compound is studied in more detail. Its major disadvantage is a high rate of irradiation swelling, inherent to the entire class of carbide fuels.

The UC-TaC compound, despite its merits relating to evaporation rate and corrosion in air, is less studied. This may be connected with the known experimental data collected at the Battelle Institute, in which an abnormally high level of UC-10%TaC sample swelling was noted at 1400°C. The authors connected this effect to the solution's thermodynamic instability [31]. Thermal and irradiation tests of UC-TaC samples at RI SIA "Lutch" showed different results. The UC-TaC samples were tested at 1600 to 1730°C and 200 to 250 W/cm^3 power release up to 0.68% FIMA burnup. X-rays of the irradiated samples demonstrated their phase stability; the change in lattice spacing does not exceed 0.008 Å. An influence of the carbide solution composition and stoichiometry on the irradiation behavior was noted, but optimizing these parameters with the goal of reducing swelling calls for additional investigations. Comparative values of irradiation swelling for the promising high-temperature fuel compositions [8, 26] are presented in Figure 8.8. The swelling rate of the carbide fuel composition is much higher than the swelling rate of uranium nitride, as well as of carbonitride and carbosulphide.

With the goal of reducing the carbide fuel swelling rate, a study of the influence of the as-fabricated sample density on the swelling rate was undertaken.

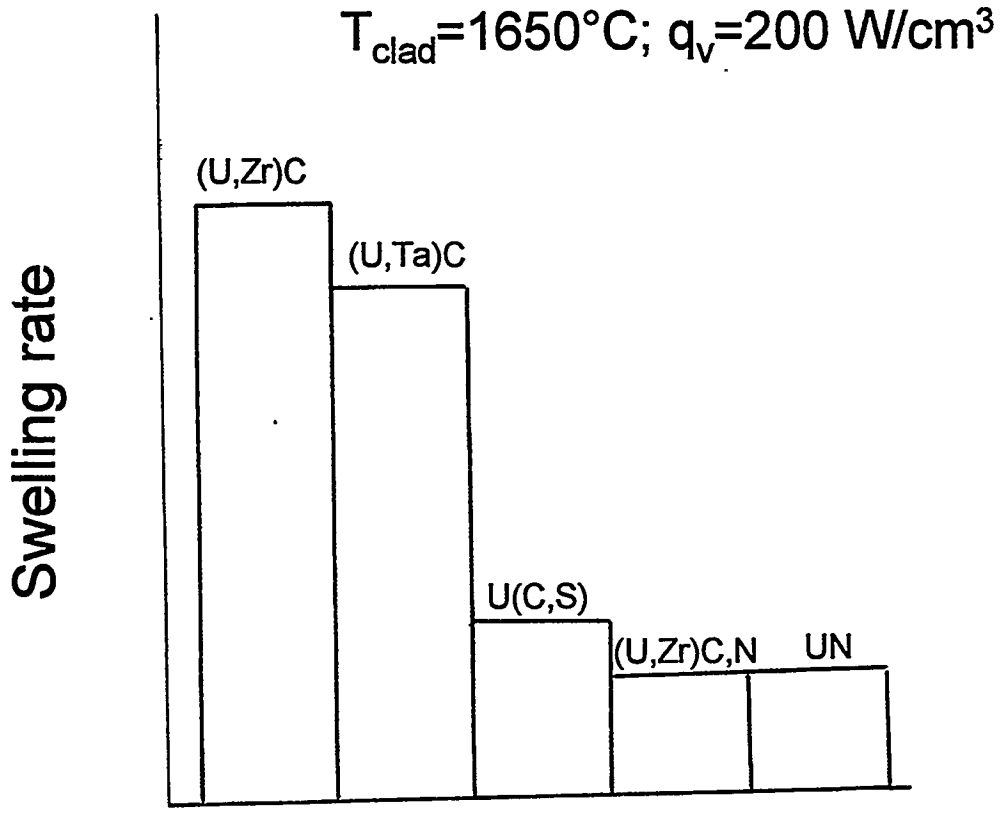

Figure 8.8. Swelling rate of alternative fuel compositions.

From experimental data and extrapolations, the qualitative effect of porosity on the swelling rate was determined [26]. This dependence is shown in Figure 8.9. Introduction of a 10 to 12% porosity reduces irradiation swelling by 2 to 2.5 times.

8.3. Calculational Study of Lifetime Behavior for TFEs with Promising Fuel Compositions

A calculational study on the feasibility of the use of carbide compositions [26] reviewed UC-ZC and UC-TaC solid solutions having porosity ε ranging from 3 to 8% as fuel. The calculations were conducted for the power mode of a bimodal system with output power of 13 kW and 55 to 58 TFEs installed in it. Fuel-element operation was characterized by an emitter temperature of 1525°C and power release density of q_V=65 to 70 W/cm^3. No appreciable fuel mass transfer occurs under these conditions. The comparison was made on the value of emitter-unit deformation caused by fuel swelling. A strengthened single-crystal tungsten alloy was considered as the emitter material. The emitter thickness, including its emissional coating, was taken to be 1.5 mm. The free volume within the fuel element was assumed to be 40%. The calculations were performed with a computer program [32] that contained the values provided in the previous section of this chapter for the fuel composition swelling rate and its porosity dependence. Results are given in Figures 8.10 and 8.11, which show time dependencies of the relative emitter deformation D/D_0 and the relative change in channel dimensions in the fuel stack d/d_0, i.e., the ratio of current to initial diameter.

It is obvious from the calculational results that, when using UC-ZrC carbide compound with a 10% porosity, the relative emitter deformation does not exceed 0.15%, which is far lower than the ~2% tolerable value. The relative constriction of stack channels does not exceed ~30%. For the UC-TaC composition, such high geometric stability is also obtained by use of a high density fuel with a ~3% porosity. In this case, the emitter deformation late in its 10-year life does not exceed 0.85%, and the stack-channel constriction, 50%. If a UC-TaC composition with a 10% porosity is used, the stack-channel constriction will not exceed 25%, and emitter deformation will be negligible. Thus, the calculation results point out that the specified carbide compounds in combination with definite processing and design solutions ensure a 10-year life for the bimodal installation high-temperature fuel elements.

8.4. Data on In-Pile Tests of TFEs with Promising Fuel Compositions

Promising fuel compositions were mostly tested in multi-cell TFEs. Nikolaev et al. and Gontar et al. [33, 34] provided some of the results from experiments on diverse structural and fuel materials in 5- and 7-cell TFEs of two types, with communicating and partly separated IEG and fuel-element cavities. The tests were

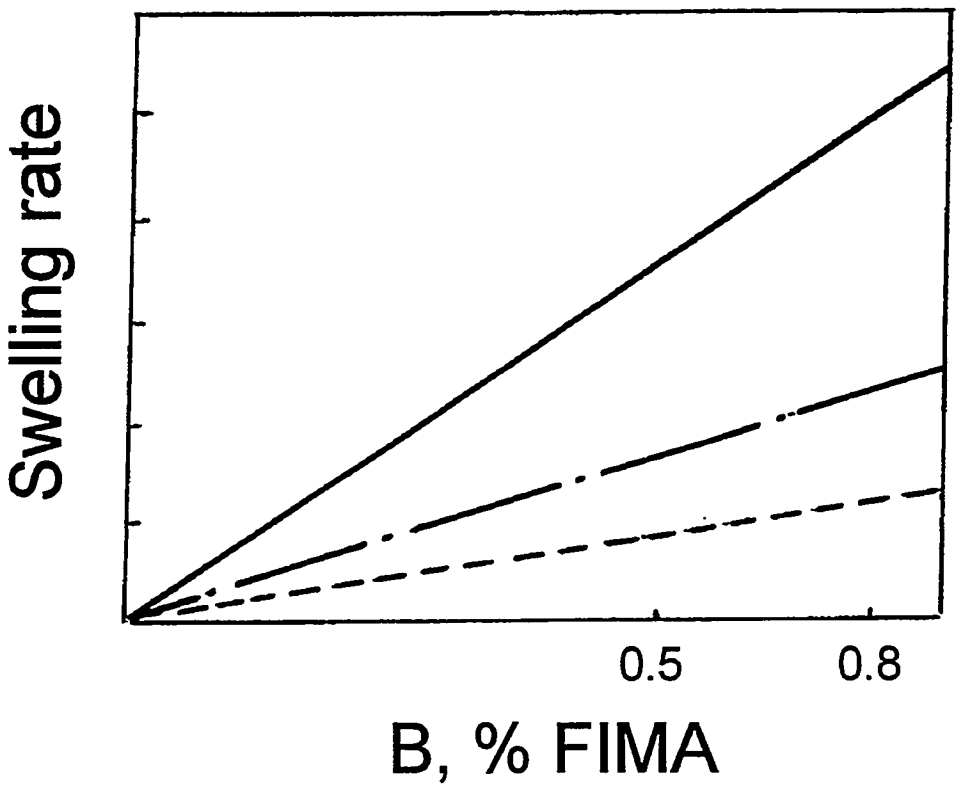

Figure 8.9. Carbide fuel swelling rate vs. burnup [26]:
——— 99% TD;
—·—· 89% TD;
- - - - - 79% TD.

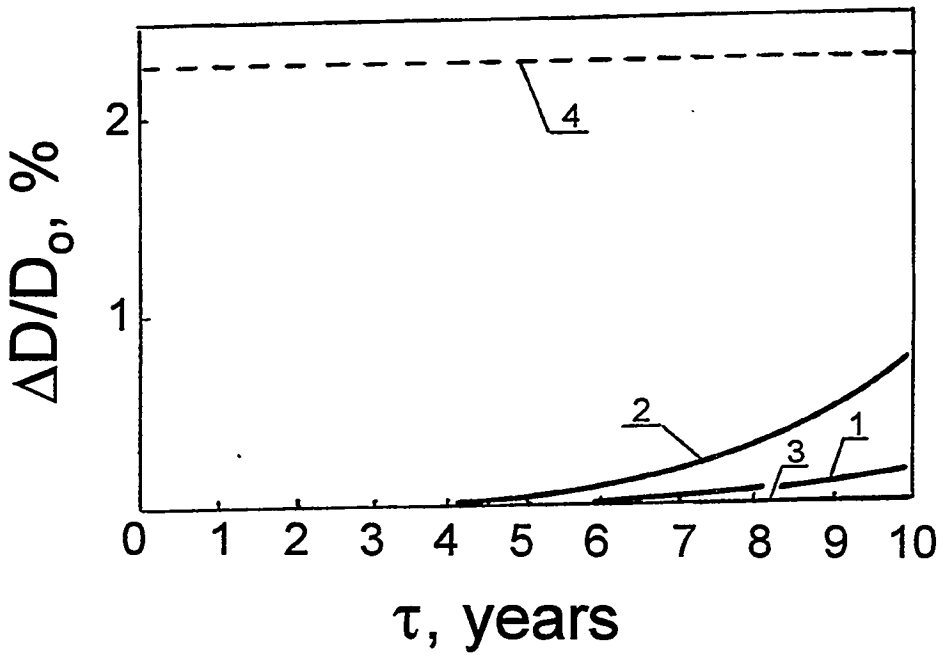

Figure 8.10. Time dependence of emitter deformation for various fuel compositions [32]:

1 - $U_{0.8}Zr_{0.2}C$; $\varepsilon = 10\%$;
2 - $U_{0.8}Ta_{0.2}C$; $\varepsilon = 3\%$;
3 - $U_{0.8}Ta_{0.2}C$; $\varepsilon = 10\%$;
4 - Tolerable emitter deformation.

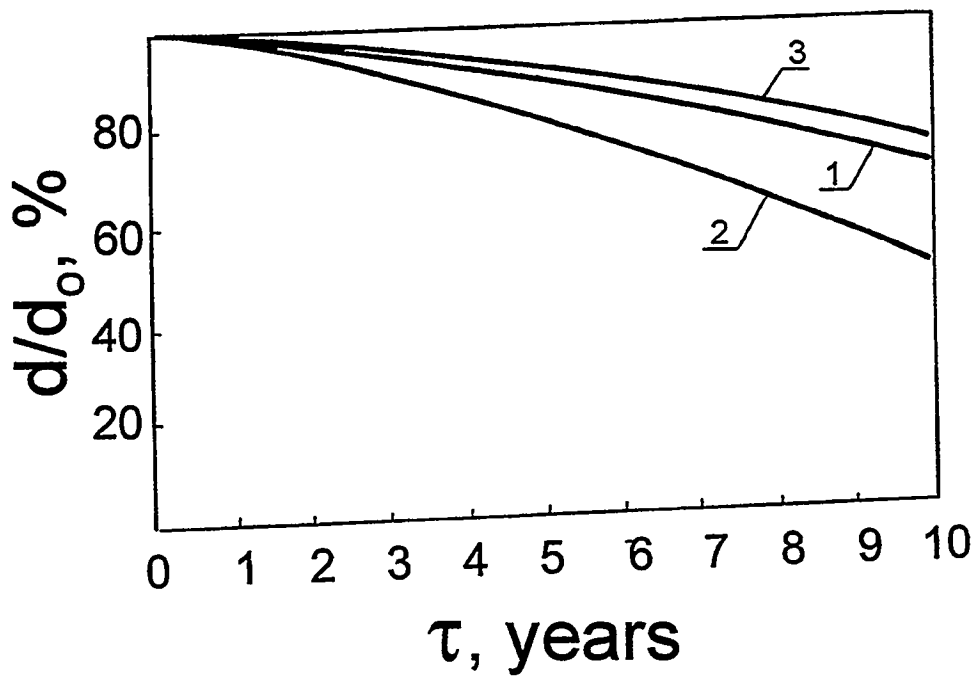

Figure 8.11. Relative change in fuel-stack channel size vs. time [32]:
1 - $U_{0.8}Zr_{0.2}C$; $\varepsilon = 10\%$;
2 - $U_{0.8}Ta_{0.2}C$; $\varepsilon = 3\%$;
3 - $U_{0.8}Ta_{0.2}C$; $\varepsilon = 10\%$.

performed in the IVV-2M and VVR-SM water-moderated, water-cooled research reactors. Features of the TFE designs in which the tests were executed, test conditions, and fuel compositions tested are described in Chapter 6 (see Table 6.7).

The loop channels used for the tests provided the required neutron, thermal, and vacuum test parameters. The loop channel systems provided the required level of heat release, adjustment, and measurement of the TFE collector temperature, continuous gas evacuation from the fuel-element/IEG cavities with control of the intensity and composition of gas flux, and adjustment and control of cesium vapor pressure in the IEG.

Most of TFE parameters that determine the level of power generated and the stable operation time may be referred to the category of "unmeasurable" characteristics. These include the work function and TFE electrode emissivity, individual TFE insulation parameters and their change during lifetime, collector pack thermal resistance, etc. These parameters are governed by the initial characteristics of the materials and processes used. In addition, many of them, specifically the emission and radiating parameters, are susceptible to phenomena occurring within TFEs and IEGs, e.g., to chemical reaction between the materials and gaseous phase or evaporation and diffusion of fuel components into the IEG.

In the 20-year period of TFE development at RI SIA "Lutch," including tests of over 35 loop channels [3], a collection of procedures has been created that identify the condition of the TFE in the tests of promising structural and fuel materials [35]. Registering and processing of volt-ampere characteristics in the TFE operation vacuum mode determine the emitter work function and temperature and the electrodes' reduced emissivity. This method assesses the initial condition of the electrode materials and the influence of TFE thermal/vacuum preparation on these parameters, and it estimates the potential effect of evaporated products and gas release from the fuel on the electrodes' emissive and radiating properties.

In the course of testing, the TFE was recurrently shifted to the diffusion operation mode to track the in-life change of the emissive and radiating parameters of the electrodes.

Registration and joint processing of sets of isopower and isothermal volt-ampere characteristics in the ignited TFE operation mode determined the heat release in the fuel stack.

Short-circuit malfunctions, which are commonly connected with emitter cladding deformation, were identified by registering the individual TFE collectors' temperature change after a jumpwise change in the load current. Behaviors of the transient processes relating to a normally functioning TFE and to its short-circuit state are qualitatively different. This allows the moment of a cell electrode's short-circuit to be recorded and thus different fuel-element designs or materials having different mechanical properties to be compared.

The investigations carried out after completion of the in-pile tests assessed the general condition of the TFE, its tightness, the insulation units' electric resistance, dimensions, and surface condition. The units, joints, and materials incorporated in a TFE were examined from the viewpoint of materials science and technology.

The analysis in Chapter 6 of results on oxide fuel confirmed the feasibility of hypostoichiometric uranium dioxide.

Analysis of the test results has revealed that the use of uranium carbosulphide, USC, at T_f=1840°C in a TFE with communicating fuel-element and IEG cavities (RM-2T1 No9) and of carbide solid solution UC-TaC at T_f=1880°C in a TFE with partly separated cavities (SKAT-4), given an oxygen content in them of $2 \cdot 10^{-2}$ to $5 \cdot 10^{-2}$% mass, does not change the thermal or electrical parameters of electrodes or the converter power characteristics. Complete stability of the interelectrode gap is maintained for up to 5000 hrs under severe thermocycling [33].

Post-irradiation investigations of the fuel elements containing the carbosulphide fuel, tested at fuel temperatures of 1700 to 1850°C, have ascertained a good operability of these fuel elements [33] :

- cladding deformation is absent;
- the channels to remove GFP are free;
- uranium carbosulphide fuel-stack phase composition has not altered after tests;
- gas-induced swelling of the carbosulphide fuel constituted 4.1%, while the emitter diameter did not change, indicating a satisfactory combination of mechanical properties of the fuel and W-Nb-alloy cladding at the test temperature of 1400 to 1570°C on the cladding and 1700 to 1850°C on the fuel;
- no reaction between the carbosulphide and cladding materials and fuel element parts of single-crystal tungsten was detected.

Finally, fuel elements with fuel stacks of UC-TaC solid solution demonstrated their favorable operability and stability of characteristics during the entire testing time. Post-irradiation examination of the fuel elements tested in the SKAT-4 loop channel is not yet completed.

8.5. References

1. Gontar, A.S., Sotnikov, V.N., and Shulepov, L.N. "Uranium Dioxide Mass Transfer Influence on the Operationability of Gas Exhaust Device in Thermionic Fuel Element." Report at the Branch Jubilee Conference. "Nuclear Power in the Space." Obninsk, 1990.
2. Devien, M. *Flowing and Heat Exchange of Rarefied Gases.* Moscow: Foreign Literature Publisher, 1962, 188 p.

3. Shulepov, L.N. "Mass Transfer in a Cylindrical Channel with Evaporation and Condensation on the Channel Walls." *Eng.-Phys. Jour.*, 1978, v. XXXV, No. 1, pp. 82-86.
4. Freshley, M.D., Brite, D.W., Daniel, J.L., et al. "Irradiation Induced Densification of UO_2 Pellet Fuel." *Jour. Nucl. Mater.*, 1976, v. 62, No. 2-3, pp. 138-166.
5. Archer, L.G., Littlechild, J.E., and Watson, R.H. "Short Term Irradiation Behavior of Controlled Porosity Fuel." *Jour. Nucl. Mater.*, 1979, v. 81, No. 1-2, pp. 107-112.
6. Small, G.J. "Densification of Uranium Dioxide during Thermal Reactor Irradiation." *Res Mechanica*, 1986, v. 18, pp. 51-93.
7. Ross, A.M. "Irradiation Behaviour of Fision-gas Bubbles and Sintering Pores in UO_2. *Jour. Nucl. Mater.*, 1969, v. 30, No. 1-2, pp. 134-142.
8. Nikolaev, Yu.V. "Development and Investigation of the Materials for a Thermionic Nuclear Power Plant of Direct Conversion in SIA "Lutch." Report at the Fourth Specialist Conference "Nuclear Power in Space. Materials. Fuel". Podolsk, 1993.
9. Rakitskaya, E.M., Gontar, A.S., and Galkin, E.A. "Thermal Stability of Hyperstoichiometric and Hypostoichiometric Uranium Dioxide with Various Porosities." *Proc. 11th Symp. on Space Nuclear Power and Propulsion.* Albuquerque, 1994, part 1, pp. 81-86.
10. Gridnev, A.A., Gontar, A.S., Nikolaev, Yu.V., et al. "Migration of Micro- and Macropores within Porous Uranium Dioxide in Temperature Gradient Field." Report at the 4th Interbranch Conference on Irradiated Materials Science/Technology. Dmitrovgrad, 1995.
11. Gontar, A.S., Nelidov, M.V., and Nikolaev, Yu.V. "The Problems of Thermionic Fuel Element Development." Report at the 4th Branch Jubilee Conference "Nuclear Power in the Space:, Obninsk, 1990.
12. Eremeev, V.S., Panov, A.S., Fiveisky, E.V., et al. "Thermodynamics", IAEA, Vienna, 1966, v. 2, p. 1617.
13. Weinberg, A.F., Jang, L., and Hudson, R.G. "Materials and Fuels for High-Temperature Nuclear Energy Applications." Massachusetts, 1964, p. 73.
14. Kotelnikov, R.B., Bashlykov, S.N., Kashtanov, A.I., et al. *High-Temperature Nuclear Fuel.* Moscow: Atomizdat, 1978, 432 p.
15. Khromov, Yu.F., and Lyutikov, R.A. "Some Thermodynamic Characteristics of UN_y Uranium Nitride." *Atomic Energy*, 1980, v. 49, iss.1, pp. 25-28.
16. Holleck, H. *Double and Triple Carbide/Nitride systems of Refractory Metals.* Moscow: Metallurgia, 1988.
17. Holley, C.E., Rand, M.H., and Storms, E.K. "The Chemical Thermodynamics of Actinide Elements and Compounds." Part 6. "The Actinide Carbides", IAEA, Vienna, 1984.

18. Holleck, H., and Kleycamp, H. "Uranium Carbides," *Gmelin Handbook of Inorganic Chemistry*, 8th edition, Uranium Suppl., vol c-12, Springer Verlag B., H., New York, T, 1987.
19. Kotelnikov, R.B., Bashlykov, S.N., Kashtanov, A.I., and Menshikova, T.S. *High-Temperature Nuclear Fuel.* Moscow: Atomizdat, 1969, 368 p.
20. Zagryazkin, V.N., Panov, A.S., and Fiveisky, E.V. "Thermodynamics and Kynetics of the Interaction Between Metals and Uranium Monocarbide, Monosulphide and Carbosulphide." "Thermodynamics of Nuclear Materials". IAEA, Vienna, 1980, v. 2, pp. 171-184.
21. Kokhtev, S.A., Evstyukhin, A.I., Khromonozhkin, V.V., and Andrievsky, R.A. "Study of Uranium Vapor Pressure over Uranium Monosulphide and Carbosulphide." *Metallurgy and Physical Metallurgy of Pure Metals*, 1980, iss. 14, pp. 73-77.
22. Nikolaev, Yu.V., Khromov, Yu.F., Khromonozhkin, V.V., et al. "Some Operation Performance of Fuel Compositions: UO_2, UZr(CN), U((Zr, Nb,Ta)C, U(CS)." Report at the Branch Jubilee Conference "Nuclear Power in the Space," Obninsk, 1990.
23. Gontar, A.S., Gutnik, V.S., Zaitsev, V.A., et al. "A Prospective Fuel for Thermionic Fuel Elements." Report at the Branch Jubilee Conference "Nuclear Power in the Space," Obninsk, 1990.
24. Gontar, A.S., Gutnik, V.S., Zaitsev, V.A., et al. "A Method and Results of Comparative In-Pile Tests of High Temperature Fuel Materials." Report at the 4th Branch Conference: Nuclear Power in the Space. Materials. Fuel." Podolsk, 1993.
25. Zaitsev, V.A., Lyubimov, D.Yu., Mitrofanov, V.I., et al. "The Thermochemical Stability of Carbosulphide Fuel." Report at the 4th Branch Conference "Nuclear Power in the Space. Materials. Fuel." Podolsk. 1993.
26. Fuel for Bimodal Power/Propulsion Plants.-Review. JV "Inertek", SP-15/229, suppl. 5, 1995.
27. Gontar, A.S., Zaitsev, V.A., Mitrofanov, V.I., et al. "Advantages and Problems of Carbide Fuel Application to TRC." Report at the 4th Branch Conference "Nuclear Power in the Space. Materials. Fuel", Podolsk, 1993.
28. Nikolaev, Yu.V., Vedenyapin, G.A., and Gontar, A.S. "Carbon Diffusion in the Single Crystal Emitter." Report at the 4th Branch Conference "Nuclear Power in the Space. Materials. Fuel." Podolsk, 1993.
29. Lyubimov, D.Yu., Panov, A.S., Fedorov, E.M., and Vedenyapin, G.A. "Carbide Fuel Components Transport into the Interelectrode Gap." Report at the 4th Branch Conference "Nuclear Power in the Space. Materials. Fuel." Podolsk, 1993.
30. Gontar, A.S., Zaitsev, V.A., Lebedev, A.M., et al. "The Possibilities of Nitride Fuel Appication to TRC." Report at the 4th Branch Conference "Nuclear Power in the Space. Materials. Fuel." Podolsk. 1993.

31. Chubb, W., Starhock, V., and Keller, D. "The Factors Influencing on Nuclear Fuel Swelling at High Temperatures." *Nuclear Engineering Abroad*, 1976, No. 2, pp. 8-22.
32. Gontar, A.S., Gutnik, V.S., Nelidov, M.V., and Nikolaev, Yu.V. "Swelling of Uranium Dioxide and Deformation Behaviour of the Fuel Element at High Temperature Irradiation." *Proc. 28th Intersociety Energy Conversion Engineering Conference*, Atlanta. 1993, vol. 1, pp. 549-553.
33. Nikolaev, Yu.V., Vybyvanets, V.I., Izhvanov, O.L., et al. "Tests of Structural and Fuel Materials in TFE in Research Reactor Loop Channels." Report at the 4th Branch Conference "Nuclear Power in the Space. Materials. Fuel." Podolsk, 1993.
34. Gontar, A.S., Kucherov, R.Ya., Lapochkin, N.V., and Nikolaev, Yu.V. "Thermionic Fuel Element with Carbide Fuel." *Proc. 11th Symposium on Space Nuclear Power and Propulsion.* Albuquerque, 1994, part 2, pp. 845-850.
35. Sinyavsky, V.V. *Methods for Determination of the Thermionic Fuel Elements' Performances.* Moscow: Energoatomizdat, 1990, 184 p.

CHAPTER 9

PROMISING FUEL ELEMENT DESIGNS: CALCULATIONAL RESULTS AND EXPERIMENTAL CONFIRMATION

9.1. A Fuel Element Containing Fuel with Open Porosity at Its Ends

Mass transfer within the central channel of the oxide fuel stack can form a closed isothermal cavity at times shorter than the required lifetimes. In this case, GFP pressure will increase within the cavity formed; to remove GFPs, a gas-exhaust system is necessary. During isothermal-cavity formation, the free space near the end caps fills with a dense condensate of uranium dioxide, and heightened local cladding deformation is induced by the swelling fuel. To remove GFPs and eliminate the locally heightened cladding deformation, Gontar et al. [1] suggested the placement of solid pellets with open porosity at the ends of the fuel elements. They suggested the use of uranium dioxide with a stabilized open porosity as the end-pellet material. The performance of and experimental data on this fuel are provided in Chapter 8. The as-fabricated fuel element is diagrammed in Figure 9.1. To prevent heightened local deformation, the pellets are located at both ends of the fuel element. In fuel-element operation, the cladding and cap more efficiently redistribute the swelling of the solid uranium-dioxide pellets, because ~10% porosity uranium dioxide has a creep rate at least two orders of magnitude higher than a dense uranium dioxide with a column-type structure. This brings about reduction or complete elimination of local cladding deformation at the cap sites. The outlet in the cap to remove GFPs can be located at one end of the fuel element, as shown in Figure 9.1. At the other end there is a device to fix the fuel pellets within the fuel element. The outlet can be placed in the cap on the fixing-device side; in this case the device can function as a labyrinth, restricting fuel loss from the fuel element. To exclude the possibility, in the course of isothermal-cavity formation, of the dense uranium-dioxide condensate layer being deposited on the porous pellet surface, the porous pellets' initial height must exceed the isothermal cavity end-wall thickness, as shown in the scheme of the steady-state fuel-stack condition (Figure 9.2).

Calculations conducted to substantiate the design revealed that, for a fuel element with a fuel-stack diameter of 17 mm and central-channel diameter of 8 mm, absence of mass flow onto the solid porous pellets is guaranteed by a solid pellet height of 5 mm. Given the heat-flux density of 35 W/cm^2, the maximum temperature of the solid pellet exceeds that of the annular pellet by 50 K.

At the chosen ratio of annular-to-solid pellet size, uranium dioxide does not condense in the central zone of the solid pellets; on the contrary, partial evaporation occurs from their inner surface (Figure 9.2). At a cap temperature of 1800 K and cap outlet diameter of 2 mm, uranium-dioxide flux, incident to the

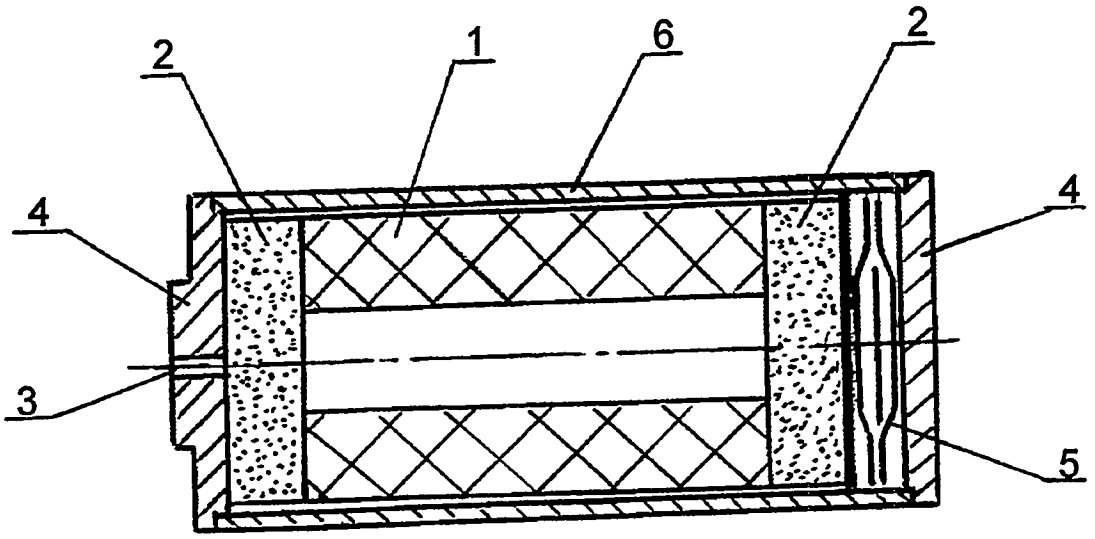

Figure 9.1. As-fabricated fuel element condition:
1 - fuel with equiaxial structure;
2 - porous fuel;
3 - outlet in cap;
4 - caps of fuel element;
5 - device fixing the fuel pellets;
6 - cladding

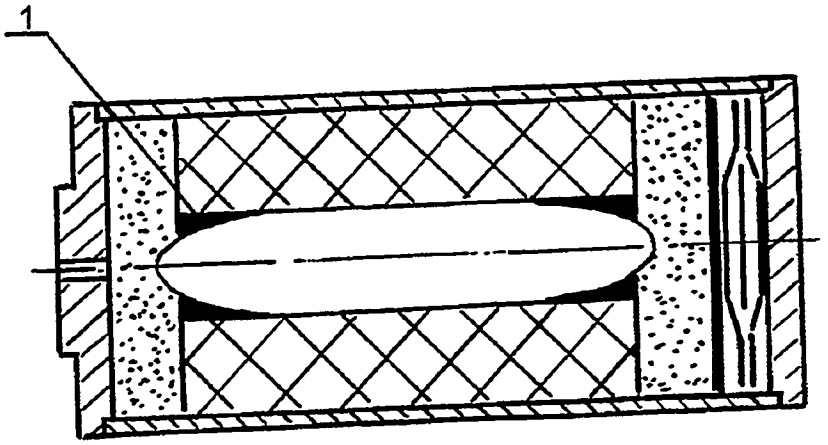

Figure 9.2. Diagram of fuel element with isothermal cavity:
1 - uranium dioxide condensate

channel inlet cross-section from the pellets, reaches ~0.1 g/year. This corresponds to a fuel volume of 1 mm^3 and thus cannot cause channel overlapping even under the worst assumption, that all the dioxide condenses immediately within the outlet channel. Estimates also show that cladding deformation in the end cap site is negligible. The fuel-element design presented in Figure 9.1 may be actualized using processes available at RI SIA "Lutch."

9.2. A Fuel Element with Inner Longitudinal Ribs on the Emitter

One way to reduce the oxide fuel temperature within a fuel element is to arrange metallic heat-conducting structural elements within it to transfer heat to the cladding. A method to reduce the fuel temperature by alternating fuel pellets and thin disks of refractory metals within the fuel stack has been studied in detail and widely applied to thermionic fuel elements [2]. At an unchanged volume fraction of the disks, a decreased pellet and disk thickness is more favorable for fuel temperature reduction [2]. The necessity for providing contact between the washers and the cladding in the course of assembly is a substantial disadvantage of the fuel stack with alternating fuel pellets and washers.

Another technique for temperature reduction of the fuel stack is the application of a cladding with longitudinal ribs. Here, the contact between ribs and cladding is provided in fabricating the cladding. Fuel as fragments of appropriate configuration and dimensions is loaded into the ready-made ribbed cladding. A study of temperature distribution within the fuel elements having the ribbed cladding for power reactors [3] has calculated that using a the fuel-element cladding diameter of 7 mm and rib height of 1.3 mm considerably reduces the fuel temperature. Maximum fuel-temperature reduction is still more urgent for the thermionic reactor converter fuel element, which is characterized by a higher cladding temperature and enlarged fuel-stack diameter. When refractory metals compatible with fuel at high temperatures are used as the cladding and rib materials in the thermionic fuel element, the ribs may extend through the full thickness of the fuel layer.

An analytical expression [4] determines the ratio of temperature drops within the fuel at a zero value of the central channel radius for a fuel element with and without ribs, at the same heat power:

$$\frac{T(0)-T_{clad}}{T_0(0)-T_{clad}}=\frac{\lambda_1}{\lambda_1(1-\alpha)+\lambda_2\alpha}, \qquad (9.1)$$

where: λ_1 and λ_2 - respectively, thermal conductivity of fuel and rib material

$\alpha=\frac{\varphi_2}{\varphi_1+\varphi_2}$ - fraction of fuel-stack volume occupied by ribs

It is evident from Equation 9.1 that temperature reduction in the fuel-stack center does not depend on the number of ribs or on heat release distribution on the fuel-stack radius.

Figure 9.3 shows the dependence, calculated using Equation 9.1, of the temperature reduction on α at λ_1=0.023 W/cm·K and λ_2=1W/cm·K. Even at a rib volume constituting 2% of the fuel-stack volume, the temperature drop within the fuel is reduced by a factor of 2. At the same time, an increase in the rib volume fraction over 10 to 15% does not substantially lower the temperature any further. For the case of alternating fuel pellets and metal washers, the maximum temperature reduction is also defined by Equation 9.1 [4]. So, given small height of the fuel pellets, the efficiency of use of a metal as ribs and washers is the same with respect to lowering the temperature in the fuel stack center.

When using the ribs, the maximum fuel temperature may be reached within the fuel fragment volume rather than on the central channel surface; therefore the matter of interest is more complete information on the temperature fields, as well as an investigation of the dependence of the temperature distribution on the height, number, and configuration of the ribs and optimizing these parameters. To gain these data, Gontar et al. [4] applied the computer code STEREO. The calculation was performed for a fuel element with a 2-cm diameter fuel stack and a 0.6-cm diameter stack central channel. The cladding temperature was assumed to be 1500°C. The volumetric heat release was deemed constant on the stack radius and equal to 100 W/cm^3. The dependence of the temperature reduction on the central channel surface vs. relative rib volume calculated for the above conditions is presented as Curve 2 in Figure 9.3.

For optimizing the rib parameters, Gontar et al. [4] calculated a relation between the maximum central-channel temperature and rib number, height, and shape. The calculations showed that the strongest effect on channel-center temperature is exerted by rib height; therefore extending the ribs through the entire thickness of the fuel layer is advisable. The calculations revealed that a rib number in excess of six does not lead to any significant reduction in maximum temperature. To determine the influence of rib configuration, triangular and trapezoidal ribs were calculated, but the effect of rib shape was insignificant.

The calculations [4] were conducted for two versions: with ideal fuel/ribbed-cladding contact and fuel/rib contact only, with a gap between the fuel and cladding. Creating a specific design for the latter version does not present any particular difficulty. Calculational results [4] are displayed in Figure 9.4 as a set of isotherms for a fuel fragment sited between adjacent ribs. A maximum temperature is reached in the fuel fragment center but not on the central-channel surface. It follows from the figure that, given six ribs extending throughout the fuel layer, the maximum temperature difference on the central-channel surface for the cases of contact and fuel/cladding gap is ~50 K. This difference, without the ribs, can exceed 1,000 degrees. Thus, the ribs efficiently reduce the temperature

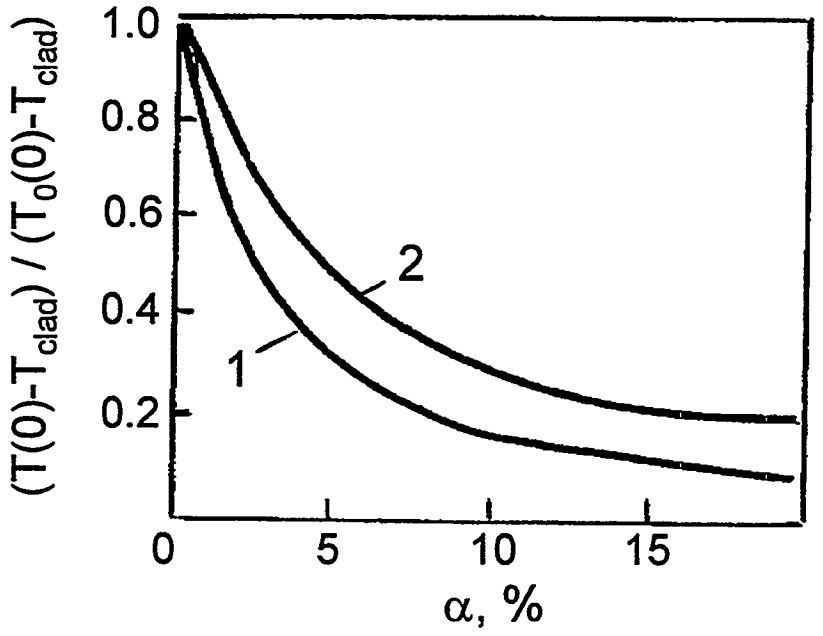

Figure 9.3. Temperature drop reduction vs. relative rib volume:
1 - calculation using Equation 9.1;
2 - numeral calculation for six ribs extending to central channel surface of 3 mm radius

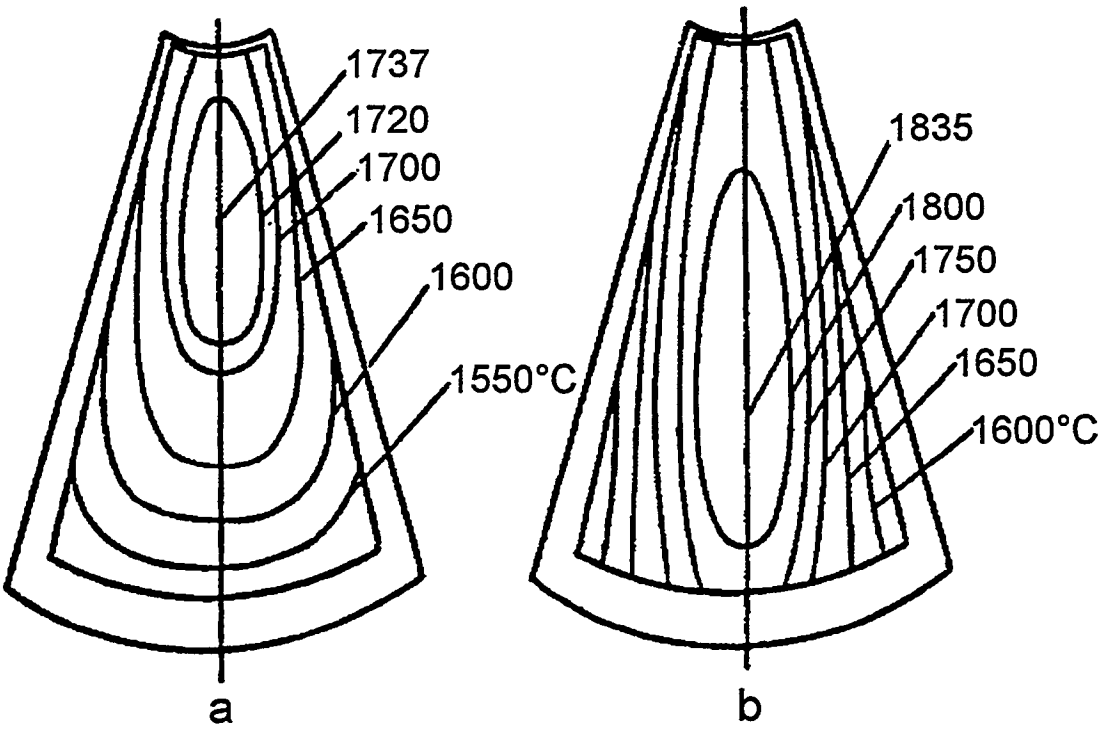

Figure 9.4. Isotherms in fuel element with ribbed cladding:
a, b - respectively, contact and gap between fuel and cladding

even when the fuel/cladding gap is present. Sharp temperature reduction results in lowering the fuel-evaporation rate and in the long-term existence of a gap in the immediate vicinity of the cladding, preventing the effects of freely swelling fuel on the cladding. This is one factor decreasing cladding deformation. In addition, a free volume, into which the gap is eventually transformed in the course of mass transfer, will be located in the maximum temperature zone—i.e., in this case, within the fuel fragment volume—and will more efficiently damp out the fuel swelling than the central-channel free volume.

To compare the effectiveness of the internal ribbing and introduction of washers ideally contacting the cladding, the temperature fields within the fuel element with the same metal content (10%) in washers and in six ribs have been calculated [4]. The calculation showed that the central-channel surface temperatures are close, in this case. So, for 4-mm-thick pellets, the maximum central-channel surface temperature reaches 1700°C and, for the six ribs containing the same amount of metal, 1720°C.

Fabrication of the longitudinal ribs on the fuel-element cladding also enhances the stiffness of the cladding.

9.3. A Fuel Element with a Gas-Exhaust Device Separated from Fuel by a Screen

Chapter 4 considered a gas-exhaust device as a pipe extending into the central isothermal cavity. To restrict fuel migration, an endpiece with a capillary channel is located at the pipe tip, with an outlet to the central cavity. Section 4.2.2 considered the operability of such a gas-exhaust system under conditions of uranium-dioxide condensation on the GED. As this consideration shows, a fuel layer on the endpiece that is significantly thicker than the capillary-channel diameter can disable the GED for a long period. Kornilov et al. [5] suggested isolating the volume into which the capillary channel enters from the fuel by a thin-walled screen, which may be made of tungsten or its alloys. The surface of the screen's central zone, falling within the isothermal cavity, may be perforated, allowing the GFPs to migrate into the inner screen cavity and then to leave through the GED. Fuel passing through the screen perforations will be predominantly condensed in the coldest parts of the intrascreen cavity, i.e., at the end caps. If the perforation conductivity is far lower than that of the channel, the fuel vapor will expand within the screen. So, an appropriate choice of the total perforation area may significantly lower the intrascreen fuel vapor pressure and eliminate fuel condensation on the GED surface at the capillary channel site. Calculations [6], as applied to TOPAZ-3 installation, show that for an 0.8-cm diameter thin-walled screen, the total perforation area must not exceed 1 mm^2.

Long-term functioning of a thin-walled tungsten screen in oxygen-containing atmosphere over uranium dioxide may be ensured, as shown in Section 1.3.4, only

by using hypostoichiometric uranium dioxide. To reduce the interaction between the screen and oxygen, a getter can be applied to the screen surface to consume the oxygen [5].

Section 3.4 noted that the greatest danger of fuel condensation on the GED surface arises early in the operational period, when the GED is not attached to the fuel and the temperature is higher. Thus, the screen can play a favorable role even when it is functional only early in the operational period, when isothermal-cavity formation occurs.

9.4. TFE with Nitride Fuel

A key requirement for nuclear fuel in space NPSs is a high volume concentration of fissile material. This parameter eventually determines the minimum feasible system weight and overall size. Fast reactors are especially sensitive to this parameter. Among high-temperature fuel materials, uranium nitride has the highest fissile-material content (ρ=13.52 g/cm^3, as compared with 9.67 g/cm^3 for UO_2) [7]. This fuel also is superior to the oxide in a number of other thermal and physical characteristics (see Chapter 8).

Interest in the nitride fuel has recently grown both at RI SIA "Lutch" (see, e.g., [8, 9]) and among foreign developers of space NPSs [10, 11].

However, this fuel also raises a number of specific problems. UN_x application to high-temperature fuel elements (in excess of 1500 K) is complicated because of the very narrow homogeneity range (x=1-0.985). Because uranium-nitride evaporation is incongruent, a liquid uranium phase, incompatible with the emitter material, may form in the ventilated fuel elements.

Some of the calculations and designs for the creation of high-temperature TFEs based on nitride fuel have been reviewed by Borodastov et al. and Von Jhle and Rust [2, 3].

9.4.1. Gas-Tight Fuel Element

It is commonly accepted that UO_2-based gas-tight fuel-element designs are unpromising because of the high rates of emitter deformation under the effect of GFP pressure generated within the fuel element. Calculational study results obtained at RI SIA "Lutch" agree. Data provided in Chapter 4 show that the oxide fuel gas-tight element life is restricted to 1 to 1.5 years.

Use of uranium nitride having a high thermal conductivity (about one order of magnitude higher than UO_2's), however, considerably reduces the mean fuel temperature and consequently lowers GFP release and the pressure generated within the fuel element. In addition, the higher fissile material concentration in uranium nitride permits enlargement of the fuel-element free volume, which additionally reduces the GFP pressure. The improvement in the emitter's

geometric stability is also enhanced due to the power law stress (pressure) dependence of the creep rate.

The gas-tight fuel-element life was estimated by Gontar et al. [9]. Here, for comparison, analogous estimates were made for a uranium dioxide-based fuel element for a typical configuration and temperature conditions of thermionic fuel-element operation: emitter diameter, 18 mm; emitter thickness, 1 mm; emitter temperature, 1500 to 1600°C; and free volume in the UO_2 fuel-element cavity (basic variant), 20%. The density of both fuel compositions was assumed to be 95% TD.

Single-crystal tungsten and its alloy are considered as the emitter material. The creep rate of the alloy, due to solid-solution hardening, is about 3 orders of magnitude lower than that of the non-alloyed tungsten (see Chapter 2).

Over the extended lifetime, structural modification of uranium dioxide occurs at the considered temperature; the calculations for the UO_2-based fuel element were performed for two dioxide structural conditions: equiaxial and columnar grains. The free swelling rate of the fuels being compared was assumed to be in accordance with their ampule-type test results.

The fuel-stack temperature conditions were calculated taking into account the relevant values of thermal conductivities of the fuels being compared. The value of free volume in the fuel element based on UN, in comparison with the basic UO_2 variant, was corrected (in the direction of its increase because of a higher fissile component content per unit volume), proceeding from the condition of a zirconium hydride-moderated reactor criticality.

To improve the estimated fuel-element lifetime prediction, the GFP release was defined from two models: diffusional [12] and activational [13]. The study revealed that the values of GFP release obtained using the different models are similar; therefore, they are shown in Figure 9.5 by a single curve for each fuel.

In defining the emitter deformation, two calculational schemes were used: (a) immediate effect of the released GFP pressure on the emitter, and (b) gas effect on the emitter through fuel swelling. The estimates of fuel-element lifetime (assessed on the criterion of electrode short circuit) are given in Figures 9.6 and 9.7. When using the single-crystal tungsten emitter, the lifetimes of both UO_2- and UN-based fuel elements are of little practical interest. However, after substituting the strengthened single-crystal tungsten alloy for the previous material, the UN-fuel-element lifetime meets the requirement specified for the first stage of the space NPS development (τ=3 to 5 years [14]). At an emitter temperature T=1500°C, the lifetime reaches 5 years even assuming complete GFP release from the fuel (f=1). With a rise of emitter temperature to 1600°C, the fuel element lifetime is ~3 years.

Additional calculations were conducted to determine other potential restrictions on the applicability of such fuel-element designs.

Estimates of the change in the stoichiometric coefficient in the course of burnup and nitrogen losses through the emitter showed that during the entire 5-

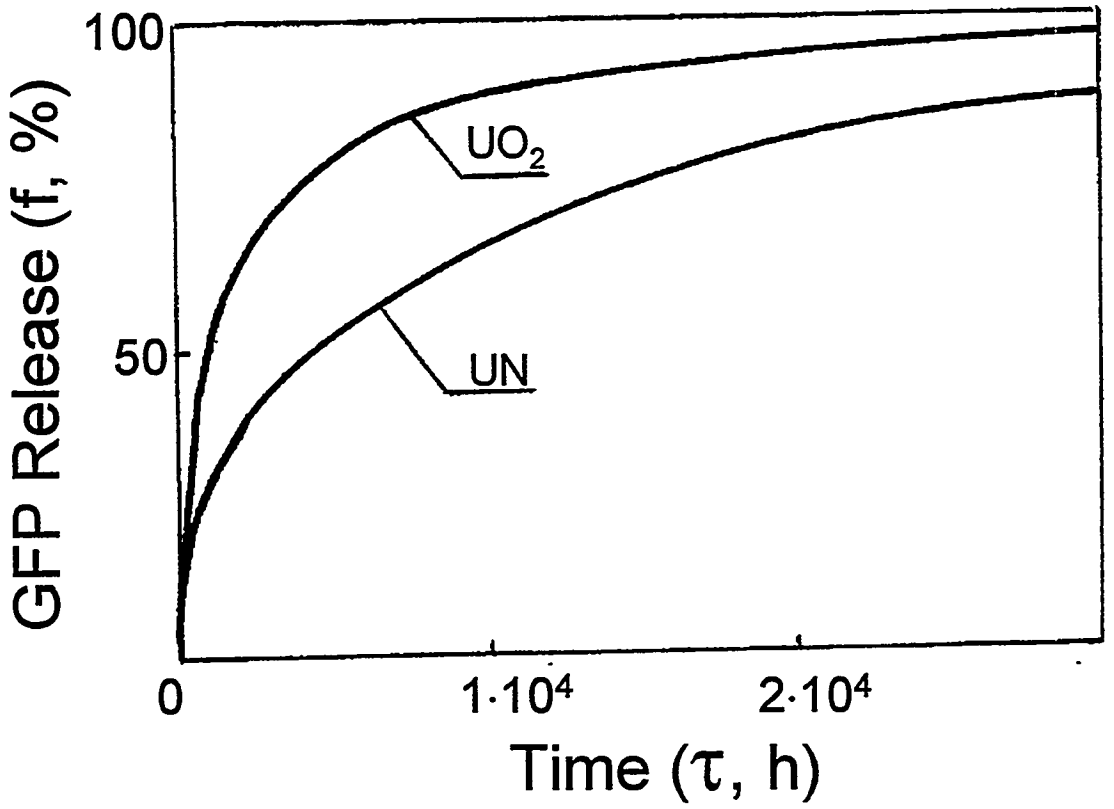

Figure 9.5. GFP release in fuel elements based on UN and UO_2 vs. time [9].

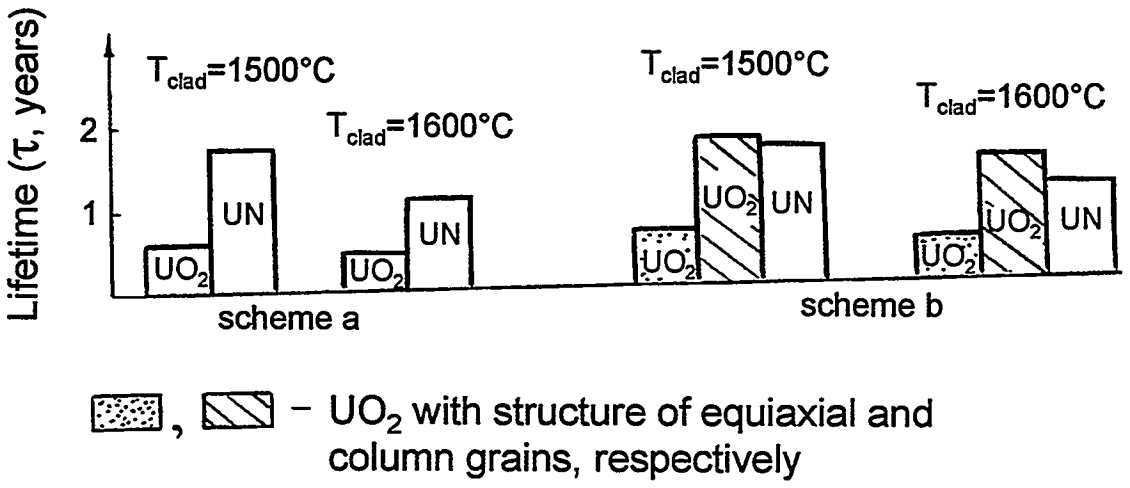

Figure 9.6. Estimated lifetime forecasted for TFE with tungsten emitter [9].

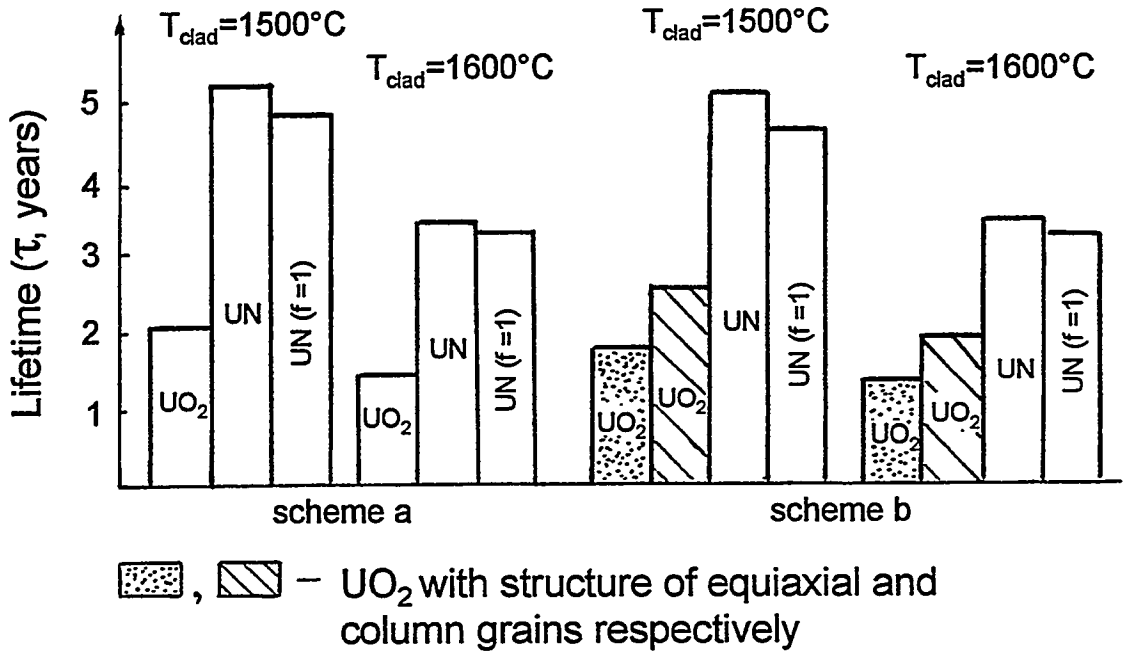

Figure 9.7. Estimated lifetime forecasted for a TFE with an emitter of strengthened tungsten alloy [9].

year life of a fuel element operated at 1500°C, uranium nitride remains in the homogeneity area. So, this fuel-element design does not demand the incorporation of any extra nitrogen sources, as the ventilated design does, which substantially simplifies the design and increases its reliability.

The nitrogen pressure in the interelectrode gap, caused by nitrogen migration through the emitter, does not exceed 0.15 Pa, which is considerably lower than the permissible level of 3 to 5 Pa [8] and thus does not affect the working of the TEC.

These results lead to the conclusion that application of uranium mononitride to the thermionic fuel element, in combination with an emitter of a strengthened single-crystal tungsten alloy, allows the use of the gas-tight design of the fuel element for lifetimes up to 5 years.

9.4.2. A Ventilated Nitride Fuel Element with Inner Nitrogen Source

As shown in the previous section, the use of nitride fuel, instead of oxide, improves the potential lifetime of a gas-tight fuel element. The life-related restrictions remain very significant, however, and they become more rigid in the transition to the next-generation fuel elements, which have a higher density of power output. Therefore, RI SIA "Lutch" also considered the possibility of applying the nitride fuel to ventilated fuel elements. The long-term existence of uranium nitride in the single phase can be ensured by maintaining the nitrogen pressure within the fuel element at a level exceeding the equilibrium nitrogen pressure over uranium nitride at the lower boundary of the homogeneity area. Kucherov et al. and Zaitsev et al. [8, 15] examined the possibility of using uranium nitride together with other metal nitrides. Given slow-enough leakage of nitrogen, the nitrides' composition on the surface is determined from the condition of constant nitrogen pressure within the fuel element. If the nitrogen pressure lies in the range corresponding to nitrogen pressure over single-phase uranium nitride or exceeds the latter, and a metal nitride here has a composition corresponding to the congruent evaporation condition, then despite nitrogen leakage from the fuel element, the nitrogen pressure within it will remain constant. Nitrogen losses in uranium nitride will practically stop, and its composition will remain stable until all the metal nitride has been volatilized. Titanium nitride possibily can be used to hold the nitrogen pressure [8]; it is congruently evaporated, given $UN_{0.79}$ composition [16].

Figure 9.8 displays the temperature dependence of nitrogen pressure over nitrides. According to the data of RI SIA "Lutch" [17, 18] and some other data [16, 19], nitrogen pressures over UN and over congruently evaporated titanium nitride nearly coincide. However, there are data contradicting this conclusion [20]. Hence, the data presented in Figure 9.8 do not explicitly answer the question of the possibility of applying a UN-TiN system to thermionic fuel elements.

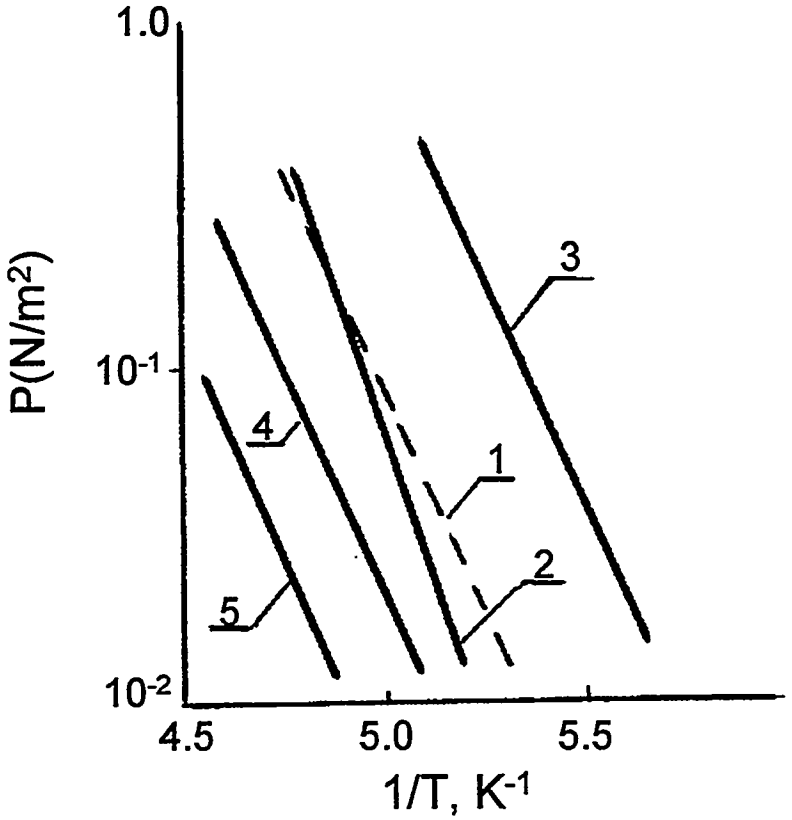

Figure 9.8. Temperature dependence of nitrogen equilibrium pressure over nitrides:

1 - titanium nitride of congruently evaporating composition [16];
2 - uranium nitride [18];
3 - uranium nitride [20];
4 - uranium carbonitride $UN_{0.48}C_{0.52}$ [20];
5 - uranium carbonitride $UN_{0.3}C_{0.7}$ [20].

In experiments on isothermal heating of uranium nitride in the presence of titanium nitride [8], vacuum isothermal annealings were carried out in tungsten containers having a 300- to 450-μm effusive hole. $UN_{0.966}$ specimens were tested as disks with a 13-mm diameter and 3 to 5 mm height, coated by $TiN_{0.92}$ 50 μm thick. The container walls were coated in the same way. In testing a portion of the uranium nitride specimens, there was an additional solid-phase source provided by nitrogen from titanium nitride as plates of 2×3×8 mm size and $UN_{0.794}$ composition located within the container. Isothermal annealing at 2150 K for 100 hrs did not change the surface structure of either variant, judging by x-ray diffraction analysis data [8]. Possibly nitrogen leakage did not yet result in the congruently evaporating composition of titanium nitride coating or in reaching the uranium nitride homogeneity area lower boundary. Longer-duration experiments may be necessary [8].

Results of calculations of nitrogen movement beyond the fuel element through an orifice in the 2-mm thick cap, depending on the orifice diameter and nitrogen pressure within the fuel element, are given in Table 9.1. A 1-g pellet, comprising 0.2 g nitrogen, at 2000 K and 0.4-mm diameter orifice, is able to ensure fuel-element operability for 5 years. Estimates showed that the contribution provided by diffusion flow of nitrogen through a 1-mm-thick tungsten fuel-element cladding at T=2000 K may be neglected.

In a TFE design with communicating fuel-element and IEG cavities, GFPs as well as nitride decomposition products are removed through the IEG. Therefore a titanium coating, with a mass 5 times greater than nitrogen, should be formed at a TFE manufacturing stage on the gas-exhaust channel walls beyond the fuel-element-cap hole. The work function of titanium coated by cesium is 1.4 to 1.8 eV, and it appears, when condensed on the collector, not to deteriorate TEC characteristics [21]; however, there is a danger of sputtering titanium onto the insulator surface and short-circuiting the electrodes. Nitrogen at pressures below 3 to 5 Pa does not appreciably affect the TEC operation [22].

Table 9.1. Nitrogen leakage (g/year) through orifice in cap of 2-mm thickness vs. orifice diameter and nitrogen pressure [8]

P_{N2}, Torr	d, mm				
	0.05	0.1	0.2	0.4	0.6
10^{-4}	$1.38 \cdot 10^{-5}$	$1.07 \cdot 10^{-4}$	$8 \cdot 10^{-4}$	$5.8 \cdot 10^{-3}$	0.0176
10^{-3}	$1.38 \cdot 10^{-4}$	$1.07 \cdot 10^{-3}$	$8 \cdot 10^{-3}$	$5.8 \cdot 10^{-2}$	0.176
10^{-2}	$1.38 \cdot 10^{-3}$	$1.07 \cdot 10^{-2}$	$8 \cdot 10^{-2}$	0.58	1.76

As shown in Figure 9.8, if uranium carbonitride is used, nitrogen pressure is significantly lowered. This circumstance essentially reduces the nitrogen expenditure and the required amount of nitrides supplying the fuel element with nitrogen. But the carbonitride, like the nitride, has a narrow homogeneity area, therefore RI SIA "Lutch" has mainly studied uranium-zirconium carbonitride, $U_{1-y}Zr_yC_{1-x}N_x$ [15]. This fuel has a wide homogeneity area and low nitrogen vapor pressure in the lower phase boundary. A broad range of nitrides—specifically, titanium, vanadium, chromium, et al. nitrides—have been considered as the nitride to supply additional nitrogen [15]. Techniques to improve the thermal stability of uranium nitride using protective diffusional barriers were considered on the basis of equations describing the kinetics of nitrogen diffusion and evaporation [15].

9.5. U^{233}-Based Fuel Elements

At present, a new generation of materials and space NPS reactor designs, with improved operation and life-time characteristics, is under development. Specifically, for the thermionic reactor-converters, power increases up to 50 to 100 (and several hundreds) kilowatt and lifetimes up to 7 to 10 years are being considered [23]. The possibility of creating a hybrid reactor, combining the operation modes of nuclear-powered rocket engines and thermionic converters, is under examination [23, 24].

The search for and development of promising materials for such NPSs are often constrained by neutronic operational requirements. Therefore, in a number of cases, a fuel with increased concentration of the fissile component at maximum densities and enrichments is used; for such cases, the driver elements should be provided in the reactor core design [23].

Use of U^{233} and related fuel compositions as the fissile material opens fundamentally new perspectives. In this case, the reactor neutron conditions should substantially improve. The available reactivity reserve grows by ~25% [23], and there is not only the possibility of reducing system mass and size, but also of mitigating the conditions under which the reactor units must operate, including the fuel element.

It may be possible to additionally strengthen the emitter by thickening it, to improve the reliability of operation of fuel-element gas-exhaust devices, and to enlarge fuel porosity and free volume within the fuel element.

Calculational data on the TOPAZ-1 reactor for U^{233}-based fuel [23] reveal that use of U^{233}, with no change in overall size of TFE and reactor as whole, makes possible a number of important modifications to the TFE design, aimed at lengthening its life and improving its reliability:

- emitter cladding of W-3%Ta alloy;
- thickening the cladding up to 1.5 mm;

- hollow fuel pellets with hole diameter up to 4.5 mm; and
- widening, within permissible bounds from the viewpoint of TFE volt-ampere characteristics, of the interelectrode gap (fully available emitter deformation is increased up to $\Delta d/d=12\%$; tolerable deformation, up to ~8%).

9.6. References

1. Gontar, A.S., Nelidov, M.V., Nikolaev, Yu.V., and Shulepov, L.N. "Fuel Element of Nuclear Reactor." Affirmative conclusion on invention application No4926194/25 (030143) of 19.03.92 (priority of 08.04.91).
2. Borodastov, S.V., Kuptsov, G.A., Milovanov, Yu.V., and Raskach F.P. "Heat and Mass Transfer in Fuel Stacks of Thermionic Fuel Elements." Report at the Branch Jubilee Conference "Nuclear Power in the Space," Obninsk, 1990.
3. Von Jhle, P., and Rust, K. "Brennstabe mit Innenrippen." *Atomkernenergie*, 1970, Bd. 16, Lfg. 3, pp. 231-232.
4. Gontar, A.S., Sotnikov, V.N., and Shulepov, L.N. "Investigation of Influence of Inner Ribbing the Fuel Element Cladding on Fuel Temperature." *Atomic Energy*, 1995, v. 79, iss. 1, pp. 69-71.
5. Kornilov, V.A., Sinyavsky, V.V., and Yuditsky, V.D. *Inventions Official Bulletin of the Russian Federation Committee on Patents and Trade Marks.* 1994, No. 22, p.160.
6. Gontar, A.S., Shulepov, L.N., Kukin, E.B., et al. "Calculational Grounds for Design Versions of TOPAZ-3 Reactor Fuel Elements." Report of JV "Inertek", Podolsk, 1993.
7. Kotelnikov, R.B., Bashlykov, S.N., Kashtanov, A.I., and Menshikova, T.S. *High Temperature Nuclear Fuel, 2nd Ed.* Moscow: Atomizdat, 1978, 432 p.
8. Kucherov, R.Ya., Chromov, Yu.F., Shulepov, L.N., et al. "On Possibility of Creation of High Temperature Uranium Nitride Fuel Element." Report at the Branch Jubilee Conference "Nuclear Power in the Space." Obninsk, 1990.
9. Gontar, A.S., Kukin, E.B., Nelidov, M.V., and Nikolaev, Yu.V. "Possibilities of Using Alternative Fuels in a Thermionic Fuel Element." *Proc. 26th Intersociety Energy Conversion Engineering Conf.*, 1991.
10. Matthews, R., Chidester, K., Hoth, C., et al. "Fabrication and Testing of Uranium Nitride Fuel for Space Power Reactors." *Jour. Nucl. Mater.*, 1988, v. 151, No. 3, pp. 334-344.
11. Matthews, R. "Irradiation performance of Nitride Fuels." Report at the 4th Branch Conference "Nuclear Power in the Space. Materials. Fuel." Podolsk, 1993.
12. Lastman, B. *Radiation Phenomena in Uranium Dioxide.* Mocow: Atomizdat, 1964, 288 p.

13. Zakrzhevskaya, I.V., Momot, G.V., Ponomarev-Stepnoy, N.N, et al. "A Study of Gaseous Fission Products Leakage from Uranium Dioxide in High Temperature Tests." *Radiation Safety and NPS Protection*, iss. 2, Moscow: Atomizdat, 1976, 256 p.
14. Ponomarev-Stepnoy, N.N. "Nuclear Power in Space." *Atomic Energy*, v. 86, iss. 6, 1980, pp. 371-374.
15. Zaitsev, A.S., Gontar, A.S., Lebedev, A.M., et al. "Possibility of Nitride Fuel Application to TRC." Report at the 4th Branch Conference "Nuclear Power in the Space. Materials. Fuels." Podolsk, 1993.
16. Hoch, M., Dingrady, D., and Jonston, H.L. "The Vaporisation of TiN and ZrN." *J. Amer. Ceram. Soc.*, 1955, v. 77, pp. 304-306.
17. Andrievsky, R.A., Khromov, Yu.F., Svistunov, D.E., and Yurkova, R.S. "Partial Thermodynamic Characteristics of Titanium Nitride." *Jour. Phys. Chem.*, 1983, v. 57, pp. 1641-1644.
18. Khromov, Yu.F., and Lyutikov, R.A. "Partial Thermodynamic Properties of UNy in Homogeneity Area." *Atomic Energy*, 1980, v. 49, iss. 1, pp. 25-30.
19. Tagawa, H. "Phase Relations and Thermodynamic Properties of the Uranium-Nitrogen Systems." *Jour. Nucl. Mater.*, 1971, v. 51, pp. 78-89.
20. Ikeda, Y., Tataki, M., and Matsumoto, G. "Vaporisation of Uranium-Carbon-Nitrogen System." *Jour. Nucl. Mater.*, 1976, v. 59, pp. 103-111.
21. Fomenko, V.S. *Emission Properties of Materials*. Handbook. Kiev: Naukova Dumka, 1981.
22. Androsov, V.N., Ishvanov, O.L., Modin, V.A., Nikolaev, Yu.V., et al. "The Effect of the Nitrogen Mixture on the Characteristics of the Thermionic Converter." *Proc. 24th Intersociety Energy Conversion Engineering Conf.* New York, 1989.
23. Raskach, F.P., Murogov, V.M., and Troyanov, M.F. "The prospects of U-233-Based Fuel Use." Report at the 4th Branch Conference "Nuclear Power in the Space. Materials. Fuel." Podolsk, 1993.
24. Ponomarev-Stepnoi, N.N., Ogloblin, B.G., Nikolaev, Yu.V., Gontar A.S., et al. "Conceptual Design of the Bimodal Nuclear Power and Propulsion System Based on the "Topaz-2" Type Thermionic Reactor-Converter with the Modernized Single-cell Thermionic Fuel Elements." *Proc. 12th Symp. on Space Nuclear Power and Propulsion.* Albuquerque, 1995, part 2, pp. 755-760.

CHAPTER 10

PROMISING DEVELOPMENTS

A number of promising developments based on previously approved solutions and materials adopted at RI SIA "Lutch" are considered here. Such an approach will reduce the scope of required investigations and speed attainment of practical results from these developments.

10.1. Fuel Element for Power/Propulsion Systems

Ponomarev-Stepnoi et al. and Gontar et al. [1, 2] reviewed the conceptual discussions of a bimodal space system, developed on the basis of updated single-cell TFEs. The system combines the functions of the nuclear-powered rocket engine and an electric power source. This can lighten total spacecraft weight and simultaneously increase the instrumentation payload. This would allow, for example, a transition from high-power launch vehicles such as the Titan-4 to lower-power rockets such as the Atlas-2AC for launch into near-Earth orbits. Related savings would be about $20 million per launch [3].

The bimodal system under development provides electricity to on-board systems of a spacecraft with a power consumption of 20 kW (at electrical power of 25 kW in the reactor terminals). In a power/propulsion mode, an ~80 N thrust is produced with simultaneous ~5 kW electrical supply to on-board systems. The basic bimodal-system parameters are presented in Table 10.1.

As the reactor of a nuclear power propulsion system (NPPS), an updated thermionic reactor-converter is used; it is zirconium hydride-moderated, containing 88 single-cell TFEs, and adapted to pass hydrogen through the hot fuel element to produce thrust for the propulsion mode of operation.

The single-cell TFE structure developed for the TOPAZ-2 system of heightened power has been the basis for the TFE design scheme [1, 2].

The TFE design is portrayed in Figure 10.1. The TFE consists of the following parts: emitter (1) and collector (2) of the thermionic convertor, separated by an interelectrode gap (3); end leads (4-7), providing bilateral two-terminal current collection; ceramic-metal units (8-12), sealing the IEG cavity and insulating the leads from each other and from the reactor case. Separation of the collector from the reactor case is through insulation (13). The IEG is fixed with the aid of spacers (14) located in the collector. Cesium vapor feeds the IEG through a channel (15).

A fuel stack (16) is placed within the emitter to heat the hydrogen and emitter.

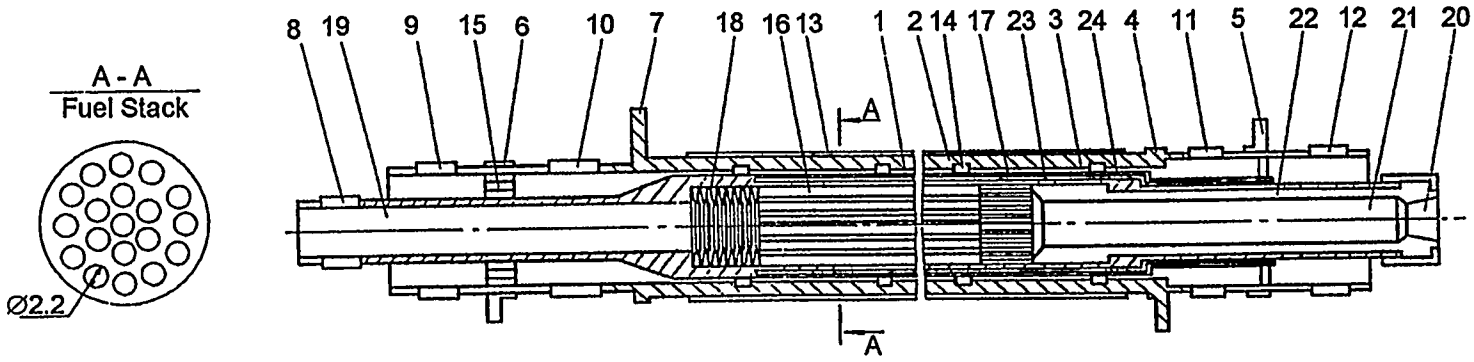

Figure 10.1. Schematic design of the TFE of a bimodal space nuclear power/propulsion system.

Table 10.1. Bimodal-system parameters [1]

Parameter	Value
Electric power in terminals of reactor-converter:	
in power mode	25
in combined mode	> 7
Thrust in propulsion mode, N	100 (possible to be increased up to 800)
Lifetime:	
- in power mode, years	7 to 10
- in propulsion mode, hrs	250

The stack is a cylindrical block with axial channels (see Section A-A). On one side, the stack abuts against a supporting grate (17), to which it is pressed by a spring (18). Hydrogen enters the IEG through a channel (19) in the TEC current lead, heats up within the TFE core, and passes through the exhaust channel (21) into a nozzle (20). Heat shielding (22) protects the TEC end parts.

To prevent hydrogen from migrating through the emitter and filling the IEG, which would adversely affect TFE power characteristics, the design includes additional cladding (23) and a ventilating channel (24) communicating with the vacuum of space. A possible method for reducing hydrogen penetration into the IEG using diffusion barriers (of, e.g., BeO, WAl_x, WB_y, or WC_x) has been analyzed [2].

The main geometric characteristics and materials of the fuel element are given in Table 10.2.

The hypostoichiometric composition of the fuel, (C/(U+Zr)=0.95-0.99), prevents a metallic uranium phase from appearing in the carbide fuel by reaction with hydrogen.

Thermal and hydraulic calculations of TFE operation in the propulsion mode have shown that altering the heat power of the TFE in the range of 9 to 84 kW can provide the required thrust of the bimodal system: from 100 to 800 N, with ~779 s specific impulse.

Basic parameters of TFE operation in the above mode vs. heat power level are contained in Table 10.3. TFE mean electric power is 200 to 250 W, and the system's full electric power reaches 15 kW [2].

In the power mode, the required level of electrical output power, W_{system}= 20 kW, and output power in the reactor terminals, W_{term}=25 kW, are provided at a TFE mean output power of W_{TFE}=285 W. The calculated thermal/electric parameters of the TFE in this mode are presented in Table 10.4.

Table 10.2. Geometric characteristics and materials of the TFE for a bimodal system [2]

Parameter	Value, Material
Length of Core, mm	400
Inner Diameter of Emitter, mm	17.1
Thickness of Emitter, mm	2.1
Width of IEG, mm	0.5
Free Volume in Fuel Element, %	40
Number of Holes in Fuel Stack	19
Diameter of Hole in Fuel Stack, mm	2.2
Fuel	hypostoichiometric uranium-zirconium alloy monocarbide ($U_{0.8}Zr_{0.2}C$)
Porosity of Fuel, %	10
Emitter	strengthened single crystal tungsten alloy
Spacers	scandia

Table 10.3. Parameters of TFE with drain gap [1]

Parameter	Version							
	1	2	3	4	5	6	7	8
Thermal Power, kW	9	11.8	24.2	34.2	44.2	54.2	64.2	84.2
Thermal Power for Hydrogen Heatup, kW	4.6	7.8	20.0	30.0	40.0	50.0	60.0	79.9
Thermal Power for Electricity Production, kW	4.4	4.0	4.2	4.2	4.2	4.2	4.2	4.3
Gas Temperature at TFE Core Outlet, K	2191	2155	2169	2169	2167	2165	2168	2166
Maximum Temperature of Fuel Stack, K	2387	2349	2432	2458	2472	2483	2496	2510
Maximum Temperature of Emitter, K	2029	1965	2083	2112	2127	2138	2150	2163
Maximum Temperature of Collector, K	842	875	876	876	877	877	878	880
Propellant Flow Rate, 10^{-4} kg/s	1.991	3.511	8.92	13.63	17.82	22.29	26.66	35.57

Table 10.4. TFE parameters vs. number and output voltage of circuits connected in parallel in reactor terminals [1]

Parameter	Value					
Number of TFE Circuits Connected in Parallel in Reactor	2	2	2	3	3	3
Output Voltage in Reactor Terminals, V	18	28	38	18	28	38
Output Voltage of TFE, V	0.41	0.64	0.87	0.62	0.96	1.30
Current, A	695	445	330	460	295	220
Heat Power of TFE, kW	-	4.15	4.10	4.15	4.10	4.25
Maximum Temperature of Emitter, °C	-	1570	1610	1570	1625	1665

TFE thermal power is here Q_{TFE}=4.10 to 4.25 kW, and the maximum emitter temperature does not exceed 1570 to 1665°C.

Calculational studies of fuel-element behavior during its life and analysis of the effectiveness of the design and processing solutions (see Table 10.2) were carried out using computer codes normalized to available results of in-pile investigations of irradiation swelling of carbide-composition fuel specimens. For $U_{0.8}Zr_{0.2}C$ of carbide composition, having an initial porosity ε=10% and open porosity fraction $\varepsilon_{open}/\varepsilon \geq$10-25%, the fuel stack channels maintain their operability for their entire 10-year life, judging by GFP removal and damping of the swelling. The relative channel contraction is ~25% over its lifetime. Deformation of an emitter made of a strengthened single-crystal tungsten alloy is negligible [2].

The bimodal system fuel-element lifetime behavior is also reviewed in Chapter 8.

10.2. Fuel Element for NPS with Out-of-Core Converter

For power supply of a number of space programs, e.g., the American SP-100 project, development of an NPS having an out-of-core system of heat-to-elecricity conversion is foreseen. Specifically, developments of one such NPS is based on the thermoelectric method of power conversion and uses a liquid-lithium-cooled fast reactor, the fuel stacks of which are fabricated from uranium nitride. Polycrystal alloys based on niobium (PWC-11) and tantalum (ASTAR-811c) are assumed to be used as the fuel-element cladding.

Table 10.5. Comparison between niobium alloys and single-crystal molybdenum alloys [4].

Parameter	PWC-11	D-43	Mo-mono1	Mo-mono2
Stress causing 1% Creep Deformation, for 1000 hrs, MPa	20	30	50	65
Cladding Weight, Related to PWC-11 Cladding, at Their Equal Creep Resistances (G/G_{PWC-11}),%	100	70	50	40

Comparison of the properties of these materials with molybdenum-single crystal alloys [4] showed that the molybdenum alloys (at typical temperatures of such fuel-element operating conditions, i.e., at T≈1200°C) are far superior in creep resistance to niobium alloys (see Figure 10.2 and Table 10.5) and similar to ASTAR tantalum alloy with 8 to 10% tungsten (see Figure 10.3). At the same creep resistance the single-crystal molybdenum alloy cladding is 2 to 2.5 times lighter than PWC-11 alloy (see Table 10.5).

Another virtue of the molybdenum alloys is that, unlike ASTAR-811c and PWC-11 used in the SP-100, they do not need protective coatings to ensure compatability between the cladding and nitride fuel (molybdenum is compatible with UN at T=1500 to 1700°C for 10,000 hrs [4]).

The molybdenum alloys have undergone long-term (up to 2 years) in-pile testing in the course of perfecting the TOPAZ-2 TFE, where the emitter temperature changed along the emitter length from ~1550°C to ~1100°C. Thus, the single-crystal molybdenum alloys may evidently be applied effectively within the framework of the SP-100 program.

Design and Data in the Calculational Study. We now consider the results of calculational investigations on fuel elements for NPSs with an out-of-core converter (like SP-100), the cladding of which is fabricated from a single-crystal molybdenum alloy [4].

The fuel element has been developed for use in a power system like the SP-100. A schematic design is displayed in Figure 10.4.

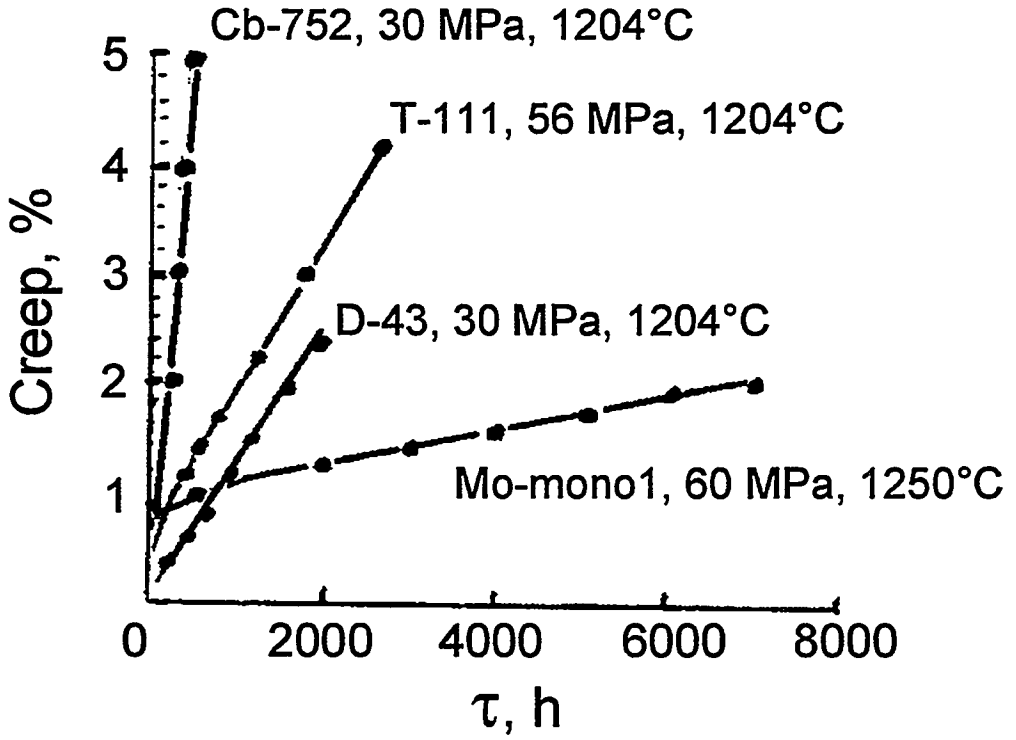

Figure 10.2. Creep curves for polycrystal alloys of niobium and tantalum and single-crystal molybdenum alloy [4].

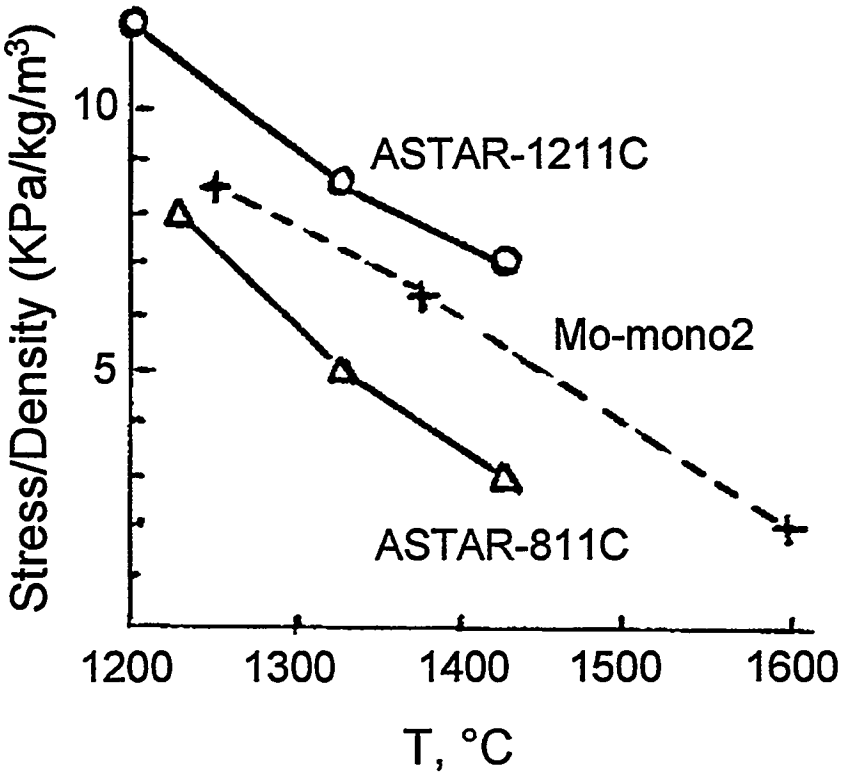

Figure 10.3. Stress producing 1% creep deformation for 1,000 hrs, related to material density [4].

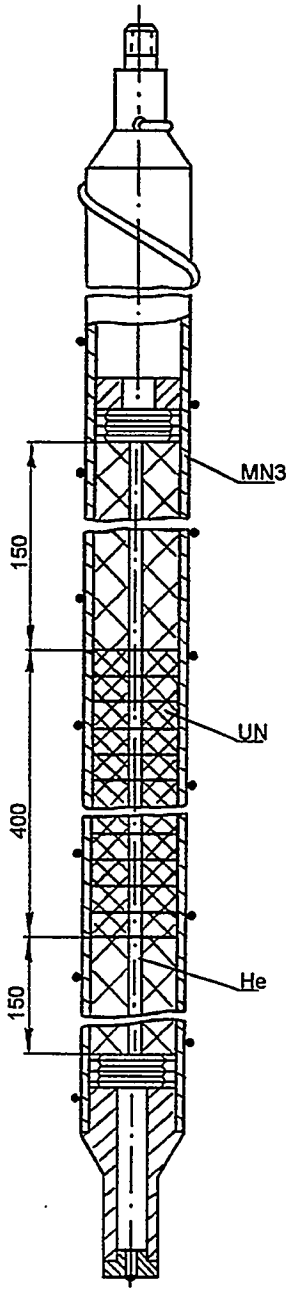

Figure 10.4. Fuel-element design scheme.

MN3 single-crystal molybdenum alloy is used as the cladding material. The outer cladding diameter is assumed to be ~10 mm, and cladding thickness, ~0.64 mm. Uranium nitride is used as the fuel stack material. Its density ranges from 90 to 95% TD.

To reduce the fuel-stack temperature, the fuel element's inner cavity is filled with a highly heat-conductive gas such as helium.

Calculational investigations of the fuel-element lifetime behavior and optimization of its design parameters were carried out using a computer code to simulate the occurrence of basic lifetime-governing processes in a gas-tight fuel element. This code considers the following factors:

- change in fuel-element temperature during operation;
- GFP release from the fuel stack and change in the thermal conductivity of the gaseous mixture within the IEG because of highly-conductive helium dilution with gaseous fission products;
- fuel-stack swelling and change in the stack/cladding gap size;
- cladding creep under internal gas pressure (given a gap between fuel stack and cladding) and fuel-stack swelling (given contact).

Calculation and optimization of the design were carried out for a 7-year fuel-element life. Experimental in-pile test data on uranium nitride free swelling at temperatures ranging from 1200 to 1500°C were used.

The calculations studied the influence of initial pressure when filling the fuel-element cavity with helium (P^{init}=0.02 to 0.5 MPa) and the effect of fuel density (ρ=90 to 95% TD), the width of the stack/cladding initial gap (δ^{init}=0.1-0.3 mm), and the value of fuel-element free volume relative to fuel-stack volume (V_k= 0.5 to 1.0).

Results for a maximum density of heat release in the fuel of 145 W/cm^3 are shown in Figures 10.5 to 10.7. Analysis of the results reveals that, for all cases, the maximum fuel-stack temperature never exceeds 1400°C (see Figure 10.5). This temperature is reached at the minimum considered helium pressure P^{init}=0.02 MPa and fuel density ρ=90% TD. Raising the initial pressure to P^{init}=0.1 MPa reduces the temperature to ~1300°C for ρ=90% TD and to ~1260°C for a fuel density of 95% TD. Under the latter helium pressure (P^{init}=0.1 Mpa) and at fuel density ranging from ρ=90 to 95% TD, cladding deformation becomes negligible for the entire 7-year life (see Figure 10.6).

A pressure of P^{init}=0.1 MPa is optimal when filling the fuel element with helium and is chosen to be applied to the suggested fuel-element design.

It follows from the above results that the free volume within the fuel element may be limited to V_k=0.5.

Data from parametric calculations substantiate the choice of the initial cladding/fuel gap width (Figure 10.7). The optimal value is ~0.13 mm. Widening the gap leads both to a rise in fuel temperature in early operation $\left(T_f^{max}(\tau = 0)\right)$ and

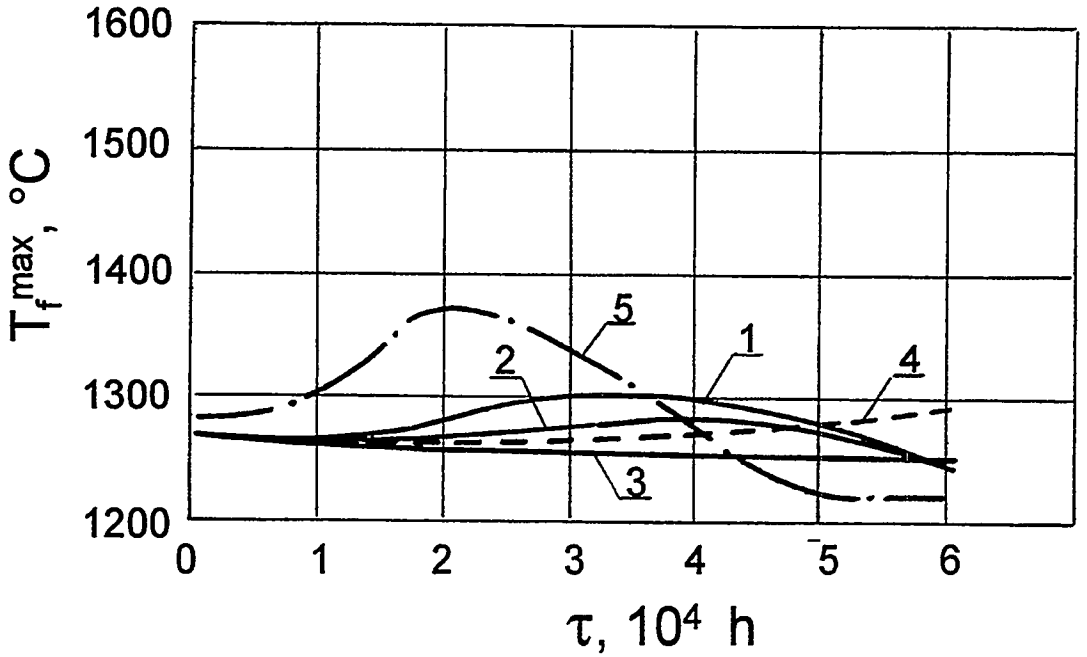

Figure 10.5. Time dependence of maximum fuel temperature:
1 - ρ=90% TD, V_k=0.5, P^{init}=0.1 MPa;
2 - ρ=90% TD, V_k=1.0, P^{init}=0.1 MPa;
3 - ρ=95% TD, V_k=0.5, P^{init}=0.1 MPa;
4 - P^{init}=0.5 MPa, ρ=90% TD, V_k=0.5;
5 - P^{init}=0.02 MPa, ρ=90% TD, V_k=0.5.

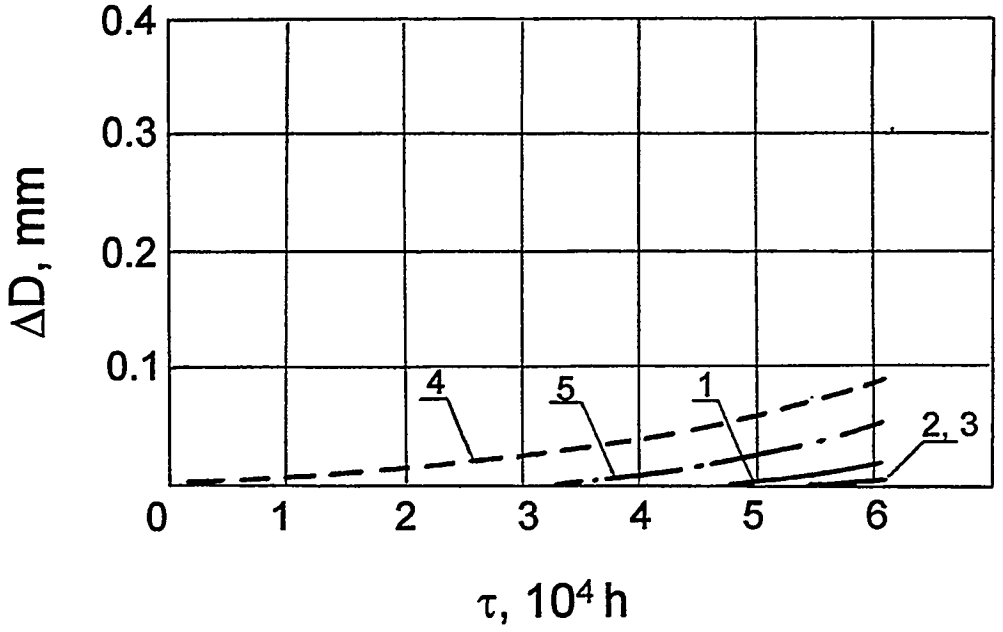

Figure 10.6. Time dependence of maximum change of fuel-element cladding diameter:
1 - ρ=90% TD, V_k=0.5, P^{init}=0.1 MPa;
2 - ρ=90% TD, V_k=1.0, P^{init}=0.1 MPa;
3 - ρ=95% TD, V_k=0.5, P^{init}=0.1 MPa;
4 - P^{init}=0.5 MPa, V_k=0.5, ρ=90% TD;
5 - P^{init}=0.02 MPa, V_k=0.5, ρ=90% TD.

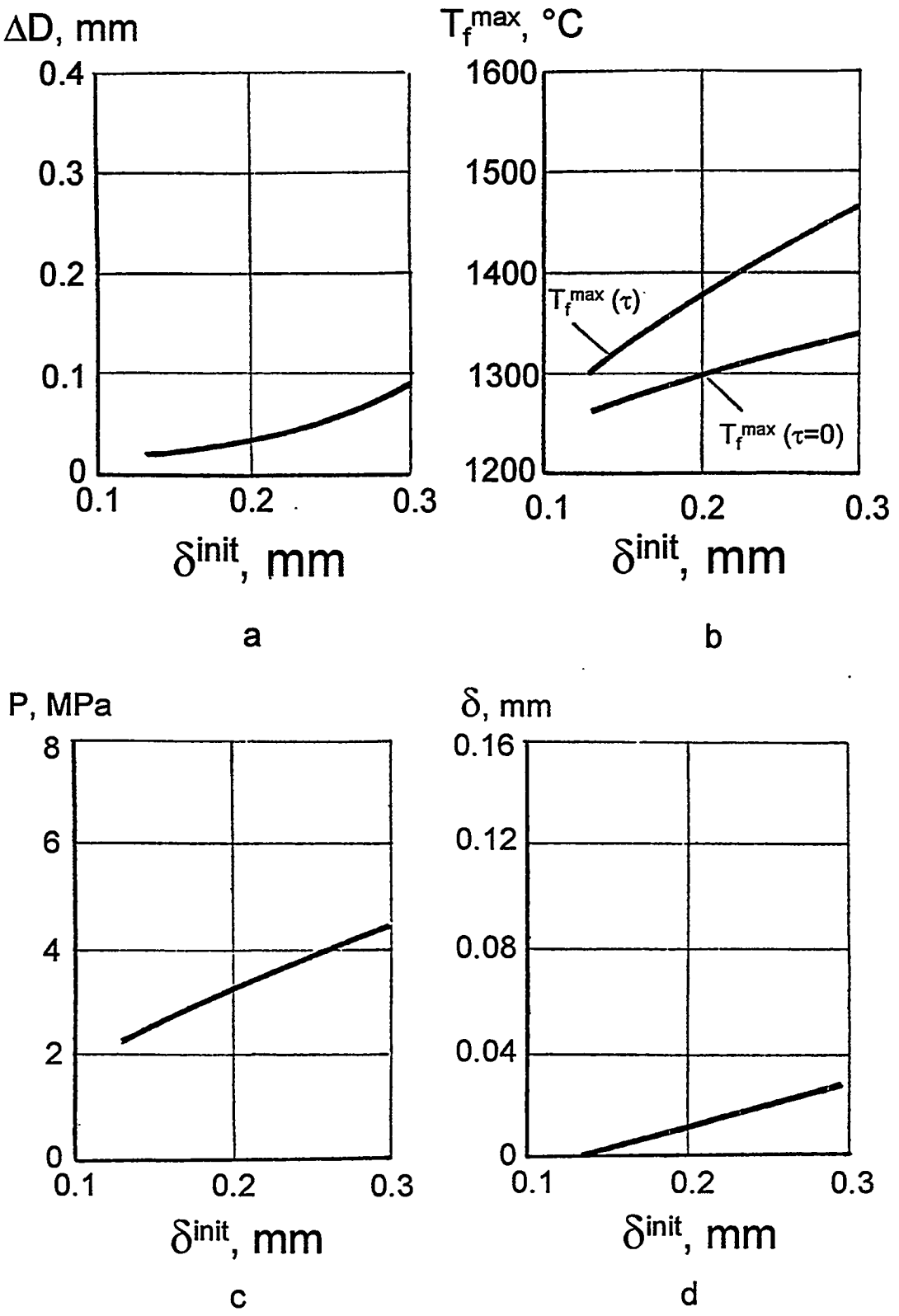

Figure 10.7. Infuence of initial value (δ^{init}) of cladding/fuel gap on main operation and lifetime parameters of fuel element (τ=7 years; V_k=0.5; ρ=90% TD, P^{init}=0.1 MPa).

to its subsequent elevation during further operation $\left(T_T^{max}(\tau)\right)$ (see Figure 10.7b). A gap of δ^{init}=0.13 cm is entirely closed only late in the lifetime specified (see Figure 10.7d), and the pressure within the fuel element, by the end of the campaign, does not exceed ~2 MPa, for this case (see Figure 10.7c).

Thus, the gas-tight fuel-element design of the NPSs, clad by MN3 single-crystal molybdenum alloy, provides a 7-year lifetime. Use of that alloy and optimization of the main fuel-element design parameters ensure high geometric stability of the cladding during the entire NPS campaign specified.

10.3. References

1. Ponomarev-Stepnoi, N.N., Ogloblin, B.G., Nikolaev, Yu.V., et al. "Conceptual design of the bimodal nuclear power and propulson system based on the "Topaz-2" type thermionic reactor-converter with the modernized single-cell thermionic fuel elements." *Proc. 12th Symposium on Space Nuclear Power and Propulsion.* Albuquerque, 1995, part 2, pp. 755-760.
2. Gontar, A.S., Nikolaev, Yu.V., et al. "Conceptual Design of TFE for Bimodal Space Nuclear Power/Propulsion Plant." Executed under the contract between STC "Istok" RI SIA "Lutch" (Russia) and Rockwell International Corporation Rocketdyne Division (USA). Podolsk, 1994.
3. Kennedy, F.G., and Vanek, V. "Summary of the bimodal satellite mission study." *Proc. 11th Symposium on Space Nuclear Power and Propulsion.* Albuquerque, 1994, part 3, pp. 1385-1390.
4. Nikolaev, Yu.V., Kolesov, V.S., et al. "Molybdenum and tungsten single crystal alloys with abnormally high creep strength for space nuclear power and propulsion systems." *Proc. 10th Symposium on Space Nuclear Power and Propulsion.* Albuquerque, 1993, part 1, pp. 267-274.

CHAPTER 11

METHODS FOR PROLONGING FUEL-ELEMENT LIFE AND PRINCIPAL DIRECTIONS OF FURTHER RESEARCH

In the course of efforts aimed at the TOPAZ program, RI SIA "Lutch" has gained considerable experience in solving the problem of TFE life extension and executed a vast scope of calculational and experimental investigations, including collection and generalization of data on long-term in-pile TFE tests both in loop channels of research reactors (single and multi-cell TFEs) and in experimental prototype TRCs (single-cell TFE).

A flow chart of research on the TFE designs under development, showing only the principal directions of these investigations, is shown in Figure 11.1.

The results of calculational and experimental studies produced the following basic solutions to prevent short circuit (the main type of failure) and simultaneously increase TFE power and lengthen TFE life:

- GFP removal from the fuel-element inner cavity;
- use of single-crystal emitter materials having high creep resistance;
- use of hypostoichiometric uranium dioxide to ensure compatability between fuel and fuel-element structural elements;
- optimizing fuel composition, structure, and temperature operating conditions to minimize swelling;
- organization of the required free volume in the fuel element, and its effective utilization during the entire lifetime;
- use of TFE design with separated cavities to provide stability of emission characteristics;
- use of spacer materials resistant to cesium plasma.

To secure these solutions, RI SIA "Lutch" developed and implemented fabrication processes for single-crystal emitters from high-temperature molybdenum and tungsten alloys having no previously existing analogues. Similar efforts were undertaken with respect to materials for spacers and for promising fuel compositions. These developments have produced a TOPAZ-2 single-cell fuel element that did not fail during ~1.5 years' testing in an experimental prototype TRC and that manifested stable electrical-output parameters. The test data and subsequent examination in hot cells demonstrate the preservation of fuel-element operability: emitter deformation along most of the TFE length is not significantly outside the tolerance zone for related fabrication processes. Fuel-element lifetime is predicted, on the basis of data from calculational and experimental investigations, to be not shorter than 3 years [1].

Results of multi-cell TFE tests in research-reactor loop channels indicate that the high geometric stability of the emitter and the stability of the converter power-

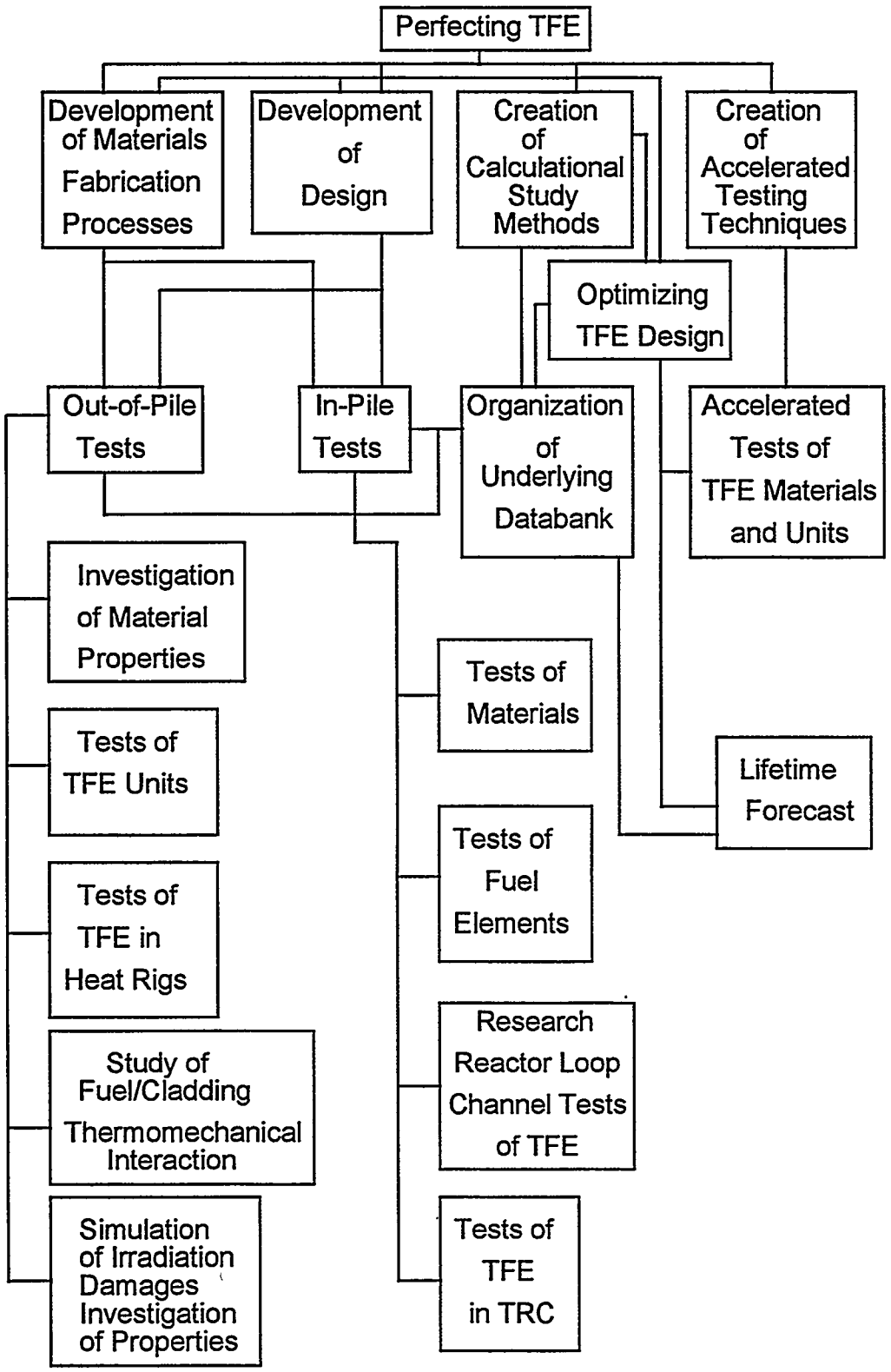

Figure 11.1. Flow chart of principal directions in thermionic fuel element design.

output characteristics have been achieved under severe thermocycling characteristic of this type of testing [2].

The experience gained, the scientific and technical potential created, and the unique materials developed may be successfully applied to the development of high-power TFEs of thermionic NPSs in a wide range of power—tens to several hundreds of kilowatts—and with lifetimes of 7 to 10 years [3]. Thus, for example, the basic design decisions and materials approved in the course of perfecting the TOPAZ-2 TFE allowed, within a short time, the creation for the Space-R reactor of a single-cell TFE design having electric power enhanced to W=300 to 400 W and an estimated lifetime of 7 to 10 years [4]. These TFE tests using electrical heating were jointly performed by a Russian/American team; in the course of testing, the TFE's high electrical output parameters were ascertained.

Notwithstanding the large scope of investigations completed, questions concerning lifetimes up to 10 years call for further advances in some calculational and experimental areas:

- development of accelerated testing methods for materials, structural units, and the TFE as a whole, to estimate its lifetime using results of short-term tests. Specifically, there must be advanced developments of fabrication processes for materials, in which either irradiation-induced processes are accelerated, or the materials' as-fabricated condition imitates the structure and other distinctive features of an irradiated material. This will shorten the time and reduce the expense for in-pile tests and allow studies of irradiation effects on material properties under out-of-pile conditions. Methods of irradiated-materials science must also be improved.
- development and perfection of comprehensive calculational procedures and software for the lifetime behavior of single and multi-cell TFEs. The work calls for extension of underlying data-sets on material properties under long-term irradiation, as well as advancing theoretical models and calculational methods for major lifetime-determining processes within the fuel element.
- studies of the influence of automated reactor-converter controls on fuel-element serviceability during long-term operation and of optimization of operating conditions.

These efforts should improve the operational reliability and simultaneously enhance the power and life extension of TFEs under development.

11.1. References

1. Vybyvanets, V.I., Gontar, A.S., Gordinsky, V.L., et al. "Experimental Elaboration of Single-Cell TFE in Heat and In-Pile Tests." Report at the Branch Jubilee Conference "Nuclear Power in the Space." Obninsk, 1990.
2. Nikolaev, Yu.V., Vybyvanets, V.I., Izhvanov, O.L., Gontar, A.S., et al. "Tests of Structural and Fuel Materials in Research Reactor Loop Channels. Report

at the 4th Branch Conference "Nuclear Power in the Space. Materials. Fuel." Podolsk, 1993.
3. Nikolaev, Yu.V. "R&D at RI SIA "Lutch" in the Area of Direct Conversion NPPs." Report at the 4th Branch Conference "Nuclear Power in Space. Materials. Fuel." Podolsk, 1993.
4. Nicolaev, Yu.V., Eremin, S.A., and Gontar, A.S. "A single-cell TFE mock-up of the thermionic nuclear power system "Space-R"." *Proc. 12th Symp. on Space Nuclear Power and Propulsion.* Albuquerque, 1995, part 2, pp. 815-820.

Distribution

MS 0459	John M. Taylor, 5335	(5)
MS 0734	Daniel M. Mulder, 6403	(20)
MS 0744	Albert C. Marshall, 6403	(2)
MS 0342	Kevin R. Zavadil, 1823	(2)
MS 0718	Regina L. Hunter, 6643	(20)
MS 0718	Evan C. Dudley, 6643	(1)
MS 9018	Central Technical Files, 8940-2	(1)
MS 0899	Technical Library, 4414	(5)
MS 0619	Review & Approval Desk, 12630 For DOE/OSTI	(2)